



BRNO UNIVERSITY OF TECHNOLOGY

VYSOKÉ UČENÍ TECHNICKÉ V BRNĚ

CENTRAL EUROPEAN INSTITUTE OF TECHNOLOGY BUT

STŘEDOEVROPSKÝ TECHNOLOGICKÝ INSTITUT VUT

**SEMIANALYTICAL APPROACH TO SIMULATIONS IN
NANOPHOTONICS**

SEMIANALYTICKÝ PŘÍSTUP K SIMULACÍM V NANOFOTONICE

DOCTORAL THESIS

DIZERTAČNÍ PRÁCE

AUTHOR

AUTOR PRÁCE

Ing. Martin Hrtoň

SUPERVISOR

ŠKOLITEL

prof. RNDr. Tomáš Šikola, CSc.

BRNO 2021

Summary

Numerical simulations have become an indispensable part of the design process in nanophotonics, which inevitably led to the development of specialized software dedicated to this task. Although there is a number of capable and commercially available options that can serve that purpose, many applications require data analysis that goes beyond the standardly offered analysis tools. The data post-processing lies at the focus of this thesis, with emphasis on the development of semianalytical models that are tailored specifically to each type of experiment, providing better insight into its physical background and improved agreement between theory and measurements. A major part of the thesis is dedicated to the plasmon enhanced electron paramagnetic resonance (PE EPR), a novel technique employing metallic antennas for enhancing the interaction between light and materials exhibiting magnetic spin transitions. Fundamental principles of this effect are laid down and a model facilitating rapid optimization of antenna arrays for thin film PE EPR spectroscopy is presented. Particular attention is paid to the current distribution and to advantages it offers when dealing with far-field projections and electromagnetic interaction between objects. This is further demonstrated on several applications, namely the phase imaging of metasurfaces using coherence controlled holographic microscope, the design of a metasurface-based fan-out element, and the multipolar analysis of far-fields generated by objects embedded within stratified media.

Abstrakt

Numerické simulace se staly nedílnou součástí procesu navrhování v nanofotonice, což nevyhnutelně vedlo k vývoji softwaru specializovaného pro tento úkol. Ačkoli je zde celá řada komerčně dostupných produktů, mnohé aplikace vyžadují datovou analýzu, která překračuje standardní výbavu těchto nástrojů. Zpracování výsledků simulací je těžištěm této práce, kdy důraz je kladen zejména na vývoj semianalytických modelů ušitých na míru jednotlivým experimentům. Spolu s lepší shodou mezi teorií a měřeními tyto modely poskytují také cenný vhled do studovaných fyzikálních procesů. Hlavní část této práce je věnována plazmonicky zesílené elektronové paramagnetické rezonanci (PE EPR), nové metodě využívající kovové antény pro zesílení interakce mezi zářením a materiály s magnetickými přechody mezi spinovými stavy. Jsou zde objasněny základní principy řídící tento jev a představen model umožňující rychlou optimalizaci polí antén pro PE EPR spektroskopii tenkých vrstev. Zvláštní pozornost je pak věnována roli indukovaného proudu a možnostem, které nabízí při projekcích do dalekého pole nebo počítání elektromagnetické interakce mezi objekty. Toto je dále demonstrováno na několika aplikacích, jmenovitě fázovém zobrazování metapovrchů pomocí koherencí řízeného holografického mikroskopu, designu optického prvku pro generování pole svazků na bázi metapovrchu a multipólové analýze elektromagnetických vln emitovaných objekty nacházejícími se uvnitř multivrstvy.

Keywords

plasmonics, nanophotonics, electron paramagnetic resonance, metasurfaces

Klíčová slova

plazmonika, nanofotonika, elektronová paramagnetická rezonance, metapovrchy

HRTOŇ, Martin. *Semianalytical approach to simulations in nanophotonics*. Brno, 2021. Doctoral thesis. Brno University of Technology. Central European Institute of Technology BUT. Supervisor Tomáš Šíkola.

Hereby I declare that I have created this work autonomously under a scientific supervision of Prof. RNDr. Tomáš Šikola, CSc. All sources, references and literature used or excerpted during the elaboration of this work are properly cited and listed in the complete reference.

Ing. Martin Hrtoň

Contents

Acknowledgements	1
Introduction	2
1 Plasmon enhanced EPR	6
1.1 Dynamic permeability model of paramagnetic materials	11
1.2 EPR interaction model	14
1.3 Antenna array interaction model	28
1.4 Benchmark tests	42
1.5 Antenna array optimization	46
1.6 Antenna array as a thin anisotropic layer	52
1.7 Rigorous treatment of the plasmon enhanced EPR effect	57
1.8 Summary and outlook	66
2 Miscellany of applications	68
2.1 Phase imaging of metasurfaces	68
2.2 Tailoring the far-field response of metasurfaces	72
2.3 Multipole expansion in stratified media	79
Conclusions	92
Appendix A	94
Appendix B	104
Bibliography	107
List of Publications	111
Attachments	112

Acknowledgements

My journey towards this thesis was long, winding and seemingly endless. I am, therefore, immensely grateful to my family and friends for their boundless patience and the relentless support they offered me during those eight years it took me to finish my doctoral studies. Special thanks go to my supervisor Prof. Tomáš Šikola, who is largely responsible for the friendly, inspiring, and altogether wonderful atmosphere permeating the rooms of our institute. I count his advices, his trust in my work, and the freedom he granted me to be amongst the chief catalysts of my scientific and personal growth. In that regard, I also wish to express my thanks to Radek Kalousek, Vlastimil Krápek, Petr Dvořák, Filip Ligmajer, and my other colleagues, who are constantly pitching me interesting ideas and valuable advices and whose friendship I deeply cherish.

Introduction

In recent years, numerical simulations have gradually become an integral part of the research in the fields of plasmonics and nanophotonics. An easy access to powerful computer clusters and availability of versatile simulation software spearheaded the progress in many areas ranging from metasurfaces and non-linear optics to light-matter interaction in 2D materials and various photonic devices. Systems that were previously considered to be too complex and impractical to simulate numerically can be nowadays tackled almost effortlessly. This was mostly facilitated by the rapid upsizing of the computation resources and the development of simulation software with specialized functionalities going beyond the ordinary scenario of calculating the field in the vicinity of a single particle illuminated by a plane wave.

This thesis strives to supplement this territory of advanced simulation analysis with a concept that relies on the current distribution induced within simulated objects rather than the fields generated by it. It should be stressed that this approach is by no means groundbreaking or overly innovative, but the author believes that it might be worthwhile to point out its advantages to the scientific community. Namely that the current distribution is better suited for the far-field radiation analysis and it is also more handy for the task of calculating the response of systems that cannot be fitted into a single simulation (e.g. large area metasurfaces or finite antenna arrays). Considering the fact that many of the measurements performed within our research group take place in the far-field and involve antenna arrays, the pursuit of this alternative approach seems to be relevant. Even though its implementation goes inevitably hand in hand with a substantial amount of programming, it also means that the resulting analysis procedures can be easily modified to suit the various situations one might encounter. In this way, we are gradually building at our institute a superstructure of methods that use the results provided by commercially available simulation software to calculate quantities that better reflect the experimental configuration and other aspects of our measurements. This effort to develop models that go beyond the standard analysis tools offered by the current versions of simulation software is essentially the common denominator of all the various research topics presented in this thesis and its title aims to highlight this fact.

To illustrate the benefits of using the current distribution instead of the electric field, let us review the standard procedure for calculating the far-field projections in software like Lumerical FDTD or Comsol. Using the method of stationary phase [1], it can be shown that the electromagnetic wave emitted by a set of spatially confined sources is, at sufficiently large distances, polarized perpendicularly to its propagation direction and it can be directly linked to the angular spectrum representation [2] of the fields near the sources. Setting the source region close to the origin of the coordinate system and denoting $\vec{s} = (s_x, s_y, s_z) = (\frac{x}{r}, \frac{y}{r}, \frac{z}{r})$ the unit vector spanning all the possible scattering directions, the electric field at the distance r from the origin then reads

$$\vec{E}_{\text{FF}}(s_x, s_y) = -2\pi i k s_z \frac{e^{ikr}}{r} \vec{E}(s_x k, s_y k, 0), \quad (\text{I.1})$$

where k designates the wavenumber and $\vec{E}(q_x, q_y, 0)$ stands for the Fourier representation of the fields within the $z = 0$ plane. Note that throughout this thesis, we employ the following definition of the spatial Fourier transform

$$\vec{E}(\vec{q}, z) = \frac{1}{4\pi^2} \iint_{-\infty}^{\infty} d\vec{r}_{\parallel}^2 e^{-i\vec{q}\cdot\vec{r}_{\parallel}} \vec{E}(\vec{r}_{\parallel}, z), \quad (\text{I.2})$$

$$\vec{E}(\vec{r}_{\parallel}, z) = \iint_{-\infty}^{\infty} d\vec{q}^2 e^{i\vec{q}\cdot\vec{r}_{\parallel}} \vec{E}(\vec{q}, z), \quad (\text{I.3})$$

with \vec{r}_{\parallel} and \vec{q} denoting the lateral spatial coordinates and frequencies, respectively.

Generally, the fields generated by the sources extend over a large area (depending on the presence of a substrate and other factors), the simulation region is, however, usually limited—at least in the case of the widely used finite difference time domain (FDTD) and finite element (FEM) methods. That inevitably leads to a cutoff in the integration over the spatial coordinates during the evaluation of the above Fourier transform. Assuming the simulation region has the shape of a cube with a side L , the Fourier representation of the fields captured within the simulation reads

$$\vec{E}_{\text{sim}}(\vec{q}, z) = \frac{1}{4\pi^2} \iint_{\Omega_{\text{sim}}} d\vec{r}_{\parallel}^2 e^{-i\vec{q}\cdot\vec{r}_{\parallel}} \vec{E}(\vec{r}_{\parallel}, z) = \frac{1}{4\pi^2} \iint_{-\infty}^{\infty} d\vec{r}_{\parallel}^2 e^{-i\vec{q}\cdot\vec{r}_{\parallel}} \text{rect}\left(\frac{x}{L}\right) \text{rect}\left(\frac{y}{L}\right) \vec{E}(\vec{r}_{\parallel}, z), \quad (\text{I.4})$$

where the rectangular function $\text{rect}(x)$ is defined as

$$\text{rect}(x) = \begin{cases} 1 & : |x| \leq \frac{1}{2} \\ 0 & : |x| > \frac{1}{2} \end{cases}. \quad (\text{I.5})$$

Recalling that the rectangular function forms a Fourier pair with the sinc function (sinus cardinalis)

$$\frac{1}{2\pi} \int_{-\infty}^{\infty} dx e^{-iqx} \text{rect}\left(\frac{x}{L}\right) = \frac{1}{2\pi} \int_{-\frac{L}{2}}^{\frac{L}{2}} dx e^{-iqx} = \frac{L}{2\pi} \text{sinc}\left(\frac{qL}{2}\right) \quad (\text{I.6})$$

we find that the Fourier transform calculated from the fields enclosed within the spatially limited simulation region amounts to the convolution of the actual Fourier transform with the sinc function

$$\begin{aligned} \vec{E}_{\text{sim}}(\vec{q}, z) &= \frac{1}{4\pi^2} \iint_{-\infty}^{\infty} d\vec{r}_{\parallel}^2 \iint_{-\infty}^{\infty} d\vec{q}'^2 e^{-i(\vec{q}-\vec{q}')\cdot\vec{r}_{\parallel}} \vec{E}(\vec{q}', z) \text{rect}\left(\frac{x}{L}\right) \text{rect}\left(\frac{y}{L}\right) = \\ &= \iint_{-\infty}^{\infty} d\vec{q}'^2 \frac{L^2}{4\pi^2} \text{sinc}\left[\left(q_x - q'_x\right)\frac{L}{2}\right] \text{sinc}\left[\left(q_y - q'_y\right)\frac{L}{2}\right] \vec{E}(\vec{q}', z). \end{aligned} \quad (\text{I.7})$$

As a consequence, the angular spectrum becomes plagued by artificial ripples that increase in magnitude as we shrink the simulation region. The only remedy is to make it large enough so that it covers the entire area where the fields are appreciable. Naturally, that is accompanied by longer simulation times and higher memory requirements.

The current distribution, on the other hand, is not vexed by this issue, since it is strictly confined to the simulated object and the finite size of the simulation region entails in that respect no loss of data. Invoking the Green's function formalism [2], the electric field generated by the object can be written as

$$\vec{E}(\vec{r}) = \int_V d\vec{r}'^3 \vec{G}(\vec{r}, \vec{r}') \vec{P}(\vec{r}'), \quad (\text{I.8})$$

where the dyadic Green's function $\vec{G}(\vec{r}, \vec{r}')$ fully describes the electric field created by a point source at every position in space and $\vec{P}(\vec{r}')$ stands for the polarization currents induced within the object. Assuming translational invariance of the environment hosting our object along the lateral spatial coordinates (that covers the majority of situations we encounter in our experiments), the convolution

of the dyadic Green’s function with the current distribution translates into a simple product between their respective Fourier transforms in the reciprocal space

$$\vec{E}(\vec{q}, z) = 4\pi^2 \int dz' \vec{G}(\vec{q}, z, z') \vec{P}(\vec{q}, z'). \quad (\text{I.9})$$

As we have stated above, the current distribution is not affected—in contrast to the electric field—by the cutoff at the simulation region boundary and its Fourier representation is, therefore, devoid of any undesired artefacts. Note that this improvement in accuracy with which one can calculate the far-fields generated by an object comes at the price of a more complex procedure that also requires the knowledge of the dyadic Green’s function and its angular spectrum representation. Fortunately, the most common and relevant case of a multilayer substrate with parallel planar interfaces belongs to the list of situations in which these quantities are known and happen to possess a tractable form.

It is perhaps questionable, whether the increased precision in far-field calculations can be perceived as a sufficient incentive to use this elaborate procedure. Putting aside the fact that the simulation regions can be made smaller (which also leads to shorter simulation times), our concept relying on currents enables the user to evaluate quantities that are inaccessible with the standard approach. As an example, we can think of a situation, in which the simulation region contains several mutually interacting objects and we would like to investigate them separately. The fields generated by the individual objects are mixed together and they cannot be decoupled, unlike the current distributions which are totally independent entities. That allows us to evaluate not only the far-field pattern for each object separately, but also the near-field or any other imaginable quantity. In fact, we use this feature in Section 2.3 to calculate the multipole expansion of Babinet dimers, i.e. a sandwich structures consisting of two Babinet-complementary antennas (in this case a diabolo antenna and an aperture of the same shape).

Another benefit derived from working with the current distribution is its easy handling when it comes to calculations involving large arrays of interacting antennas that cannot be fitted into a single simulation (e.g. due to an unfeasible memory requirements). For example, in our earlier study on the phase measurements of plasmonic metasurfaces using coherence controlled holographic microscopy (see Section 2.1 and the full article in [Attachments](#)), we approximated arrays of metallic discs by a set of electric point dipoles with moments proportionate to the integral over the current distribution induced within those discs. For larger structures, such as the titanium dioxide pillars often encountered in dielectric metasurfaces, this simplification becomes inadequate and it is necessary to use the full distribution.

This class of systems, i.e. dense arrays of strongly interacting structures, reveals yet another advantage offered by the approach we try to promote here: if we simulate a small finite array of identical objects (let us say 3×3), but choose to illuminate only the one in the center—a standard option provided by the widely used Lumerical FDTD Solutions—we obtain a current distribution that fully captures the interaction of that object with its immediate neighbors. At the same time, we suppress considerably effects arising from the disparity between the various sites within the array (the response of objects positioned in the center of an array and on its edge are different). Furthermore, by adding to the current distribution induced within the central object also the sum of the distributions induced within its neighbors, we can account for the indirect excitation stemming from the illumination of the adjacent objects (this is facilitated by the fact that all the objects are identical). In this manner, we can fully capture the interaction between adjoining structures and by increasing the size of the array to 5×5 , 7×7 , and so on, we can even include the interaction with the more distant relatives. Note that the reason for using this sophisticated procedure and not the simple and straightforward periodic boundary conditions is that the latter often leads to occurrence of unrealistically sharp features caused by the excitation of lattice resonances. In some cases, e.g. large arrays of identical antennas, this might be desirable, but in metasurfaces, where the individual constituents usually vary in optical properties, it is not. To put this whole concept into some perspective, we employed it during the

creation of a database of building blocks for dielectric metasurfaces that was subsequently utilized for the design of a 28×28 beam fan-out element. The theoretical results of this project pursued together with the Czech company Meopta are briefly outlined in Section 2.2.

Last but not least, current distributions played a crucial role also in our study of the plasmon enhanced electron paramagnetic resonance (EPR) that actually represents the bulk of this thesis (see Chapter 1) and that happens to be a part of an H2020 FET project dedicated to the development of a novel, spatially resolved technique for material analysis combining plasmonics, atomic force microscopy and EPR (<https://www.peter-instruments.eu>). Putting aside the various models developed for the purpose of elucidating the fundamental mechanisms governing this effect, the practical calculations aimed at finding the optimal antenna array design for EPR spectroscopy relied heavily on the concept of current distribution—not only for the purpose of characterizing the far-field response of antenna arrays, but more importantly, it served as a groundwork for a model we developed to account for the interaction between antennas that allowed us to avoid time demanding simulations of large arrays and to perform rapid optimization over several array and substrate parameters.

Regarding the amount of credit the author can take for the work presented in this thesis, the entire main body (unless explicitly stated otherwise) can be attributed to him. As for the articles listed in [Attachments](#), the author is responsible for the calculations and to some degree also for writing of the manuscripts. That said, it is obvious that none of that would see the light of day without the collaboration and inspirational discussions with my colleagues and other researchers.

1. Plasmon enhanced EPR

Electron paramagnetic resonance (EPR), also known as electron spin resonance (ESR), represents an experimental technique widely used in material analysis [3, 4]. Fundamentally, it is very similar to the more familiar nuclear magnetic resonance (NMR), as both rely on the interaction between magnetic moments and electromagnetic radiation. They differ only in the source of the magnetic moments—while NMR makes use of the nuclear spin, EPR exploits transitions between electron spin states. From the practical point of view, there is, however, a substantial difference between these two techniques, both in the instrumentation and the signal analysis. This partially stems from the fact that there is a relatively low number of naturally occurring paramagnetic materials. This might be perceived as a serious disadvantage, but it also opens the door to labeling techniques, where a tracer molecule containing an electron spin center is attached to an object of interest. The spin center interacts with its surroundings and this interaction is imprinted into the detected EPR signal, thus providing us with information about the properties of the target object [5, 6]. Furthermore, using multiple spin labels and their mutual interaction, one can even indirectly map the structure of complex synthetic and biological macromolecules [7, 8]. There is an abundant variety of EPR applications spanning the fields of physics, chemistry, biology, and even archeology, but their comprehensive overview is beyond the scope of this thesis and we refer the reader to [9–11] for further information on this topic.

The fundamental mechanism behind EPR is the Zeeman effect: In presence of a strong static magnetic field, potential energy of an electron depends on the orientation of its spin angular momentum, which ultimately leads to a splitting of electron energy levels. It can be most easily demonstrated on the case of a single unpaired electron with two possible spin orientations given by the spin quantum number $m_s = \pm\frac{1}{2}$. Recalling that the magnetic dipole moment of an electron is anti-parallel to its spin angular momentum and its magnitude is one Bohr magneton μ_B , the energy difference ΔE between those two spin states simply reads

$$\Delta E = g_e \mu_B B, \quad (1.1)$$

where g_e denotes the electron g -factor ($g_e \approx 2$ for a free electron) and B is the strength of the static external magnetic field. Assuming the electron is initially in the state with the lower energy, it can be promoted to the higher energy level by a photon, provided its energy matches the splitting energy ΔE . This resonant process is schematically depicted in Figure 1.1.

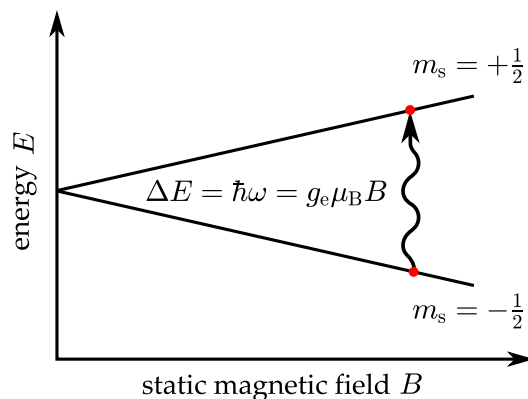


Figure 1.1: Splitting of an electron energy level in a static magnetic field. An electron transition can be induced by a photon with an energy $\hbar\omega$ that matches the energy difference ΔE between two states with opposite spin orientations.

Clearly, the energy of the electron transition is not fixed, but it depends on the magnitude of the external magnetic field: the stronger is the field, the higher is the frequency of the electromagnetic

radiation necessary to induce the transition. Measurements at high frequencies offer in general a better resolution and sensitivity, it comes, however, at a price of increased demands on the instrumentation. For example, standard measurements in the 10 – 100 GHz range require magnetic field strengths up to 3 T. In order to push the operating frequency to 1 THz, one would need a 30 T magnet. At the same time, the issue of frequency scaling is not limited only to the magnets, but it concerns also sources, spectrometers, resonators, and other components of the EPR machine.

In this regard, this thesis aims to investigate the potential of plasmonic antenna arrays to boost the signal in high-field EPR measurements of thin films. Since standard single-mode cavity resonators become too small to be manufactured in the THz spectral range, a different type of design must be found. While there are several viable alternatives [12], including various Fabry-Perot resonators with very high quality factors [13, 14], the design involving plasmonic antennas is appealing due to its relative simplicity and robustness. Another promising prospect is the possibility to mount a single plasmonic antenna on an AFM tip and build that way a scanning EPR probe, a novel concept that is currently being developed in part by our research group.

In contrast to other spectroscopic techniques such as the surface enhanced infrared absorption (SEIRA), where the plasmonic antennas are used to enhance the interaction between light and electric dipoles associated with molecular bonds, we aim to improve the coupling between electromagnetic waves and magnetic moments of electron spins, i.e. instead of antennas that exhibit strong local electric fields, we look for designs with magnetic hotspots. There is a number of antenna types fitting that requirement and each has its specific advantages. Crosses [15], for example, offer moderate field enhancement with polarization independent response, split ring resonators [16] boast with an excellent field enhancement over large area, and diabolo antennas [17] possess a very strong and localized magnetic hotspot. In our investigation of plasmonic antennas as potential candidates for replacing standard EPR resonators, we have decided to focus mainly on diabolo antennas since their magnetic hotspot is relevant to the envisioned EPR scanning probe and, as it will be shown later, they could be perspective also for large area thin film EPR spectroscopy.

Diabolo antenna consists of two large triangular wings connected by a narrow bridge, which means current is allowed to flow freely between the two sections of the antenna, a situation that is quite different from the perhaps more familiar concept of a bowtie antenna, where the wings are separated by a small gap. The working principle of a diabolo antenna is illustratively depicted in Figure 1.2(a). If an oscillating electric field is applied along the long axis of the diabolo, electrons in the wings are forced to flow back and forth through the bridge. The narrower the bridge is, the higher is the current density and consequently also the magnetic field around it. As indicated in Figure 1.2(b), there is quite a number of parameters that can be tuned to achieve the optimal performance of the diabolo antenna for a given application.

To provide the reader with some estimate of the attainable magnetic field enhancements, we plot in Figure 1.2(c) the simulated distribution of the magnetic field within a plane 20 nm above a single diabolo antenna with resonance at 3 THz ($\lambda = 100 \mu\text{m}$). Its length was $L = 11.4 \mu\text{m}$, height $H = 100 \text{ nm}$, the vertex angle of the triangular wings $\vartheta = 60^\circ$, while both the length and the width of the bridge were set to $G = 500 \text{ nm}$ and $W = 200 \text{ nm}$, respectively. Regarding the materials, the diabolo antenna was made of gold (fitted Drude model [18]) and placed on top of a silicon substrate with refractive index $n = 3.41$. Furthermore, the structure was illuminated from the top by a plane wave at normal incidence. As one would expect, the map of the magnetic field clearly shows a hotspot around the bridge of the diabolo antenna, with a maximum value of the magnetic field enhancement close to 80. Even though this number may seem quite large, the volume of the hotspot is relatively small and the overall signal enhancement for the EPR spectroscopy of thin films might be therefore comparatively lower. On the other hand, the apparent strong localization of the hotspot could be beneficial for the envisioned EPR microscopy. For completeness, we also show the electric field distribution of the same antenna in Figure 1.2(d), where the dipolar character of the charge distribution with the highest field intensity at the corners and far edges of the antenna is clearly visible. Note that the reason for plotting

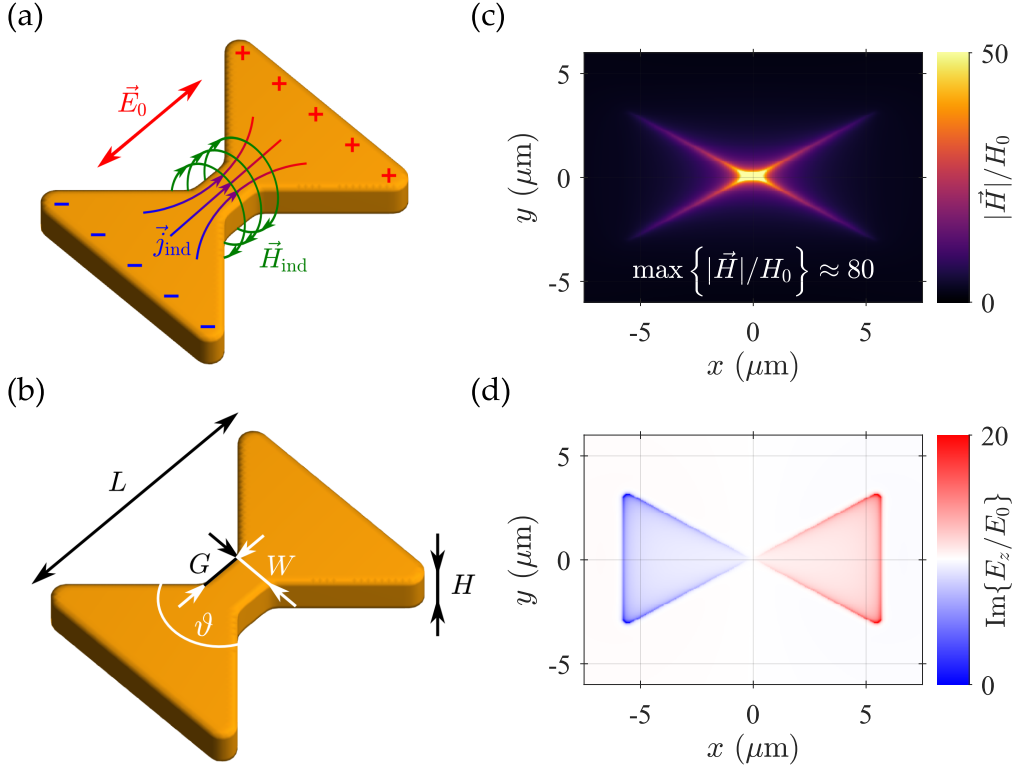


Figure 1.2: (a) The existence of a magnetic hotspot in a diabolo antenna is the result of funneling current through a narrow bridge connecting two large electron reservoirs. (b) Various parameters of the diabolo antenna that can be tuned to attain optimal antenna performance. (c) Magnetic field distribution 20 nm above a diabolo antenna with a fundamental resonance at 3 THz. The magnetic field enhancement in the hotspot reaches values up to 80 when tuned to the plasmonic resonance. (d) Map of the z -component of the electric field reveals the dipolar character of the fundamental resonance with a single node at the center of the antenna.

the imaginary part of E_z/E_0 is the fact that right in the resonance, the driving field and the field associated with the plasmon mode are mutually shifted in phase by $\pi/2$.

Since EPR is a spectroscopic technique, it is implicit that we need to know the response of our plasmonic structure within a certain frequency range. Using finite-difference time-domain (FDTD) calculations, we can simulate such a response quite efficiently. As FDTD simulations in the THz region can be rather time-consuming, especially when the structure has small features such as the narrow bridge in the large diabolo antenna, we decided at first to examine its behaviour in the infrared spectral region. The simulations (see Figure 1.3) revealed that the resonant wavelength scales linearly with the length of the diabolo antenna (similarly to a simple rod antenna). This enables us to easily tailor the size of the diabolo to the desired operation frequency. Similar behaviour was also observed for the maximum value of the magnetic field enhancement.

To confirm this simple linear scaling law experimentally, several antenna arrays with various nominal resonance frequencies were fabricated and subsequently measured using the Fourier transform infra-red spectroscopy (FTIR). At the same time, we also varied the array pitch to assess the effects of inter-antenna interaction on the spectral position and quality of the resonance. Naturally, this pressed us to run another set of simulations that would mimic the behaviour of the entire antenna array. Working under the assumption that the response of an antenna is most affected by its immediate neighbours and long range interaction can be neglected, we settled for simulations of a 5×5 sub-arrays, which are computationally not too demanding and proved to be adequate for our purposes.

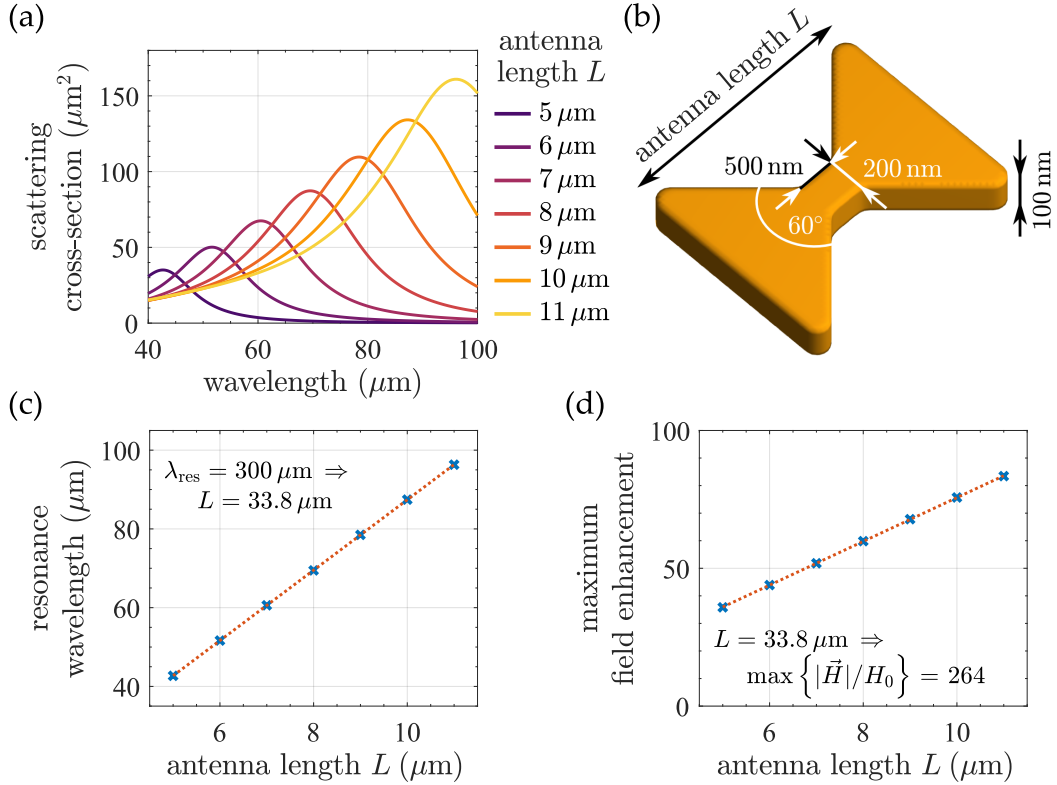


Figure 1.3: (a) Scattering cross-section spectra of diablo antennas with lengths varying between 5 and 11 μm . The simulation settings and remaining geometrical parameters [see panel (b)] were kept the same as for the diablo antenna shown in Figure 1.2. (c) Simulations indicate that the resonance wavelength λ_{res} scales linearly with the antenna length L , making any adjustments to the operation frequency quite straightforward. Extrapolation of the linear dispersion to the THz spectral range then yields antenna length approximately 34 μm for a plasmonic resonance centered at 1 THz. (d) The maximum magnetic field enhancement also exhibits a linear dependence on the antenna length, with projected value around 250 at the 1 THz frequency.

The experimental spectra along with the results of FDTD calculations are plotted in Figure 1.4. Since the outputs of the measurements and simulations are different quantities (relative reflectance vs. scattering efficiency), their comparison cannot be absolute. It does not prevent us, however, from making some conclusions regarding the general behaviour and spectral positions of the observed plasmonic resonances. Firstly, the linear scaling of the resonance frequency with the antenna length was corroborated both by the experiment and the simulations of the small sub-arrays. Secondly, the deviation of the actual resonance frequency from the nominal one depends on the array pitch (it gets larger as the arrays become denser). This is not surprising, as the nominal frequencies were based on single antenna simulations and the more closely are the antennas packed, the stronger is their mutual interaction and the impact on their collective response. Nevertheless, this effect should be taken into account when designing antenna arrays required to operate at a specific frequency. Lastly, the simulations enabled us to identify the origin of the secondary peak that was not perceptible in the calculations of solitary antennas and which becomes more and more pronounced as the array pitch is decreased. It turns out that it belongs to the transverse mode of the diablo antenna, i.e. plasmonic oscillations perpendicular to the long axis of the diablo. Still, in terms of its spectral position, it is well separated from the fundamental mode and we can easily neglect it in our further analysis.

Apart from the length, one could naturally run simulation sweeps over all the remaining geometrical parameters of the diablo antenna and various substrate and antenna materials, but without the

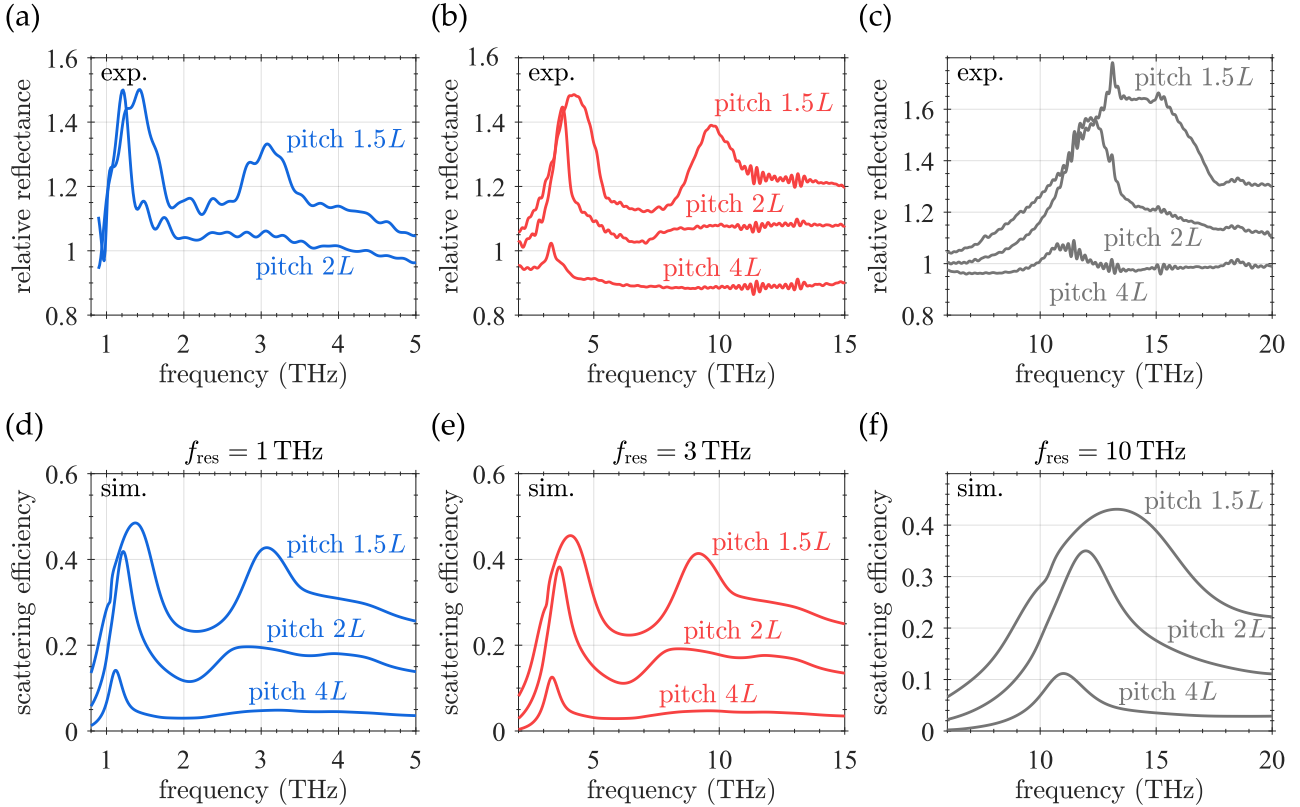


Figure 1.4: The top row panels show the measured relative reflectance of diabolo antenna arrays designed to operate at 1 THz (a), 3 THz (b), and 10 THz (c). These nominal resonance frequencies were determined from the linear scaling law observed for solitary antennas and shown in Figure 1.3. The actual resonance frequencies differ from the nominal ones and the magnitude of this spectral shift depends mainly on the array pitch, which we gradually decreased from 4 multiples of the antenna length L to $2L$ and finally to $1.5L$. The bottom row panels (d), (e), and (f) show the simulated scattering efficiency (defined as the ratio of the scattering and geometrical cross-sections) of 5×5 diabolo antenna arrays with the same geometrical parameters as their counterparts in (a), (b), and (c). Despite the substantial reduction of the array size in the simulations, the agreement with the experimental data is very satisfactory. Note that the source employed in the FTIR spectrometer used for the measurement was unpolarized. This is reflected also in the calculations where each of the plotted spectra is a sum of the results obtained for two mutually orthogonal polarizations. The appearance of the secondary peak (that gets more pronounced as we decrease the pitch array) can be then traced to the excitation of the diabolo antenna along its shorter axis. All the antenna arrays were fabricated by Peter Kepič and subsequently characterized by Filip Ligmajer. The results of their work are presented here with their permission.

knowledge which quantity should be optimized to achieve the best performance in EPR experiments, such an effort would be rather pointless. To that end, we developed an analytical model that comprehensively describes the interaction between a plasmonic antenna and an EPR material and enables us to identify the so far missing figure of merit necessary for the antenna design optimization. Before we move on to the presentation of this model and its outputs, we need, however, to understand more deeply the EPR process, namely the mathematical description of the interaction between electromagnetic radiation and the electron spins. This is crucial not only for gaining a better insight into the problem, but also for the ability to incorporate an EPR material into numerical simulations and thus validate the findings and observations inferred from the analytical model.

1.1. Dynamic permeability model of paramagnetic materials

Our intention to include EPR-active materials into electromagnetic simulations, so that we can rigorously assess the effect of plasmonic antennas on the strength of the EPR signal, goes hand in hand with the necessity to introduce the magnetic interaction in a form that is compatible with the standard tools used for optical simulations. In most of them, the dynamical permeability $\mu(\omega)$ is the parameter that carries the information about how a material responds to an external magnetic field. The EPR community, on the other hand, works primarily with electron spins and their magnetic moments. The two approaches can be unified, provided the collective behaviour of the spins can be described by a macroscopic magnetization vector \vec{M} and the response to the external magnetic field \vec{H} is linear, i.e. $\vec{M} = \vec{\chi}_m \vec{H}$, where $\vec{\chi}_m$ stands for the magnetic permeability tensor. We shall further treat the electrons within the magnetic material as isolated so that their gyromagnetic ratio is simply $\gamma_e \approx -e/m_e$, where e designates the elementary charge and m_e stands for the electron rest mass. Even though there are certain classes of EPR effects that are lost by making these approximations, the fundamental mechanism leading to resonant absorption of electromagnetic radiation is preserved. Anyway, as our interest lies mainly in the understanding of the basic interaction between plasmonic antennas and the spin centers, this simplified description of their collective response is utterly sufficient for our purposes. The influence of the plasmonic antennas on the more complex EPR effects can be in future assessed by generalizing the findings presented in this thesis.

The time evolution of the macroscopic magnetization vector associated with the electron spins can be phenomenologically described by the Bloch equations [10, 19]

$$\frac{d\vec{M}}{dt} = \vec{M} \times \gamma_e \left[\vec{B}_{\text{stat}} + \vec{B}_{\text{osc}}(t) \right] - \vec{R} \left(\vec{M}(t) - \vec{M}_0 \right), \quad (1.2)$$

where the relaxation term $\vec{R} \left(\vec{M}(t) - \vec{M}_0 \right)$ ensures that after switching off the perturbing time-dependent field $\vec{B}_{\text{osc}}(t)$, the magnetization tends to some equilibrium value \vec{M}_0 given by the static magnetic field \vec{B}_{stat} . For simplicity, let us suppose that our static magnetic field is oriented along the z -axis, while the vector of the perturbing field lies in the xy -plane, i.e. the static and the perturbing fields are perpendicular to each other. Moreover, we shall assume that the perturbing field oscillates with a frequency ω and is circularly polarized with handedness determined by the sign in the expression for B_y . Namely, the plus sign corresponds to the left-handed (\odot) and the minus sign to the right-handed (\ominus) circular polarization.

$$B_x = B_{\text{osc}} \cos \omega t, \quad (1.3)$$

$$B_y = \pm B_{\text{osc}} \sin \omega t, \quad (1.4)$$

$$B_z = B_{\text{stat}}. \quad (1.5)$$

With such a definition of magnetic fields, the Bloch equations read

$$\frac{dM_x}{dt} = \gamma_e (M_y B_z - M_z B_y) - \frac{M_x}{T_2}, \quad (1.6)$$

$$\frac{dM_y}{dt} = \gamma_e (M_z B_x - M_x B_z) - \frac{M_y}{T_2}, \quad (1.7)$$

$$\frac{dM_z}{dt} = \gamma_e (M_x B_y - M_y B_x) - \frac{M_z(t) - M_0}{T_1}. \quad (1.8)$$

Introduction of two different relaxation times T_1 and T_2 reflects the fact that the transverse components of the magnetization vector (with respect to the static field) usually relax to the equilibrium at a

1.1. DYNAMIC PERMEABILITY MODEL OF PARAMAGNETIC MATERIALS

different rate than the longitudinal one. In the stationary state, the longitudinal magnetization will be constant so that only the transverse components will vary with time, hence

$$M_x = \alpha_1^x \cos \omega t + \alpha_2^x \sin \omega t, \quad (1.9)$$

$$M_y = \alpha_1^y \cos \omega t + \alpha_2^y \sin \omega t, \quad (1.10)$$

$$M_z = \text{const.}, \quad (1.11)$$

where the coefficients $\alpha_i^{x,y}$ are yet to be determined. After inserting all these expressions into Bloch equations, capitalizing on the time invariance of M_z and comparing separately terms containing $\cos \omega t$ and $\sin \omega t$, we obtain

$$\pm \alpha_1^x = \pm M_0 \frac{\gamma_e B_{\text{osc}} \Omega_{\pm} T_2^2}{1 + \Omega_{\pm}^2 T_2^2 + \gamma_e^2 B_{\text{osc}}^2 T_1 T_2}, \quad (1.12)$$

$$\pm \alpha_2^x = \mp M_0 \frac{\gamma_e B_{\text{osc}} T_2}{1 + \Omega_{\pm}^2 T_2^2 + \gamma_e^2 B_{\text{osc}}^2 T_1 T_2}, \quad (1.13)$$

$$\pm \alpha_1^y = M_0 \frac{\gamma_e B_{\text{osc}} T_2}{1 + \Omega_{\pm}^2 T_2^2 + \gamma_e^2 B_{\text{osc}}^2 T_1 T_2}, \quad (1.14)$$

$$\pm \alpha_2^y = M_0 \frac{\gamma_e B_{\text{osc}} \Omega_{\pm} T_2^2}{1 + \Omega_{\pm}^2 T_2^2 + \gamma_e^2 B_{\text{osc}}^2 T_1 T_2}, \quad (1.15)$$

$$M_z = M_0 \frac{1 + \Omega_{\pm}^2 T_2^2}{1 + \Omega_{\pm}^2 T_2^2 + \gamma_e^2 B_{\text{osc}}^2 T_1 T_2}, \quad (1.16)$$

$$\Omega_{\pm} = \omega \pm \omega_0, \quad (1.17)$$

where the Larmour frequency $\omega_0 = \gamma_e B_{\text{stat}}$ is inherently related to the energy of the magnetic transition between the two possible spin states of our system. Note that the transition is always sensitive only to one of the two circular polarization states. Which one depends on the orientation of the static magnetic field \vec{B}_{stat} . If it points in the positive direction of the z -axis, the transition is induced by the left-handed polarization (keep in mind that $\gamma_e < 0$), while for the opposite orientation, it is the right-handed polarization that is being absorbed by the magnetic material.

As we are looking for a complex anisotropic tensor ξ that would allow us to link the magnetization and the perturbing magnetic field by a simple linear constitutive relation $\vec{M} = \xi \vec{B}$, it will be more convenient to switch to complex notation and work with expressions that describe the system's response to linearly polarized perturbing fields instead of the circularly polarized ones. Let us start with a perturbing magnetic field polarized along the x -axis, $\vec{B}_{\text{osc}} = B_{\text{osc}} \text{Re} \{ e^{-i\omega t} \} \hat{x}$, where \hat{x} denotes the unit vector in the direction of the x -axis. The components of the tensor ξ can be constructed from the coefficients $\alpha_i^{x,y}$ by taking their appropriate linear combination ($\hat{x} \sim \frac{\circlearrowleft + \circlearrowright}{2}$).

$$M_x = \text{Re} \{ \xi_{xx} B_{\text{osc}} e^{-i\omega t} \} = B_{\text{osc}} (\text{Re} \{ \xi_{xx} \} \cos \omega t + \text{Im} \{ \xi_{xx} \} \sin \omega t), \quad (1.18)$$

$$M_y = \text{Re} \{ \xi_{yx} B_{\text{osc}} e^{-i\omega t} \} = B_{\text{osc}} (\text{Re} \{ \xi_{yx} \} \cos \omega t + \text{Im} \{ \xi_{yx} \} \sin \omega t), \quad (1.19)$$

$$M_{x(y)} = \frac{+\alpha_1^{x(y)} + -\alpha_1^{x(y)}}{2} \cos \omega t + \frac{+\alpha_2^{x(y)} + -\alpha_2^{x(y)}}{2} \sin \omega t, \quad (1.20)$$

After comparing the terms in front of $\cos \omega t$ and $\sin \omega t$, we obtain

$$\xi_{xx} = \frac{M_0 \gamma_e \omega_0}{\omega_0^2 - \omega'^2}, \quad (1.21)$$

$$\xi_{yx} = -i \frac{M_0 \gamma_e \omega'}{\omega_0^2 - \omega'^2}, \quad (1.22)$$

with $\omega' = \omega + i/T_2$. Please note that in the above expression, we have entirely omitted the term $\gamma_e^2 B_{\text{osc}}^2 T_1 T_2$, which is justifiable for sufficiently low microwave source powers. The two remaining unknown components of $\vec{\xi}$ can be deduced in a similar manner. If we set the perturbing magnetic field to $\vec{B}_{\text{osc}} = B_{\text{osc}} \text{Re} \{ e^{-i\omega t} \} \hat{y}$ and recall that $\hat{y} \sim \frac{\circlearrowleft - \circlearrowright}{2}$, transverse components of the magnetization vector read

$$M_x = \text{Re} \{ i \xi_{xy} B_{\text{osc}} e^{-i\omega t} \} = B_{\text{osc}} (-\text{Im} \{ \xi_{xy} \} \cos \omega t + \text{Re} \{ \xi_{xy} \} \sin \omega t), \quad (1.23)$$

$$M_y = \text{Re} \{ i \xi_{yy} B_{\text{osc}} e^{-i\omega t} \} = B_{\text{osc}} (-\text{Im} \{ \xi_{yy} \} \cos \omega t + \text{Re} \{ \xi_{yy} \} \sin \omega t), \quad (1.24)$$

$$M_{x(y)} = \frac{+\alpha_1^{x(y)} - \alpha_1^{x(y)}}{2} \cos \omega t - \frac{+\alpha_2^{x(y)} + \alpha_2^{x(y)}}{2} \sin \omega t, \quad (1.25)$$

Then, comparison of the terms in front of $\cos \omega t$ and $\sin \omega t$ yields

$$\xi_{xy} = i \frac{M_0 \gamma_e \omega'}{\omega_0^2 - \omega'^2}, \quad (1.26)$$

$$\xi_{yy} = \frac{M_0 \gamma_e \omega_0}{\omega_0^2 - \omega'^2}. \quad (1.27)$$

The complex tensor $\vec{\xi}$ can be now written in the following compact form

$$\vec{\xi} = \frac{M_0 \gamma_e}{\omega_0^2 - \omega'^2} \begin{bmatrix} \omega_0 & i\omega' & 0 \\ -i\omega' & \omega_0 & 0 \\ 0 & 0 & 0 \end{bmatrix}, \quad (1.28)$$

where we have drawn on the fact that the magnetic transition can be induced only by a magnetic field that oscillates in the plane perpendicular to the static magnetic field and all the components associated with the z -axis are therefore zero. Although the above expression already links the magnetization vector to the magnetic field, standard material relations are defined for the auxiliary magnetic field \vec{H} . Recalling that $\vec{B} = \mu_0 \vec{\mu} \vec{H}$ and $\vec{M} = \vec{\xi} \vec{B} = \vec{\chi} \vec{H} = (\vec{\mu} - \vec{I}) \vec{H}$, where $\vec{\chi}$ represents the magnetic susceptibility tensor, we find the relation between $\vec{\xi}$ and the magnetic permeability $\vec{\mu}$ to be

$$\vec{\mu} = (\vec{I} - \mu_0 \vec{\xi})^{-1}, \quad (1.29)$$

which eventually leads to

$$\vec{\mu} = \begin{bmatrix} 1 + \frac{\kappa(\omega_0 - \kappa)}{(\omega_0 - \kappa)^2 - \omega'^2} & i \frac{\kappa \omega'}{(\omega_0 - \kappa)^2 - \omega'^2} & 0 \\ -i \frac{\kappa \omega'}{(\omega_0 - \kappa)^2 - \omega'^2} & 1 + \frac{\kappa(\omega_0 - \kappa)}{(\omega_0 - \kappa)^2 - \omega'^2} & 0 \\ 0 & 0 & 1 \end{bmatrix}. \quad (1.30)$$

where $\kappa = M_0 \gamma_e \mu_0$. So far, the sensitivity of our system to the handedness of the oscillating magnetic field was encoded in the polarity of the static magnetic field B_{stat} . If we express it explicitly, i.e.

$B_{\text{stat}} = \pm |B_{\text{stat}}|$, and change the Larmour frequency ω_0 and the magnetization M_0 accordingly, the magnetic permeability tensor becomes

$$\vec{\mu} = \begin{bmatrix} 1 + \frac{\kappa(\omega_0 - \kappa)}{(\omega_0 - \kappa)^2 - \omega'^2} & \pm i \frac{\kappa\omega'}{(\omega_0 - \kappa)^2 - \omega'^2} & 0 \\ \mp i \frac{\kappa\omega'}{(\omega_0 - \kappa)^2 - \omega'^2} & 1 + \frac{\kappa(\omega_0 - \kappa)}{(\omega_0 - \kappa)^2 - \omega'^2} & 0 \\ 0 & 0 & 1 \end{bmatrix}. \quad (1.31)$$

The Larmour frequency is now defined as $\omega_0 = \gamma_e |B_{\text{stat}}|$, $\kappa = |M_0| \gamma_e \mu_0$ and the choice of the sign in the off-diagonal components explicitly states whether the static magnetic field points in the positive (upper) or the negative (lower) direction of the z -axis.

Even though the above model is already suitable both for analytical calculations and implementation into majority of available simulation tools, it can be recast into a slightly more tractable form if we put it into perspective and consider some realistic values for its parameters. Assuming the density of the spin centers n_s is of the order of 10^{27} m^{-3} and the magnitude of the static magnetic field is such that the magnetic transition occurs at 300 GHz, then $\kappa = |M_0| \gamma_e \mu_0 = \frac{1}{2} \mu_0 \hbar n_s \gamma_e^2 \approx 0.001 \omega_0$ which means it can be safely neglected against ω_0 . Furthermore, since the linewidths of EPR transitions are generally very narrow, ω' in the numerator of μ_{xy} and μ_{yx} can be replaced by $-\omega_0$ (the minus sign comes from the fact that $\gamma_e < 0$). Consequently, the magnetic permeability tensor can be now expressed in terms of a single Lorentzian function $\chi(\omega)$

$$\chi(\omega) = \frac{\kappa\omega_0}{\omega_0^2 - \omega^2 - 2i\omega/T_2}, \quad (1.32)$$

$$\vec{\mu} = \begin{bmatrix} 1 + \chi(\omega) & \mp i\chi(\omega) & 0 \\ \pm i\chi(\omega) & 1 + \chi(\omega) & 0 \\ 0 & 0 & 1 \end{bmatrix}. \quad (1.33)$$

This symmetrical form of the dynamical permeability tensor clearly demonstrates the sensitivity of EPR transitions to circular polarization and we shall further use it in the analysis of the interaction between magnetic materials and plasmonic antennas. Due to a restriction inherent to our software (Lumerical FDTD) that the permeability tensor can possess only diagonal anisotropy, we will also need the following simplified version

$$\vec{\mu}_D = \begin{bmatrix} 1 + \chi(\omega) & 0 & 0 \\ 0 & 1 + \chi(\omega) & 0 \\ 0 & 0 & 1 \end{bmatrix}. \quad (1.34)$$

Note, that by dropping the off-diagonal terms, all the characteristic features of the magnetic transition are preserved, except the sensitivity to circular polarization, which is inevitably lost. This is, however, acceptable to us, since we use the FDTD simulations of antennas covered by a magnetic material only for validation purposes.

Finally, we would like to point out that when one chooses to follow the $e^{i\omega t}$ convention (used e.g. in Comsol), appropriate changes in signs have to be made. As it turns out, the resulting permeability tensor is just the complex conjugate of the one derived above.

1.2. EPR interaction model

To better understand how the plasmonic antenna interacts with the magnetic material and which parameters of the antenna should be optimized to maximize the EPR signal, we adopted a simple analytical model, in which the antenna is treated as a point dipole [20]. Despite this gross simplification,

the model proved to be rather accurate and provided a valuable insight into the mechanism of the interaction. The validity of this approximation is further underlined by work of other research groups, e.g. analysis of the interplay between scattering and absorption in SEIRA [21]. In the following, we shall at first derive an analytical model for a single antenna without any magnetic interaction. Later, we shall incorporate it as a perturbation to the response of the bare antenna. Finally, we shall adjust the single antenna model to the case of an infinite antenna array which is perhaps more pertinent to the real EPR spectroscopic measurements.

Let us start with writing down the equation of motion for the electric dipole moment \vec{p} associated with the plasmonic antenna

$$\frac{d^2\vec{p}}{dt^2} + \gamma_i \frac{d\vec{p}}{dt} + \omega_0^2 \vec{p} = \beta \vec{E}(t), \quad (1.35)$$

where ω_0 designates the natural resonance frequency of the antenna, γ_i its ohmic losses and the factor β ties the electric dipole moment to the electric field $\vec{E}(t)$ that drives it. Assuming a harmonic time dependence $e^{-i\omega t}$ for both the driving electromagnetic wave and the antenna response, the previous equation becomes

$$\vec{p}(\omega_0^2 - \omega^2 - i\omega\gamma_i) = \beta (\vec{E}_0 + \vec{E}_{RR}). \quad (1.36)$$

Note that the driving field comprises not only the incident field \vec{E}_0 but also the field \vec{E}_{RR} emitted by the dipole itself. This back-action is often described as the radiation reaction force [2] and it is necessary to include it in order to account for the scattering losses. In fact, this term grows in importance as we shift towards the THz spectral region and eventually, scattering becomes the primary loss channel into which the plasmonic antenna dissipates the energy imparted by the incident electromagnetic wave. Since the radiation reaction term reflects the scattering properties of the antenna, the exact expression for it depends on the surroundings of the antenna. Assuming it is embedded inside a homogeneous medium with a refractive index n , the power radiated by the antenna reads

$$P_{\text{rad}} = \frac{n^3 \omega^4 |\vec{p}|^2}{12\pi \varepsilon_0 c^3}, \quad (1.37)$$

with c denoting the speed of light and ε_0 the vacuum permittivity. At the same time, this radiated power has to be identical to the rate with which the antenna dissipates energy [2]

$$P_{\text{rad}} = \frac{dW}{dt} = -\frac{1}{2} \int_V dV \operatorname{Re} \left\{ \vec{j}^* \cdot \vec{E} \right\} = \frac{\omega}{2} \operatorname{Im} \left\{ \vec{p}^* \cdot \vec{E}_{RR} \right\}, \quad (1.38)$$

where we used the fact that in the case of a point dipole, the current density reads $\vec{j} = -i\omega\vec{p}\delta(\vec{r})$, with $\delta(\vec{r})$ being the Dirac delta function. The expression for the radiation reaction term can then be readily deduced by comparing Equations (1.37) and (1.38)

$$\vec{E}_{RR} = i \frac{n^3 \omega^3}{6\pi \varepsilon_0 c^3} \vec{p}. \quad (1.39)$$

Its insertion into Eq. (1.36) and introduction of a parameter $\gamma_r = n^3\beta/(6\pi\varepsilon_0c^3)$ allows us to express the dipole moment of the antenna in the following concise form

$$\vec{p} = \frac{6\pi\varepsilon_0c^3}{n^3} \frac{\gamma_r}{\omega_0^2 - \omega^2 - i\omega(\gamma_i + \gamma_r\omega^2)} \vec{E}_0. \quad (1.40)$$

The new parameter γ_r plays a similar role as γ_i , except it corresponds to radiative losses. It is worth noting that according to the above equation, the ohmic losses become more dominant as we decrease the frequency. This would seem to be, however, in contradiction with our previous statement that it

is actually the other way around. The catch is hidden in the distinction between making ω smaller and shifting the whole system towards lower frequencies. The latter is usually achieved by making the antenna larger and it is well known that scattering scales with the object size more rapidly than the absorption [22]. In our model, this will be reflected in the gradual relative increase of γ_r with respect to γ_i , with scattering ultimately gaining the upper hand.

The optical properties of antennas are usually described in terms of their scattering and absorption cross-sections. With the expression for the dipole moment of the antenna at hand, these two quantities are readily calculated using the following formulas

$$C_{\text{sca}} = \frac{n^3 \omega^4 |\vec{p}|^2}{12\pi \varepsilon_0 c^3 I_0} = \frac{6\pi c^2}{n^2} \frac{\gamma_r^2 \omega^4}{(\omega_0^2 - \omega^2)^2 + \omega^2 (\gamma_i + \gamma_r \omega^2)^2}, \quad (1.41)$$

$$C_{\text{abs}} = -\frac{\omega}{2I_0} \text{Im} \left\{ \vec{p}^* \cdot (\vec{E}_0 + \vec{E}_{\text{RR}}) \right\} = \frac{6\pi c^2}{n^2} \frac{\gamma_r \gamma_i \omega^2}{(\omega_0^2 - \omega^2)^2 + \omega^2 (\gamma_i + \gamma_r \omega^2)^2}. \quad (1.42)$$

where $I_0 = \frac{1}{2} \varepsilon_0 c n |\vec{E}_0|^2$ stands for the intensity of the incident electromagnetic wave. Note that while the calculation of the radiative energy dissipation in Eq. (1.38) involves only the field \vec{E}_{RR} emitted by the antenna itself, the losses due to absorption are related to the total field at the position of the antenna. To verify the plausibility of this model, we tried to fit it to the spectra obtained from fully numerical FDTD simulations of a single gold diabolo antenna on top of a silicon substrate. The fitting parameters were the resonance frequency ω_0 , the refractive index n , and the scattering and absorption rates γ_r and γ_i . The reason for n not to be fixed is the presence of the air-silicon interface. The model was derived under the assumption of a homogeneous environment and by letting n to be a free parameter, we can compensate for this anisotropy. Figure 1.5 then shows the comparison between the calculated and fitted spectra. Apparently, the analytical model can quite adequately reproduce the results of numerical simulations, despite the crude approximation of the antenna as a point dipole. For completeness, we also present the optimal fitting parameters of the model: $\omega_0 = 2.04 \cdot 10^{12} \text{ s}^{-1}$, $n = 3.86$, $\gamma_i = 0.022 \omega_0$, $\gamma_r \omega_0^2 = 0.269 \omega_0$. This confirms our notion that scattering is the primary loss channel for THz metallic antennas.

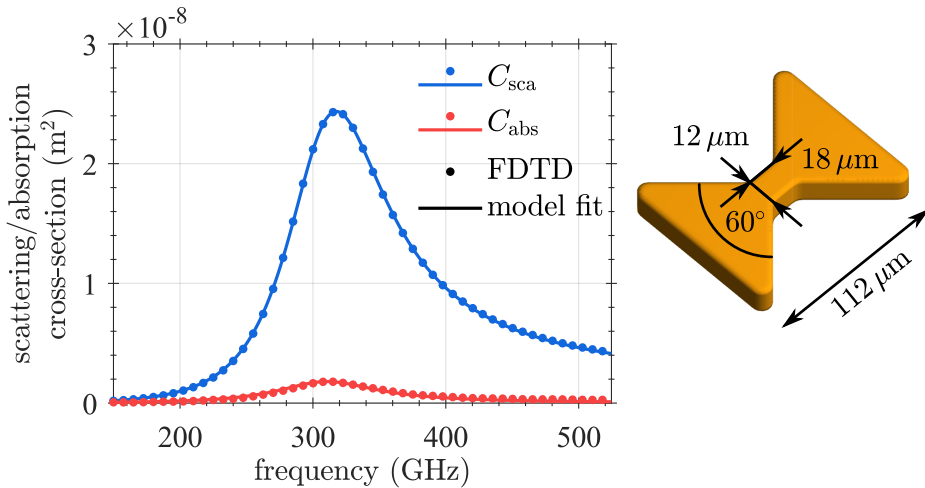


Figure 1.5: Scattering (blue) and absorption (red) cross-sections of a single $112 \mu\text{m}$ gold diabolo antenna placed on top of a silicon substrate calculated by FDTD (solid line). The spectra were subsequently fitted (dots) using the analytic formulas given by Eq. (1.41) and Eq. (1.42). The values of the other relevant geometrical parameters (except the antenna height which we set to 200 nm) are specified in the schematical drawing of the diabolo antenna on the right.

So far, we have considered the medium, in which the antenna is embedded, to be non-magnetic. At this point, we shall cover the antenna by a thin layer of a material with a single magnetic transition at a frequency ω_m that coincides with the antenna resonance. Recalling Section 1.1, the magnetic properties of such a material can be described by a frequency dependent anisotropic permeability tensor $\vec{\mu}$. As the magnetic transitions in EPR are usually rather weak, we shall assume that both the charge distribution inside and field distribution outside the antenna will remain the same as before and the only parameter that will change is the overall amplitude of the plasmonic oscillation. This amounts to treating the magnetic material as a first order perturbation. There are several possible approaches to the evaluation of how the presence of the magnetic material affects the response of the antenna. We chose one based on energy dissipation considerations. First, let us write down the general expression for the energy dissipation within some volume V

$$\frac{dW}{dt} = \int_V dV \left(\vec{H} \cdot \frac{\partial \vec{B}}{\partial t} + \vec{E} \cdot \frac{\partial \vec{D}}{\partial t} + \vec{j} \cdot \vec{E} \right). \quad (1.43)$$

Assuming harmonic time dependence and taking the average over one cycle, previous equation becomes

$$\frac{dW}{dt} = \frac{\omega}{2} \int_V dV \operatorname{Im} \left\{ \vec{H}^* \cdot \vec{B} + \vec{E}^* \cdot \vec{D} + \vec{j}^* \cdot \vec{E} \right\}. \quad (1.44)$$

If we further assume that there are no external currents and the electric displacement \vec{D} and magnetic field \vec{B} satisfy the constitutive relations $\vec{D}(\omega) = \varepsilon_0 \varepsilon(\omega) \vec{E}(\omega)$ and $\vec{B}(\omega) = \mu_0 \mu(\omega) \vec{H}(\omega)$, Equation 1.44 can be rewritten as

$$\frac{dW}{dt} = \frac{\omega}{2} \int_V dV \left(\mu_0 \mu'' |\vec{H}|^2 + \varepsilon_0 \varepsilon'' |\vec{E}|^2 \right), \quad (1.45)$$

where μ'' and ε'' denote the imaginary part of the magnetic permeability and electric permittivity, respectively. If we now realize that the second term on the right hand side must be connected to the ohmic losses inside the antenna,

$$C_{\text{abs}} = \frac{6\pi c^2}{n^2} \frac{\gamma_r \gamma_i \omega^2}{(\omega_0^2 - \omega^2)^2 + \omega^2 (\gamma_i + \gamma_r \omega^2)^2} = \frac{\omega \varepsilon_0 \varepsilon''(\omega)}{2I_0} \int_V dV |\vec{E}(\omega)|^2, \quad (1.46)$$

we can use the similarity between the electric and magnetic losses displayed in Eq. (1.45) and introduce the latter via a magnetic loss rate $\gamma_m(\omega)$, i.e. a parameter analogous to γ_i . As a consequence, the expression for the electric dipole moment given by Eq. (1.40) will change to

$$\vec{p}^m = \frac{6\pi \varepsilon_0 c^3}{n^3} \frac{\gamma_r}{\omega_0^2 - \omega^2 - i\omega [\gamma_i + \gamma_m(\omega) + \gamma_r \omega^2]} \vec{E}_0 \quad (1.47)$$

and there will be now a magnetic contribution to the absorption cross-section

$$\frac{6\pi c^2}{n^2} \frac{\gamma_r \gamma_m(\omega) \omega^2}{(\omega_0^2 - \omega^2)^2 + \omega^2 [\gamma_i + \gamma_m(\omega) + \gamma_r \omega^2]^2} = \frac{\omega \mu_0 \mu''(\omega)}{2I_0} \int_V dV |\vec{H}(\omega)|^2. \quad (1.48)$$

Note that unlike γ_r and γ_i , γ_m is a function of frequency. This stems from the fact that the linewidth of magnetic transitions is generally much narrower than the linewidth of the plasmonic resonance and the strength of the magnetic interaction can therefore change quite rapidly on the scale of the plasmonic resonance. At the same time, it is safe to assume that majority of the other terms in Eq. (1.48), including the magnetic field distribution of the antenna, are constant within the spectral region spanned by the magnetic transition and any frequency dependence in $\gamma_m(\omega)$ comes solely from the permeability $\mu(\omega)$ of the magnetic material. Therefore, if the distribution of the magnetic field around the antenna is known (e.g. from FDTD simulations), Equation (1.48) allows us to determine

the magnetic loss rate $\gamma_m(\omega)$ in terms of the other parameters (in the spirit of the perturbation method, we presume that they remain unchanged by the magnetic interaction).

In the light of the above argument, the magnetic contribution to the absorption cross-section now becomes

$$\frac{6\pi c^2}{n^2} \frac{\gamma_r \gamma_m(\omega)}{[\gamma_i + \gamma_m(\omega) + \gamma_r \omega_0^2]^2} = \frac{\omega_0 \mu_0 \mu''(\omega)}{2I_0} \int_V dV |\vec{H}(\omega_0)|^2, \quad (1.49)$$

where all the terms except $\gamma_m(\omega)$ and $\mu(\omega)$ were approximated by their value at the frequency of the magnetic resonance, which incidentally coincides with the resonance frequency of the antenna ω_0 . Let us now focus on the right hand side of Eq. (1.49). After insertion of $I_0 = \frac{1}{2}\mu_0 c |\vec{H}_0|^2$, it can be rewritten as

$$\frac{\omega_0 \mu_0 \mu''(\omega)}{2I_0} \int_V dV |\vec{H}(\omega_0)|^2 = \frac{\omega_0}{c} \mu''(\omega) \int_V dV \frac{|\vec{H}(\omega_0)|^2}{|\vec{H}_0|^2} = \frac{\omega_0}{c} \mu''(\omega) V \eta_{\text{avg}}, \quad (1.50)$$

where the newly introduced parameter

$$\eta_{\text{avg}} = \frac{1}{V} \int_V dV \frac{|\vec{H}(\omega_0)|^2}{|\vec{H}_0|^2} \quad (1.51)$$

stands for the average enhancement of the second power of the magnetic field within the volume V occupied by the magnetic material. To avoid this rather unwieldy definition, we shall adopt a more manageable, albeit slightly less precise designation for this quantity: average magnetic field enhancement. Also note that we used here a slightly different expression for the intensity of the incident electromagnetic wave than before—it lacks the refractive index of the surrounding medium. Though it may seem inconsistent, it has to do with the fact that we shall eventually extract the magnetic field distribution around the antenna from an exact FDTD simulation, where we implicitly assume that the incident wave propagates from an environment with a refractive index equal to 1. In other words, to ensure the proper scaling of the magnetic losses with respect to the absorption and scattering cross-sections in our analytical model, we have to use an incident intensity that is consistent with the magnetic field distribution entering the calculation of the magnetic loss rate.

Up to this point, we have implicitly presumed the magnetic permeability to be isotropic, but as we have learnt in the previous section, this is not true for EPR materials. Clearly, we should have considered the more general constitutive relation $\vec{B}(\omega) = \mu_0 \vec{\mu}(\omega) \vec{H}(\omega)$ during the evaluation of Eq. (1.44). We did it to keep the derivation lucid, knowing that the anisotropy has no effect on the major points of the presented concept and that it ultimately affects only the way how the average magnetic field enhancement is calculated: Invoking the magnetic permeability tensor given by Eq. (1.33), the magnetic losses amount to

$$\begin{aligned} \frac{dW}{dt} &= \frac{\mu_0 \omega}{2} \int_V dV \text{Im} \left\{ \begin{bmatrix} H_x^* & H_y^* & H_z^* \end{bmatrix} \begin{bmatrix} 1 + \chi(\omega) & \mp i\chi(\omega) & 0 \\ \pm i\chi(\omega) & 1 + \chi(\omega) & 0 \\ 0 & 0 & 1 \end{bmatrix} \begin{bmatrix} H_x \\ H_y \\ H_z \end{bmatrix} \right\} = \\ &= \frac{\mu_0 \omega}{2} \int_V dV \text{Im} \{ \chi''(\omega) (|H_x|^2 \pm iH_x H_y^* \mp iH_x^* H_y + |H_y|^2) \} = \frac{1}{2} \mu_0 \omega \chi''(\omega) \int_V dV |H_x \mp iH_y|^2. \end{aligned} \quad (1.52)$$

If we next express the in-plane (i.e. parallel to the plane of the antenna) components of the magnetic field in terms of the left-hand (H°) and right-hand (H^\ominus) circularly polarized contributions

$$H_x = \frac{H^\circ + H^\ominus}{2}, \quad (1.53)$$

$$H_y = \frac{H^\circ - H^\ominus}{2i}, \quad (1.54)$$

the parameter η_{avg} representing the average magnetic field enhancement becomes

$$\eta_{\text{avg}}^{\circ/\ominus} = \frac{1}{V} \int_V dV \frac{|H^{\circ/\ominus}(\omega_0)|^2}{|H_0^{\circ/\ominus}|^2}. \quad (1.55)$$

The decision which polarization of the magnetic field to choose then depends on the orientation of the static external magnetic field—the left-handed (\circ) for \vec{B}_{stat} pointing in the positive direction of the z -axis and the right-handed (\ominus) for the opposite orientation. This sensitivity to circular polarization can be tracked all the way back to the Bloch equations describing the time evolution of the electron spins. Since the FDTD software we use for validation of the interaction model can accommodate only permeability tensors with a diagonal anisotropy, we need to evaluate the magnetic loss term also for the simplified version of the permeability tensor given by Eq. (1.34). In that case, the resulting average magnetic field enhancement reads

$$\eta_{\text{avg}}^{\parallel} = \frac{1}{V} \int_V dV \frac{|\vec{H}^{\parallel}(\omega_0)|^2}{|\vec{H}_0^{\parallel}|^2}, \quad (1.56)$$

where the symbol \parallel indicates, that we take into account only the components parallel to the plane of the antenna and the air-substrate interface. Generally, any anisotropy in the dynamic permeability can be incorporated into the model simply by adjusting the expressions for the average magnetic field enhancement η_{avg} and the imaginary part of the magnetic permeability $\mu''(\omega)$, without any need to change the overall notation. For the particular anisotropies discussed above, $\mu''(\omega)$ is replaced by $\chi''(\omega)$ from Eq. (1.32).

The last issue that needs to be addressed before we can finally determine $\gamma_m(\omega)$ is the scaling of the magnetic field $\vec{H}(\omega_0)$. At the very beginning, we have assumed that even though its distribution remains unaffected by the magnetic interaction, its overall amplitude should be allowed to vary in accordance with the changes in the amplitude of the dipole moment of the antenna. This degree of freedom can be simply implemented by multiplying the magnetic field by the ratio of the dipole moment magnitudes $|\vec{p}^m|/|\vec{p}|$ calculated in the presence and in the absence of the magnetic interaction. The right hand side of Eq. (1.49) then reads

$$\frac{\omega_0}{c} \mu''(\omega) V \eta_{\text{avg}} \frac{|\vec{p}^m(\omega_0)|^2}{|\vec{p}(\omega_0)|^2} = \frac{\omega_0}{c} \mu''(\omega) V \eta_{\text{avg}} \frac{(\gamma_i + \gamma_r \omega_0^2)^2}{[\gamma_i + \gamma_m(\omega) + \gamma_r \omega_0^2]^2}. \quad (1.57)$$

Insertion of Eq. (1.57) into Eq. (1.49) eventually leads to the expression for the magnetic loss rate $\gamma_m(\omega)$

$$\gamma_m(\omega) = \frac{\omega_0 n^2}{6\pi c^3} \mu''(\omega) V \eta_{\text{avg}} \frac{(\gamma_i + \gamma_r \omega_0^2)^2}{\gamma_r}. \quad (1.58)$$

To verify that our assumptions about the strength of the magnetic interaction were correct and the use of the perturbation approach is valid, it is necessary to evaluate the above expression using some realistic values for the magnetic permeability and the average magnetic field enhancement.

Assuming that each spin center comprising the magnetic material carries a magnetic moment of one Bohr magneton μ_B , the imaginary part of the magnetic permeability given by Eq. (1.32) becomes

$$\mu''(\omega) = \chi''(\omega) = \frac{\mu_0 \hbar n_s \gamma_e^2 \omega_m \frac{\omega}{\tau}}{(\omega_m^2 - \omega^2)^2 + 4 \frac{\omega^2}{\tau^2}}, \quad (1.59)$$

where n_s designates the density of spin centers, γ_e the electron gyromagnetic ratio, and τ the relaxation time of the magnetic transition. Choosing $n_s = 5 \cdot 10^{27} \text{ m}^{-3}$ and $\tau = 0.1 \text{ ns}$, the maximum value of the imaginary part of the magnetic permeability reads $\mu''(\omega_m) = 0.51$. All that now remains to do is to set the value of the product $V \eta_{\text{avg}}$. For the sake of simplicity, let us suppose that a $1 \mu\text{m}$ thick layer made of the magnetic material described above covers the $112 \mu\text{m}$ long diabolo antenna already considered in Figure 1.5. Furthermore, let us assume that the layer is not infinite but it was etched away so that there is nothing left except a $170 \mu\text{m} \times 170 \mu\text{m}$ large square with the antenna in its center. The average magnetic field enhancement within this volume is according to the FDTD simulations $\eta_{\text{avg}} = \eta_{\text{avg}}^{\parallel} \approx 13.5$ and the resulting magnetic loss rate equals $\gamma_m(\omega_m) = 0.021 \omega_0$. This value seems to be reasonably small to justify the use of the perturbation approach for the description of the magnetic interaction between the antenna and the magnetic material.

With the magnetic loss rate $\gamma_m(\omega)$ determined, let us now write down the new expressions for the scattering and absorption cross-sections

$$C_{\text{sca}}^{\text{m}} = \frac{6\pi c^2}{n^2} \frac{\gamma_r^2 \omega^4}{(\omega_0^2 - \omega^2)^2 + \omega^2 [\gamma_i + \gamma_m(\omega) + \gamma_r \omega^2]^2}, \quad (1.60)$$

$$C_{\text{abs}}^{\text{m}} = \frac{6\pi c^2}{n^2} \frac{\gamma_r [\gamma_i + \gamma_m(\omega)] \omega^2}{(\omega_0^2 - \omega^2)^2 + \omega^2 [\gamma_i + \gamma_m(\omega) + \gamma_r \omega^2]^2}. \quad (1.61)$$

In the context of EPR experiments, we are interested mainly in the changes of the scattering properties of the antenna. Subtraction of Eq. (1.41) from Eq. (1.60) yields

$$\Delta C_{\text{sca}} = \frac{6\pi c^2}{n^2} \gamma_r^2 \omega^4 \left\{ \frac{1}{(\omega_0^2 - \omega^2)^2 + \omega^2 [\gamma_i + \gamma_m(\omega) + \gamma_r \omega^2]^2} - \frac{1}{(\omega_0^2 - \omega^2)^2 + \omega^2 (\gamma_i + \gamma_r \omega^2)^2} \right\}, \quad (1.62)$$

As before, all the terms except $\gamma_m(\omega)$ can be considered approximately constant within the spectral interval spanned by the magnetic transition. After fixing ω to ω_0 , the above expression becomes

$$\Delta C_{\text{sca}} = \frac{6\pi c^2}{n^2} \gamma_r^2 \omega_0^2 \left\{ \frac{1}{[\gamma_i + \gamma_m(\omega) + \gamma_r \omega_0^2]^2} - \frac{1}{(\gamma_i + \gamma_r \omega_0^2)^2} \right\}. \quad (1.63)$$

This can be further simplified by expanding the term with the magnetic loss rate into a Taylor series and by keeping only those terms linear in $\gamma_m(\omega)$.

$$\Delta C_{\text{sca}} \approx -\frac{6\pi c^2}{n^2} \frac{2\gamma_m(\omega) \gamma_r^2 \omega_0^2}{(\gamma_i + \gamma_r \omega_0^2)^3}. \quad (1.64)$$

Finally, replacement of $\gamma_m(\omega)$ with its full form given by Eq. (1.58) leads to

$$\Delta C_{\text{sca}} \approx -\frac{2\omega_0}{c} \mu''(\omega) V \eta_{\text{avg}} \frac{\gamma_r \omega_0^2}{\gamma_i + \gamma_r \omega_0^2} \approx -\frac{2\omega_0}{c} \mu''(\omega) V \eta_{\text{avg}}, \quad (1.65)$$

where we have also utilized the fact that $\gamma_r \omega_0^2 \gg \gamma_i$. Apparently, the interaction of the antenna with the magnetic material should manifest itself as a dip in the scattering spectrum and the magnitude of

this dip should be directly proportional to the average magnetic field enhancement around the antenna. To corroborate this finding, we calculated the scattering cross-section of a diabolo antenna covered by a magnetic layer using FDTD solver and compared it to the spectrum obtained from the analytical model. We used exactly the same antenna geometry as in the calculation shown in Figure 1.5 and the parameters of the magnetic layer were identical to those used for the estimation of the magnetic loss rate γ_m made earlier. The two spectra are plotted together in Figure 1.6 and the agreement between the numerical simulation and the analytical prediction is rather good, with the latter underestimating the exact value only by 25%.

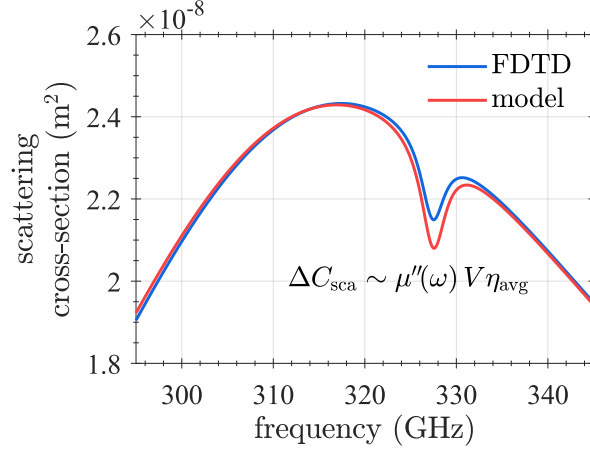


Figure 1.6: Scattering cross-section of a single $112 \mu\text{m}$ gold diabolo antenna placed on top of a silicon substrate and covered by a material with a magnetic transition at a frequency of 327.5 GHz , calculated by FDTD (blue) and the analytical formula (red) given by Eq. (1.60). The magnetic transition manifests itself as a pronounced dip in the spectrum. The analytical model predicts that the magnitude of the dip ΔC_{sca} is proportional to the average magnetic field enhancement $\eta_{\text{avg}} = \eta_{\text{avg}}^{\parallel}$ within the volume V occupied by the magnetic material and the imaginary part of its permeability $\mu''(\omega)$.

The fact that the simple analytical model derived above is able to correctly describe the interaction between the antenna and the magnetic material is important for several reasons. Firstly, it gives us an intelligible picture of how the plasmonically enhanced EPR signal is formed: the magnetic transitions imprint themselves via near field interaction into the optical response of the antenna and this information is then carried to the detector within the radiation emitted by the plasmonic antenna. This is, in fact, practically the same process as the one standing behind surface enhanced infrared absorption spectroscopy (SEIRA), except the interaction and the transitions encountered in SEIRA are electric in their nature. Secondly, the analytical model tells us that the main attribute that determines the performance of an antenna in EPR spectroscopy is the average magnetic field enhancement η_{avg} . In other words, this is the parameter that should serve as a figure of merit in the search for an optimal antenna design. The last major contribution of the analytical model is the downscaling of the time required to assess, for example, the performance of an antenna or to estimate the strength of the EPR signal for a different magnetic material. Without the model, one would be forced to run a full set of simulations for any sweep over one of the parameters of the magnetic layer, e.g. its thickness, spin density etc.

To summarize it, the analytical model enables us to characterize any antenna and its potential for EPR spectroscopy solely on the basis of our knowledge of the magnetic field distribution around the antenna and therefore independently of the particular choice of a magnetic material. On the other hand, the model is also not without its flaws. There is a certain ambiguity in the definition of the average magnetic field enhancement η_{avg} since it depends on the volume of the region in which we choose to evaluate it. If we want to make comparison between various antennas, it is not clear what

the lateral size of this region should be. Furthermore, EPR analysis of thin magnetic films requires a significant field enhancement over a large area and for that purpose, an array of antennas would be more fitting. To that end, we decided to develop another variant of the model, in which the solitary antenna would be replaced by a periodic antenna array.

Let us start by writing down a general expression for the polarization vector \vec{P} that fully describes the charge and current distribution within the antenna array

$$\vec{P}(\vec{r}, \omega) = f(\vec{r})\varepsilon_0\chi_e(\omega)\vec{E}(\vec{r}, \omega) = \alpha(\vec{r})\vec{E}(\vec{r}, \omega), \quad (1.66)$$

where $\chi_e(\omega)$ denotes the electric susceptibility of the metal from which the antennas are made of, and $f(\vec{r})$ represents a binary function that defines the distribution of the metal in space (and incidentally the overall geometry of the antenna array). Not to make the problem needlessly complicated, we shall for the time being disregard the presence of a substrate and treat the array as if it was free-standing. We shall incorporate its effects in the final steps of the derivation. Invoking the Green's function formalism [2], the electric field at any point in space can be consequently written as a sum of the incident field $\vec{E}_0(\vec{r}) = \vec{E}_0 \exp(ikz)$ and the field generated by the antennas

$$\vec{E}(\vec{r}) = \vec{E}_0(\vec{r}) + \int d\vec{r}'^3 \vec{G}(\vec{r}, \vec{r}') \vec{P}(\vec{r}'), \quad (1.67)$$

where the dyadic Green's function $\vec{G}(\vec{r}, \vec{r}')$ determines the response of the system at \vec{r} due to a point dipole located at \vec{r}' . Insertion of Eq. (1.67) into Eq. (1.66) then leads to a self-consistent equation for the polarization vector \vec{P}

$$\vec{P}(\vec{r}) = \alpha(\vec{r}) \left[\vec{E}_0(\vec{r}) + \int d\vec{r}'^3 \vec{G}(\vec{r}, \vec{r}') \vec{P}(\vec{r}') \right]. \quad (1.68)$$

Since the system is periodic, the polarizability factor $\alpha(\vec{r})$ of the whole array is essentially the polarizability factor of a single antenna $\alpha_0(\vec{r})$ copied repeatedly to form the array lattice. In mathematical notation,

$$\alpha(\vec{r}) = \sum_j \alpha_0(\vec{r} - \vec{R}_j), \quad (1.69)$$

with the summation running over all the sites in the array lattice defined by a set of position vectors \vec{R}_j . In the light of this periodicity, we find it more convenient to switch to the reciprocal space, where the polarizability factor transforms into

$$\alpha(\vec{q}, z) = \frac{1}{(2\pi)^2} \iint_{-\infty}^{\infty} d\vec{r}'_{\parallel} \alpha(\vec{r}') e^{-i\vec{q}\cdot\vec{r}'_{\parallel}} = \alpha_0(\vec{q}, z) \sum_j e^{-i\vec{q}\cdot\vec{R}_j}. \quad (1.70)$$

Note that since the array is two dimensional, the inverse Fourier transform is calculated only over the lateral coordinates \vec{r}'_{\parallel} , while the vertical coordinate z is left as it was. To keep things simple, let us now assume that the array is rectangular with the same period equal to L in the two lateral directions and that the height of the antennas (≈ 200 nm) is negligible compared to the wavelength so that it can be effectively treated as a 2D structure and the z dependence can be dropped (this is perfectly justifiable in the THz region, where the wavelength is in hundreds of microns). Application of the following equality

$$\sum_{n=-\infty}^{\infty} \exp(iqnL) = \frac{2\pi}{L} \sum_{n=-\infty}^{\infty} \delta\left(q - n\frac{2\pi}{L}\right), \quad (1.71)$$

then leads to

$$\alpha(\vec{q}) = \alpha_0(\vec{q}) \left(\frac{2\pi}{L} \right)^2 \sum_{m,n=-\infty}^{\infty} \delta(\vec{q} - \vec{q}_{mn}), \quad (1.72)$$

with the wavevector \vec{q}_{mn} defined as $\vec{q}_{mn} = (2\pi m/L, 2\pi n/L)$. Next, we need to transform into the reciprocal space also the polarization vector $\vec{P}(\vec{r}) = \vec{P}(\vec{r}_{\parallel}) \delta(z)$ (the delta function reflects the 2D character of the antenna). Denoting $\vec{P}(\vec{q})$ and $\vec{G}(\vec{q})$ the inverse Fourier transforms of $\vec{P}(\vec{r}_{\parallel})$ and $\vec{G}(\vec{r}_{\parallel})$, exploiting the convolution theorem and recalling that the incident wave is planar and propagates in the direction perpendicular to the antenna array, Equation (1.68) becomes

$$\vec{P}(\vec{q}) = \alpha(\vec{q}) \vec{E}_0 + (2\pi)^2 \iint_{-\infty}^{\infty} d\vec{q}'^2 \alpha(\vec{q} - \vec{q}') \vec{G}(\vec{q}') \vec{P}(\vec{q}'). \quad (1.73)$$

The above equation is, among other things, the cornerstone of the Fourier expansion method [23]. It also nicely illustrates the fact that the antenna facilitates the scattering of the incident wave into other directions (or into evanescent waves) by providing the additional momentum that is necessary to overcome the associated momentum mismatch. Anyway, replacement of the general polarizability factor by the expression from Eq. (1.72) and use of the filtration property of the delta function effectively shrinks the space of allowed wavevectors to the set \vec{q}_{mn}

$$\vec{P}(\vec{q}_{mn}) = \left(\frac{2\pi}{L} \right)^2 \alpha_0(\vec{q}_{mn}) \left[\vec{E}_0 + (2\pi)^2 \sum_{m',n'=-\infty}^{\infty} \vec{G}(\vec{q}_{mn} - \vec{q}_{m'n'}) \vec{P}(\vec{q}_{mn} - \vec{q}_{m'n'}) \right]. \quad (1.74)$$

Despite this reduction in complexity, the above system of equations is generally still too involved and further simplifications are necessary. Ultimately, we are looking for a single equation analogous to Eq. (1.35) that would adequately describe the collective response of the whole antenna array. The solution is to impose a restriction on the distance between the antennas in the periodic array. If we make the pitch subwavelength, destructive interference will suppress radiation in all directions except $\vec{q} = \vec{0}$. In other words, the antenna array will behave on the outside as a homogeneous medium that can be described by some effective reflection and transmission coefficients. Adopting this "dense" array approximation, the system of equations (1.74) can be cast into a more illuminating form if we single out the equation for $\vec{P}(\vec{0})$ and rearrange some of its elements

$$\vec{P}(\vec{0}) - \left(\frac{2\pi}{L} \right)^2 \alpha_0(\vec{0}) (2\pi)^2 \sum_{\vec{q}_{mn} \neq \vec{0}} \vec{G}(\vec{q}_{mn}) \vec{P}(\vec{q}_{mn}) = \left(\frac{2\pi}{L} \right)^2 \alpha_0(\vec{0}) \left[\vec{E}_0 + (2\pi)^2 \vec{G}(\vec{0}) \vec{P}(\vec{0}) \right]. \quad (1.75)$$

This equation bears a conspicuous resemblance to the equation of motion for a single antenna given by (1.36). In the term $(2\pi)^2 \vec{G}(\vec{0}) \vec{P}(\vec{0})$ on the right hand side, we easily recognize the radiation reaction force that is responsible for radiative losses (the fact that $\vec{P}(\vec{0})$ is the only component that radiates into the far-field is the consequence of our "dense" array approximation). The left hand side of Equation (1.75) then contains interaction of $\vec{P}(\vec{0})$ with the evanescent components of the polarization vector $\vec{P}(\vec{r})$. It is our assumption that the result of this interaction is again a response that can be adequately described by a single Lorentz oscillator with a resonance frequency ω_0 and an intrinsic damping rate γ_i , i.e.

$$\vec{P}(\vec{0}) (\omega_0^2 - \omega^2 - i\omega\gamma_i) = \beta \left[\vec{E}_0 + (2\pi)^2 \vec{G}(\vec{0}) \vec{P}(\vec{0}) \right]. \quad (1.76)$$

At this point, it only remains to express the dyadic Green's function $\vec{G}(\vec{0})$ in terms of known parameters. We have so far considered the antenna array to be free-standing, but ultimately, we would

like it to be placed on top of a substrate with a refractive index n . As it turns out, its incorporation is easily accomplished by replacing the incident electric field in Eq. (1.76) with $t_p \vec{E}_0$, where the Fresnel transmission coefficient $t_p = 2/(n+1)$ accounts for the reduction in the amplitude of the driving field due to the reflections at the air-substrate interface. Similar treatment is required also for the radiation reaction term. Referring the reader to [Appendix A](#) for the angular spectrum representation of the dyadic Green's function $\vec{G}(\vec{0})$, the equation for the component $\vec{P}(\vec{0})$ in the presence of a substrate reads

$$\vec{P}(\vec{0}) (\omega_0^2 - \omega^2 - i\omega\gamma_i) = \beta \left[t_p \vec{E}_0 + i t_p \frac{\omega}{2\varepsilon_0 c} \vec{P}(\vec{0}) \right]. \quad (1.77)$$

Finally, by introducing the radiative loss rate $\gamma_r = \beta t_p / (2\varepsilon_0 c)$, we acquire the desired analytical model for the response of an infinite antenna array

$$\vec{P}(\vec{0}) = \frac{2\varepsilon_0 c \gamma_r}{\omega_0^2 - \omega^2 - i\omega(\gamma_i + \gamma_r)} \vec{E}_0. \quad (1.78)$$

To assess its plausibility, we need to ascertain whether it can be successfully fitted to the exact spectra calculated by numerical simulations. While the optical response of a solitary antenna is usually evaluated in terms of its scattering and absorption cross-section, an extended antenna array is best characterized by its transmittance T and reflectance R . Let us start with the transmittance, defined as the ratio between the transmitted and the incident power

$$T = \frac{\frac{1}{2}\varepsilon_0 c n |\vec{E}^{\text{tr}}|^2}{\frac{1}{2}\varepsilon_0 c |\vec{E}_0|^2}. \quad (1.79)$$

The electric field amplitude of the transmitted wave \vec{E}^{tr} is simply the sum of the incident electric field and the field generated by the antenna array

$$\vec{E}^{\text{tr}} = t_p \left[\vec{E}_0 + i \frac{\omega}{2\varepsilon_0 c} \vec{P}(\vec{0}) \right]. \quad (1.80)$$

Its insertion into Eq. (1.79) yields

$$T = (1 + r_p) t_p \left| 1 + \frac{i\omega\gamma_r}{\omega_0^2 - \omega^2 - i\omega(\gamma_i + \gamma_r)} \right|^2 = n t_p^2 \frac{(\omega_0^2 - \omega^2)^2 + \omega^2 \gamma_i^2}{(\omega_0^2 - \omega^2)^2 + \omega^2 (\gamma_i + \gamma_r)^2}. \quad (1.81)$$

Similarly, the amplitude of the reflected wave \vec{E}^{ref} reads

$$\vec{E}^{\text{ref}} = -r_p \vec{E}_0 + i t_p \frac{\omega}{2\varepsilon_0 c} \vec{P}(\vec{0}), \quad (1.82)$$

where $r_p = (n-1)/(n+1)$ stands for the Fresnel reflection coefficient of the air-substrate interface. The ratio of the reflected and the incident power then gives us the reflectance

$$R = \frac{\frac{1}{2}\varepsilon_0 c |\vec{E}^{\text{ref}}|^2}{\frac{1}{2}\varepsilon_0 c |\vec{E}_0|^2} = \left| -r_p + t_p \frac{i\omega\gamma_r}{\omega_0^2 - \omega^2 - i\omega(\gamma_i + \gamma_r)} \right|^2 = \frac{r_p^2 (\omega_0^2 - \omega^2)^2 + \omega^2 (r_p \gamma_i + \gamma_r)^2}{(\omega_0^2 - \omega^2)^2 + \omega^2 (\gamma_i + \gamma_r)^2}. \quad (1.83)$$

Finally, the power dissipation in the antenna array due to ohmic losses can be quantified in terms of the absorbance

$$A = 1 - R - T = t_p \frac{2\omega^2 \gamma_r \gamma_i}{(\omega_0^2 - \omega^2)^2 + \omega^2 (\gamma_i + \gamma_r)^2}. \quad (1.84)$$

The structure that we used to test the validity of the new analytical model was an array of gold diabolo antennas (length $112 \mu\text{m}$) placed on top of a silicon substrate. The distance between antennas was set to $170 \mu\text{m}$ (a value that is subwavelength in both air and silicon throughout the spectral region of our interest) and the fitting parameters of the model were the resonance frequency ω_0 , the radiative loss rate γ_r and the absorption loss rate γ_i . The comparison between the calculated and fitted spectra is shown in Figure 1.7. Even though the fit is not perfect, it still adequately reproduces the numerically calculated transmission and reflection spectra. For completeness, we also list the optimal fitting parameters of the model: $\omega_0 = 2.25 \cdot 10^{12} \text{ s}^{-1}$, $\gamma_i = 0.021 \omega_0$, $\gamma_r = 0.319 \omega_0$.

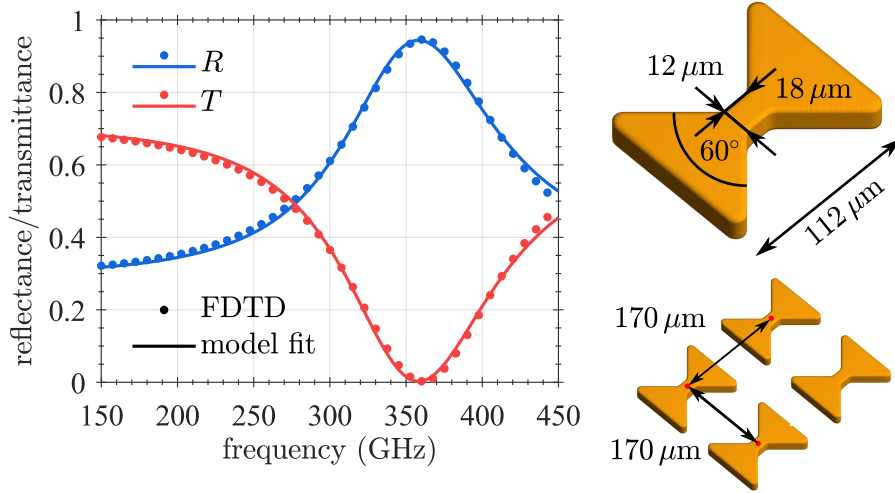


Figure 1.7: Reflectance (blue) and transmittance (red) spectra of an infinite antenna array calculated by FDTD (solid line). The spectra were subsequently fitted (dots) using the analytic formulas given by Eq. (1.83) and Eq. (1.81). The array was built from $112 \mu\text{m}$ gold diabolo antennas placed on top of a silicon substrate and the distance between individual antennas was fixed to $170 \mu\text{m}$. The height of the antennas was set to 200 nm .

The inclusion of the losses due to the interaction of the antenna array with a magnetic layer can be carried out in the same manner as we did with the solitary antenna, i.e. by introducing a phenomenological magnetic loss rate $\gamma_m(\omega)$ into the expression for the polarization vector $\vec{P}(\vec{0})$

$$\vec{P}^m(\vec{0}) = \frac{2\varepsilon_0 c \gamma_r}{\omega_0^2 - \omega^2 - i\omega [\gamma_i + \gamma_m(\omega) + \gamma_r]} \vec{E}_0. \quad (1.85)$$

This will ultimately lead to new expressions for the transmittance, reflectance, and absorbance

$$T^m = n t_p^2 \frac{(\omega_0^2 - \omega^2)^2 + \omega^2 [\gamma_i + \gamma_m(\omega)]^2}{(\omega_0^2 - \omega^2)^2 + \omega^2 [\gamma_i + \gamma_m(\omega) + \gamma_r]^2}, \quad (1.86)$$

$$R^m = \frac{r_p^2 (\omega_0^2 - \omega^2)^2 + \omega^2 [r_p \gamma_i + r_p \gamma_m(\omega) + \gamma_r]^2}{(\omega_0^2 - \omega^2)^2 + \omega^2 [\gamma_i + \gamma_m(\omega) + \gamma_r]^2}, \quad (1.87)$$

$$A^m = t_p \frac{2\omega^2 \gamma_r [\gamma_i + \gamma_m(\omega)]}{(\omega_0^2 - \omega^2)^2 + \omega^2 [\gamma_i + \gamma_m(\omega) + \gamma_r]^2}. \quad (1.88)$$

The magnetic loss rate $\gamma_m(\omega)$ can be determined from the relation between the absorbance A^m and the general expression for energy dissipation given by Eq. (1.45). Namely, power lost within one unit cell of the periodic antenna array reads

$$A^m I_0 S_{\text{cell}} = I_0 S_{\text{cell}} t_p \frac{2\omega^2 \gamma_r [\gamma_i + \gamma_m(\omega)]}{(\omega_0^2 - \omega^2)^2 + \omega^2 [\gamma_i + \gamma_m(\omega) + \gamma_r]^2} = \frac{\omega}{2} \int_{V_{\text{cell}}} dV \left(\mu_0 \mu'' |\vec{H}|^2 + \varepsilon_0 \varepsilon'' |\vec{E}|^2 \right), \quad (1.89)$$

where S_{cell} stands for the area of the unit cell and the integration volume V_{cell} is the product of the unit cell area and the thickness d of the magnetic layer covering the antenna array. Note that for the sake of simplicity, we again treat the magnetic material as isotropic, knowing that any anisotropy can be easily incorporated later. Apparently, the absorption can be broken down into two distinct parts—the ohmic losses in the metal and the energy dissipation inside the magnetic layer—and we are interested in the latter

$$\frac{2t_p \omega^2 \gamma_r \gamma_m(\omega)}{(\omega_0^2 - \omega^2)^2 + \omega^2 [\gamma_i + \gamma_m(\omega) + \gamma_r]^2} = \frac{\omega}{2I_0 S_{\text{cell}}} \int_{V_{\text{cell}}} dV \mu_0 \mu'' |\vec{H}(\omega)|^2. \quad (1.90)$$

Provided one makes a couple of assumptions about the nature of the magnetic transition and the response of the antenna array, the above equation can be used to determine $\gamma_m(\omega)$. Firstly, we expect the linewidth of the magnetic transition to be much narrower than the linewidth of the plasmonic resonance, so that the magnetic field distribution of the antenna array and other terms in Eq. (1.90) can be considered to be nearly constant within the spectral range spanned by the magnetic transition and they can be therefore approximated by a single value taken at the frequency ω_0 (recall that the frequency of the transition ω_s is set to coincide with the plasmonic resonance). Secondly, we suppose that while the interaction with the magnetic layer can affect the amplitude of the magnetic field generated by the antenna array, its distribution remains the same. Adopting these assumptions, Equation (1.90) can be rewritten as

$$\frac{2t_p \gamma_r \gamma_m(\omega)}{[\gamma_i + \gamma_m(\omega) + \gamma_r]^2} = \frac{\omega_0}{2I_0 S_{\text{cell}}} \frac{|\vec{P}^m(\vec{0}, \omega_0)|^2}{|\vec{P}(\vec{0}, \omega_0)|^2} \int_{V_{\text{cell}}} dV \mu_0 \mu'' |\vec{H}(\omega_0)|^2, \quad (1.91)$$

where the factor $|\vec{P}^m(\vec{0}, \omega_0)|^2/|\vec{P}(\vec{0}, \omega_0)|^2$ accounts for the drop in the amplitude of the plasmonic oscillations supported by the antenna array due to the increased damping. Upon replacing the intensity of the incident electromagnetic wave with $I_0 = \mu_0 c/2 |\vec{H}_0|^2$ and rearranging some of the terms in the above equation, we obtain the expression for the magnetic loss rate $\gamma_m(\omega)$

$$\gamma_m(\omega) = \frac{\omega_0 (\gamma_r + \gamma_i)^2}{c} \frac{\mu'' d}{2t_p \gamma_r} \frac{1}{V_{\text{cell}}} \int_{V_{\text{cell}}} dV \frac{|\vec{H}(\omega_0)|^2}{|\vec{H}_0|^2} = \frac{\omega_0 (\gamma_r + \gamma_i)^2}{c} \frac{\mu'' d}{2t_p \gamma_r} \eta_{\text{avg}}. \quad (1.92)$$

With $\gamma_m(\omega)$ at hand, we can proceed with validation of the analytical model against numerical simulations. The thickness of the magnetic layer was set to $d = 2.4 \mu\text{m}$ and the parameters of the magnetic permeability were chosen to be the same as in the case of the solitary antenna. The comparison between the spectra predicted by the analytical model and those obtained from FDTD simulations is shown in Figure 1.8. The analytical model reproduces the exact spectra quite well, including the magnitude of the imprint that the magnetic transition leaves in the underlying plasmonic resonance of the antenna array. Note that while there is a dip in the power reflected by the system, the transmittance shows a bump that is relatively smaller in its magnitude. This would suggest that an experimental setup in the reflection configuration might offer some advantage over a setup in the transmission configuration. Conveniently, the analytical model enables us to analyse and quantify the strength of the EPR signal in both of them. In the transmission mode, the EPR signal amounts to the difference between the response in the presence and in the absence of the magnetic layer

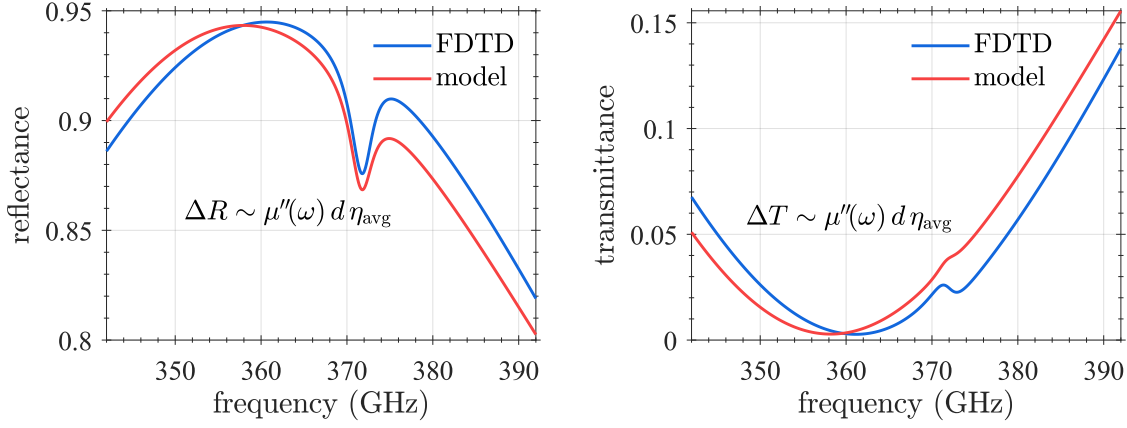


Figure 1.8: Reflectance (left panel) and transmittance (right panel) spectra of an infinite antenna array covered by a material with a magnetic transition at a frequency of 372 GHz, calculated by FDTD (blue) and the analytical formulas (red) given by Eq. (1.87) and Eq. (1.86). The thickness d of the magnetic layer was set to $1 \mu\text{m}$, while the parameters of the array were the same as in Figure 1.7. The magnetic transition manifests itself as a pronounced dip in the reflection spectrum and a comparatively smaller bump in the transmittance spectrum. The analytical model predicts that their magnitude is proportional to the average magnetic field enhancement $\eta_{\text{avg}} = \eta_{\text{avg}}^{\parallel}$ within the magnetic layer and the imaginary part of its permeability $\mu''(\omega)$.

$$\begin{aligned} \Delta T(\omega_0) &= T^{\text{m}}(\omega_0) - T(\omega_0) = (1 + r_{\text{p}}) t_{\text{p}} \left\{ \frac{[\gamma_{\text{i}} + \gamma_{\text{m}}(\omega)]^2}{[\gamma_{\text{i}} + \gamma_{\text{m}}(\omega) + \gamma_{\text{r}}]^2} - \frac{\gamma_{\text{i}}^2}{(\gamma_{\text{i}} + \gamma_{\text{r}})^2} \right\} \approx \\ &\approx (1 + r_{\text{p}}) t_{\text{p}} \frac{2\gamma_{\text{i}}\gamma_{\text{m}}(\omega)}{(\gamma_{\text{i}} + \gamma_{\text{r}})^2} = \frac{\omega_0}{c} \mu'' d \eta_{\text{avg}} (1 + r_{\text{p}}) \frac{\gamma_{\text{i}}}{\gamma_{\text{r}}}. \end{aligned} \quad (1.93)$$

Similarly, the EPR signal in the reflection mode corresponds to

$$\begin{aligned} \Delta R(\omega_0) &= R^{\text{m}}(\omega_0) - R(\omega_0) = \frac{[r_{\text{p}}\gamma_{\text{i}} + r_{\text{p}}\gamma_{\text{m}}(\omega) + \gamma_{\text{r}}]^2}{[\gamma_{\text{i}} + \gamma_{\text{m}}(\omega) + \gamma_{\text{r}}]^2} - \frac{(r_{\text{p}}\gamma_{\text{i}} + \gamma_{\text{r}})^2}{(\gamma_{\text{i}} + \gamma_{\text{r}})^2} \approx \\ &\approx -t_{\text{p}} \frac{2\gamma_{\text{m}}(\omega) \gamma_{\text{r}} (r_{\text{p}}\gamma_{\text{i}} + \gamma_{\text{r}})}{(\gamma_{\text{i}} + \gamma_{\text{r}})^3} = -\frac{\omega_0}{c} \mu'' d \eta_{\text{avg}} \frac{r_{\text{p}}\gamma_{\text{i}} + \gamma_{\text{r}}}{\gamma_{\text{i}} + \gamma_{\text{r}}}. \end{aligned} \quad (1.94)$$

Our model reveals that the ratio $\Delta R(\omega_0)/\Delta T(\omega_0)$, i.e. the parameter that can be used to assess the performance of the two configurations relative to each other, does not depend on our choice of the magnetic material. It is entirely determined by the properties of the antenna array and in this particular geometry, $\Delta R(\omega_0)/\Delta T(\omega_0) \approx 15$. Interestingly, the situation is completely reversed when we evaluate relative changes instead

$$\frac{\Delta T(\omega_0)}{T(\omega_0)} = \frac{\omega_0}{c} \mu'' d \eta_{\text{avg}} \frac{(\gamma_{\text{i}} + \gamma_{\text{r}})^2}{\gamma_{\text{i}}\gamma_{\text{r}}} \approx \frac{\omega_0}{c} \mu'' d \eta_{\text{avg}} \frac{\gamma_{\text{r}}}{\gamma_{\text{i}}}, \quad (1.95)$$

$$\frac{\Delta R(\omega_0)}{R(\omega_0)} = -\frac{\omega_0}{c} \mu'' d \eta_{\text{avg}} \frac{\gamma_{\text{i}} + \gamma_{\text{r}}}{r_{\text{p}}\gamma_{\text{i}} + \gamma_{\text{r}}} \approx -\frac{\omega_0}{c} \mu'' d \eta_{\text{avg}}. \quad (1.96)$$

This is due to the fact that while the reflectance of the antenna array dramatically rises within the plasmonic resonance, its transmittance approaches zero and even a small perturbation can cause a

large relative change in the measured signal. The decision, which configuration is more suitable for the EPR spectroscopy, might therefore depend on the signal to noise ratio and other parameters of the detection system that will be eventually used in measurements.

Let us conclude this section by summarizing the key findings and observations it contains. First of all, the strength of the EPR signal is proportional to the average magnetic field enhancement η_{avg} within the volume occupied by the magnetic material. It does not apply only to the geometries investigated above, i.e. the solitary antenna and the dense antenna array. It holds universally, as long as the magnetic interaction is weak and it can be perceived only as a small perturbation to the system. As a consequence, we identified η_{avg} as the figure of merit in the search for a design that maximizes the EPR plasmonic enhancement effect. Secondly, during this optimization procedure, we should keep in mind that only the magnetic field components perpendicular to the static magnetic field will participate in the magnetic interaction, a fact that we can track to the anisotropic nature of the magnetic permeability describing the collective response of magnetic centers. The last point concerns the limitations of the presented analytical models, more specifically the geometries that we have considered. Neither the solitary antenna nor the infinite antenna array are particularly suitable as a representation of a realistic sample for plasmon enhanced EPR. The signal from a single antenna would be too weak, while strong lattice resonances give rise to unphysical features in the optical response of antenna arrays (note that by making our array dense, it did not support any lattice resonances and we could therefore disregard them in the above model). The natural solution would be to focus on finite antenna arrays instead. Those can be, however, quite costly to simulate, making any optimization over multiple parameters virtually impossible. In order to remedy that, we developed a semi-analytical model that allows us to efficiently calculate the response of a finite antenna array of an arbitrary size and pitch. The derivation and results of this model are presented in the next section.

1.3. Antenna array interaction model

The standard approach to calculating the response of large finite antenna arrays is to replace individual antennas with point dipoles and evaluate their interaction in terms of lattice sums. This, so called, coupled dipole approximation (CDA) has been successfully employed to gain insight into the problematics of diffractive coupling in periodic arrays [24, 25]. It turns out that the long range interaction between antennas gives rise to lattice resonances that can significantly alter their overall response and even grant them an entirely new functionality. Lattice resonances can be, for example, used to control the linewidth of plasmonic resonances and consequently improve the sensitivity of techniques based on phase-shift detection [26]. They can further enhance emission efficiency of molecules and quantum dots [27–29], facilitate large phase modulation in actively tunable arrays based on graphene [30, 31] and lead to extraordinary transmission in periodic arrays of holes [32].

We also intend to exploit the lattice resonances, in this instance to boost the EPR signal. The basic formulation of the coupled dipole approximation is, however, too crude to provide reliable description of diatomic antenna arrays and their optical response in the THz spectral region. More specifically, even though it can offer some qualitative estimates, we deem it insufficient for the purpose of design optimization, where quantitative precision is vital. To that end, we devised a semi-analytical interaction model that combines the framework of the coupled dipole approximation [33] with numerical simulations and elements of the waveguide theory. It is built on the notion that the charge distribution of an antenna can be written as a linear combination of eigenmodes that are specific to the particular antenna geometry and the mutual interaction between antennas does not change the nature of these eigenmodes, it affects only their excitation amplitudes (the second assumption is valid as long as the antennas are not clumped together too closely). We adhere to the coupled dipole approximation in the sense that the response of individual antennas in the spectral range of our interest can be described by a single quantity, namely the excitation amplitude of the fundamental antenna mode (in contrast to

the electric dipole moment encountered in the standard CDA). To implement this idea into the existing CDA framework, we borrowed the concept of overlap integrals from the waveguide theory, where the excitation amplitude of a mode essentially represents a measure of how well the spatial profile of an external field matches the field distribution of that particular mode. For the purpose of our model, this just needs to be slightly reformulated: the excitation amplitude of the fundamental antenna mode reflects the similarity between its charge distribution and the spatial profile of the driving field which comprises both the incident electromagnetic wave and the field generated by other antennas. Finally, we should stress that the charge distribution of the fundamental antenna mode, a crucial ingredient of the whole model, is extracted from numerical simulations of a solitary antenna.

Having outlined all the key aspects of our interaction model for antenna arrays, we shall go through them now in more detail and build step by step the underlying mathematical framework. Let us start with writing down the general self-consistent equation for the polarization vector $\vec{P}(\vec{r}, \omega)$ within a plasmonic antenna in the absence of any external field

$$\vec{P}(\vec{r}, \omega) - \alpha(\vec{r}, \omega) \int d\vec{r}'^3 \vec{G}(\vec{r}, \vec{r}', \omega) \vec{P}(\vec{r}', \omega) = 0, \quad (1.97)$$

where the spatial dependence of the polarizability factor $\alpha(\vec{r}, \omega)$ carries the information about the antenna geometry and the dyadic Green's function $\vec{G}(\vec{r}, \vec{r}', \omega)$ accounts for the interaction between different parts of the antenna. We shall denote the solutions $\vec{\mathcal{P}}_n(\vec{r}, \omega)$ to the above equation as natural eigenmodes of the antenna and assume that any current distribution can be expressed as their linear combination

$$\vec{P}(\vec{r}, \omega) = \sum_n p_n(\omega) \vec{\mathcal{P}}_n(\vec{r}, \omega), \quad (1.98)$$

with excitation amplitudes $p_n(\omega)$ representing the weights of the individual eigenmodes. Note that here and in what follows, we freely interchange the polarization vector for the current distribution, even though we are well aware that they are not the same. They are, however, closely related ($\vec{j} = \partial \vec{P} / \partial t$) and during this derivation, we can treat them as a single entity without doing any harm.

In the visible region, the eigenmodes of plasmonic antennas are often spectrally overlapping, i.e. the maxima of excitation amplitudes $p_n(\omega)$ are close together and it can be difficult, for example, to tell them apart in the scattering spectrum or the electric field distribution (this of course largely depends on the type of illumination and possibly other parameters—here we refer to the most common scenario involving a plane wave illumination under normal incidence). In the THz spectral range, on the other hand, the modes are usually well separated, as evidenced both by the simulations and the reflectance measurements of diabolos arrays presented earlier in Figure 1.4 on page 10. The fact, that the fundamental dipolar mode (and incidentally also the mode associated with the largest magnetic field enhancement) practically dominates the response of the diablo antenna throughout the spectral window of our interest, entitles us to disregard all the other eigenmodes and reduce the sum in Eq. (1.98) to a single term

$$\vec{P}(\vec{r}, \omega) = p(\omega) \vec{\mathcal{P}}(\vec{r}, \omega). \quad (1.99)$$

At the same time, it enables us to extract the current distribution of the fundamental mode directly from FDTD simulations, without any need to perform an actual eigenmode expansion. There is a certain ambiguity in the definition of the fundamental mode $\vec{\mathcal{P}}(\vec{r}, \omega)$, we eventually settled on the following version

$$\vec{\mathcal{P}}(\vec{r}, \omega) = \frac{\vec{P}_{\text{sim}}(\vec{r}, \omega) \|\vec{\mathcal{E}}_0(\vec{r}, \omega)\|}{\frac{1}{V} \int_V d\vec{r}'^3 \vec{P}_{\text{sim}}(\vec{r}', \omega) \cdot \vec{\mathcal{E}}_0^*(\vec{r}', \omega)}, \quad (1.100)$$

where the norm $\|\vec{\mathcal{E}}_0(\vec{r}, \omega)\| = \sqrt{\frac{1}{V} \int_V d\vec{r}^3 |\vec{\mathcal{E}}_0(\vec{r}, \omega)|^2}$ denotes the average value of the incident electric field within the volume V of an antenna and the current distribution extracted from the numerical simulations $\vec{P}_{\text{sim}}(\vec{r}, \omega)$ is divided by an overlap integral with the electric field distribution of the incident electromagnetic wave $\vec{\mathcal{E}}_0(\vec{r}, \omega)$ to eliminate any dependence on the illumination. It turns out that this normalization is not really necessary, one could directly designate $\vec{\mathcal{P}}(\vec{r}, \omega)$ as the current distribution of the fundamental mode. It allows us, however, to compare spatial profiles of the fundamental eigenmode at different frequencies and between different simulations, an option that can be sometimes useful and elucidating. Similarly to $\vec{P}_{\text{sim}}(\vec{r}, \omega)$, the field distribution of the incident electromagnetic wave $\vec{\mathcal{E}}_0(\vec{r}, \omega)$ should be extracted from reference simulations without antennas to suppress possible errors due to discretization and any other artifacts inherent to the simulation software.

If we now take a step further and consider a whole ensemble of mutually interacting diablo antennas, it is our assumption that the current distribution of the fundamental eigenmode in each antenna remains the same, the only quantity that changes is the excitation amplitude. Denoting $\alpha(\omega)$ the proportionality factor between the excitation amplitude and the amplitude $E_0(\omega)$ of the incident electromagnetic wave, the weight of the fundamental eigenmode in the i -th antenna of the ensemble amounts to

$$p_i(\omega) = \alpha(\omega) \left[E_0(\omega) + \sum_j g_{ij}(\omega) p_j(\omega) \right]. \quad (1.101)$$

The above equation represents a linear equation system for the excitation amplitudes that is easily solvable by direct inversion, provided we are able to determine the parameters $g_{ij}(\omega)$ capturing the mutual interaction between antennas. The measure of how much one antenna affects another is not simply given by the strength of the field that the former generates at the position of the latter (like in the case of point dipoles), but it depends also on its spatial profile, namely how well it matches the current distribution of the fundamental eigenmode. Designating $\vec{\mathcal{E}}_j(\vec{r}, \omega)$ as the field generated by the fundamental eigenmode of the j -th antenna at the position of the i -th antenna, the interaction parameter reads

$$g_{ij}(\omega) = \frac{\int_V d\vec{r}^3 \vec{\mathcal{P}}^*(\vec{r}, \omega) \cdot \vec{\mathcal{E}}_j(\vec{r}, \omega)}{\int_V d\vec{r}^3 \vec{\mathcal{P}}^*(\vec{r}, \omega) \cdot \vec{\mathcal{E}}_0(\vec{r}, \omega)}. \quad (1.102)$$

The division by the overlap integral containing the incident field distribution ensures that the above expression is compatible with the amplitude scaling defined in Eq. (1.101): if the field generated by j -th antenna $p_j(\omega) \vec{\mathcal{E}}_j(\vec{r}, \omega)$ was identical to the field distribution of the incident electromagnetic wave $E_0(\omega) \vec{\mathcal{E}}_0(\vec{r}, \omega)$, the interaction term $g_{ij}(\omega) p_j(\omega)$ would be equal to E_0 , effectively doubling the amplitude of the incident wave. The last parameter that remains to be determined is the proportionality factor $\alpha(\omega)$ in Eq. (1.101). Using the definition of the fundamental eigenmode from Eq. (1.100) and demanding that in the limit of a solitary antenna, the above expressions lead to the original current distribution $\vec{P}_{\text{sim}}(\vec{r}, \omega)$ extracted from numerical simulations, we obtain the following equality

$$\vec{P}_{\text{sim}}(\vec{r}, \omega) = \alpha(\omega) \vec{\mathcal{P}}(\vec{r}, \omega) = \alpha(\omega) \frac{\vec{P}_{\text{sim}}(\vec{r}, \omega) \|\vec{\mathcal{E}}_0(\vec{r}, \omega)\|}{\frac{1}{V} \int_V d\vec{r}^3 \vec{P}_{\text{sim}}(\vec{r}, \omega) \cdot \vec{\mathcal{E}}_0^*(\vec{r}, \omega)}. \quad (1.103)$$

The comparison of the terms on the left and right hand side then yields

$$\alpha(\omega) = \frac{1}{\|\vec{\mathcal{E}}_0(\vec{r}, \omega)\|} \frac{1}{V} \int_V d\vec{r}^3 \vec{P}_{\text{sim}}(\vec{r}, \omega) \cdot \vec{\mathcal{E}}_0^*(\vec{r}, \omega). \quad (1.104)$$

Note that in the course of determining $\alpha(\omega)$, we implicitly set the amplitude of the incident wave to $E_0(\omega) = 1$ and we could have done so from the very beginning. The reason for introducing this apparently redundant parameter into the above formalism is to keep open the option of having an inhomogeneous illumination. We have assumed so far that the complex amplitude of the incident wave is the same for all the antennas in the ensemble, but the experimental setup will most probably employ beams with a gaussian or possibly some other spatial profile. We can account for that simply by letting $E_0(\omega)$ to vary from antenna to antenna. In the mathematical notation, this amounts to adding an index i to the respective term in Eq. (1.101)

$$p_i(\omega) = \alpha(\omega) \left[E_{0i}(\omega) + \sum_j g_{ij}(\omega) p_j(\omega) \right]. \quad (1.105)$$

Equations (1.99)–(1.105) constitute the groundwork on which the rest of our interaction model is built on. It still remains to specify the exact procedure for calculating the interaction parameter $g_{ij}(\omega)$ or the quantities characterizing the overall response of the antenna array, but these issues are of a rather technical nature. The essential aspects of the whole concept, including the underlying assumptions and approximations, are contained in the paragraphs above.

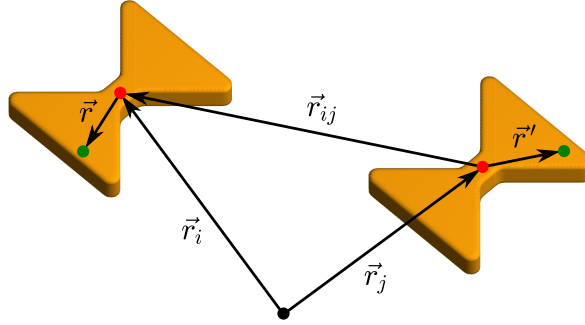


Figure 1.9: Definition of the various position vectors involved in the evaluation of the interaction between antennas. The red dots mark the centers of the antennas, while the green ones refer to the positions of the source (\vec{r}') and the target point (\vec{r}), at which the field generated by that source is calculated.

Next, let us focus on the interaction parameter $g_{ij}(\omega)$, namely its evaluation in the case of two identical antennas located some distance apart. Marking the vector connecting the centers of the two antennas as \vec{r}_{ij} , the electric field generated by the j -th antenna at a position \vec{r} within the i -th antenna can be written as

$$\vec{\mathcal{E}}_j(\vec{r}, \omega) = \int_V d\vec{r}'^3 \vec{G}(\vec{r} + \vec{r}_{ij}, \vec{r}', \omega) \vec{\mathcal{P}}(\vec{r}', \omega), \quad (1.106)$$

where the vectors \vec{r} and \vec{r}' are measured relatively to the position vectors \vec{r}_i and \vec{r}_j of the respective antenna centers. To help the reader to get a grip on the roles played by these various vectors, we schematically depict the considered coordinate system in Figure 1.9. Finally, insertion of $\vec{\mathcal{E}}_j(\vec{r}, \omega)$ into Eq. (1.102) yields

$$g_{ij}(\omega) = \frac{\int_V d\vec{r}^3 \vec{\mathcal{P}}^*(\vec{r}, \omega) \cdot \int_V d\vec{r}'^3 \vec{G}(\vec{r} + \vec{r}_{ij}, \vec{r}', \omega) \vec{\mathcal{P}}(\vec{r}', \omega)}{\int_V d\vec{r}^3 \vec{\mathcal{P}}^*(\vec{r}, \omega) \cdot \vec{\mathcal{E}}_0(\vec{r}, \omega)}. \quad (1.107)$$

The dyadic Green's function $\vec{G}(\vec{r}, \vec{r}', \omega)$ linking the electric field to its source generally depends on the environment. While there exists a closed form expression for $\vec{G}(\vec{r}, \vec{r}', \omega)$ in a homogenous space,

there is none for geometries that contain a substrate—even the presence of a single planar interface between two media poses in this respect an insurmountable obstacle. Fortunately, the possibility to decompose the free space dyadic Green’s function into plane waves and treat their reflection at the planar interface between the substrate and the superstrate individually allows us to express $\vec{G}(\vec{r}, \vec{r}', \omega)$ as a Fourier integral

$$\vec{G}(\vec{r}, \vec{r}', \omega) = \iint_{-\infty}^{\infty} d\vec{q}^2 \vec{G}(\vec{q}, z, z', \omega) e^{i\vec{q} \cdot (\vec{r}_{\parallel} - \vec{r}'_{\parallel})}. \quad (1.108)$$

We should stress that the presence of a substrate does not disrupt the translational invariance of the dyadic Green’s function along the lateral coordinates (parallel to the substrate surface), i.e. $\vec{G}(\vec{r}, \vec{r}', \omega) = \vec{G}(\vec{r}_{\parallel} - \vec{r}'_{\parallel}, z, z', \omega)$, which entitles us to perform the above plane wave expansion.

The fact that the Fourier components $\vec{G}(\vec{q}, z, z', \omega)$ are readily accessible, while $\vec{G}(\vec{r}, \vec{r}', \omega)$ requires prior integration, brings us to the alluring alternative of switching to the reciprocal space and evaluating the interaction parameter $g_{ij}(\omega)$ there. Expressing the current distribution of the fundamental eigenmode in terms of its Fourier spectrum and making the notation less cumbersome by dropping the dependence on ω for a moment, the numerator in Eq. (1.107) becomes

$$g_{ij} \sim \int_V d\vec{r}^3 \iint_{-\infty}^{\infty} d\vec{q}^2 e^{-i\vec{q} \cdot \vec{r}_{\parallel}} \vec{P}^*(\vec{q}, z) \cdot \int_V d\vec{r}'^3 \vec{G}(\vec{r} + \vec{r}_{ij}, \vec{r}') \iint_{-\infty}^{\infty} d\vec{q}'^2 e^{i\vec{q}' \cdot \vec{r}'_{\parallel}} \vec{P}(\vec{q}', z'). \quad (1.109)$$

After changing the order of integrations and expanding the equation by $e^{i\vec{q}' \cdot (\vec{r}_{\parallel} + \vec{r}_{ij})} e^{-i\vec{q}' \cdot (\vec{r}_{\parallel} + \vec{r}_{ij})}$, we obtain

$$g_{ij} \sim \iint_{-\infty}^{\infty} d\vec{q}^2 \iint_{-\infty}^{\infty} d\vec{q}'^2 \int_V d\vec{r}^3 e^{-i(\vec{q} - \vec{q}') \cdot \vec{r}_{\parallel}} e^{i\vec{q}' \cdot \vec{r}_{ij}} \vec{P}^*(\vec{q}, z) \cdot \int_V d\vec{r}'^3 \vec{G}(\vec{r} + \vec{r}_{ij}, \vec{r}') e^{-i\vec{q}' \cdot (\vec{r}_{\parallel} + \vec{r}_{ij} - \vec{r}'_{\parallel})} \vec{P}(\vec{q}', z'), \quad (1.110)$$

where the last integral can be partly recognized as the inverse Fourier transform (note that since we deal with a two dimensional antenna array, \vec{r}_{ij} is always parallel to the substrate surface)

$$\vec{G}(\vec{q}', z, z', \omega) = \frac{1}{4\pi^2} \int d\vec{r}'^2_{\parallel} \vec{G}(\vec{r}_{\parallel} + \vec{r}_{ij} - \vec{r}'_{\parallel}, z, z') e^{-i\vec{q}' \cdot (\vec{r}_{\parallel} + \vec{r}_{ij} - \vec{r}'_{\parallel})}. \quad (1.111)$$

Finally, by exploiting the identity $\frac{1}{4\pi^2} \int d\vec{r}'^2_{\parallel} e^{-i(\vec{q} - \vec{q}') \cdot \vec{r}_{\parallel}} = \delta^2(\vec{q} - \vec{q}')$, we acquire the following expression for $g_{ij}(\omega)$

$$g_{ij}(\omega) = \frac{(4\pi^2)^2 \iint_{-\infty}^{\infty} d\vec{q}^2 \int dz \int dz' e^{i\vec{q} \cdot \vec{r}_{ij}} \vec{P}^*(\vec{q}, z, \omega) \cdot \vec{G}(\vec{q}, z, z', \omega) \vec{P}(\vec{q}, z', \omega)}{\int_V d\vec{r}^3 \vec{P}^*(\vec{r}, \omega) \cdot \vec{\mathcal{E}}_0(\vec{r}, \omega)}. \quad (1.112)$$

The evaluation of the interaction parameter in the reciprocal space leads to a Fourier integral that enables us, using fast Fourier transform (FFT) algorithm, to calculate $g_{ij}(\omega)$ for a whole set of inter-antenna separations \vec{r}_{ij} in a single pass. It turns out, however, that certain aspects of FFT, namely its periodic nature and the cutoff of high spatial frequencies, give rise to inaccuracies that render this approach unsuitable. There is no other option but to perform the integration in the real space.

First, let us recast Equation (1.107) into a form more convenient for numerical processing. After expressing the scalar and tensor product in terms of a double sum and adopting the substitution $\vec{r}'_{\parallel} = \vec{s} + \vec{r}_{\parallel}$, it becomes

$$\begin{aligned}
 g_{ij}(\omega) &\sim \int dz \int dz' \int d\vec{r}_{\parallel}^2 \vec{\mathcal{P}}^*(\vec{r}_{\parallel}, z) \cdot \int d\vec{r}'_{\parallel}{}^2 \vec{G}(\vec{r}_{\parallel} + \vec{r}_{ij} - \vec{r}'_{\parallel}, z, z') \vec{\mathcal{P}}(\vec{r}'_{\parallel}, z') = \\
 &= \int dz \int dz' \int d\vec{r}_{\parallel}^2 \sum_{uv} \mathcal{P}_u^*(\vec{r}_{\parallel}, z) \int d\vec{r}'_{\parallel}{}^2 G_{uv}(\vec{r}_{\parallel} + \vec{r}_{ij} - \vec{r}'_{\parallel}, z, z') \mathcal{P}_v(\vec{r}'_{\parallel}, z') = \\
 &= \sum_{uv} \int dz \int dz' \int d\vec{r}_{\parallel}^2 \mathcal{P}_u^*(\vec{r}_{\parallel}, z) \int d\vec{s}^2 G_{uv}(\vec{r}_{ij} - \vec{s}, z, z') \mathcal{P}_v(\vec{s} + \vec{r}_{\parallel}, z'). \quad (1.113)
 \end{aligned}$$

where the summation runs over all the possible combinations of the Cartesian coordinates. If we now change the order of integrations and replace \vec{r}_{\parallel} with $-\vec{s}'$, we obtain

$$g_{ij}(\omega) \sim \sum_{uv} \int dz \int dz' \int d\vec{s}^2 G_{uv}(\vec{r}_{ij} - \vec{s}, z, z') \int d\vec{s}'^2 \mathcal{P}_v(\vec{s} - \vec{s}', z') \mathcal{P}_u^*(-\vec{s}', z). \quad (1.114)$$

The two two-dimensional convolutions over the lateral coordinates, together with the summation and the double integration over the z -coordinate add up to a computationally time consuming procedure, with the most critical part being the numerical calculation of the dyadic Green's function $\vec{G}(\vec{s}, z, z')$ for every possible combination of z and z' . The overall complexity of this procedure can be substantially reduced if some simplifications based on the geometrical parameters of our antennas are adopted. Recognizing that the height of the plasmonic structures (≈ 200 nm) is minute compared to both their lateral dimensions (30-150 μm) and the optical wavelength (300-1000 μm) in the THz and sub-THz spectral range, the dependence of $\vec{G}(\vec{s}, z, z')$ on the vertical coordinates z and z' can be neglected and approximated by the value taken at the surface of the substrate $\vec{G}(\vec{s}, z, z') \approx \vec{G}(\vec{s}, 0, 0) = \vec{G}(\vec{s})$ (note that we implicitly set the boundary between the substrate and the superstrate to $z = 0$). As a consequence, the integration over z and z' is now limited only to the current distribution of the fundamental mode and the expression for $g_{ij}(\omega)$ simplifies to

$$g_{ij}(\omega) = \frac{\sum_{uv} \int d\vec{s}^2 G_{uv}(\vec{r}_{ij} - \vec{s}, \omega) \int d\vec{s}'^2 \mathcal{P}_v(\vec{s} - \vec{s}', \omega) \mathcal{P}_u^*(-\vec{s}', \omega)}{\int_V d\vec{r}^3 \vec{\mathcal{P}}^*(\vec{r}, \omega) \cdot \vec{\mathcal{E}}_0(\vec{r}, \omega)}, \quad (1.115)$$

where $\vec{\mathcal{P}}(\vec{s})$ stands for the z -integrated current distribution $\int dz \vec{\mathcal{P}}(\vec{s}, z)$.

The above formula for the interaction parameter is suitable for a practical implementation and we employ it in all further calculations including the parameter optimization of antenna arrays. Its crucial ingredient is the dyadic Green's function, which has, as we have mentioned earlier, no closed form representation in the real space (at least in the presence of a substrate). There is, however, an integral representation that relies on the decomposition of fields into plane waves. Here, we shall just list the final expressions without delving into their detailed derivation, for that we refer the reader to e.g. Principles of Nano-Optics [2], Chapter 10.

Let us start with writing down the angular spectrum representation of the free space dyadic Green's function $\vec{G}_0(\vec{r}, \vec{r}')$

$$\vec{G}_0(\vec{r}_{\parallel} - \vec{r}'_{\parallel}, z, z') = \frac{i\omega^2 \mu_0}{8\pi^2} \iint_{-\infty}^{\infty} d\vec{q}^2 \vec{M}(\vec{q}) e^{i\vec{q} \cdot (\vec{r}_{\parallel} - \vec{r}'_{\parallel})} e^{ik_z |z - z'|}, \quad (1.116)$$

with k_z defined as $k_z = \sqrt{k^2 - |\vec{q}|^2}$ and components of the tensor $\vec{M}(\vec{q})$ given by

$$\vec{M}(\vec{q}) = \frac{1}{k^2 k_z} \begin{bmatrix} k^2 - q_x^2 & -q_x q_y & \mp q_x k_z \\ -q_x q_y & k^2 - q_y^2 & \mp q_y k_z \\ \mp q_x k_z & \mp q_y k_z & k^2 - k_z^2 \end{bmatrix}. \quad (1.117)$$

The choice of the sign in $\vec{M}(\vec{q})$ depends on the relative positions of the source and the point at which the field is calculated: the upper sign applies for $z > z'$, the lower one for when the situation is reversed. Furthermore, $k = \omega/c$ denotes the free space wavenumber and implicitly sets the threshold between the propagating ($|\vec{q}| \leq k$) and evanescent ($|\vec{q}| > k$) waves.

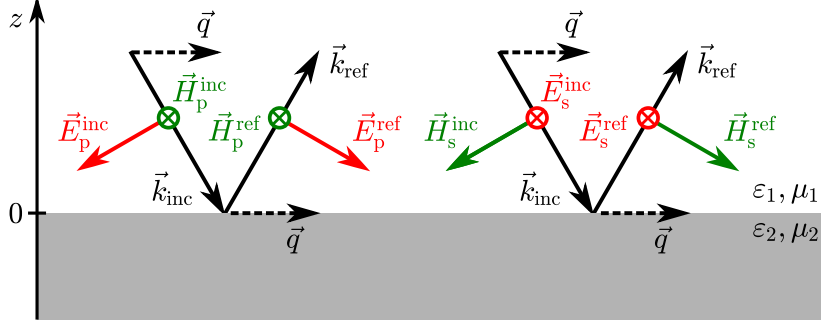


Figure 1.10: Specular reflection of an electromagnetic wave at a planar interface between two media, each characterized by a permittivity ε and a permeability μ . The amplitude of the reflected wave depends, besides the optical properties of those media, on the propagation direction \vec{k}_{inc} and the polarization (designated by the subscripts s and p) of the incident wave. The mutual orientation of the electric and magnetic fields in those two possible polarization states is indicated by the red (electric) and green (magnetic) arrows. Note that this particular geometrical representation is valid only for propagating waves, visualization of evanescent waves would require some minor modifications. The essential aspects of the reflection process, i.e. the distinction between the two polarization states and the conservation of the lateral momentum, would be, however, preserved.

When a substrate is added, each wave undergoes a reflection at the substrate-superstrate interface and the amplitude of the reflected wave depends on the polarization and the propagation direction of the original one. Usually, this process is described in terms of the Fresnel reflection coefficients $r_p(\vec{q})$ and $r_s(\vec{q})$, where the subscripts p and s, derived from the German words for parallel and perpendicular, differentiate between the two possible polarization states of the incident wave: $r_p(\vec{q})$ for waves with the electric field oscillating within the plane perpendicular to the substrate surface and $r_s(\vec{q})$ for waves with the electric field aiming strictly along the substrate-superstrate interface. The situation is schematically depicted in Figure 1.10. To acquire a dyadic Green's function that would account for the presence of a substrate, we just need to break down the tensor $\vec{M}(\vec{q})$ into two parts corresponding to the two different polarizations and multiply each with a respective Fresnel reflection coefficient. Denoting them $\vec{M}_s^{\text{ref}}(\vec{q})$ and $\vec{M}_p^{\text{ref}}(\vec{q})$, the total dyadic Green's function in the $z > 0$ halfspace then reads

$$\vec{G}(\vec{r}_{\parallel} - \vec{r}'_{\parallel}, z, z') = \frac{i\omega^2 \mu_0 \mu_1}{8\pi^2} \iint_{-\infty}^{\infty} d\vec{q}^2 \left\{ \vec{M}_0(\vec{q}) e^{ik_{z1}|z-z'|} + \left[\vec{M}_p^{\text{ref}}(\vec{q}) + \vec{M}_s^{\text{ref}}(\vec{q}) \right] e^{ik_{z1}(z+z')} \right\} e^{i\vec{q} \cdot (\vec{r}_{\parallel} - \vec{r}'_{\parallel})}, \quad (1.118)$$

$$\vec{M}_0(\vec{q}) = \frac{1}{k_1^2 k_{z1}} \begin{bmatrix} k_1^2 - q_x^2 & -q_x q_y & \mp q_x k_{z1} \\ -q_x q_y & k_1^2 - q_y^2 & \mp q_y k_{z1} \\ \mp q_x k_{z1} & \mp q_y k_{z1} & k_1^2 - k_{z1}^2 \end{bmatrix}, \quad (1.119)$$

$$\vec{M}_p^{\text{ref}}(\vec{q}) = \frac{-r_p(\vec{q})}{k_1^2 |\vec{q}|^2} \begin{bmatrix} q_x^2 k_{z1} & q_x q_y k_{z1} & q_x |\vec{q}|^2 \\ q_x q_y k_{z1} & q_y^2 k_{z1} & q_y |\vec{q}|^2 \\ -q_x |\vec{q}|^2 & -q_y |\vec{q}|^2 & -|\vec{q}|^4 / k_{z1} \end{bmatrix}, \quad (1.120)$$

$$\vec{M}_s^{\text{ref}}(\vec{q}) = \frac{r_s(\vec{q})}{k_{z1} |\vec{q}|^2} \begin{bmatrix} q_y^2 & -q_x q_y & 0 \\ -q_x q_y & q_x^2 & 0 \\ 0 & 0 & 0 \end{bmatrix}. \quad (1.121)$$

Note that the tensor \vec{M}_0 is the same as the one given by Eq. (1.117), except the free space wavenumber k was replaced with $k_1 = \sqrt{\varepsilon_1 \mu_1} \omega / c$ and the vertical component of the wavevector k_z made way for $k_{z1} = \sqrt{k_1^2 - |\vec{q}|^2}$, by which we account for the possibility that the superstrate might be some medium with a refractive index different from 1 (similar changes were adopted for all the other relevant terms in the above equations). Finally, recalling that we decided to drop the dependence of the dyadic Green's function on the vertical coordinates z and z' and approximate it by its value at the substrate surface, the full $\vec{G}(\vec{r}, \vec{r}')$ from Eq. (1.118) reduces to

$$\vec{G}(\vec{r}_{\parallel} - \vec{r}'_{\parallel}) = \vec{G}(\vec{r}_{\parallel} - \vec{r}'_{\parallel}, 0, 0) = \frac{i\omega^2 \mu_0 \mu_1}{8\pi^2} \iint_{-\infty}^{\infty} d\vec{q}^2 \left[\vec{M}_0(\vec{q}) + \vec{M}_p^{\text{ref}}(\vec{q}) + \vec{M}_s^{\text{ref}}(\vec{q}) \right] e^{i\vec{q} \cdot (\vec{r}_{\parallel} - \vec{r}'_{\parallel})}. \quad (1.122)$$

From the computational point of view, the above set of equations is already quite manageable. One can, however, avoid the double integral by switching to polar coordinates (q, φ) , where the integration over the azimuthal angle φ can be carried out analytically [2, 34] (provided that the substrate material is isotropic, i.e. the Fresnel coefficients depend only on the magnitude of the lateral wavevector $|\vec{q}| = q$). Before we do that, it is useful to set the origin of the coordinate system to coincide with the position of the source so that the following coordinate transformation can be implemented

$$x - x' = x = r \cos \psi, \quad (1.123)$$

$$y - y' = y = r \sin \psi. \quad (1.124)$$

This enables us, after converting the integral in Eq. (1.122) to polar coordinates, to write down the individual components of the dyadic Green's function in the following illuminating form

$$G_{uv}(r, \psi) = \frac{i\omega^2 \mu_0 \mu_1}{8\pi^2} \int_0^{\infty} dq \int_0^{2\pi} d\varphi q e^{iqr \cos(\varphi - \psi)} M_{uv}(q, \varphi). \quad (1.125)$$

The exponential factor in the above equation is characteristic for Bessel functions (it often appears in their integral representations). For our purposes, we shall require mainly the following two identities [35] featuring the Bessel function of the first kind $J_n(qr)$

$$\int_0^{2\pi} d\varphi \cos n\varphi e^{iqr \cos(\varphi - \psi)} = 2\pi i^n J_n(qr) \cos n\psi, \quad (1.126)$$

$$\int_0^{2\pi} d\varphi \sin n\varphi e^{iqr \cos(\varphi - \psi)} = 2\pi i^n J_n(qr) \sin n\psi, \quad (1.127)$$

where the various harmonics of the cosine and sine functions are directly linked to the order of the Bessel function n . By employing these mathematical relations, we dispose of the integral over the azimuthal angle, which leaves us only with a single integral over q for each component of the dyadic Green's function that have to be evaluated numerically (there are 9 components, but the number of integrals that need to be calculated is actually smaller). After several straightforward steps involving the use of basic trigonometric identities, these components are found to be

$$G_{xx}(r, \psi) = \frac{i\omega^2 \mu_0 \mu_1}{8\pi} \int_0^\infty dq \left\{ \frac{q}{k_1^2 k_{z1}} [(2k_1^2 - q^2) J_0(qr) + q^2 J_2(qr) \cos 2\psi] + r_s(q) \frac{q}{k_{z1}} [J_0(qr) + J_2(qr) \cos 2\psi] - r_p(q) \frac{q k_{z1}}{k_1^2} [J_0(qr) - J_2(qr) \cos 2\psi] \right\}, \quad (1.128)$$

$$G_{yy}(r, \psi) = \frac{i\omega^2 \mu_0 \mu_1}{8\pi} \int_0^\infty dq \left\{ \frac{q}{k_1^2 k_{z1}} [(2k_1^2 - q^2) J_0(qr) - q^2 J_2(qr) \cos 2\psi] + r_s(q) \frac{q}{k_{z1}} [J_0(qr) - J_2(qr) \cos 2\psi] - r_p(q) \frac{q k_{z1}}{k_1^2} [J_0(qr) + J_2(qr) \cos 2\psi] \right\}, \quad (1.129)$$

$$G_{xy}(r, \psi) = G_{yx}(r, \psi) = \frac{i\omega^2 \mu_0 \mu_1}{8\pi} \sin 2\psi \int_0^\infty dq J_2(qr) \left[\frac{q^3}{k_1^2 k_{z1}} + r_s(q) \frac{q}{k_{z1}} + r_p(q) \frac{q k_{z1}}{k_1^2} \right]. \quad (1.130)$$

$$G_{xz}(r, \psi) = \frac{\omega^2 \mu_0 \mu_1}{4\pi} \cos \psi \int_0^\infty dq \frac{q^2}{k_1^2} J_1(qr) [1 + r_p(q)], \quad (1.131)$$

$$G_{yz}(r, \psi) = \frac{\omega^2 \mu_0 \mu_1}{4\pi} \sin \psi \int_0^\infty dq \frac{q^2}{k_1^2} J_1(qr) [1 + r_p(q)], \quad (1.132)$$

$$G_{zz}(r, \psi) = \frac{i\omega^2 \mu_0 \mu_1}{4\pi} \int_0^\infty dq \frac{q^3}{k_1^2 k_{z1}} J_0(qr) [1 + r_p(q)], \quad (1.133)$$

$$G_{zx}(r, \psi) = \frac{\omega^2 \mu_0 \mu_1}{4\pi} \cos \psi \int_0^\infty dq \frac{q^2}{k_1^2} J_1(qr) [1 - r_p(q)], \quad (1.134)$$

$$G_{zy}(r, \psi) = \frac{\omega^2 \mu_0 \mu_1}{4\pi} \sin \psi \int_0^\infty dq \frac{q^2}{k_1^2} J_1(qr) [1 - r_p(q)]. \quad (1.135)$$

Even though it is not strictly necessary, it proves to be beneficial if we express the electric field generated by the source in the polar basis instead of the cartesian one. By doing that, we slightly decrease the number of integrals that have to be evaluated and incidentally also gain a more lucid representation of $\vec{G}(r, \psi)$ with no mixing between the various harmonics of the trigonometric functions. The polar projections $G_{r\beta}(r, \psi)$ and $G_{\psi\beta}(r, \psi)$, where β represents any of the Cartesian coordinates, are readily obtained from the cartesian ones by taking their appropriate linear combination

$$G_{r\beta}(r, \psi) = \cos \psi G_{x\beta}(r, \psi) + \sin \psi G_{y\beta}(r, \psi) \quad (1.136)$$

$$G_{\psi\beta}(r, \psi) = -\sin \psi G_{x\beta}(r, \psi) + \cos \psi G_{y\beta}(r, \psi). \quad (1.137)$$

Utilizing the above relations, the radial and the azimuthal components of the dyadic Green's function read

$$G_{rx}(r, \psi) = \frac{i\omega^2 \mu_0 \mu_1 k_1}{8\pi} \cos \psi I_1(k_1 r), \quad (1.138)$$

$$G_{\psi x}(r, \psi) = -\frac{i\omega^2 \mu_0 \mu_1 k_1}{8\pi} \sin \psi I_2(k_1 r), \quad (1.139)$$

$$G_{ry}(r, \psi) = \frac{i\omega^2 \mu_0 \mu_1 k_1}{8\pi} \sin \psi I_1(k_1 r), \quad (1.140)$$

$$G_{\psi y}(r, \psi) = \frac{i\omega^2 \mu_0 \mu_1 k_1}{8\pi} \cos \psi I_2(k_1 r), \quad (1.141)$$

$$G_{rz}(r, \psi) = \frac{\omega^2 \mu_0 \mu_1 k_1}{4\pi} \int_0^\infty d\lambda \lambda^2 J_1(\lambda k_1 r) [1 + r_p(\lambda)], \quad (1.142)$$

$$G_{\psi z}(r, \psi) = 0, \quad (1.143)$$

with the integrals $I_1(k_1 r)$ and $I_2(k_1 r)$ defined as

$$I_1(k_1 r) = \int_0^\infty d\lambda \left\{ \frac{\lambda}{\sqrt{1-\lambda^2}} [(2-\lambda^2) J_0(\lambda k_1 r) + \lambda^2 J_2(\lambda k_1 r)] + r_s(\lambda) \frac{\lambda}{\sqrt{1-\lambda^2}} [J_0(\lambda k_1 r) + J_2(\lambda k_1 r)] - r_p(\lambda) \lambda \sqrt{1-\lambda^2} [J_0(\lambda k_1 r) - J_2(\lambda k_1 r)] \right\}, \quad (1.144)$$

$$I_2(k_1 r) = \int_0^\infty d\lambda \left\{ \frac{\lambda}{\sqrt{1-\lambda^2}} [(2-\lambda^2) J_0(\lambda k_1 r) - \lambda^2 J_2(\lambda k_1 r)] + r_s(\lambda) \frac{\lambda}{\sqrt{1-\lambda^2}} [J_0(\lambda k_1 r) - J_2(\lambda k_1 r)] - r_p(\lambda) \lambda \sqrt{1-\lambda^2} [J_0(\lambda k_1 r) + J_2(\lambda k_1 r)] \right\}. \quad (1.145)$$

It is worth noting that we changed the integration variable in the above integrals to $\lambda = q/k_1$ so that they are all now only a function of a single dimensionless parameter $k_1 r$. This change highlights the fact that all the above integrals do not explicitly depend on frequency, ω enters them only through the parameter $k_1 r$ in the argument of the Bessel functions. This is of a great practical import since it allows us, for a given substrate, to calculate the dyadic Green's function only once for a sufficient range of values of the parameter $k_1 r$ and save it into a database. The value of the dyadic Green's function for some specific frequency ω and distance r can be then simply recovered from such a database using interpolation.

We should stress that the above notion is built on the assumption that the substrate can be considered semi-infinite and its optical properties constant within the spectral range relevant to EPR. While the latter seems to be a reasonable requirement, the thickness of typical substrates will be in reality probably comparable to or even less than the optical wavelengths encountered in the EPR spectroscopy. It turns out, however, that introduction of a finite substrate does not pose a serious problem. The presence of the additional interface will affect only the Fresnel reflection coefficients. More specifically, reflections at the bottom surface of a substrate with a thickness d will give rise to an exponential factor $\exp(2ik_{z2}d)$ in the functions $r_p(\lambda)$ and $r_s(\lambda)$, where $k_{z2} = \sqrt{k_2^2 - k_1^2 \lambda^2} = k_2 \sqrt{1 - (\varepsilon_1 \mu_1)/(\varepsilon_2 \mu_2) \lambda^2}$ denotes the vertical component of the wavevector describing the propagation of a plane wave inside the substrate. Capitalizing on the analogy with the parameter $k_1 r$, we can expand our previous statement and point out that the integrals appearing in Eqs. (1.128)-(1.145) do not explicitly depend on ω even in the presence of a finite substrate. The frequency enters those

expressions only indirectly through the parameters $k_1 r$ and $k_2 d$. Consequently, we can still build a database of dyadic Green's functions that can be used to quickly find their value at any frequency ω and at any distance r within a certain interval, except now the interpolation will be performed within a two-dimensional parameter space spanned by $k_1 r$ and $k_2 d$.

Let us briefly comment on the necessity of creating a database of dyadic Green's functions. If our goal was to calculate the response of only one particular antenna array, its creation could be considered superfluous, but for a design optimization, where multiple geometrical parameters are varied, the existence of such a database is without a doubt vital. On that note, it is equally important to possess a similar database for the interaction parameter $g_{ij}(\omega)$, since its tabulation in terms of the inter-antenna separation \vec{r}_{ij} can substantially reduce the time required for finding the optimal spacing between antennas within an array.

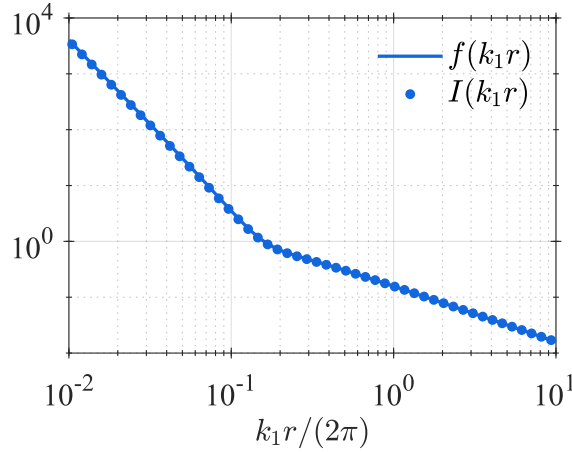


Figure 1.11: Validation of the integration procedure employed in the calculation of the dyadic Green's function. The extension of the integration path into the complex plane and the cut-off of high frequency contributions using the Hann function (dots) leads only to minute deviations from the exact analytical expression (solid line).

One of the last issues that should be addressed before we embark on the benchmark tests of the array interaction model is the integration procedure used for the computation of the above dyadic Green's function. Inspection of Eqs. (1.144) and (1.145) reveals two potential difficulties: the first are the singularities such as $1/\sqrt{1-\lambda^2}$ or those lurking inside the Fresnel reflection coefficient, the second is the overall slow convergence of the integrals for small values of the parameter $k_1 r$. A common solution to these problems is to extend the integration path into the complex plane [2], i.e. add a small imaginary part to the integration variable q . To further improve the rate of convergence, we also decided to multiply the integrands by the Hann function $g(q)$ defined as

$$g(q) = \left\{ \begin{array}{ll} \frac{1}{2} + \frac{1}{2} \cos\left(\frac{2\pi q}{q_{\max}}\right), & q \leq q_{\max} \\ 0, & q > q_{\max} \end{array} \right\}. \quad (1.146)$$

The parameter q_{\max} , acting effectively as a new upper integration limit, was dynamically varied depending on the value of the parameter $k_1 r$. The validity of these steps is demonstrated by Figure 1.11, where the integral $I(k_1 r)$ —appearing, for example, in Eq. (1.133) and evaluated using the integration procedure outlined above—is compared to the exact analytical solution $f(k_1 r)$ given below

$$f(k_1 r) = i \frac{e^{ik_1 r}}{k_1 r} \left[\frac{1}{(k_1 r)^2} - \frac{i}{k_1 r} - 1 \right] = \int_0^{\infty} d\lambda \frac{\lambda^3}{\sqrt{1-\lambda^2}} J_0(\lambda k_1 r) = I(k_1 r). \quad (1.147)$$

The relative difference between those two was, in this particular calculation, well below 5% in the $k_1 r / (2\pi) < 1$ range and less than 0.1% for $k_1 r / (2\pi) \geq 1$. The precision could be improved by increasing the value of the parameter q_{\max} , but considering the whole spectrum of approximations that were adopted up to this point, the merits would not probably outweigh the inevitable increase in the computation time.

With the dyadic Green's function at hand, we are finally able to calculate the interaction parameter $g_{ij}(\omega)$ and using Eq. (1.105), subsequently determine the excitation amplitudes of the fundamental eigenmode in the antenna ensemble. The last missing piece of the "puzzle" is a tool that would enable us to characterize the overall response of the ensemble. One option is to look at the total scattering cross-section, others include calculation of the scattering amplitude along the propagation direction of the incident electromagnetic wave (de facto the extinction) or the integral magnetic field enhancement around the antennas. We shall address them one by one, starting with the scattering cross-section $C_{\text{sca}}(\omega)$ defined as the total scattered power divided by the intensity of the incident plane wave $I_0(\omega)$. Referring the reader to Appendix A for the detailed derivation of the far-field projections in stratified media, the scattering cross-section can be broken down into two contributions $C_{\text{sca}}^{\uparrow}(\omega)$ and $C_{\text{sca}}^{\downarrow}(\omega)$ corresponding to the power radiated into the upper (\uparrow) and lower (\downarrow) halfspaces

$$C_{\text{sca}}^{\uparrow}(\omega) = 4\pi^2 \iint_{q \leq k_1} d\vec{q}^2 \frac{k_{z1}}{k_1} \frac{|\vec{E}_{\text{ens}}^{\uparrow}(\vec{q}, \omega)|^2}{|\vec{E}_0(\omega)|^2} = \frac{4\pi^2}{|\vec{E}_0(\omega)|^2} \iint_{q \leq k_1} d\vec{q}^2 \frac{k_{z1}}{k_1} \left| \begin{bmatrix} E_{\text{src}}^{+s}(\vec{q}, \omega) + r_{1n}^s(\vec{q}, \omega) E_{\text{src}}^{-s}(\vec{q}, \omega) \\ E_{\text{src}}^{+p}(\vec{q}, \omega) + r_{1n}^p(\vec{q}, \omega) E_{\text{src}}^{-p}(\vec{q}, \omega) \end{bmatrix} \right|^2, \quad (1.148)$$

$$C_{\text{sca}}^{\downarrow}(\omega) = 4\pi^2 \iint_{q \leq k_n} d\vec{q}^2 \frac{k_{zn}}{k_1} \frac{|\vec{E}_{\text{ens}}^{\downarrow}(\vec{q}, \omega)|^2}{|\vec{E}_0(\omega)|^2} = \frac{4\pi^2}{|\vec{E}_0(\omega)|^2} \iint_{q \leq k_n} d\vec{q}^2 \frac{k_{zn}}{k_1} \left| \begin{bmatrix} t_{1n}^s(\vec{q}, \omega) E_{\text{src}}^{-s}(\vec{q}, \omega) \\ t_{1n}^p(\vec{q}, \omega) E_{\text{src}}^{-p}(\vec{q}, \omega) \end{bmatrix} \right|^2. \quad (1.149)$$

where the electric field $\vec{E}_{\text{ens}}^{\uparrow/\downarrow}(\vec{q}, \omega)$ generated by the ensemble of antennas in those two halfspaces is expressed in the two component basis of s- and p-polarized waves. The Fresnel reflection $r_{1n}^{s/p}(\vec{q}, \omega)$ and transmission $t_{1n}^{s/p}(\vec{q}, \omega)$ coefficients account for the interaction of the downward emitted waves with the substrate (the use of the subscript n was made in preparation for a situation, when the substrate is finite, possibly made of several layers). The electric field amplitudes $E_{\text{src}}^{\pm s/p}(\vec{q}, \omega)$ of the upward (+) and downward (-) emitted waves are calculated from the Fourier components of the ensemble current distribution $\vec{P}_{\text{ens}}(\vec{q}, \omega)$

$$\begin{bmatrix} E_{\text{src}}^{+s}(\vec{q}, \omega) \\ E_{\text{src}}^{+p}(\vec{q}, \omega) \end{bmatrix} = \frac{i\omega^2 \mu_0 \mu_1}{2k_{z1}} \begin{bmatrix} -\frac{q_y}{q} & \frac{q_x}{q} & 0 \\ \pm \frac{q_x}{q} \frac{k_{zj}}{k_j} & \pm \frac{q_y}{q} \frac{k_{zj}}{k_j} & -\frac{q}{k_j} \end{bmatrix} \begin{bmatrix} P_{\text{ens}}^x(\vec{q}, \omega) \\ P_{\text{ens}}^y(\vec{q}, \omega) \\ P_{\text{ens}}^z(\vec{q}, \omega) \end{bmatrix}. \quad (1.150)$$

In the real space, the ensemble current distribution $\vec{P}_{\text{ens}}(\vec{r}, \omega)$ is constructed from a set of spatially shifted distributions of the fundamental eigenmode $\vec{P}(\vec{r}, \omega)$, each weighted by the respective excitation amplitude $p_i(\omega)$ previously determined from Eq. (1.105) of the interaction model. Replacing the full current distribution with its z -integrated value (an acceptable approximation considering the deeply subwavelength vertical size of our antennas)

$$\vec{P}_{\text{ens}}(\vec{r}_{\parallel}, \omega) = \sum_i \vec{P}_i(\vec{r}_{\parallel}, \omega) = \sum_i p_i(\omega) \vec{P}(\vec{r}_{\parallel} - \vec{r}_i, \omega) = \sum_i p_i(\omega) \int dz \vec{P}(\vec{r}_{\parallel} - \vec{r}_i, z, \omega), \quad (1.151)$$

the Fourier representation of the ensemble current distribution can be written as a product of the current distribution of the fundamental eigenmode and the structure factor $\sum_i p_i(\omega) e^{-i\vec{q} \cdot \vec{r}_i}$

$$\begin{aligned}
 \vec{P}_{\text{ens}}(\vec{q}, \omega) &= \frac{1}{4\pi^2} \iint_{-\infty}^{\infty} d\vec{r}_{\parallel}^2 \vec{P}_{\text{ens}}(\vec{r}_{\parallel}, \omega) e^{-i\vec{q}\cdot\vec{r}_{\parallel}} = \sum_i p_i(\omega) \frac{1}{4\pi^2} \iint_{-\infty}^{\infty} d\vec{r}_{\parallel}^2 \vec{P}(\vec{r}_{\parallel} - \vec{r}_i, \omega) e^{-i\vec{q}\cdot\vec{r}_{\parallel}} = \\
 &= \vec{P}(\vec{q}, \omega) \sum_i p_i(\omega) e^{-i\vec{q}\cdot\vec{r}_i}.
 \end{aligned} \tag{1.152}$$

As it turns out, this factorization can be extended all the way up to the level of the far-field representation of the electric fields

$$\vec{E}_{\text{ens}}^{\uparrow/\downarrow}(\vec{q}, \omega) = \vec{E}_{\text{sng}}^{\uparrow/\downarrow}(\vec{q}, \omega) \sum_i p_i(\omega) e^{-i\vec{q}\cdot\vec{r}_i}, \tag{1.153}$$

where the electric field $\vec{E}_{\text{sng}}^{\uparrow/\downarrow}(\vec{q}, \omega)$ generated by the fundamental eigenmode in the upper and lower halfspaces is constructed in the same way as $\vec{E}_{\text{ens}}^{\uparrow/\downarrow}(\vec{q}, \omega)$, except the ensemble current distribution $\vec{P}_{\text{ens}}(\vec{q}, \omega)$ in Eq. (1.150) has to be swapped for $\vec{P}(\vec{q}, \omega)$. Consequently, the expressions for the scattering cross-section become

$$C_{\text{sca}}^{\uparrow}(\omega) = 4\pi^2 \iint_{q \leq k_1} d\vec{q}^2 \frac{k_{z1}}{k_1} \frac{|\vec{E}_{\text{sng}}^{\uparrow}(\vec{q}, \omega)|^2}{|\vec{E}_0(\omega)|^2} \left| \sum_i p_i(\omega) e^{-i\vec{q}\cdot\vec{r}_i} \right|^2, \tag{1.154}$$

$$C_{\text{sca}}^{\downarrow}(\omega) = 4\pi^2 \iint_{q \leq k_n} d\vec{q}^2 \frac{k_{zn}}{k_1} \frac{|\vec{E}_{\text{sng}}^{\downarrow}(\vec{q}, \omega)|^2}{|\vec{E}_0(\omega)|^2} \left| \sum_i p_i(\omega) e^{-i\vec{q}\cdot\vec{r}_i} \right|^2. \tag{1.155}$$

The next quantity that can be used to assess the response of antenna arrays (and is closely related to the extinction) is the scattering amplitude in the directions associated with the propagation of the incident wave. In a homogeneous space, this would be simply the radiation scattered along the wavevector \vec{k}_0 of the incident wave. In the presence of a substrate, however, one should rather consider the propagation directions of the transmitted and specularly reflected waves. Even though these two distinctive scattering amplitudes can be in principle used for characterization of any ensemble of antennas, our interest in them stems mainly from their importance for the case of regular dense arrays that can be effectively regarded as possibly anisotropic, but homogeneous 2D materials. The fact that their optical response can be then described in terms of effective Fresnel coefficients is used later in this chapter in our analysis of Fabry-Perot modes and their practical impact on measurements.

Since the use of an illumination in the form of a plane wave would, in this instance, lead to calculations involving an infinite antenna array (to deserve the denomination "homogeneous", the extent of our artificial 2D material needs to be at least the same or larger than the lateral size of the source wave), we settled for a gaussian beam with a large enough waist radius w_0 for it to be a passable approximation of a plane wave. Assuming the waist of the beam coincides with the plane $z=0$ forming the base of the antennas, the amplitudes $E_{0i}(\omega)$ of the driving electric field appearing in Eq. (1.105) become a gaussian function of the antenna positions $\vec{r}_i = (x_i, y_i)$

$$E_{0i}(x_i, y_i, \omega) = E_0(\omega) \exp\left(-\frac{x_i^2 + y_i^2}{w_0^2}\right), \tag{1.156}$$

where $E_0(\omega)$ stands for the amplitude of the electric field in the center of the beam. The optical response of the whole system including the substrate can be conveniently expressed in terms of effective Fresnel reflection $r_{\text{eff}}(\omega)$ and transmission $t_{\text{eff}}(\omega)$ coefficients relating the total field reflected from $\vec{E}_{\text{tot}}^{\uparrow}(\vec{0}, \omega)$ and transmitted through $\vec{E}_{\text{tot}}^{\downarrow}(\vec{0}, \omega)$ the system to the field of the impinging beam $\vec{E}_0(\vec{0}, \omega)$

$$\begin{aligned}
 r_{\text{eff}}(\omega) &= \frac{\vec{E}_{\text{tot}}^{\uparrow}(\vec{0}, \omega) \cdot \vec{E}_0^*(\vec{0}, \omega)}{|\vec{E}_0(\vec{0}, \omega)|^2} = \frac{[\vec{E}_{\text{ens}}^{\uparrow}(\vec{0}, \omega) + r_{1n}(\omega)\vec{E}_0(\vec{0}, \omega)] \cdot \vec{E}_0^*(\vec{0}, \omega)}{|\vec{E}_0(\vec{0}, \omega)|^2} = \\
 &= r_{1n}(\omega) + \frac{4\pi}{\omega_0^2} \frac{\vec{E}_{\text{sng}}^{\uparrow}(\vec{0}, \omega) \cdot \vec{E}_0^*(\omega)}{|\vec{E}_0(\omega)|^2} \sum_i p_i(\omega), \tag{1.157}
 \end{aligned}$$

$$\begin{aligned}
 t_{\text{eff}}(\omega) &= \frac{\vec{E}_{\text{tot}}^{\downarrow}(\vec{0}, \omega) \cdot \vec{E}_0^*(\vec{0}, \omega)}{|\vec{E}_0(\vec{0}, \omega)|^2} = \frac{[\vec{E}_{\text{ens}}^{\downarrow}(\vec{0}, \omega) + t_{1n}(\omega)\vec{E}_0(\vec{0}, \omega)] \cdot \vec{E}_0^*(\vec{0}, \omega)}{|\vec{E}_0(\vec{0}, \omega)|^2} = \\
 &= t_{1n}(\omega) + \frac{4\pi}{\omega_0^2} \frac{\vec{E}_{\text{sng}}^{\downarrow}(\vec{0}, \omega) \cdot \vec{E}_0^*(\omega)}{|\vec{E}_0(\omega)|^2} \sum_i p_i(\omega), \tag{1.158}
 \end{aligned}$$

with the angular spectrum representation of the gaussian beam given by

$$\vec{E}_0(q_x, q_y, \omega) = \vec{E}_0(\omega) \frac{\omega_0^2}{4\pi} \exp\left[-\frac{\omega_0^2 (q_x^2 + q_y^2)}{4}\right]. \tag{1.159}$$

Note that while there might be other possible formulations, our definition of the effective Fresnel coefficients via the $\vec{q}=\vec{0}$ Fourier component of the electric field complies best with the original definition based on the response of the system to a plane wave propagating at normal incidence.

The third and perhaps the most relevant quantity that we employ in characterization of antenna arrays in EPR is the average magnetic field enhancement $\eta_{\text{avg}}^{\circ/\circ}$. As we have shown in the previous section, it is the primary parameter that determines whether the structure is suitable for the EPR spectroscopy. In other words, this is the quantity that should be maximized in our search for the optimal antenna array design. Invoking its definition given by Eq. (1.55), the average magnetic field enhancement within an EPR layer of thickness h_{EPR} uniformly covering an antenna array reads

$$\eta_{\text{avg}}^{\circ/\circ}(\omega, h_{\text{EPR}}) = \frac{1}{V} \int_V dV \frac{|H^{\circ/\circ}(\vec{r}, \omega)|^2}{|H_0^{\circ/\circ}(\vec{r}, \omega)|^2}, \tag{1.160}$$

where the choice, which circular polarization to take, depends on the orientation of the static magnetic field. Assuming the array consists of $N \times N$ antennas and it can be broken down into N^2 identical cells, each with an area S_{cell} , the single volume integral becomes a sum of integrals over the individual cells

$$\frac{1}{V} \int_V dV \rightarrow \frac{1}{N^2 V_{\text{cell}}} \sum_i^{N^2} \int_{V_{\text{cell}}} dV = \frac{1}{N^2 S_{\text{cell}} h_{\text{EPR}}} \sum_i^{N^2} \iint_{S_{\text{cell}}} d\vec{r}_{\parallel}^2 \int_{z_0(\vec{r}_{\parallel})}^{z_0(\vec{r}_{\parallel})+h_{\text{EPR}}} dz. \tag{1.161}$$

Note that the limits of integration over the vertical coordinate z are a function of the lateral position \vec{r}_{\parallel} . This just reflects the terrace-like nature of the surface onto which the EPR-active material is deposited (simply put, EPR layer copies the profile created by the antennas).

The total magnetic field $H^{\circ/\circ}(\vec{r}, \omega)$ in Eq. (1.160) can be written as a sum of the field generated by the antennas $H_{\text{ens}}^{\circ/\circ}(\vec{r}, \omega)$ and the field $H_0^{\circ/\circ}(\vec{r}, \omega)$ that would be detected in their absence. The calculation of $H_{\text{ens}}^{\circ/\circ}(\vec{r}, \omega)$ from the ensemble current distribution and its subsequent integration over each cell might be computationally quite demanding. That situation can be avoided, if the following approximation is embraced. Let us suppose that the magnetic field of an antenna is mostly localized close to its surface and the growth of the average enhancement rapidly falls off as we increase the integration area beyond the immediate vicinity of this antenna. In that case, we can neglect the contributions of the antennas to the magnetic field in the surrounding cells and replace $H_{\text{ens}}^{\circ/\circ}(\vec{r}, \omega)$

with the magnetic field of a single antenna $H_{\text{sng}}^{\circ/\circ}(\vec{r}, \omega)$ weighted by the corresponding excitation amplitude $p_i(\omega)$. Finally, after realizing that $H_{\text{sng}}^{\circ/\circ}(\vec{r}, \omega)$ can be obtained directly from the solitary antenna simulations, the procedure for calculating the average magnetic enhancement is simplified substantially

$$\begin{aligned} \eta_{\text{avg}}^{\circ/\circ}(\omega, h_{\text{EPR}}) &= \frac{1}{N^2 V_{\text{cell}}} \sum_i^{N^2} \int_{V_{\text{cell}}} dV \frac{\left| H_0^{\circ/\circ}(\vec{r}, \omega) + \frac{p_i(\omega)}{\alpha(\omega)} H_{\text{sim}}^{\circ/\circ}(\vec{r}, \omega) \right|^2}{|H_0^{\circ/\circ}(\vec{r}, \omega)|^2} = \\ &= 1 + \frac{\sum_i^{N^2} |p_i(\omega)|^2}{N^2 V_{\text{cell}} |\alpha(\omega)|^2} \int_{V_{\text{cell}}} dV \frac{|H_{\text{sim}}^{\circ/\circ}(\vec{r}, \omega)|^2}{|H_0^{\circ/\circ}(\vec{r}, \omega)|^2} + 2\text{Re} \left\{ \frac{\sum_i^{N^2} p_i(\omega)}{N^2 V_{\text{cell}} \alpha(\omega)} \int_{V_{\text{cell}}} dV \frac{H_0^{\circ/\circ*}(\vec{r}, \omega) H_{\text{sim}}^{\circ/\circ}(\vec{r}, \omega)}{|H_0^{\circ/\circ}(\vec{r}, \omega)|^2} \right\}, \end{aligned} \quad (1.162)$$

where the proportionality factor $\alpha(\omega)$ from Eq. (1.101) ensures proper scaling between $H_{\text{sng}}^{\circ/\circ}(\vec{r}, \omega)$ and the magnetic field $H_{\text{sim}}^{\circ/\circ}(\vec{r}, \omega)$ extracted from the simulations. The validity of the above approach was verified by FDTD simulations of antenna dimers, showing only minor discrepancies between the integrations of the full field and the field cut-off at the cell boundary even for small antenna separations. This issue is further discussed in the following section dedicated to benchmark tests of the antenna array interaction model.

1.4. Benchmark tests

To verify the validity and assess the limits of our approximate model for interacting plasmonic antennas, we used it to calculate the response of an antenna dimer in various configurations and environments and compared the results to those obtained from exact FDTD simulations. In all the benchmark tests, the dimer was composed of two identical diabolo antennas, the only parameters that were varied were their mutual separation, and thickness and material composition of the substrate. At the same time, the only external input to the interaction model was the current distribution induced within a single antenna placed on top of a semi-infinite substrate.

The aim of the first test (probably the most fundamental and crucial) was to ascertain whether the interaction model is able to correctly reproduce the scattering cross-section spectra of two antennas separated by distances that are relevant to our overarching ambition of finding the optimal parameters of antenna arrays for the plasmon enhanced EPR spectroscopy. Figure 1.12 gives evidence that our interaction model passed this test almost effortlessly, with only slight deviations from the exact FDTD spectra even for antennas merely $20 \mu\text{m}$ apart (Δx equal to $100 \mu\text{m}$), which amounts, in this instance, to the quarter of their length.

This auspicious result surpassed our expectations and prompted us to proceed with tests involving various substrate configurations, the first one being $200 \mu\text{m}$ silicon dioxide layer on top of a semi-infinite silicon block. The purpose of this calculation was mainly of technical nature, namely to check whether the reflections at interfaces of multilayer systems were properly implemented into the computation routines for the antenna interaction parameter and the radiation emitted into the far-field. The resulting scattering cross-section spectra were again validated against exact FDTD simulations (see Figure 1.13), revealing a very good agreement between the two approaches.

That enabled us, eventually, to consider an experimentally more relevant case of antennas on top of a finite, free standing substrate. Unlike the previous configuration, this type of substrate supports guided modes that can both mediate interaction between antennas and trap or carry away a portion of the energy that would otherwise reach the far-field detectors. At the same time, it prevents us from comparing directly the results of the interaction model and the FDTD simulations in terms of the

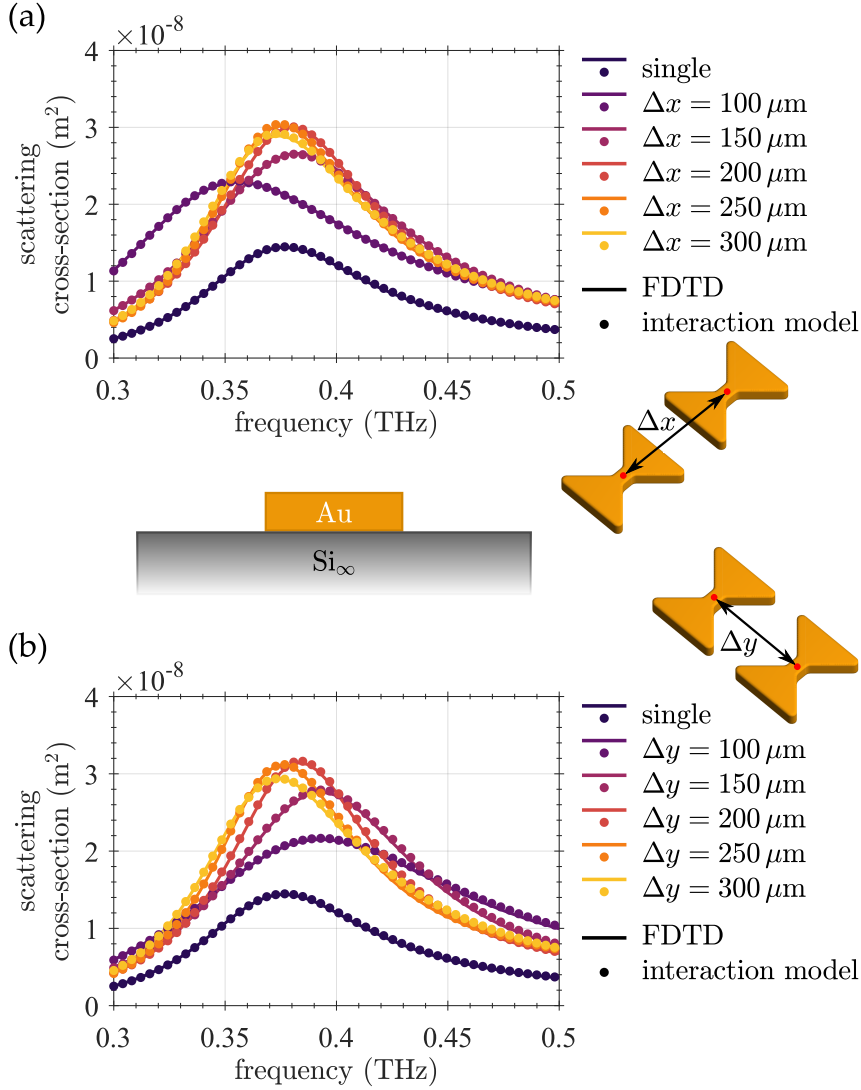


Figure 1.12: Scattering cross-section of an antenna dimer placed on top of a semi-infinite silicon substrate, where the spectra calculated by our antenna interaction model (dots) are compared to those obtained from FDTD simulations (solid line). The dimer consisted of two identical diabolo antennas, each $80\ \mu\text{m}$ in length, and two different orientations were studied: the diabolos were aligned either along their (a) long or (b) short axis, with a mutual separation (center to center) ranging from $300\ \mu\text{m}$ down to $100\ \mu\text{m}$. The interaction model performed exceedingly well, reproducing accurately the FDTD spectra even at separation distances (edge to edge) corresponding to a fraction of the antenna length.

scattering cross-section (although not impossible, it can be somewhat tricky to separate the far-fields from the guided modes in the latter). Recognizing this hindrance, we chose to evaluate the average magnetic field enhancement $\eta_{\text{avg}}^{\circ}$ instead—not only it gave us means to validate our method, it also enabled us to check the correct implementation and reveal certain limits of the simplified procedure outlined in the previous section: it is built on the premise that the near-fields of individual antennas do not overlap. But as Figure 1.14 indicates, this condition is not always fulfilled, inevitably leading to perceptible deviations from the correct values (in this instance, it happens only for very small antenna separations). This should be kept in mind during any antenna array optimization, especially when collective antenna modes are expected to affect the overall magnetic field distribution. In that case, our simplified procedure is completely inadequate and a different approach should be considered. On that

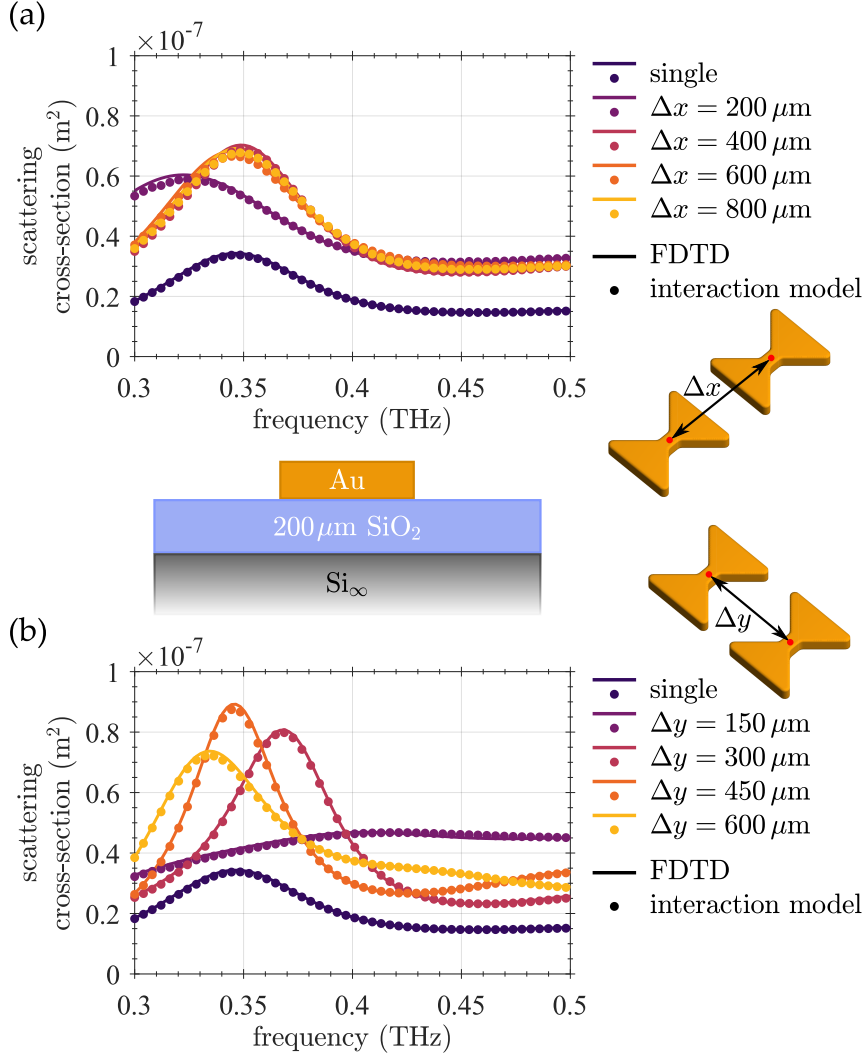


Figure 1.13: Validation of the antenna interaction model against FDTD simulations in the presence of a layered substrate (200 μm of fused silica on top of a semi-infinite silicon block). The object of study was an antenna dimer formed by two identical, 140 μm long diablo antennas aligned either along their (a) long or (b) short axis. Apart from their mutual separation, every other parameter of the antennas was kept fixed. The comparison of the scattering cross-section spectra calculated by the interaction model (dots) and the exact spectra obtained from the FDTD simulations (solid line) revealed only minor differences between the two approaches, reinforcing further the good impression instilled by our interaction model in the benchmark tests involving the semi-infinite silicon substrate.

note, the systems investigated in this thesis are not particularly inclined to support these collective modes. Therefore, it is plausible to assume that the magnetic field enhancement derives mainly from the near-field and that the above simplified procedure can be employed despite its apparent shortcomings.

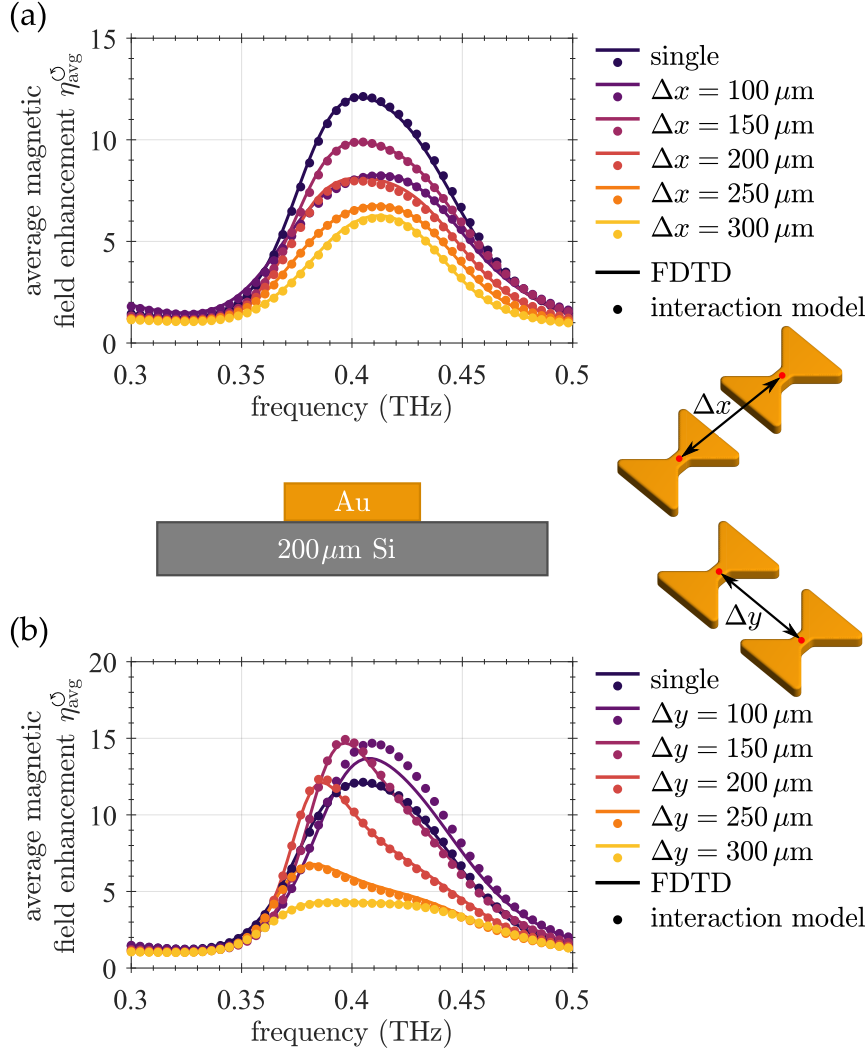


Figure 1.14: Average magnetic field enhancement $\eta_{\text{avg}}^{\odot}$ around an antenna dimer as a function of the frequency and the antenna separation distances (a) Δx and (b) Δy . The dimer consists of two $80 \mu\text{m}$ long diabolo antennas and is situated on top of a $200 \mu\text{m}$ thick silicon substrate, capable of supporting lateral waveguide modes that can mediate interaction between antennas. The perceptible discrepancy between the spectra supplied by the interaction model and the FDTD simulations at small antenna separations illustrates the limitations of the simplified procedure for calculating the average magnetic field enhancement in antenna arrays. For it to be valid, the overlap between the magnetic field generated by individual antennas has to be minimal.

1.5. Antenna array optimization

The antenna array optimization presented in this thesis was carried out with the specific intent of testing the whole concept of plasmon enhanced EPR spectroscopy experimentally. As such, the specimen is required to conform to the technical specifications of the EPR machine situated at the University of Stuttgart, where the testing is eventually going to take place. The diameter of the bore through which the sample is inserted into the strong magnetic field inside the helium cryostat limits the size of the sample roughly to $3\text{ mm} \times 3\text{ mm}$. Furthermore, the experimental setup enables the employment of the double pass transmission configuration, where the sample is placed on top of a mirror, thus enhancing the interaction of the spins with the incident THz radiation. To that end, we decided to consider not only the slightly unrealistic case of a completely free standing substrate, but also the configuration with a gold mirror glued to its back side. Lastly, the choice of the operation frequency is largely limited by the source bandwidth and the maximum value of the static magnetic field that can be attained at the sample location. In the case of the EPR machine currently used at the University of Stuttgart, this amounts to a frequency window between 300 and 400 GHz. Note that even though the calculations presented here focus on this particular spectral interval, the transition to a different operation frequency can be achieved simply by scaling appropriately the optimal antenna array geometrical parameters.

Clearly, our object of study, i.e. an array of diabolo antennas placed on top of a dielectric substrate, possesses many degrees of freedom that can be optimized in order to achieve maximum performance in the EPR spectroscopy measurements. Apart from the geometrical parameters of the individual diabolo antennas, we can tune the pitch of the array in two independent lateral directions (assuming the array is rectangular) or change the material and the thickness of the substrate that supports it. Optionally, we can also play with the material beneath the substrate, making it, for example, metallic and thus obtain the aforementioned mirror configuration. Due to the considerable extent of the space spanned by these various parameters, we decided to limit ourselves only to two substrate materials: silicon (Si) and fused silica (SiO_2) with refractive indices $n_{\text{Si}} \approx 3.4$ and $n_{\text{SiO}_2} \approx 2$. As for the antenna parameters, we varied the wing angle (i.e. the vertex angle of the triangles forming the diabolo) together with the length and the width of the diabolo bridge, while the overall length of the antenna was fixed—to $80\ \mu\text{m}$ in the case of silicon and to $140\ \mu\text{m}$ in the case of the fused silica substrate—ensuring that the antenna resonance falls somewhere within or close to the target frequency window. Another parameter that was always kept the same was the height of the antenna, set for the sake of easy future fabrication by electron lithography to 200 nm.

Our first step in the optimization process was to understand how the individual antenna parameters affect the figure of merit, in this instance the average magnetic field enhancement within a thin layer covering the antenna array. As our antenna interaction model allows for a rapid search over the various array configurations and to a lesser extent also over the substrate thickness, while any change in the geometry of individual antennas requires a separate FDTD simulation, we adjusted accordingly also the resolution of the initial sweeps over these various parameters. More specifically, for each antenna geometry and a set of six substrate thicknesses (∞ , $100\ \mu\text{m}$, $200\ \mu\text{m}$, \dots , $500\ \mu\text{m}$), we searched for the best array configuration granting the maximum average field enhancement. This search spanned array pitches in the interval of 1.4 to 5.0 with a step of 0.1 multiples of the antenna length. The results of these parameter sweeps are comprehensively shown in Figures 1.15–1.17. The common hallmark in these calculations is a strong dependence of the array response on the substrate thickness. Apart from that, one can observe certain trends linked to the geometrical parameters of the individual antennas, but except the case of an infinite silicon block, these tend to be obscured by the effects originating from the finite thickness of the substrate.

The most plausible and natural explanation for this behaviour is the formation of Fabry-Perot oscillations between the upper and lower side of the silicon substrate: depending on the frequency, these oscillations can either boost or suppress the field driving the antennas, leading to the percepti-

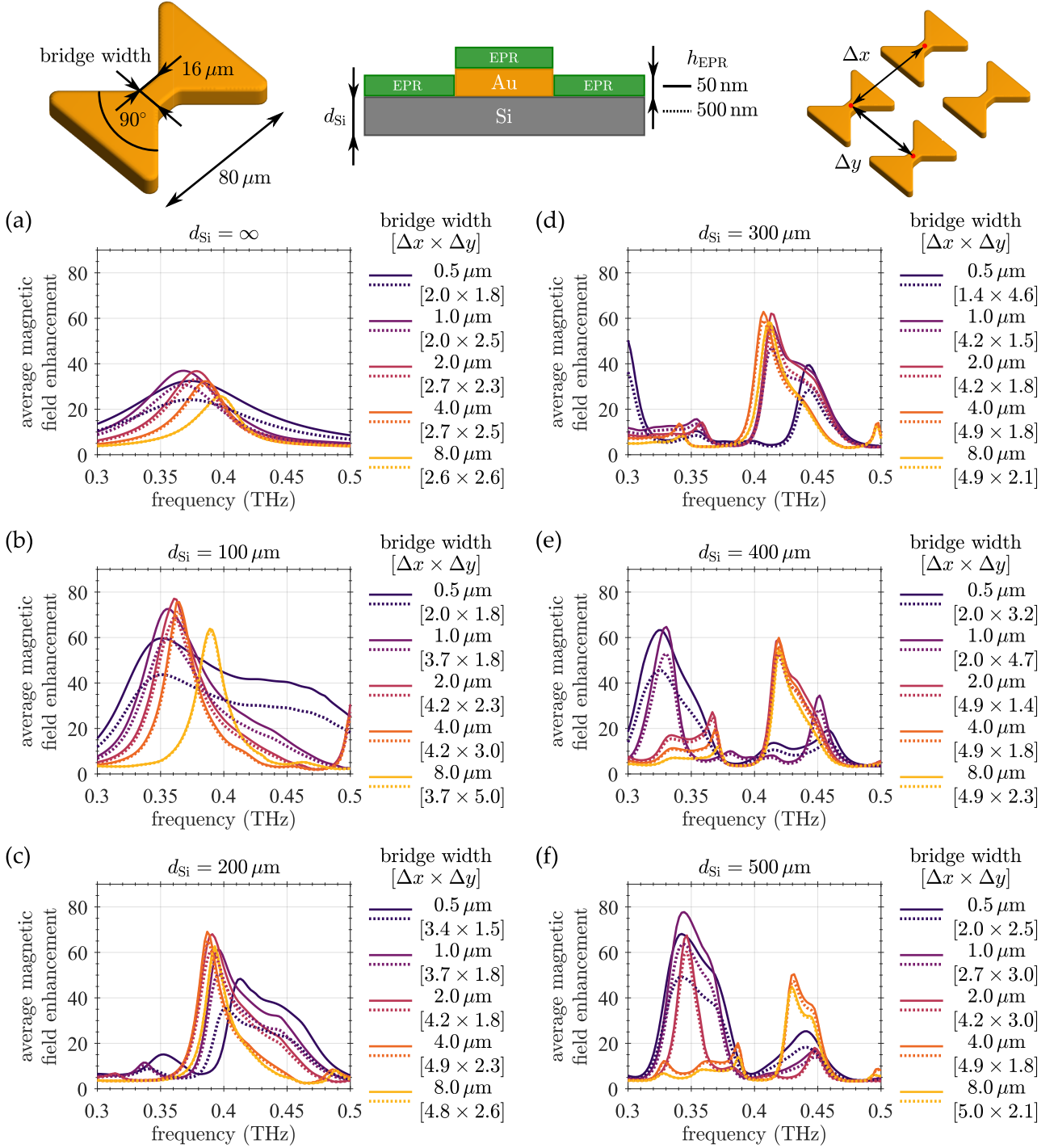


Figure 1.15: Average magnetic field enhancement within a thin layer covering a $3 \text{ mm} \times 3 \text{ mm}$ antenna array as a function of frequency for various widths of the diabolo bridge. Other geometrical parameters of the antennas were kept fixed, their values are specified in the schematic drawing at the top. Each panel (a-f) corresponds to a different thickness of the silicon substrate and the line style (solid vs. dotted) discriminates between the two different thicknesses (50 nm vs. 500 nm) of the layer within which the field enhancement was evaluated. The numbers in the square brackets indicate the array pitches Δx and Δy (expressed in multiples of the antenna length) that gave the largest field enhancement for the particular combination of the bridge width and the substrate thickness.

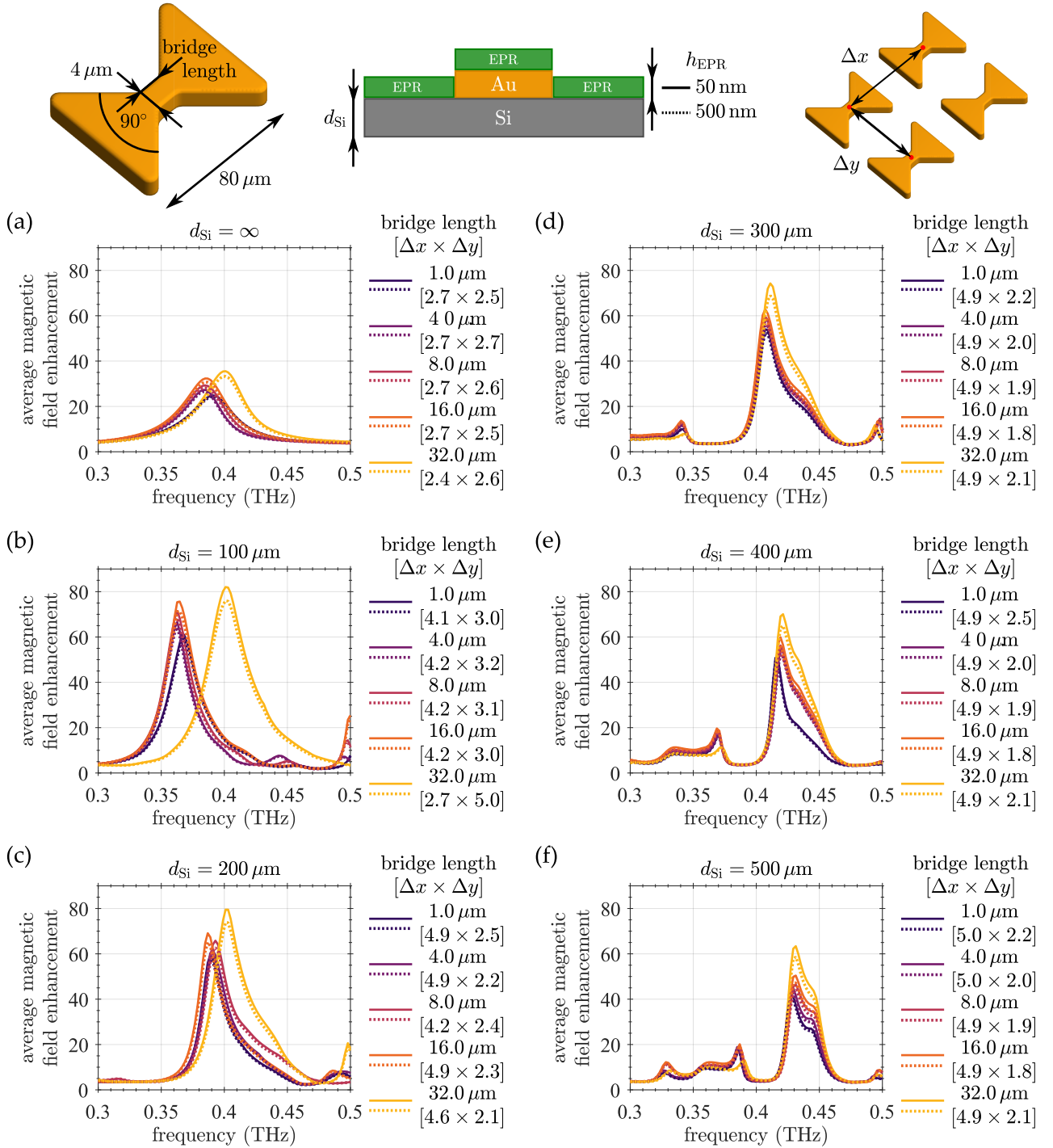


Figure 1.16: Average magnetic field enhancement within a thin layer covering a 3 mm \times 3 mm antenna array as a function of frequency for various lengths of the diabolo bridge. Other geometrical parameters of the antennas were kept fixed, their values are specified in the schematic drawing at the top. Each panel (a-f) corresponds to a different thickness of the silicon substrate and the line style (solid vs. dotted) discriminates between the two different thicknesses (50 nm vs. 500 nm) of the layer within which the field enhancement was evaluated. The numbers in the square brackets indicate the array pitches Δx and Δy (expressed in multiples of the antenna length) that gave the largest field enhancement for the particular combination of the bridge length and the substrate thickness.

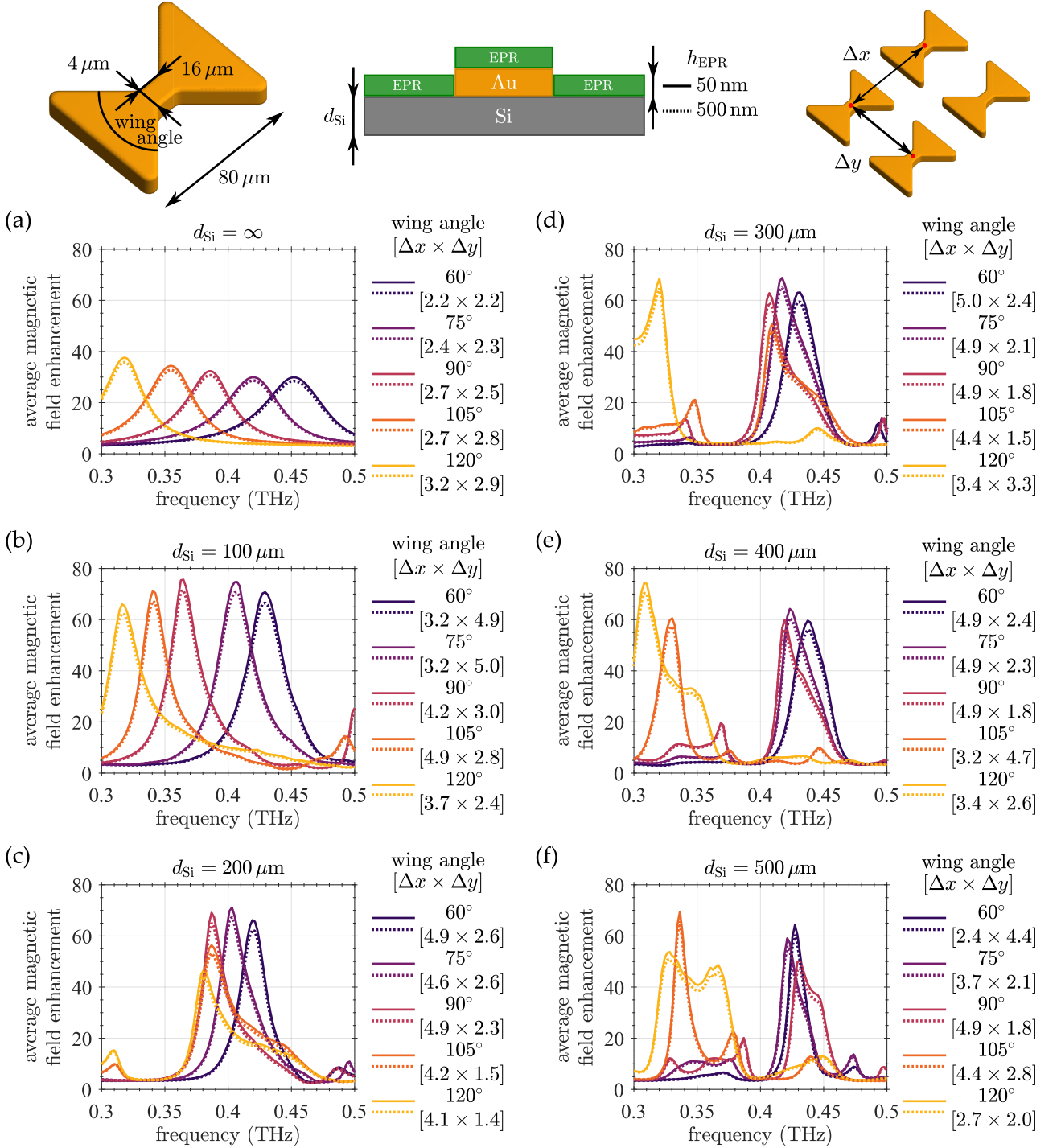


Figure 1.17: Average magnetic field enhancement within a thin layer covering a $3 \text{ mm} \times 3 \text{ mm}$ antenna array as a function of frequency for various wing angles of the diabolo antenna. Other geometrical parameters of the antennas were kept fixed, their values are specified in the schematic drawing at the top. Each panel (a-f) corresponds to a different thickness of the silicon substrate and the line style (solid vs. dotted) discriminates between the two different thicknesses (50 nm vs. 500 nm) of the layer within which the field enhancement was evaluated. The numbers in the square brackets indicate the array pitches Δx and Δy (expressed in multiples of the antenna length) that gave the largest field enhancement for the particular combination of the wing angle and the substrate thickness.

ble modulation observed in our calculations. This interpretation is further reinforced by the refined sweeps over the substrate thickness shown in Figure 1.18 and the simplified model treating the antenna array as a thin anisotropic layer presented in Section 1.6. More specifically, the frequency vs. substrate thickness maps of the average magnetic field enhancement plotted in Figure 1.18 reveal a set of periodically occurring bands that are consistent with the picture of a broad plasmonic resonance modulated by narrower Fabry-Perot oscillations that are getting sharper (notice the gradual slanting of the bands) as we increase the substrate thickness. Similar behaviour can be observed also in the configuration with the gold mirror underneath the substrate, as evidenced by the average magnetic field enhancement maps displayed in Figure 1.19. Interestingly, this mirror configuration generally yields significantly larger field enhancements than those we attained in the free standing substrates. This apparent amplification of the Fabry-Perot oscillations in the presence of a mirror further underlines their importance for the design development of a functional sample for EPR spectroscopy measurements.

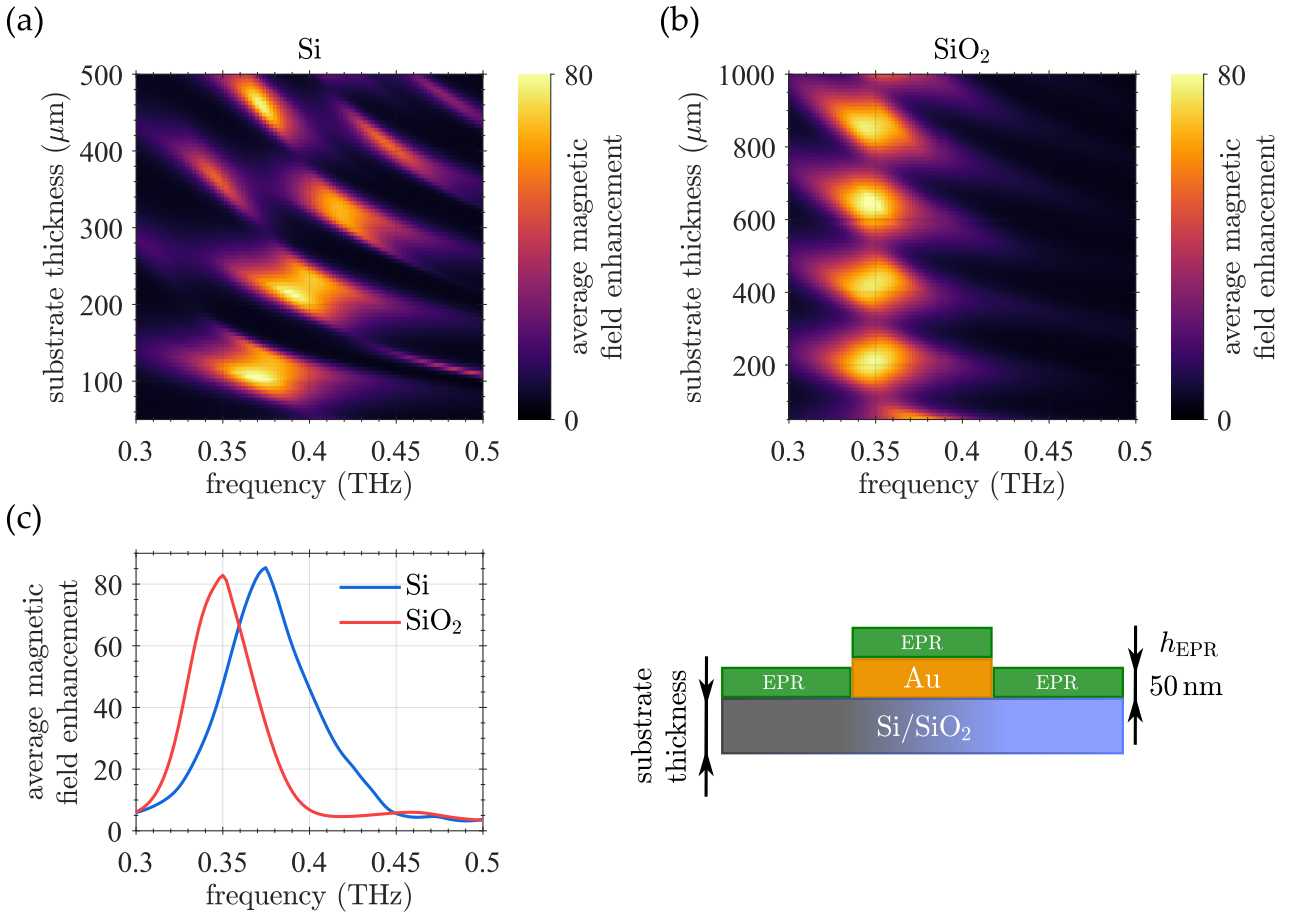


Figure 1.18: Average magnetic field enhancement within a 50 nm layer covering a $3\text{ mm} \times 3\text{ mm}$ antenna array as a function of frequency and substrate thickness. Two different substrates were considered: (a) silicon and (b) fused silica. The bands apparent in the field enhancement maps can be attributed to the formation of Fabry-Perot oscillations between the top and bottom sides of the substrate. Panel (c) then shows two spectra, one for each substrate material, corresponding to sets of antenna and substrate parameters that exhibited the largest average magnetic field enhancement. These sets match those listed in Table 1.1 in the section dedicated to free standing substrates.

If we accept the premise that the substrate thickness essentially affects only the overall efficiency with which the antennas are driven and it has no direct effect on the magnetic field distribution (none of

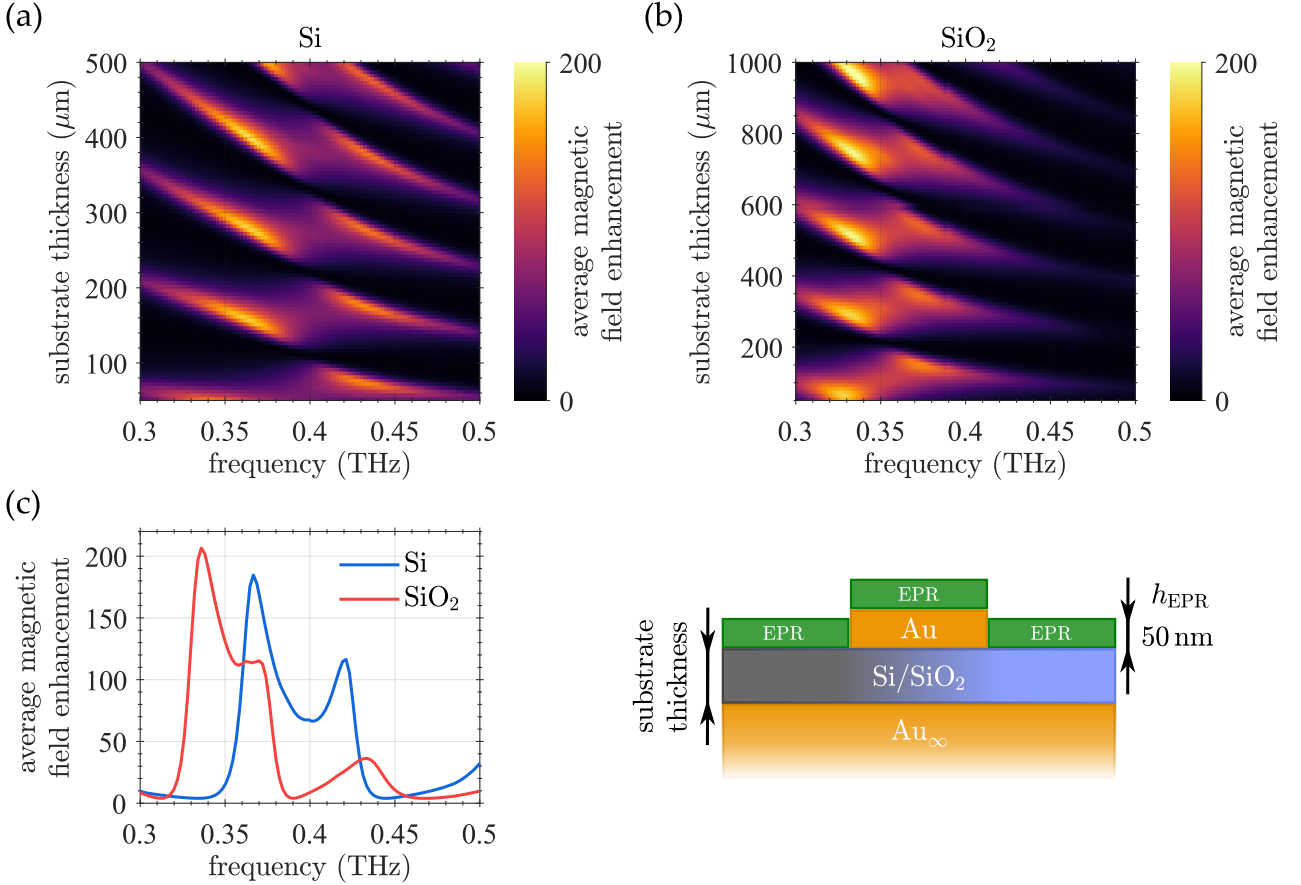


Figure 1.19: Average magnetic field enhancement within a 50 nm layer covering a 3 mm \times 3 mm antenna array as a function of frequency and substrate thickness. As in Figure 1.18, two different substrates were considered—(a) silicon and (b) fused silica—except in this instance, the bottom side of the substrate was attached to a gold mirror. The bands apparent in the field enhancement maps can be attributed to the formation of Fabry-Perot oscillations between the top and bottom sides of the substrate. Panel (c) then shows two spectra, one for each substrate material, corresponding to sets of antenna and substrate parameters that exhibited the largest average magnetic field enhancement. These sets match those listed in Table 1.1 in the section dedicated to substrates placed on top of a gold mirror.

the calculations we performed suggested that it would be otherwise), we can simplify the optimization procedure by decoupling this parameter from the rest. The subsequent finer sweeps over the wing angle and the length and the width of the bridge brought a surprising discovery: the saturation of the average magnetic field enhancement that is largely independent of the antenna parameters. In other words, as long as we allow the array pitch and the substrate thickness to relax to their optimal values at which the plasmonic resonance coincides with a maximum in the Fabry-Perot oscillations, the average magnetic field enhancement never exceeds a certain value, whatever the antenna geometry is. At this point, we are still not clear about the reasons for this peculiar behaviour. It seems to do with the fact that for highly reflecting structures such as our diabolo antennas, there is a limit to the magnitude of the current that can flow through the antennas, since they cannot reflect more power than the source provides. With a finite total amount of current at our disposal, we can only play with its distribution, which in the case of the diabolo antenna arrays, fails to bring any significant improvement to their performance. The situation could be different in other antenna types and configurations, where the current flow is more intricate and where there is more leeway for its build-up.

substrate material	antenna length (μm)	bridge length (μm)	bridge width (μm)	substrate thickness (μm)	array pitch ($\mu\text{m} \times \mu\text{m}$)	maximum enhancement
free standing substrate						
Si	80	32	2	110	272×224	85
SiO ₂	140	64	2	640	392×336	83
substrate + gold mirror						
Si	80	32	2	400	176×168	185
SiO ₂	140	64	2	960	308×336	206

Table 1.1: The optimized antenna array parameters for the various substrate configurations considered in this study (the wing angle equal to 90° in all cases). Presence of a gold mirror can significantly boost the magnetic field enhancement, while variation of the substrate material or parameters of individual antennas seems to have only limited impact on the overall performance.

To summarize the matter, we did not succeed in finding a single antenna design that would outperform the rest, but rather came to the conclusion that within the parameter space spanned in our optimization attempts, there seem to be many equivalent options with no apparent winner. Therefore, we chose one representative set of parameters for each substrate configuration that we studied. They are listed in Table 1.1, together with the maximum values of the average magnetic field enhancement reached within a 50 nm thick layer covering the antennas. The full spectra are plotted in Figures 1.18(c) and 1.19(c). Though not overwhelming (traditional Fabry-Perot resonators employed in EPR boast with signal enhancement factors larger by a one order of magnitude [13]), these values for the magnetic field enhancement represent a definitive improvement when compared to the simple double pass transmission setup and as such could translate into a perceptible boost of the EPR signal in the thin film spectroscopy.

1.6. Antenna array as a thin anisotropic layer

The search for the optimal antenna array parameters maximizing the average magnetic field enhancement that was carried out in the previous section led us to the conclusion that the Fabry-Perot oscillations building up between the top and the bottom sides of the substrate mainly control the amplitude of the field driving the antennas, but besides that, they have only a little impact on the magnetic field distribution or the interaction between antennas. In other words, they scale the overall response of the antenna array, but otherwise leave it intact.

To provide the reader with a more solid evidence for our statements than just the field enhancement maps shown in Figures 1.18 and 1.19, we decided to develop an analytical model, in which the antenna array is perceived as a thin anisotropic layer that can be effectively characterized in terms of Fresnel reflection and transmission coefficients. If our conclusions are correct, the response of the whole system, i.e. the antenna plus the finite substrate, should then amount to the reflection from (or the transmission through) a slab with modified optical properties at one of its interfaces. Denoting the two different polarizations of the incident electric field by the superscripts ⁰ (polarization along the long axis of the diabolo) and ⁹⁰ (polarization along its short axis, i.e. rotated by 90 degrees), the amplitudes of the reflected and transmitted waves are according to the effective model equal to

$$r_{\text{eff}}^{0/90} = r_{12}^{0/90} + \frac{t_{12}^{0/90} t_{21}^{0/90} r_{23}^{0/90} e^{2ik_2d}}{1 - r_{21}^{0/90} r_{23}^{0/90} e^{2ik_2d}}, \quad (1.163)$$

$$t_{\text{eff}}^{0/90} = \frac{t_{12}^{0/90} t_{23}^{0/90} e^{ik_2d}}{1 - r_{21}^{0/90} r_{23}^{0/90} e^{2ik_2d}}, \quad (1.164)$$

where the substrate thickness d and the wavenumber k_2 largely determine, whether the waves bouncing between the top and bottom interfaces of the slab will add up constructively, destructively or something in between. Assuming the antenna array is located on the upper side of the substrate, the reflection and transmission coefficients $r_{23}^{0/90}$, $r_{32}^{0/90}$ and $t_{23}^{0/90}$, $t_{32}^{0/90}$ associated with the bottom side are just the ordinary Fresnel coefficients for an interface between two media

$$r_{23}^{0/90} = \frac{n_3 - n_2}{n_3 + n_2}, \quad (1.165)$$

$$r_{32}^{0/90} = \frac{n_2 - n_3}{n_2 + n_3}, \quad (1.166)$$

$$t_{23}^{0/90} = \frac{2n_2}{n_3 + n_2}, \quad (1.167)$$

$$t_{32}^{0/90} = \frac{2n_3}{n_2 + n_3}. \quad (1.168)$$

The situation at the upper interface is, on the other hand, slightly more complicated. Apart from the ordinary Fresnel coefficients, there have to be also additional terms accounting for the presence of the antenna array. Invoking our antenna interaction model—namely Equations (1.157) and (1.158) quantifying the amplitudes of the waves scattered from a dense antenna array illuminated by a broad gaussian beam—the reflection and transmission coefficients associated with the upper side of the substrate can be written as

$$r_{12}^{0/90}(\omega) = \frac{n_2 - n_1}{n_2 + n_1} + \frac{4\pi}{w_0^2} \frac{\uparrow \vec{E}_{12}^{0/90}(\vec{0}, \omega) \cdot \vec{E}_0^{0/90*}(\omega)}{|\vec{E}_0^{0/90}(\omega)|^2}, \quad (1.169)$$

$$r_{21}^{0/90}(\omega) = \frac{n_1 - n_2}{n_1 + n_2} + \frac{4\pi}{w_0^2} \frac{\downarrow \vec{E}_{21}^{0/90}(\vec{0}, \omega) \cdot \vec{E}_0^{0/90*}(\omega)}{|\vec{E}_0^{0/90}(\omega)|^2}, \quad (1.170)$$

$$t_{12}^{0/90}(\omega) = \frac{2n_1}{n_2 + n_1} + \frac{4\pi}{w_0^2} \frac{\downarrow \vec{E}_{12}^{0/90}(\vec{0}, \omega) \cdot \vec{E}_0^{0/90*}(\omega)}{|\vec{E}_0^{0/90}(\omega)|^2}, \quad (1.171)$$

$$t_{21}^{0/90}(\omega) = \frac{2n_2}{n_1 + n_2} + \frac{4\pi}{w_0^2} \frac{\uparrow \vec{E}_{21}^{0/90}(\vec{0}, \omega) \cdot \vec{E}_0^{0/90*}(\omega)}{|\vec{E}_0^{0/90}(\omega)|^2}, \quad (1.172)$$

where $\uparrow/\downarrow \vec{E}_{ij}^{0/90}(\vec{0}, \omega)$ stands for the $\vec{q}=0$ Fourier component of the electric field emitted by the antenna array either upwards (\uparrow) or downwards (\downarrow). The order of the indices in the subscript then indicates, whether the antenna array was illuminated from the top (1_2) or from the bottom (2_1). Finally, w_0 designates the width of the Gaussian beam, while $\vec{E}_0^{0/90}$ denotes the electric field in its center. The above mathematical framework perhaps best illustrates the aims of this section: by replacing the response of the antenna array at a particular frequency with a single fixed number, we effectively freeze it and prevent any additional objects (e.g. the bottom interface between the substrate and the air or a mirror) from affecting the mutual interaction of antennas within the array.

For the purpose of verifying our conjectures regarding the role played by the Fabry-Perot oscillations, we chose as a subject of our study a $9\text{ mm} \times 9\text{ mm}$ antenna array with a silicon as the supporting substrate. To suppress any scattering outside the $\vec{q}=0$ direction, we fixed the array pitches along the x and y axes to double of the antenna length, which was in this instance equal to $80\ \mu\text{m}$. The width of the illuminating Gaussian beam was set to 3 mm , making it a passable approximation for a plane wave in this spectral range.

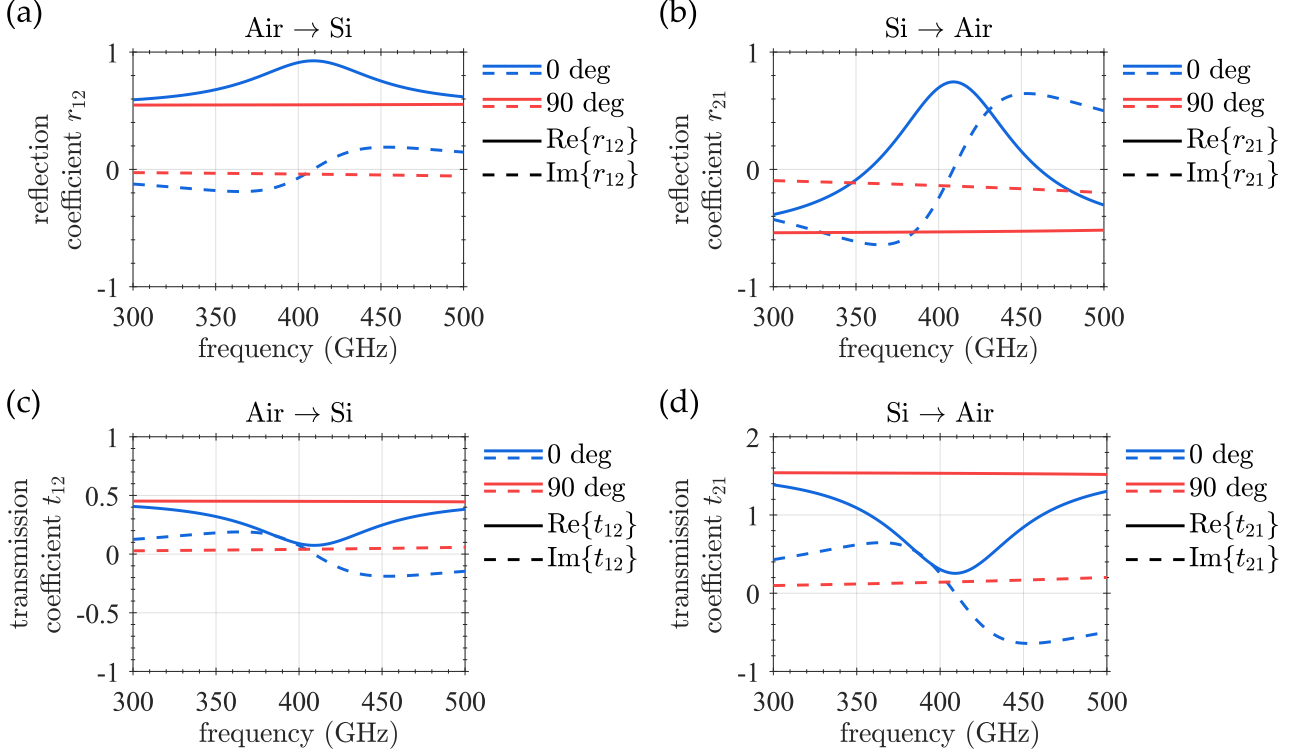


Figure 1.20: Effective reflection and transmission coefficients characterizing a single planar silicon-air interface infused with a dense array of diabolite antennas. The red and blue color discriminates between the two mutually orthogonal polarizations of the incident electric field, while the line style specifies, whether the real (solid) or the imaginary (dashed) part of the coefficient is being considered. Finally, the arrows indicate, whether the incoming wave propagates from air to silicon (left panels) or vice versa (right panels). Note how the response of the system strongly depends on the polarization. When in the active position (0 deg), the antenna array essentially acts as a mirror, but it is practically transparent, if we rotate the polarization by 90 degrees. In the case of the Si \rightarrow Air reflection coefficient plotted in (b), this massive anisotropy (stemming from the excitation of the fundamental dipolar mode in the diabolite antennas) causes a complete sign reversal as we switch between the active (0 deg) and inactive (90 deg) positions.

The spectral dependences of the reflection and transmission coefficients characterizing this system are plotted in Figure 1.20. Clearly, the antenna array hardly affects the waves polarized along the short axis of the diabolite antennas (90 deg), leaving the silicon substrate as the main element dictating the response of the system. As one would expect, the situation is quite different for the polarization along the long axis of the diabolite (0 deg). The efficient coupling of the incoming radiation to the dipolar mode of the antenna significantly increases the amount of the power that is reflected, while reducing substantially the transmission through the system.

Nothing prevents us now from inserting these single interface coefficients into the above analytical expressions for a finite substrate given by Eqs. (1.163) and (1.164). The acquired spectra are then presented in Figures 1.21 and 1.22, alongside the results supplied by our full antenna interaction model

presented in the previous section. Consequently, if there are any other significant effects apart from the scaling of the overall antenna array response due to the Fabry-Perot oscillations, they should manifest themselves as deviations from the effective model. To bring to light any possible dependence on the substrate thickness, we varied it in the range between $100 \mu\text{m}$ and 2 mm and only after a close inspection of the results, we were able to spot some minor discrepancies between the two approaches in the instance of very thick substrates.

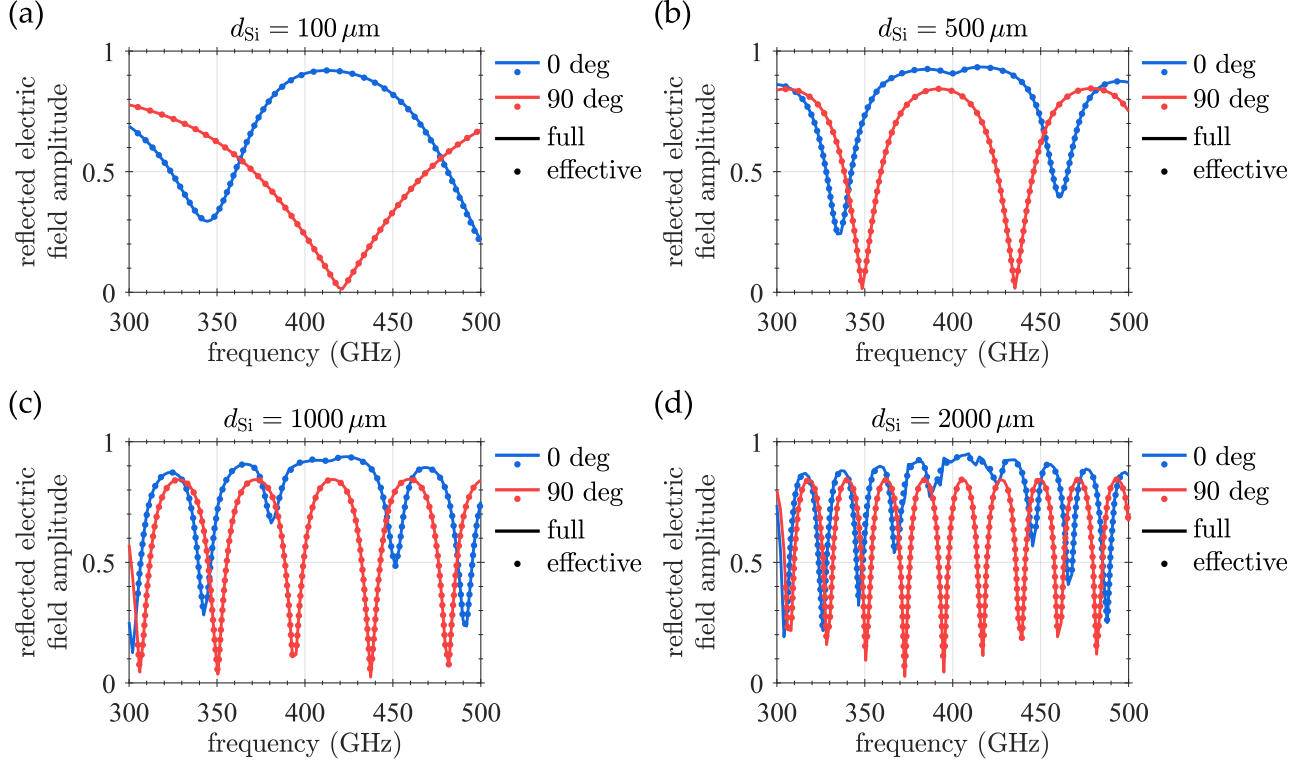


Figure 1.21: Amplitude of the wave reflected from a silicon slab with an antenna array on top of its upper surface, calculated using the full apparatus of our antenna interaction model for stratified media (solid line) and the effective model (dots), in which the response of the array is approximated by a set of Fresnel coefficients. The excellent agreement between the two approaches corroborates our notion that the reflections from the bottom interface hardly affect the mutual interaction between antennas in this type of systems. Each panel shows the spectral dependence of the reflected wave amplitude for a different substrate thickness. As it turns out, the substrate thickness affects mainly the frequency by which the Fabry-Perot oscillations modulate the spectra. Also, note the mutual spectral shift between the Fabry-Perot oscillations for the active (0 deg) and inactive (90 deg) positions of the antenna array that can be attributed to an apparent change in the optical densities perceived by the incoming wave, caused by the onset of the plasmonic resonance in the diabolo antennas.

We should point out that these calculations should not be perceived as some attempt to prove that one can always decouple the response of an antenna array from the photonic modes sustained by the substrate. In truth, we intended initially to exploit these modes and enhance the mutual interaction between antennas for the purpose of reaching higher magnetic fields, but as it turned out, the system we chose for our investigation (we mean the diabolo antenna arrays on top of silicon in general, not just this specific case of a dense array) is not particularly inclined to support them. Let us suppose for a moment that it does. Then we could, in principle, reverse our train of thought and use the above effective model, which treats the antenna array as a thin anisotropic layer, to identify any conspicuous features in the response of the system and separate them from the familiar amplitude scaling effects caused by the Fabry-Perot oscillations.

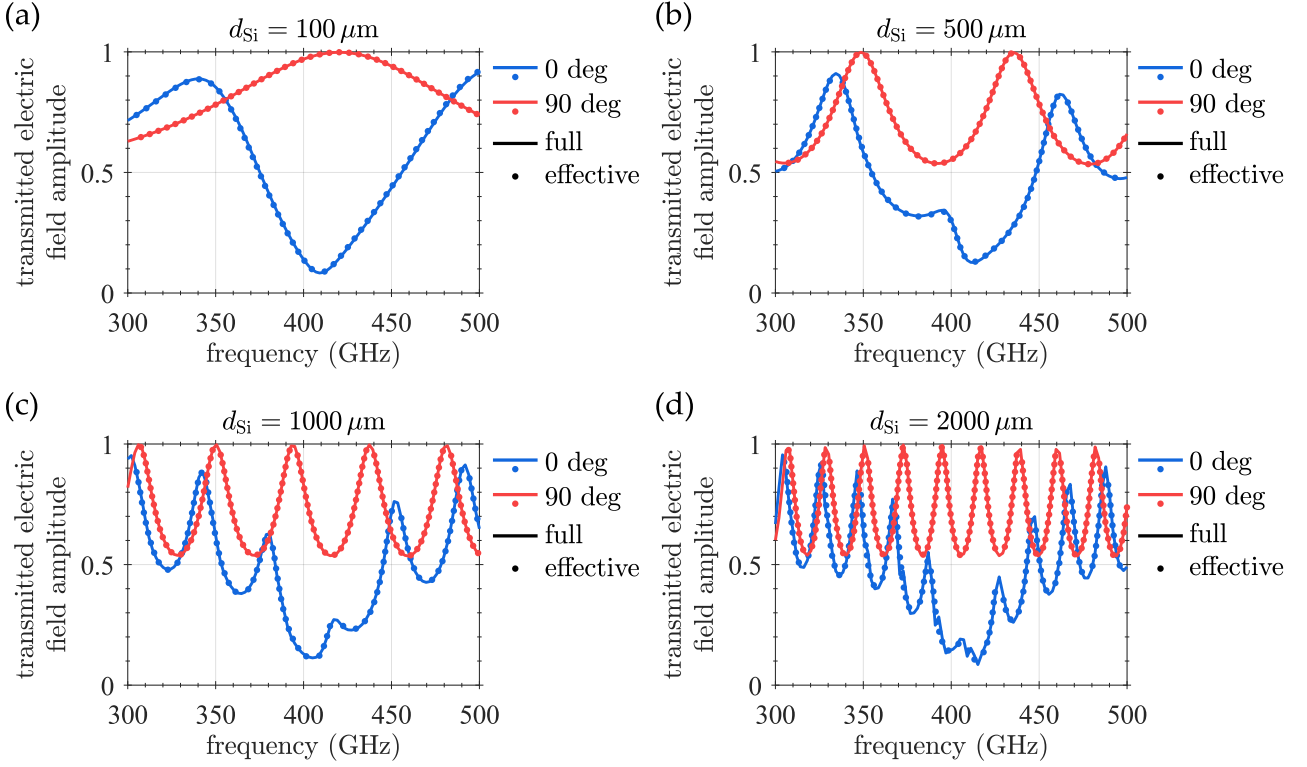


Figure 1.22: Amplitude of the wave transmitted through a silicon slab with an antenna array on top of its upper surface for various substrate thicknesses. The definition and meaning of the labels is exactly the same as in Figure 1.21. As in the case of the reflected wave amplitudes, we can observe a disalignment between the Fabry-Perot oscillations for the active (0 deg) and inactive (90 deg) positions of the antenna array, with the maximal spectral shift reached right in the center of the plasmonic resonance.

There remains one last item related to the above calculations that we deemed worthwhile to discuss, namely the spectral shift between the amplitude oscillations for the two mutually orthogonal polarizations, clearly visible in both the reflection and the transmission configurations and for all the investigated substrate thicknesses. This disparity is perhaps most striking in the $d_{\text{Si}} = 100 \mu\text{m}$ case, where one polarization is mostly reflected, while the other passes through the slab practically intact. This effect is definitely linked to the plasmonic resonance, since away from it, the oscillations—and this is far better noticeable in the thicker substrates—become much more “in phase”. A simple explanation for this behaviour can be found if we look closely on the reflection and transmission coefficients plotted in Figure 1.20. When the incident wave travels from the halfspace filled with air to the other one made up by silicon (the panels on the left), the spectra for the two polarizations are qualitatively similar—the coefficients differ in magnitude, but their phase is more or less the same. After we reverse the propagation direction (the two panels on the right), the situation, however, dramatically changes: as we hit the center of the plasmonic resonance, the phase of the reflection coefficient for the polarization along the long axis of the diabolo (0 deg) becomes shifted by π with respect to its 90 deg counterpart. That inevitably leads to a shift in the frequencies at which the Fresnel coefficients characterizing the whole slab reach their maximum or minimum, causing the palpable spectral disalignment of the Fabry-Perot oscillations for the two different polarizations of the incident electric field.

This flip in the sign can be viewed, in fact, as the consequence of a change in the contrast between optical densities perceived by the incoming wave as it propagates across the interface between air and silicon. Due to the highly reflective nature of the antenna array (at least when it finds itself in the active position with respect to the incident polarization), the environment into which the incoming

wave aims to propagate appears to be optically denser than it actually is. In the case of a wave traveling from air into silicon (Air \rightarrow Si), it does not matter as much, since silicon is already optically denser than air, but when we reverse the propagation direction (Si \rightarrow Air), it will be as if the wave hit an optically denser material (although it does not) and the phase of the reflected wave will be opposite compared to the reflection from an ordinary Si-Air interface (or one infused with an inactive antenna array).

All of this has some practical implications for experimental measurements: one might be tempted to exploit the configuration with the antenna array in the inactive position (90 deg) as a reference, hopefully expecting the Fabry-Perot oscillations to be canceled out after adopting this reference for normalization of the measurements with antennas in the active position (0 deg). Unfortunately, the mutual disalignment of the Fabry-Perot oscillations discussed above prevents us from doing so and some other type of reference should be used (e.g. a mirror).

1.7. Rigorous treatment of the plasmon enhanced EPR effect

Our understanding of how an EPR material imprints itself into the optical response of a nearby plasmonic antenna was based so far on the simplified analytical oscillator model introduced in Section 1.2, in which the term describing absorption losses suffered by the antenna was generalized to include also the magnetization currents induced within the EPR material. It led us to the realization that the magnitude of the EPR signal encoded within the radiation emitted by the antenna is directly proportional to the average magnetic field enhancement within the volume occupied by the EPR material. We subsequently used this finding in the search of an antenna array design that would maximize the plasmon enhancement effect and improve the detection limits in spectroscopic EPR measurements of thin films. Recognizing the oscillator model as possibly too rudimentary (sort of a weak point of the whole concept), the aim of this section is to provide the reader with a more rigorous description of the interaction between a plasmonic antenna and an EPR material and to corroborate our earlier statements regarding the origin and the magnitude of the EPR signature embedded within the antenna radiation.

Using the framework of modal decomposition developed earlier in Section 1.3, the measure of how the EPR material affects the excitation amplitude of the fundamental antenna mode can be expressed in terms of an interaction parameter $g_{\text{EPR}}(\omega)$

$$g_{\text{EPR}}(\omega) = \frac{\int_V d\vec{r}^3 \vec{\mathcal{P}}^*(\vec{r}, \omega) \cdot \int_{V_{\text{EPR}}} d\vec{r}'^3 \vec{G}_{\text{m}}^E(\vec{r}, \vec{r}', \omega) \vec{M}(\vec{r}', \omega)}{\int_V d\vec{r}^3 \vec{\mathcal{P}}^*(\vec{r}, \omega) \cdot \vec{\mathcal{E}}_0(\vec{r}, \omega)}. \quad (1.173)$$

Analogously to the interaction parameter $g_{ij}(\omega)$, it is calculated as an overlap integral between the current distribution of the fundamental mode and the electric field generated by the magnetization \vec{M} induced within the EPR material. The magnetization itself is then a product of the magnetic susceptibility tensor $\vec{\chi}_{\text{m}}(\vec{r}, \omega)$ —taking, for example, the form as in Eq. (1.33)—and the total magnetic field

$$\vec{M}(\vec{r}, \omega) = \vec{\chi}_{\text{m}}(\vec{r}, \omega) \vec{H}(\vec{r}, \omega) = \vec{\chi}_{\text{m}}(\vec{r}, \omega) \left[\vec{H}_0(\vec{r}, \omega) + \int_V d\vec{r}'^3 \vec{G}^H(\vec{r}, \vec{r}', \omega) \vec{\mathcal{P}}(\vec{r}', \omega) \right]. \quad (1.174)$$

Disregarding for a moment the incident magnetic field \vec{H}_0 , the above equations clearly illustrate the self-consistent nature of the plasmon enhanced EPR effect: the antenna interacts with itself via the surrounding material and this back-action then translates into the far-field emission properties of the antenna.

1.7. RIGOROUS TREATMENT OF THE PLASMON ENHANCED EPR EFFECT

Even though formally the EPR and the inter-antenna interaction parameters $g_{\text{EPR}}(\omega)$ and $g_{ij}(\omega)$ are the same, there are some practical differences, mainly the substitution of the dyadic Green's function with its variants \vec{G}_m^E and \vec{G}^H . While the former gives us the electric field distribution in the vicinity of a point magnetic dipole, these roles are interchanged in the latter, i.e. \vec{G}^H expresses the magnetic field generated by a point electric dipole. Fortunately, one can simplify the situation and avoid the calculation of two additional dyadic Green's functions by exploiting the duality between the fields generated by an electric and a magnetic dipole [2]. Namely, \vec{G}_m^E and \vec{G}^H are linked through the following relation

$$\vec{G}_m^E(\vec{r}, \vec{r}', \omega) = -\mu_0 \vec{G}^H(\vec{r}, \vec{r}', \omega) \quad (1.175)$$

that leads to a slightly modified version of the EPR interaction parameter $g_{\text{EPR}}(\omega)$

$$g_{\text{EPR}}(\omega) = \frac{-\mu_0 \int_V d\vec{r}^3 \vec{P}^*(\vec{r}, \omega) \cdot \int_{V_{\text{EPR}}} d\vec{r}'^3 \vec{G}^H(\vec{r}, \vec{r}', \omega) \vec{M}(\vec{r}', \omega)}{\int_V d\vec{r}^3 \vec{P}^*(\vec{r}, \omega) \cdot \vec{E}_0(\vec{r}, \omega)}. \quad (1.176)$$

The explicit expressions for the magnetic dyadic Green's function $\vec{G}^H(\vec{r}, \vec{r}', \omega)$ in the presence of a substrate can be derived from their electric counterparts prescribed by Eqs. (1.118)–(1.121) using the basic Maxwell-Faraday equation $i\omega\mu_0\mu\vec{H} = \nabla \times \vec{E}$

$$\vec{G}^H(\vec{r}_{\parallel} - \vec{r}'_{\parallel}, z, z') = -\frac{i\omega}{8\pi^2} \iint_{-\infty}^{\infty} d\vec{q}^2 \left\{ {}^H\vec{M}_0(\vec{q}) e^{ik_{z1}|z-z'|} + \left[{}^H\vec{M}_p^{\text{ref}}(\vec{q}) + {}^H\vec{M}_s^{\text{ref}}(\vec{q}) \right] e^{ik_{z1}(z+z')} \right\} e^{i\vec{q} \cdot (\vec{r}_{\parallel} - \vec{r}'_{\parallel})}, \quad (1.177)$$

$${}^H\vec{M}_0(\vec{q}) = \frac{1}{k_{z1}} \begin{bmatrix} 0 & \pm k_{z1} & -q_y \\ \mp k_{z1} & 0 & q_x \\ q_y & -q_x & 0 \end{bmatrix}, \quad (1.178)$$

$${}^H\vec{M}_p^{\text{ref}}(\vec{q}) = \frac{-r_p(\vec{q})}{k_{z1}|\vec{q}|^2} \begin{bmatrix} q_x q_y k_{z1} & q_y^2 k_{z1} & q_y |\vec{q}|^2 \\ -q_x^2 k_{z1} & -q_x q_y k_{z1} & -q_x |\vec{q}|^2 \\ 0 & 0 & 0 \end{bmatrix}, \quad (1.179)$$

$${}^H\vec{M}_s^{\text{ref}}(\vec{q}) = \frac{r_s(\vec{q})}{k_{z1}|\vec{q}|^2} \begin{bmatrix} -q_x q_y k_{z1} & q_x^2 k_{z1} & 0 \\ -q_y^2 k_{z1} & q_x q_y k_{z1} & 0 \\ q_y |\vec{q}|^2 & -q_x |\vec{q}|^2 & 0 \end{bmatrix}. \quad (1.180)$$

As before, we find it expedient to switch to polar coordinates

$$\rho = \sqrt{(x - x')^2 + (y - y')^2}, \quad (1.181)$$

$$\cos \psi = \frac{x - x'}{\rho}, \quad (1.182)$$

$$\sin \psi = \frac{y - y'}{\rho}, \quad (1.183)$$

where the integrals assume a form that is partially reducible to Bessel functions. Adhering to the distinction between the free space (\vec{G}_0^H) and reflected (\vec{G}_{ref}^H) contributions, the individual components of the magnetic dyadic Green's function read

$$H_{yx}^{(0)}(\vec{r}, \vec{r}') = \pm i \frac{\omega k_1^2}{4\pi} \int_0^\infty d\lambda \lambda J_0(\lambda k_1 \rho) e^{i\sqrt{1-\lambda^2} k_1 |z-z'|}, \quad (1.184)$$

$$H_{zx}^{(0)}(\vec{r}, \vec{r}') = \frac{\omega k_1^2}{4\pi} \sin \psi \int_0^\infty d\lambda \frac{\lambda^2}{\sqrt{1-\lambda^2}} J_1(\lambda k_1 \rho) e^{i\sqrt{1-\lambda^2} k_1 |z-z'|}, \quad (1.185)$$

$$H_{zy}^{(0)}(\vec{r}, \vec{r}') = -\frac{\omega k_1^2}{4\pi} \cos \psi \int_0^\infty d\lambda \frac{\lambda^2}{\sqrt{1-\lambda^2}} J_1(\lambda k_1 \rho) e^{i\sqrt{1-\lambda^2} k_1 |z-z'|}, \quad (1.186)$$

$$H_{\beta\alpha}^{(0)}(\vec{r}, \vec{r}') = -H_{\alpha\beta}^{(0)}(\vec{r}, \vec{r}'), \quad (1.187)$$

$$H_{\alpha\alpha}^{(0)}(\vec{r}, \vec{r}') = 0, \quad (1.188)$$

$$H_{yx}^{\text{ref}}(\vec{r}, \vec{r}') = i \frac{\omega k_1^2}{8\pi} [I_1^H(k_1 \rho) + \cos 2\psi I_2^H(k_1 \rho)], \quad (1.189)$$

$$H_{xy}^{\text{ref}}(\vec{r}, \vec{r}') = -i \frac{\omega k_1^2}{8\pi} [I_1^H(k_1 \rho) - \cos 2\psi I_2^H(k_1 \rho)], \quad (1.190)$$

$$H_{zx}^{\text{ref}}(\vec{r}, \vec{r}') = \frac{\omega k_1^2}{4\pi} \sin \psi I_3^H(k_1 \rho), \quad (1.191)$$

$$H_{xz}^{\text{ref}}(\vec{r}, \vec{r}') = -\frac{\omega k_1^2}{4\pi} \sin \psi I_4^H(k_1 \rho), \quad (1.192)$$

$$H_{zy}^{\text{ref}}(\vec{r}, \vec{r}') = -\frac{\omega k_1^2}{4\pi} \cos \psi I_3^H(k_1 \rho), \quad (1.193)$$

$$H_{yz}^{\text{ref}}(\vec{r}, \vec{r}') = \frac{\omega k_1^2}{4\pi} \cos \psi I_4^H(k_1 \rho), \quad (1.194)$$

$$H_{xx}^{\text{ref}}(\vec{r}, \vec{r}') = -i \frac{\omega k_1^2}{8\pi} \sin 2\psi I_2^H(k_1 \rho), \quad (1.195)$$

$$H_{yy}^{\text{ref}}(\vec{r}, \vec{r}') = -H_{xx}^{\text{ref}}(\vec{r}, \vec{r}'), \quad (1.196)$$

$$H_{zz}^{\text{ref}}(\vec{r}, \vec{r}') = 0, \quad (1.197)$$

with the integrals $I_1(k_1 \rho)$, $I_2(k_1 \rho)$, $I_3(k_1 \rho)$, and $I_4(k_1 \rho)$ defined as

$$I_1^H(k_1 \rho) = \int_0^\infty d\lambda \lambda J_0(\lambda k_1 \rho) [r^s(\lambda) - r^p(\lambda)] e^{i\sqrt{1-\lambda^2} k_1 (z+z')}, \quad (1.198)$$

$$I_2^H(k_1 \rho) = \int_0^\infty d\lambda \lambda J_2(\lambda k_1 \rho) [r^s(\lambda) + r^p(\lambda)] e^{i\sqrt{1-\lambda^2} k_1 (z+z')}, \quad (1.199)$$

$$I_3^H(k_1 \rho) = \int_0^\infty d\lambda \frac{\lambda^2}{\sqrt{1-\lambda^2}} r^s(\lambda) J_1(\lambda k_1 \rho) e^{i\sqrt{1-\lambda^2} k_1 (z+z')}, \quad (1.200)$$

$$I_4^H(k_1 \rho) = \int_0^\infty d\lambda \frac{\lambda^2}{\sqrt{1-\lambda^2}} r^p(\lambda) J_1(\lambda k_1 \rho) e^{i\sqrt{1-\lambda^2} k_1 (z+z')} \quad (1.201)$$

The evaluation of the above integrals can be efficiently carried out in the same manner as in the case of the electric dyadic Green's function, i.e. by extending the integration path into the complex plane

1.7. RIGOROUS TREATMENT OF THE PLASMON ENHANCED EPR EFFECT

and cutting off the high spatial frequencies, one can achieve rapid convergence at the expense of minor deviations at very small distances from the origin. Note that in spite of this procedure, the evaluation can take substantially more computation time than in the electric case since close to the antenna, we can no longer disregard the variations in the spatial dependence and in the polarization current along the vertical coordinate and evaluate everything in the $z = 0$ plane. That renders this whole approach not particularly suitable for extensive optimization tasks, yet it does not prevent us from the fundamental analysis of the plasmon enhanced EPR effect.

One could evaluate Eq. (1.176) as it is and compare the result with the value obtained from the approximate oscillator model, observing either good or poor agreement between the two. We deemed it to be more insightful, however, to look closer at the respective analytical expressions and try to find some link between them. If we switch to a more tractable representation of the dot and tensor-vector products in Eq. (1.176) and shuffle a bit with the order of individual terms, one acquires yet another version of the EPR interaction parameter

$$\begin{aligned} g_{\text{EPR}}(\omega) &\sim -\mu_0 \sum_{\alpha\beta} \int_V d\vec{r}^3 \mathcal{P}_\alpha^*(\vec{r}, \omega) \int_{V_{\text{EPR}}} d\vec{r}'^3 G_{\alpha\beta}^H(\vec{r}, \vec{r}', \omega) M_\beta(\vec{r}', \omega) \sim \\ &\sim -\mu_0 \sum_{\alpha\beta} \int_{V_{\text{EPR}}} d\vec{r}'^3 M_\beta(\vec{r}', \omega) \int_V d\vec{r}^3 G_{\alpha\beta}^H(\vec{r}, \vec{r}', \omega) \mathcal{P}_\alpha^*(\vec{r}, \omega). \end{aligned} \quad (1.202)$$

Similarly, the magnetic loss rate—the parameter accounting for the EPR interaction within the oscillator model prescribed by Eq. (1.58)—can be recast into the following illuminating form

$$\gamma_{\text{m}}(\omega) \sim \sum_{\beta} \int_{V_{\text{EPR}}} d\vec{r}'^3 M_\beta(\vec{r}', \omega) H_\beta^*(\vec{r}', \omega) \sim \sum_{\alpha\beta} \int_{V_{\text{EPR}}} d\vec{r}'^3 M_\beta(\vec{r}', \omega) \int_V d\vec{r}^3 G_{\beta\alpha}^{H*}(\vec{r}', \vec{r}, \omega) \mathcal{P}_\alpha^*(\vec{r}, \omega). \quad (1.203)$$

Evidently, the expression for $g_{\text{EPR}}(\omega)$ bears a strong resemblance to the one for $\gamma_{\text{m}}(\omega)$, the only difference being the absence of the complex conjugate and the interchange of the indices and the coordinate vectors in the magnetic dyadic Green's function. The question, whether this failure to reproduce exactly the predictions of the oscillator model is severe enough to discard it altogether, can be resolved only through a careful analysis of the symmetry properties of the magnetic dyadic Green's function.

Let us start by writing down the closed form expression for \vec{G}^H in free space [2] (like in the electric case, no such form exists in the presence of a substrate)

$$H_{\vec{G}}^{(0)}(\vec{r}, \vec{r}') = \frac{\omega k_1^2}{4\pi} \frac{e^{ik_1 R}}{k_1 R} \left(1 + \frac{i}{k_1 R}\right) \frac{1}{R} \begin{bmatrix} 0 & (z' - z) & (y - y') \\ (z - z') & 0 & (x' - x) \\ (y' - y) & (x - x') & 0 \end{bmatrix}, \quad (1.204)$$

where $R = \sqrt{(x - x')^2 + (y - y')^2 + (z - z')^2}$ stands for the distance between the source and the position at which the field is evaluated. Apparently, their interchange leads only to sign change and the same happens when we switch the indices, i.e. we replace $H_{G_{\alpha\beta}}^{(0)}(\vec{r}, \vec{r}')$ with $H_{G_{\beta\alpha}}^{(0)}(\vec{r}, \vec{r}')$. The fact that

$$H_{G_{\beta\alpha}}^{(0)}(\vec{r}', \vec{r}) = H_{G_{\alpha\beta}}^{(0)}(\vec{r}, \vec{r}') \quad (1.205)$$

partially lifts the discrepancy between the oscillator model and the more rigorous approach involving overlap integrals. The only problem left to solve (at least in the free space) is the absence of the complex conjugate in the latter. To that end, it proved to be instructive to evaluate the magnetic Green's function close to the origin, namely its real part. By expanding the exponential function $e^{ik_1 R}$

1.7. RIGOROUS TREATMENT OF THE PLASMON ENHANCED EPR EFFECT

into a Taylor series, it becomes clear, after several steps, that the real part of all the components of $H\tilde{G}^{(0)}(\vec{r}, \vec{r}')$ tends to zero at the origin

$$\begin{aligned} \lim_{R \rightarrow 0} \operatorname{Re} \left\{ H G_{\alpha\beta}^{(0)}(\vec{r}, \vec{r}') \right\} &\sim \lim_{R \rightarrow 0} \operatorname{Re} \left\{ \frac{\omega k_1^2}{4\pi} \frac{e^{ik_1 R}}{k_1 R} \left(1 + \frac{i}{k_1 R} \right) \right\} = \\ &= \lim_{R \rightarrow 0} \frac{\omega k_1^2}{4\pi} \operatorname{Re} \left\{ \frac{1 + ik_1 R - \frac{1}{2}k_1^2 R^2 + \dots}{k_1 R} + \frac{i - k_1 R - \frac{1}{2}ik_1^2 R^2 + \frac{1}{6}k_1^3 R^3 + \dots}{k_1^2 R^2} \right\} = \\ &= \lim_{R \rightarrow 0} \frac{\omega k_1^2}{4\pi} \left[-\frac{1}{3}k_1 R + R^2(\dots) + \dots \right] = 0. \end{aligned} \quad (1.206)$$

If we next add to $H G_{\alpha\beta}^{(0)}(\vec{r}, \vec{r}')$ its counterpart from the oscillator model $H G_{\beta\alpha}^{(0)*}(\vec{r}', \vec{r})$ (and subtract it immediately afterwards)

$$H G_{\alpha\beta}^{(0)}(\vec{r}, \vec{r}') = H G_{\alpha\beta}^{(0)}(\vec{r}, \vec{r}') + H G_{\beta\alpha}^{(0)*}(\vec{r}', \vec{r}) - H G_{\beta\alpha}^{(0)*}(\vec{r}', \vec{r}) = \Delta H G_{\alpha\beta}^{(0)}(\vec{r}, \vec{r}') - H G_{\beta\alpha}^{(0)*}(\vec{r}', \vec{r}) \quad (1.207)$$

and exploit successively the identity from Eq. (1.205) and vanishing of the real part of the magnetic Green's function at the origin

$$\lim_{R \rightarrow 0} \Delta H G_{\alpha\beta}^{(0)}(\vec{r}, \vec{r}') = \lim_{R \rightarrow 0} 2\operatorname{Re} \left\{ H G_{\alpha\beta}^{(0)}(\vec{r}, \vec{r}') \right\} = 0, \quad (1.208)$$

we find that at close range ($k_1 R \ll 1$)

$$H G_{\alpha\beta}^{(0)}(\vec{r}, \vec{r}') \approx -H G_{\beta\alpha}^{(0)*}(\vec{r}', \vec{r}). \quad (1.209)$$

This further reconciles the two approaches as the magnetic field is expected to be significant mainly close to the antenna, where the condition $k_1 R \ll 1$ should be well satisfied.

The catch that prevents us from stating conclusively that the oscillator model and its outcomes are valid is the fact that in the course of the above derivation, we have completely ignored the substrate. Inspection of Eqs. (1.189)–(1.197) immediately reveals that in its presence, no symmetry relation such as the one formulated in Eq. (1.205) exists

$$H G_{\beta\alpha}^{\operatorname{ref}}(\vec{r}', \vec{r}) \neq H G_{\alpha\beta}^{\operatorname{ref}}(\vec{r}, \vec{r}'). \quad (1.210)$$

As a consequence, the real part of the magnetic Green's function does not vanish at the origin and we fail to reproduce the desired equivalence between $G_{\alpha\beta}^H(\vec{r}, \vec{r}')$ and $G_{\beta\alpha}^{H*}(\vec{r}', \vec{r})$ as we were able in the free space. In order to ascertain the gravity of this setback, we decided to carefully examine the behaviour of the "reflected" part of the magnetic Green's function near the origin. Choosing the $H G_{yx}^{\operatorname{ref}}$ component as our subject of study, we evaluated analytically the term that thwarts our efforts to link it directly to $G_{xy}^{H*}(\vec{r}', \vec{r})$

$$\lim_{R, z \rightarrow 0} H G_{yx}^{\operatorname{ref}}(\vec{r}, \vec{r}') + H G_{xy}^{\operatorname{ref}*}(\vec{r}', \vec{r}) = \lim_{R, z \rightarrow 0} i \frac{\omega k_1^2}{4\pi} \left[\operatorname{Re} \{ I_1^H(k_1 \rho) \} + i \cos 2\psi \operatorname{Im} \{ I_2^H(k_1 \rho) \} \right] \neq 0. \quad (1.211)$$

If we look at the spatial dependence of the real and imaginary parts of the auxiliary integrals $I_1^H(k_1 \rho)$ and $I_2^H(k_1 \rho)$ shown in the left panel of Figure 1.23, it becomes clear that our difficulties arise from the singularity in the real part of the integral $I_1^H(k_1 \rho)$, while the second term involving the imaginary part of $I_2^H(k_1 \rho)$ poses no problems.

The presence of Fresnel reflection coefficients makes any general analysis of these integrals rather tricky, but luckily for us, the situation is not so chaotic close to the origin—as we approach it, high

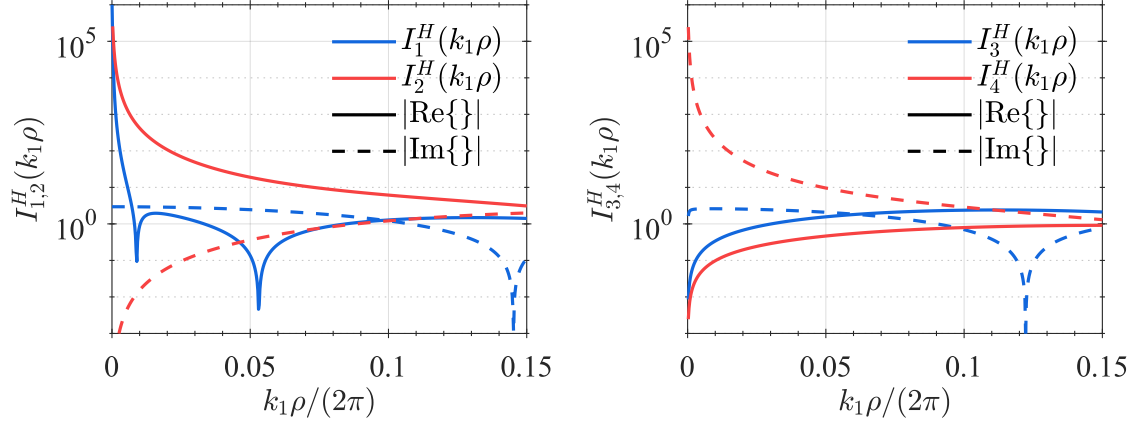


Figure 1.23: Auxiliary integrals $I_1^H(k_1\rho)$, $I_2^H(k_1\rho)$, $I_3^H(k_1\rho)$, and $I_4^H(k_1\rho)$ as a function of the lateral distance from the origin ρ . The line scan was evaluated 100 nm above a point source sitting right on top of a silicon substrate. Note the disparate behavior of the real and imaginary parts of the integral close to the origin, where one usually diverges, while the other saturates or tends to zero.

spatial frequencies gain the upper hand and represent the largest contribution to the integral. At the same time, the Fresnel coefficients saturate at large wavevectors and tend to their static limit, namely

$$r_\infty^p = \frac{\varepsilon_2 - \varepsilon_1}{\varepsilon_2 + \varepsilon_1}, \quad (1.212)$$

$$r_\infty^s = 0, \quad (1.213)$$

where ε_1 and ε_2 stand for the dielectric permittivities of the superstrate and substrate, respectively. That allows us to factor them out of the integrals

$$\begin{aligned} \lim_{R, z \rightarrow 0} I_1^H(k_1\rho) &= \lim_{R, z \rightarrow 0} \int_0^\infty d\lambda \lambda J_0(\lambda k_1\rho) [r^s(\lambda) - r^p(\lambda)] e^{i\sqrt{1-\lambda^2}k_1(z+z')} \approx \\ &\approx -r_\infty^p \int_0^\infty d\lambda \lambda J_0(\lambda k_1\rho) e^{i\sqrt{1-\lambda^2}k_1(z+z')} \end{aligned} \quad (1.214)$$

and obtain approximate expressions that can be not only evaluated analytically, but which have also a clear physical meaning: they represent the magnetic field of an image dipole mirrored by the substrate, with an amplitude dictated by the dielectric contrast between the superstrate and the substrate (the fact that it is indeed a mirror image of the original dipole stems from the plus sign between the vertical coordinates in the exponential factor). Consequently, the problematic expression from Equation (1.211) is reduced to

$$\begin{aligned} \lim_{R, z \rightarrow 0} H_{G_{yx}}^{\text{ref}*}(\vec{r}, \vec{r}') + H_{G_{xy}}^{\text{ref}}(\vec{r}', \vec{r}) &\approx -i \frac{\omega k_1^2}{4\pi} r_\infty^p \int_0^\infty d\lambda \lambda J_0(\lambda k_1\rho) e^{i\sqrt{1-\lambda^2}k_1(z+z')} \\ &= r_\infty^p H_{G_{xy}}^{(0)}(\vec{r}'_{\parallel} - \vec{r}_{\parallel}, z'+z) = r_\infty^p H_{G_{xy}}^{\text{img}}(\vec{r}', \vec{r}), \end{aligned} \quad (1.215)$$

where the superscript ^{img} indicates that this variant of the magnetic Green's function should be associated with the mirror image of the source. It seems to be evident now that the direct equivalence

1.7. RIGOROUS TREATMENT OF THE PLASMON ENHANCED EPR EFFECT

between $G_{\alpha\beta}^H(\vec{r}, \vec{r}')$ and $G_{\beta\alpha}^{H*}(\vec{r}', \vec{r})$ has to be abandoned and replaced with a new one that would account for the above extra term. One can easily derive it using the same procedure as in Eq. (1.207)

$$\begin{aligned} H_{yx}^{\text{ref}}(\vec{r}, \vec{r}') &= H_{yx}^{\text{ref}}(\vec{r}, \vec{r}') + H_{xy}^{\text{ref}*}(\vec{r}', \vec{r}) + r_{\infty}^{\text{p}} H_{xy}^{\text{img}*}(\vec{r}', \vec{r}) - \left[H_{xy}^{\text{ref}*}(\vec{r}', \vec{r}) + r_{\infty}^{\text{p}} H_{xy}^{\text{img}*}(\vec{r}', \vec{r}) \right] = \\ &= \Delta H_{yx}^{\text{ref}}(\vec{r}, \vec{r}') - \left[H_{xy}^{\text{ref}*}(\vec{r}', \vec{r}) + r_{\infty}^{\text{p}} H_{xy}^{\text{img}*}(\vec{r}', \vec{r}) \right]. \end{aligned} \quad (1.216)$$

Recalling the symmetry relation from Eq. (1.205) linking the various components of the free space magnetic Green's function, the correction term $\Delta H_{yx}^{\text{ref}}(\vec{r}, \vec{r}')$ is found to tend to zero as we approach the origin

$$\lim_{R, z \rightarrow 0} \Delta H_{yx}^{\text{ref}}(\vec{r}, \vec{r}') = \lim_{R, z \rightarrow 0} 2r_{\infty}^{\text{p}} \text{Re} \{ H_{xy}^{\text{img}}(\vec{r}', \vec{r}) \} = \lim_{R, z \rightarrow 0} 2r_{\infty}^{\text{p}} \text{Re} \left\{ H_{xy}^{(0)}(\vec{r}'_{\parallel} - \vec{r}_{\parallel}, z' + z) \right\} = 0, \quad (1.217)$$

whence it follows that at close range, $H_{yx}^{\text{ref}}(\vec{r}, \vec{r}')$ is practically equivalent to

$$H_{yx}^{\text{ref}}(\vec{r}, \vec{r}') \approx - \left[H_{xy}^{\text{ref}*}(\vec{r}', \vec{r}) + r_{\infty}^{\text{p}} H_{xy}^{\text{img}*}(\vec{r}', \vec{r}) \right]. \quad (1.218)$$

The above series of steps yields similar results also when applied to the rest of the components of the magnetic Green's function, with the exception of $H_{zx}^{\text{ref}}(\vec{r}, \vec{r}')$ and $H_{zy}^{\text{ref}}(\vec{r}, \vec{r}')$ which differ by an opposite sign in front of the term corresponding to the image dipole. We note that this inconsistency is probably connected to the disparate screening experienced by dipoles oriented in parallel or perpendicularly to a planar interface between two materials. We list here for completeness also the correction terms for some of these other magnetic Green's function components (the rest can be easily deduced from them)

$$\begin{aligned} \lim_{R, z \rightarrow 0} H_{xy}^{\text{ref}}(\vec{r}, \vec{r}') + H_{yx}^{\text{ref}*}(\vec{r}', \vec{r}) &= \lim_{R, z \rightarrow 0} -i \frac{\omega k_1^2}{4\pi} \left[\text{Re} \{ I_1^H(k_1\rho) \} - i \cos 2\psi \text{Im} \{ I_2^H(k_1\rho) \} \right] \approx \\ &\approx i \frac{\omega k_1^2}{4\pi} r_{\infty}^{\text{p}} \int_0^{\infty} d\lambda \lambda J_0(\lambda k_1\rho) e^{i\sqrt{1-\lambda^2}k_1(z+z')} = r_{\infty}^{\text{p}} H_{yx}^{(0)}(\vec{r}'_{\parallel} - \vec{r}_{\parallel}, z' + z), \end{aligned} \quad (1.219)$$

$$\begin{aligned} \lim_{R, z \rightarrow 0} H_{xz}^{\text{ref}}(\vec{r}, \vec{r}') + H_{zx}^{\text{ref}*}(\vec{r}', \vec{r}) &= \lim_{R, z \rightarrow 0} -\frac{\omega k_1^2}{4\pi} \sin \psi \left[I_4^H(k_1\rho) + I_3^{H*}(k_1\rho) \right] \approx \\ &\approx -\frac{\omega k_1^2}{4\pi} r_{\infty}^{\text{p}} \sin \psi \int_0^{\infty} d\lambda \frac{\lambda^2}{\sqrt{1-\lambda^2}} J_1(\lambda k_1\rho) e^{i\sqrt{1-\lambda^2}k_1(z+z')} = r_{\infty}^{\text{p}} H_{zx}^{(0)}(\vec{r}'_{\parallel} - \vec{r}_{\parallel}, z' + z), \end{aligned} \quad (1.220)$$

$$\begin{aligned} \lim_{R, z \rightarrow 0} H_{zx}^{\text{ref}}(\vec{r}, \vec{r}') + H_{xz}^{\text{ref}*}(\vec{r}', \vec{r}) &= \lim_{R, z \rightarrow 0} \frac{\omega k_1^2}{4\pi} \sin \psi \left[I_3^H(k_1\rho) + I_4^{H*}(k_1\rho) \right] \approx \\ &\approx \frac{\omega k_1^2}{4\pi} r_{\infty}^{\text{p}} \sin \psi \left[\int_0^{\infty} d\lambda \frac{\lambda^2}{\sqrt{1-\lambda^2}} J_1(\lambda k_1\rho) e^{i\sqrt{1-\lambda^2}k_1(z+z')} \right]^* = r_{\infty}^{\text{p}} H_{xz}^{(0)*}(\vec{r}'_{\parallel} - \vec{r}_{\parallel}, z' + z), \end{aligned} \quad (1.221)$$

$$\lim_{R, z \rightarrow 0} H_{xx}^{\text{ref}}(\vec{r}, \vec{r}') + H_{xx}^{\text{ref}*}(\vec{r}', \vec{r}) = \lim_{R, z \rightarrow 0} \frac{\omega k_1^2}{4\pi} \sin 2\psi \text{Im} \{ I_2^H(k_1\rho) \} = 0. \quad (1.222)$$

1.7. RIGOROUS TREATMENT OF THE PLASMON ENHANCED EPR EFFECT

Finally, by combining all these equations into one, we acquire a single concise expression for the magnetic dyadic Green's function

$$G_{\alpha\beta}^H(\vec{r}, \vec{r}') = - \left[G_{\beta\alpha}^{H*}(\vec{r}', \vec{r}) + r_{\infty}^p H G_{\beta\alpha}^{\text{img}*}(\vec{r}', \vec{r}) \right] + \Delta G_{\alpha\beta}^H(\vec{r}, \vec{r}'), \quad (1.223)$$

$$\vec{G}_{\text{img}}^H(\vec{r}', \vec{r}) = \begin{bmatrix} 0 & H G_{xy}^{(0)}(\vec{r}'_{\parallel} - \vec{r}_{\parallel}, z' + z) & -H G_{xz}^{(0)}(\vec{r}'_{\parallel} - \vec{r}_{\parallel}, z' + z) \\ H G_{yx}^{(0)}(\vec{r}'_{\parallel} - \vec{r}_{\parallel}, z' + z) & 0 & -H G_{yz}^{(0)}(\vec{r}'_{\parallel} - \vec{r}_{\parallel}, z' + z) \\ H G_{zx}^{(0)}(\vec{r}'_{\parallel} - \vec{r}_{\parallel}, z' + z) & H G_{zy}^{(0)}(\vec{r}'_{\parallel} - \vec{r}_{\parallel}, z' + z) & 0 \end{bmatrix} \quad (1.224)$$

that allows us to assess the validity of the oscillator model and its outcomes.

Before we do that, it remains to verify whether this entire construct is actually correct and the deviation term $\Delta \vec{G}^H(\vec{r}, \vec{r}')$ truly goes to zero as we approach the origin. To that end, we evaluated the above expressions along a line running 100 nm above a point source that is placed right on top of a silicon substrate. The results plotted in Figure 1.24 confirm that close to the source, one can approximate the magnetic dyadic Green's function with the following expression

$$\lim_{R, z \rightarrow 0} G_{\alpha\beta}^H(\vec{r}, \vec{r}') \approx - \left[G_{\beta\alpha}^{H*}(\vec{r}', \vec{r}) + r_{\infty}^p H G_{\beta\alpha}^{\text{img}*}(\vec{r}', \vec{r}) \right]. \quad (1.225)$$

Its insertion back into Equation (1.202) yields a formula for the EPR interaction parameter

$$g_{\text{EPR}}(\omega) \approx \frac{\mu_0 \int_{V_{\text{EPR}}} d\vec{r}^3 \vec{M}(\vec{r}, \omega) \cdot \left[\vec{H}_{\text{ant}}^*(\vec{r}, \omega) + r_{\infty}^p \vec{H}_{\text{img}}^*(\vec{r}, \omega) \right]}{\int_V d\vec{r}^3 \vec{P}^*(\vec{r}, \omega) \cdot \vec{E}_0(\vec{r}, \omega)} \quad (1.226)$$

that at last enables us to clearly identify the discrepancies between the oscillator model and the more rigorous approach employing the framework of overlap integrals (for clarity, the newly introduced term \vec{H}_{ant} simply denotes the magnetic field generated by the antenna). Its comparison with the expression for the magnetic loss rate given by Eq. (1.58) and now recast as

$$\gamma_{\text{m}}(\omega) \sim \int_{V_{\text{EPR}}} d\vec{r}^3 \vec{M}(\vec{r}, \omega) \cdot \left[\vec{H}_0^*(\vec{r}, \omega) + \vec{H}_{\text{ant}}^*(\vec{r}, \omega) \right] \quad (1.227)$$

tells us two things: the oscillator model lacks the extra term associated with the mirror image of the antenna (\vec{H}_{img}) and contains another one that appears to be superfluous (\vec{H}_0). Considering the systems that we are dealing with in this thesis, the weight of these individual terms will generally depend on the particular antenna geometry and the choice of the substrate.

On that note, we decided to validate our advanced EPR interaction model and to study the impact of these various terms it contains on the simplest system consisting of a single 80 μm long diabolo antenna placed on top of a semiinfinite silicon substrate. The magnetically active layer covering the antenna was 500 nm thick and it was etched away except a $160 \times 160 \mu\text{m}^2$ area with the antenna in its center. The results of the FDTD simulation and the EPR interaction model are plotted in Figure 1.25(a), showing a very good agreement between the two approaches both in terms of the linewidth and the depth of the imprint left by the magnetic material in the scattering spectrum of the antenna. The density of spins was varied to verify that the depth of the observed dip scales properly with the strength of the interaction, meanwhile the frequency and the linewidth ($\tau = 100$ ps) of the magnetic transition were kept fixed.

In order to assess the relative importance of the various terms appearing in the expression for the EPR interaction parameter and the necessity to include them in our predictions, we calculated scattering cross-section spectra for the same antenna and magnetic layer parameters as before, but using different versions of the EPR interaction parameter. Namely, the full original form $g_{\text{EPR}}^{\text{full}}(\omega)$,

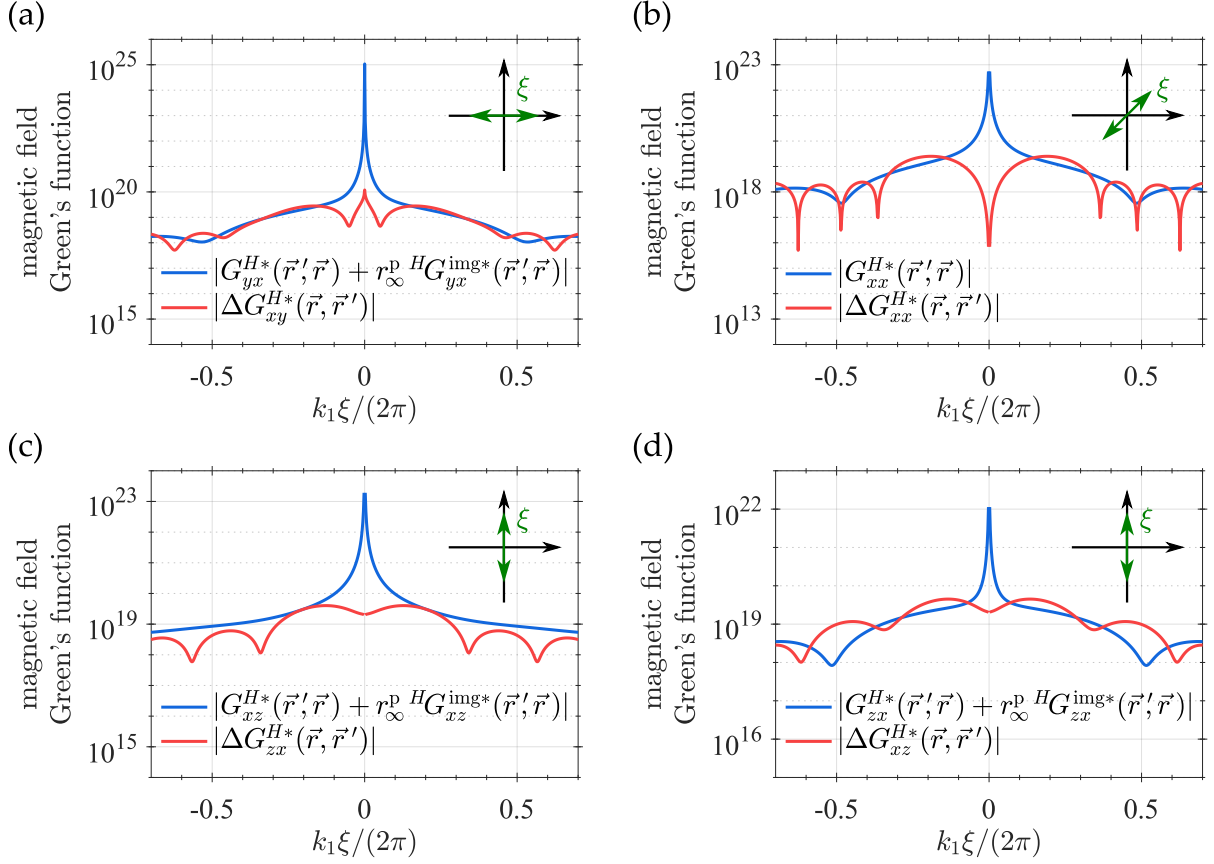


Figure 1.24: Weights of the various terms constituting the individual components of the magnetic dyadic Green's function $G_{\alpha\beta}^H(\vec{r}, \vec{r}')$. Note that close to the origin, the correction term $\Delta G_{\alpha\beta}^H(\vec{r}, \vec{r}')$ becomes negligible compared to the leading terms $G_{\beta\alpha}^H(\vec{r}', \vec{r})$ and $r_\infty^p H G_{\beta\alpha}^{\text{img}*}(\vec{r}', \vec{r})$, which supports our explanation of their origin and relative importance. The lateral line scans were evaluated 100 nm above a point source located right on top of an air-silicon interface. Also, the direction of the line scan (indicated by the green double-arrow) differs between the individual components of $G_{\alpha\beta}^H(\vec{r}, \vec{r}')$, as each possesses a different dependence on the azimuthal angle.

an approximate form deduced from the symmetry properties of the magnetic dyadic Green's function $g_{\text{EPR}}^{\text{approx}}(\omega)$, and an alternative variant based on the oscillator model $g_{\text{EPR}}^{\text{osc}}(\omega)$

$$g_{\text{EPR}}^{\text{full}}(\omega) = \frac{-\mu_0 \int_V d\vec{r}^3 \vec{\mathcal{P}}^*(\vec{r}, \omega) \cdot \int_{V_{\text{EPR}}} d\vec{r}'^3 \vec{\mathcal{G}}^H(\vec{r}, \vec{r}', \omega) \vec{M}(\vec{r}', \omega)}{\int_V d\vec{r}^3 \vec{\mathcal{P}}^*(\vec{r}, \omega) \cdot \vec{\mathcal{E}}_0(\vec{r}, \omega)}, \quad (1.228)$$

$$g_{\text{EPR}}^{\text{approx}}(\omega) = \frac{\mu_0 \int_{V_{\text{EPR}}} d\vec{r}^3 \vec{M}(\vec{r}, \omega) \cdot [\vec{H}_{\text{ant}}^*(\vec{r}, \omega) + r_\infty^p \vec{H}_{\text{img}}^*(\vec{r}, \omega)]}{\int_V d\vec{r}^3 \vec{\mathcal{P}}^*(\vec{r}, \omega) \cdot \vec{\mathcal{E}}_0(\vec{r}, \omega)}, \quad (1.229)$$

$$g_{\text{EPR}}^{\text{osc}}(\omega) = \frac{\mu_0 \int_{V_{\text{EPR}}} d\vec{r}^3 \vec{M}(\vec{r}, \omega) \cdot [\vec{H}_0^*(\vec{r}, \omega) + \vec{H}_{\text{ant}}^*(\vec{r}, \omega)]}{\int_V d\vec{r}^3 \vec{\mathcal{P}}^*(\vec{r}, \omega) \cdot \vec{\mathcal{E}}_0(\vec{r}, \omega)}. \quad (1.230)$$

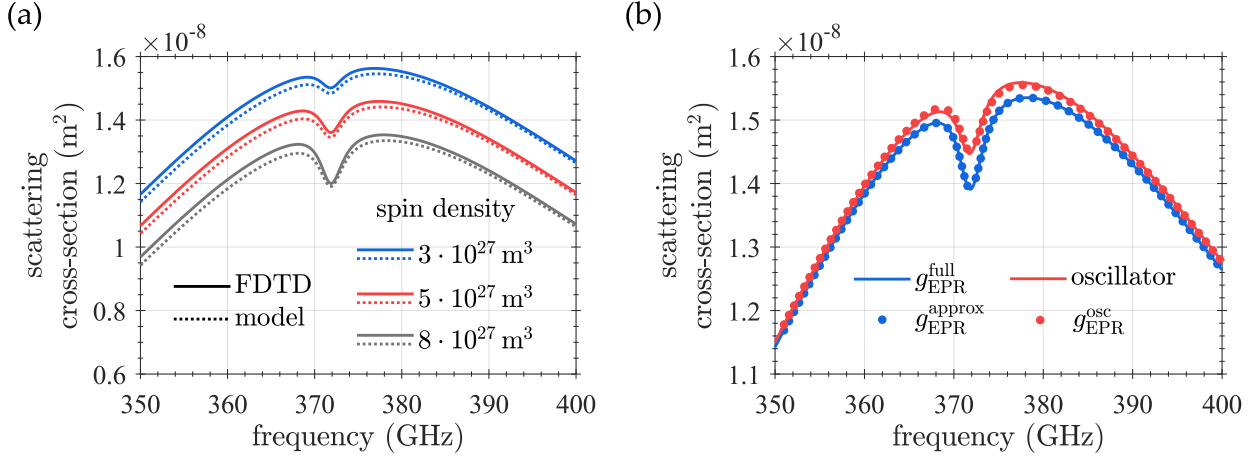


Figure 1.25: (a) Validation of the advanced EPR interaction model employing mode decomposition and overlap integrals against the exact FDTD simulations of a single 80 μm diabolo antenna on top of a silicon substrate. The three scattering cross-section spectra for the three different spin densities were artificially shifted along the vertical axis for the sake of a more lucid visualization. (b) Scattering cross-section spectra of the same plasmonic antenna as in (a), but calculated using three different variants of the EPR interaction parameter ($g_{\text{EPR}}^{\text{full}}$, $g_{\text{EPR}}^{\text{approx}}$, and $g_{\text{EPR}}^{\text{osc}}$) plus the oscillator model from Section 1.2. These results correlate well with our analysis of the plasmon enhanced EPR effect and corroborate the limited precision of the oscillator model, in which the implementation of the interaction with a magnetic transition is based solely on energy dissipation considerations.

Finally, we also fitted the scattering cross-section spectrum of a bare antenna using the analytical oscillator model introduced in Section 1.2 and after infusing it with the magnetic loss rate accounting for the EPR interaction, we obtained the last missing piece of our puzzle. Comparison with those other three spectra shown in Figure 1.25(b) demonstrates that the approximate expression for the EPR interaction parameter can more than adequately act as a substitute for the full form and that the results of the oscillator model correspond well to the situation, when the term in $g_{\text{EPR}}(\omega)$ associated with the mirror image of the antenna is replaced with the incident magnetic field. As for the quantitative difference between the oscillator model and the more accurate approach involving mode decomposition and overlap integrals, the former underestimates the magnitude of the EPR signal roughly by 25% with respect to the latter. We suspect that for other antenna geometries and substrates with very high index of refraction, this deviation could go as high as 50%. Still, it seems that from the qualitative point of view, the oscillator model captures the fundamental aspects of the plasmon enhanced EPR effect rather well. Consequently, the premise that the stronger the magnetic field is, the more pronounced also becomes the EPR signature remains valid and so does our conviction that the magnetic field enhancement is the crucial parameter that determines the performance of an antenna in EPR spectroscopy measurements.

1.8. Summary and outlook

To summarize the contents of this chapter dedicated to the study of the plasmon enhanced EPR effect: the reader was provided with an intelligible description of its fundamental aspects, using a simplified oscillator model, in which a plasmonic antenna is treated as a point dipole and its interaction with the surrounding EPR material is fully captured by a single phenomenological parameter with a clear physical meaning. According to this model, the magnitude of the footprint left by a magnetic transition in the far-field response of the antenna is directly proportional to the average magnetic field enhancement around the antenna. A more rigorous approach combining mode decomposition, FDTD

simulations and overlap integrals later revealed that this is not entirely true and for truly accurate results, some additional terms should be included. Nevertheless, the outcomes of the oscillator model proved to be qualitatively valid and from that point onward, we considered the average magnetic field enhancement to be the most crucial quantity that determines how well a particular plasmonic antenna shall perform in EPR spectroscopy measurements of thin films.

Since real sample sizes are expected to exceed the dimensions of a single antenna at least by one order of magnitude, the use of antenna arrays seems to be almost inevitable. From the computational viewpoint, it represents a certain challenge, but it also opens new avenues for shaping the response of the system using e.g. lattice resonances, possibly leading to a further amplification of the interaction between the antennas and the EPR material. To that end, we developed an advanced antenna interaction model that is capable to accurately and efficiently quantify the forces exerted by an antenna on its neighbours, even in the presence of a substrate. Despite its limitations, we are convinced that this model represents a versatile tool transferable also to other spectral regions (e.g. infra-red), where it can substantially reduce the computation times associated with the simulations of large finite antenna arrays.

We employed our antenna interaction model in the search for an optimal antenna array design that would maximize the magnitude of the signature imprinted by the EPR material into the radiation emitted by the antennas. Thanks to the ability of our model to scan rapidly over various array and substrate configurations, we managed to cover a significant portion of the space spanned by the various geometrical parameters inherent to our system. In the end, we failed at finding a design that would significantly outperform the others. In fact, our figure of merit—the average magnetic field enhancement—seemed to saturate at a certain value, unwilling to increase beyond it. This somewhat surprising result, along with the study of other types of antennas and array configurations, will be a subject of our future investigations in this research area.

On that note, it is also our intention to further expand the antenna interaction model, making it applicable to a wider range of systems. As an example, we could name arrays of inverted plasmonic structures, i.e. apertures in otherwise homogeneous metallic layers. Their potential advantage in comparison to the systems presented here in this thesis is the strong interaction between individual antennas mediated by surface plasmon polaritons that could lead to a more efficient excitation of lattice resonances and ultimately also to a better level of performance in the EPR spectroscopy measurements.

2. Miscellany of applications

2.1. Phase imaging of metasurfaces

Metasurfaces can be essentially perceived as ensembles of structures with subwavelength mutual spacing, granting them a semblance of smooth homogeneous materials. By tailoring the fundamental building blocks of a metasurface, one can locally modify its optical properties and acquire range of functions otherwise unattainable with standard optical materials [36, 37]. The modification of the optical properties can be realized in several ways, the most common being the adjustment of the geometrical parameters of the building blocks, which slightly alters the complex amplitude of the electromagnetic wave passing through the metasurface. On the global scale, the variations in phase and amplitude can result in a broad spectrum of wavefront shapes—from a simple convergent wave mimicking a passage through an ordinary lense to complex optical vortices with a nonzero orbital angular momentum [38, 39].

The practical fabrication of metasurfaces brings a question of how to verify that the resulting phase and amplitude profiles truly match those envisioned in the theoretical design. To that end, we successfully employed coherence controlled holographic microscopy (CCHM), a technique originally developed at our institute for the study of objects other than metasurfaces [40, 41]. We demonstrated that the holographic microscopy can be used for phase imaging of metasurfaces and by changing the defocus of the optical system, one can even create 3D phase maps showing how the wavefront evolves as the distance from the metasurfaces increases. We refer the reader for a more detailed discussion of this technique to [Attachments](#), where the full article can be found. Here, we would like to focus exclusively on the calculations that constituted the theoretical basis of our measurements and facilitated their correct interpretation.

The first, perhaps the most crucial step is to have a clear picture of how an image is formed in a microscope. It turns out that even the most rudimentary configuration with the image projected onto the back focal plane of an optical system made of two lenses is sufficient for understanding the key aspects of this process (an example of such a system is schematically depicted in [Figure 2.1](#)). Putting aside effects like the image inversion and magnification, the most profound impact of the optical system on the image is its inability to convey high spatial frequencies, placing a limit on the resolution with which we can discern the fine features of the subject of our studies. In other words, if we perform a plane wave decomposition of the field in the object plan (i.e. we calculate its Fourier transform), the optical system can transfer only those waves fulfilling the condition that the magnitude of their lateral wavevector \vec{q} does not exceed certain value, namely the free space wavenumber k multiplied by the numerical aperture NA of the system. In mathematical notation, this amounts to

$$\begin{aligned} \vec{E}(\vec{r}_{\text{img}}, z_{\text{img}}) &= \iint_{|\vec{q}| \leq k \text{NA}} d\vec{q}^2 e^{i\vec{q} \cdot \vec{r}_{\text{img}}} e^{ik_z(z_{\text{img}} - z_{\text{obj}})} \vec{E}(\vec{q}, z_{\text{obj}}) = \\ &= \iint_{|\vec{q}| \leq k \text{NA}} d\vec{q}^2 e^{i\vec{q} \cdot \vec{r}_{\text{img}}} e^{ik_z(z_{\text{img}} - z_{\text{obj}})} \frac{1}{4\pi^2} \iint_{-\infty}^{\infty} d\vec{r}_{\text{obj}}^2 e^{-i\vec{q} \cdot \vec{r}_{\text{obj}}} \vec{E}(\vec{r}_{\text{obj}}, z_{\text{obj}}), \end{aligned} \quad (2.1)$$

where the subscripts specify, whether we evaluate the field in the object plane (_{obj}) or the image (_{img}) plane and the meaning of the individual spatial variables can be easily deciphered by consulting [Figure 2.1](#).

Since metasurfaces are usually large area objects that cannot be fitted into a single simulation, it makes sense to calculate the response of their building blocks individually and subsequently piece them together. Considering, however, the issues one encounters when dealing with an electric field

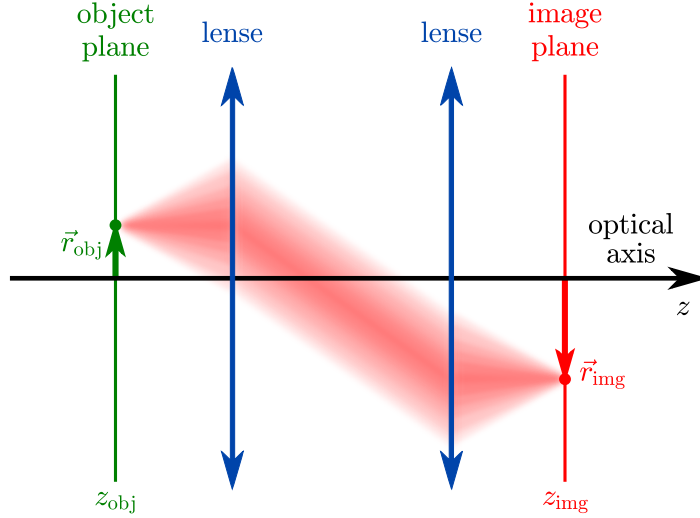


Figure 2.1: Sketch of a simple optical system roughly illustrating how an image of a metasurface is formed in the back focal plane of a CCHM microscope. Apart from inverting and magnifying the object, the optical system also removes high spatial frequencies, placing a limit on the attainable spatial resolution. Note that we use \vec{r}_{obj} to establish the lateral position with respect to the optical axis within the object plane, while \vec{r}_{img} serves the same purpose in the image plane.

distribution that suffers a cut-off at the boundary of the simulation region (see [Introduction](#) for the detailed clarification of this point), we opted for a less troublesome approach relying on the Green’s function formalism [2]

$$\vec{E}(\vec{r}_{\text{obj}}, z_{\text{obj}}) = \int_V d\vec{r}^3 \vec{G}(\vec{r}_{\text{obj}} - \vec{r}_{\parallel}, z_{\text{obj}}, z) \vec{P}(\vec{r}) = \sum_j \int_{V_j} d\vec{r}^3 \vec{G}(\vec{r}_{\text{obj}} - \vec{r}_{\parallel}, z_{\text{obj}}, z) \vec{P}_j(\vec{r}_{\parallel} - \vec{r}_j, z), \quad (2.2)$$

where the field anywhere in the object plane is given by the convolution of the dyadic Green’s function $\vec{G}(\vec{r}_{\text{obj}} - \vec{r}_{\parallel}, z_{\text{obj}}, z)$ with the global distribution of the polarization current $\vec{P}(\vec{r})$ induced within our hypothetical metasurface and where we used the fact that due to its “granular” nature, $\vec{P}(\vec{r})$ can be further broken down into distributions of currents flowing inside individual building blocks

$$\vec{P}(\vec{r}) = \sum_j \vec{P}_j(\vec{r}_{\parallel} - \vec{r}_j, z). \quad (2.3)$$

The lateral position of the building blocks within the object plane is specified by the set of vectors \vec{r}_j . Also note that we implicitly expect the environment hosting our structures to possess translational invariance along the lateral coordinates \vec{r}_{\parallel} , a requirement that is always met as long as we use planar substrates.

If we now turn our attention back to Equation (2.1) capturing the spatial filtering in optical microscopy and proceed with the evaluation of the electric field and its Fourier transform in the object plane, we obtain—after some shuffling with exponentials and the order of integration—the following equality

$$\begin{aligned}
 \vec{E}(\vec{q}, z_{\text{obj}}) &= \frac{1}{4\pi^2} \iint_{-\infty}^{\infty} d\vec{r}_{\text{obj}}^2 e^{-i\vec{q}\cdot\vec{r}_{\text{obj}}} \sum_j \int_{V_j} d\vec{r}^3 \vec{G}(\vec{r}_{\text{obj}} - \vec{r}_{\parallel}, z_{\text{obj}}, z) \vec{P}_j(\vec{r}_{\parallel} - \vec{r}_j, z) = \\
 &= \frac{1}{4\pi^2} \iint_{-\infty}^{\infty} d\vec{r}_{\text{obj}}^2 e^{-i\vec{q}\cdot\vec{r}_{\text{obj}}} \sum_j \int_{V_j} d\vec{r}^3 \vec{G}(\vec{r}_{\text{obj}} - \vec{r}_{\parallel}, z_{\text{obj}}, z) \iint_{-\infty}^{\infty} d\vec{q}'^2 e^{i\vec{q}'\cdot\vec{r}_{\parallel}} \vec{P}_j(\vec{q}', z) = \\
 &= \sum_j \int dz \iint_{-\infty}^{\infty} d\vec{q}'^2 e^{-i\vec{q}'\cdot\vec{r}_j} \iint_{-\infty}^{\infty} d\vec{r}_{\parallel}^2 e^{-i(\vec{q}-\vec{q}')\cdot\vec{r}_{\parallel}} \frac{1}{4\pi^2} \iint_{-\infty}^{\infty} d\vec{r}_{\text{obj}}^2 e^{-i\vec{q}\cdot(\vec{r}_{\text{obj}} - \vec{r}_{\parallel})} \vec{G}(\vec{r}_{\text{obj}} - \vec{r}_{\parallel}, z_{\text{obj}}, z) \vec{P}_j(\vec{q}', z) = \\
 &= \sum_j \int dz \iint_{-\infty}^{\infty} d\vec{q}'^2 e^{-i\vec{q}'\cdot\vec{r}_j} 4\pi^2 \delta(\vec{q} - \vec{q}') \vec{G}(\vec{q}, z_{\text{obj}}, z) \vec{P}_j(\vec{q}', z) = \\
 &= 4\pi^2 \int dz \vec{G}(\vec{q}, z_{\text{obj}}, z) \sum_j e^{-i\vec{q}\cdot\vec{r}_j} \vec{P}_j(\vec{q}, z), \tag{2.4}
 \end{aligned}$$

where $\vec{G}(\vec{q}, z_{\text{obj}}, z)$ and $\vec{P}_j(\vec{q}, z)$ stand for the Fourier representations of the dyadic Green's function and the current distribution induced within the j -th building block. The optical system then crops the high spatial frequencies so that only the plane waves with $|\vec{q}| \leq k \text{ NA}$ participate in the image formation

$$\vec{E}(\vec{r}_{\text{img}}, z_{\text{img}}) = 4\pi^2 \iint_{|\vec{q}| \leq k \text{ NA}} d\vec{q}^2 e^{i\vec{q}\cdot\vec{r}_{\text{img}}} e^{ikz(z_{\text{img}} - z_{\text{obj}})} \int dz \vec{G}(\vec{q}, z_{\text{obj}}, z) \sum_j e^{-i\vec{q}\cdot\vec{r}_j} \vec{P}_j(\vec{q}, z). \tag{2.5}$$

Although the above expression already permits practical calculations of the fields in the image plane, the evaluation of the integral over the allowed spatial frequencies can cause some troubles, namely occurrence of artificial ripples at the edges of the calculated image associated with the way how computers handle the calculation of Fourier transforms. One can avoid this problem, for example, by increasing the size of the image and cropping it afterwards. We found, however, the following approach utilizing the convolution of the current distribution with a point spread function of the optical system to be more reliable and ultimately also computationally less demanding.

Its employment goes hand in hand with the necessity of defining a single regular grid of points spanned by a position vector \vec{r}_i at which we shall evaluate the fields both in the object plane and in the image plane

$$\vec{r}_i \equiv \vec{r}_{\text{obj}} \equiv \vec{r}_{\text{img}}. \tag{2.6}$$

Furthermore, the current distribution needs to be projected onto this grid as well (using an interpolation procedure that preserves the total polarization current), which means we will no longer associate \vec{r}_j with the positions of the individual building blocks. Instead, it will be congruent with the position vector \vec{r}_i

$$\vec{r}_j \equiv \vec{r}_i, \tag{2.7}$$

and $\vec{P}_j(\vec{r})$ gets replaced by

$$\vec{P}_j(\vec{r}) = \delta(\vec{r}_{\parallel}) \vec{P}_j(z), \tag{2.8}$$

where $\vec{P}_j(z)$ stands for the polarization current assigned to the j -th grid point. Finally, insertion of the above expression into Equation (2.5) yields the distribution of the electric field within the image plane

$$\begin{aligned}\vec{E}(\vec{r}_i, z_{\text{img}}) &= \int dz \sum_j \iint_{|\vec{q}| \leq k \text{ NA}} d\vec{q}^2 e^{i\vec{q} \cdot (\vec{r}_i - \vec{r}_j)} e^{ik_z(z_{\text{img}} - z_{\text{obj}})} \vec{G}(\vec{q}, z_{\text{obj}}, z) \vec{P}_j(z) = \\ &= \int dz \sum_j \text{PSF}(\vec{r}_i - \vec{r}_j, z_{\text{img}}, z) \vec{P}_j(z).\end{aligned}\quad (2.9)$$

The point spread function

$$\text{PSF}(\vec{r}, z_{\text{img}}, z) = \iint_{|\vec{q}| \leq k \text{ NA}} d\vec{q}^2 e^{i\vec{q} \cdot \vec{r}} e^{ik_z(z_{\text{img}} - z_{\text{obj}})} \vec{G}(\vec{q}, z_{\text{obj}}, z), \quad (2.10)$$

an entity well known from the classical optics describing the field generated by a single point source, fully captures the propagation of electromagnetic waves through the optical system. Depending on the level of accuracy one strives to achieve, it can be modified to account for the various aberrations and optical effects occurring in a real optical system and distorting the resulting image. For the purpose of interpreting our phase measurements, however, the basic form written above, addressing solely the trimming of high spatial frequencies, is entirely sufficient.

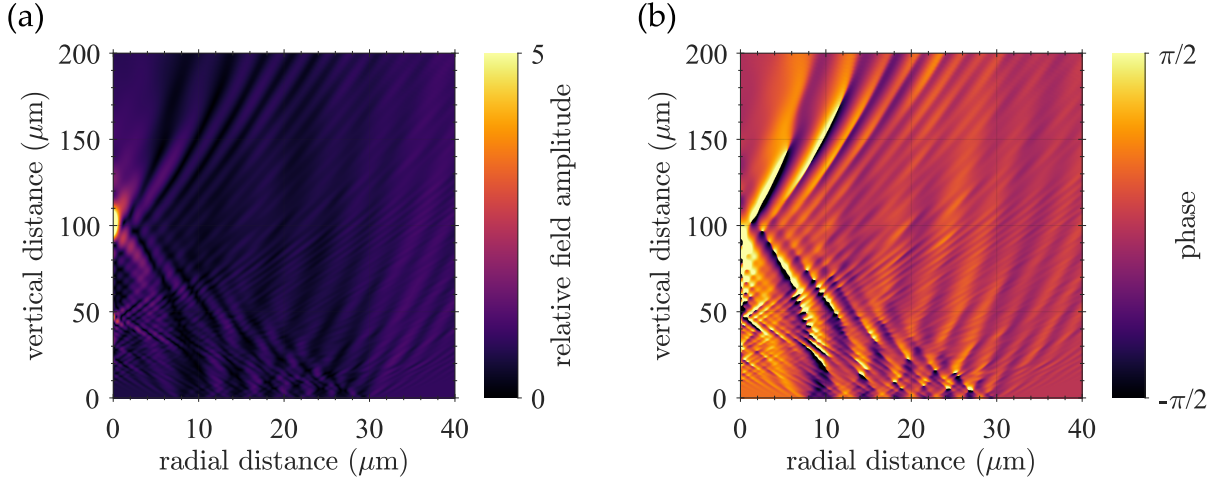


Figure 2.2: Numerically calculated amplitude (a) and phase (b) distribution of the electric field generated behind a plasmonic zone plate after it was illuminated by a plane wave. The size of the annular zones was designed to provide a focal point at the distance of $100 \mu\text{m}$ from the metasurface. Only two types of building blocks were used, namely silver discs with diameters equal to either 90 or 160 nm , yielding a phase difference between adjacent zones around $\pi/5$. Ideally, the phase should change by π at the zone boundaries, but our metasurface exhibited an acceptable focusing performance despite this modest value.

To demonstrate the usefulness of the above concept combining the Green's function formalism and the current distributions on some practical example, we show in Figure 2.2 the numerically calculated amplitude and phase distribution of an electromagnetic wave propagating behind a plasmonic metasurface specifically designed to focus light into a single spot $100 \mu\text{m}$ away from it. It consists of two types of silver discs arranged into regularly alternating concentric annuli with gradually decreasing radial size. Together, they form the so called zone plate, an optical element invented by the French physicist Augustin-Jean Fresnel already in the 19th century. The comparison with the experimental data measured by a coherence controlled holographic microscope, together with the detailed layout of the metasurface, can be found in the respective article in [Attachments](#). Our theoretical calculations not only validated the suitability of the CCHM for the characterization of phase-modulating

metasurfaces, but their careful analysis led to the elucidation of a discrepancy in the positions of the subsidiary focal points which slightly differed from those predicted by the analytical model for an ideal zone plate.

To conclude this passage dedicated to phase imaging, the presented theoretical apparatus proved to be an excellent tool for modeling the optical response of large area metasurfaces and this impression was further reinforced during the development of a metasurface-based beam splitter, which we present in the next section.

2.2. Tailoring the far-field response of metasurfaces

The ability to integrate several functions in a single optical element is perhaps one of the most important and intriguing assets offered by metasurfaces. In certain areas, they cannot compete with the classical optical elements in terms of efficiency and price, but the possibility to replace a complex optical system with a single metasurface should definitely arouse interest not only within the scientific community, but also the industry. In that respect, we have recently established collaboration with the Czech company Meopta, and started to work on several metasurface designs that could potentially improve the performance of specific optical systems, one of them being a fan-out element for parallel laser ablation [42].

It is basically an optical element that diffracts light into a set of diverging beams that upon refocusing by a lens, form a regular array of hotspots [43]. To help the reader with picturing how such a beam splitter functions, the optical paths of the individual beams as they propagate from the metasurface towards the back focal plane of the lens are outlined in Figure 2.3. In this schematical drawing, we limited ourselves to merely 4 beams, but in real devices, this number can be significantly higher. In the case of our design, we aim for an array of 28×28 beams, to be precise.

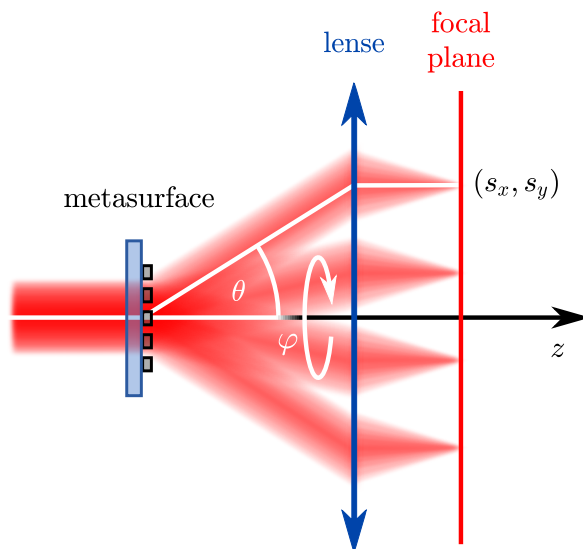


Figure 2.3: Schematical depiction of a metasurface converting an incident wave into multiple beams that, upon refocusing by a lens, form a regular array of hotspots in its back focal plane. The propagation directions of the individual beams can be conveniently described in terms of the azimuthal (φ) and declination (θ) angles or alternatively, using the directional cosines s_x and s_y defined by Eqs. (2.11) and (2.12).

Note that it is rather easy to obtain a regular beam array with a predefined angular separation, one just needs to fabricate a grating with the right pitch and the diffraction will take care of the rest. The tricky part are the additional requirements placed on the system: the beams should preferably

have an uniform intensity, the overall efficiency of the device should be as high as possible and there should not be any significant leakage of radiation in directions other than those we want. For practical reasons, it is also desirable that the intensity along the propagation direction of the original beam (the so called zeroth order) is minimal. All these constraints make the task of designing the beam splitter significantly more difficult.

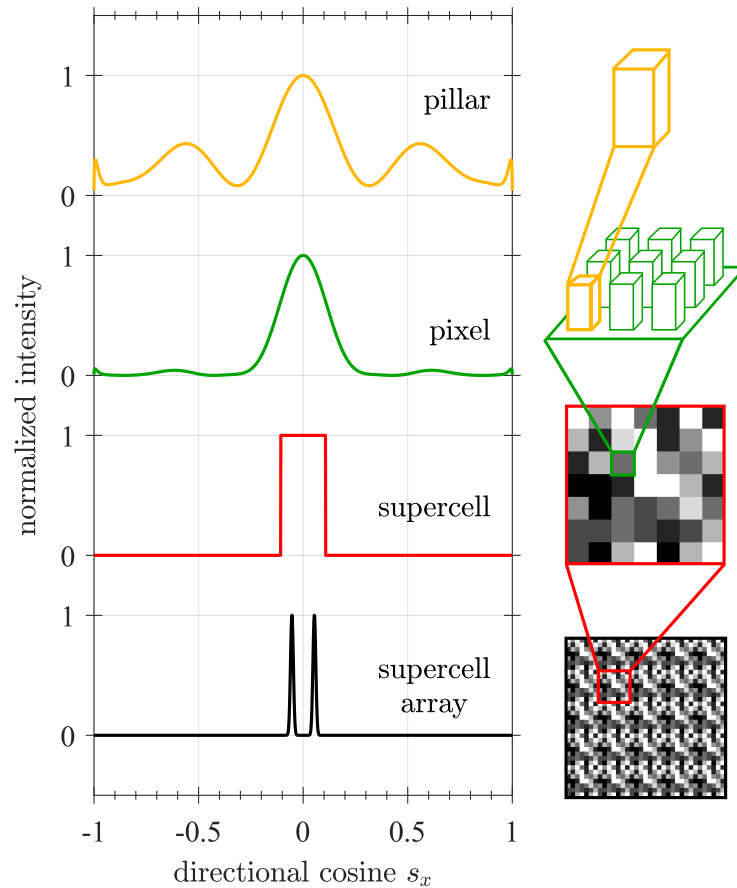


Figure 2.4: The inner structure of a metasurface for the beam array generation can be broken down into four levels. By grouping several building blocks (yellow) of the same type into a pixel (green), one can suppress the emission of radiation into directions corresponding to high declination angles. An assembly of pixels—each housing a single type of a building block—forms a supercell (red) with a far-field profile in the shape of a rectangular window. Finally, periodic repetition of the supercell (black) leads to a grating effect with regularly spaced spikes in the angular spectrum corresponding to our beam array. The spacing between the individual spikes is set through the size of the supercell, while their sharpness is determined by the number of supercells that are illuminated by the incident beam. Note that the use of the “pixel” level is not strictly necessary, we introduced it to have control over the number of free parameters in our optimization scheme.

The standard approach to solving this problem is to divide the metasurface into periodically repeating supercells [44]—the periodicity ensures the formation of beams with constant angular separation, while the inner features of the supercell are designed to yield a far-field profile in the shape of a rectangular function. The combination of those two then leads to the desired array with equally strong beams and no radiation outside the area bounded by the rectangular window. Let us for a moment forget about the suppression of the zeroth order, we shall return back to that point later on. This concept of synthesizing the far-field response of our metasurface by structuring intelligently its composition, starting at the level of individual pillars and ending with the complete optical element, is illustrated

2.2. TAILORING THE FAR-FIELD RESPONSE OF METASURFACES

in Figure 2.4. Note that apart from dividing the metasurface into supercells and building blocks, we also introduce an intermediate “pixel” level that allows us to control the computational complexity of the optimization procedure for finding the ideal metasurface design satisfying our requirements.

Regarding the mathematical description of the angular spectrum generated by the metasurface and its sub-elements, it is convenient to express it in terms of the directional cosines s_x , s_y and s_z defined as

$$s_x = \frac{x}{r} = \frac{q_x}{k} = \cos \varphi \sin \theta, \quad (2.11)$$

$$s_y = \frac{y}{r} = \frac{q_y}{k} = \sin \varphi \sin \theta, \quad (2.12)$$

$$s_z = \frac{z}{r} = \frac{k_z}{k} = \sqrt{1 - s_x^2 - s_y^2} = \cos \theta, \quad (2.13)$$

where φ designates the azimuthal and θ the declination angle. For completeness, we list also the other possible representations based on the position vector $\vec{r} = (x, y, z)$ and the propagation vector $\vec{k} = (q_x, q_y, k_z)$. Note that the z -component of the propagation vector is implicitly assumed to be positive, since throughout this section, we shall be working exclusively in the $z > 0$ halfspace (we set the $z = 0$ plane at the upper substrate surface supporting the metasurface).

Invoking once again the relation linking the far-field to the Fourier components of the near field

$$\vec{E}^\uparrow(s_x, s_y) = -2\pi i k s_z \frac{e^{ikr}}{r} \vec{E}^\uparrow(s_x k, s_y k, 0), \quad (2.14)$$

and employing the Green’s function formalism, we find the distribution of the electric field in the upper (\uparrow) hemisphere spanned by the unit vector \vec{s} to be

$$\vec{E}^\uparrow(\vec{q}, z) = 4\pi^2 \int dz' \vec{G}(\vec{q}, z, z') \vec{P}(\vec{q}, z'), \quad (2.15)$$

where $\vec{G}(\vec{q}, z, z')$ designates the dyadic Green’s function and $\vec{P}(\vec{q}, z)$ stands for the Fourier transform of the polarization current distribution $\vec{P}(\vec{r})$ induced within the metasurface. Considering its structured nature, we can break the current distribution down to the level of its smallest constituents, the individual building blocks. Using the cascade of position vectors displayed in Figure 2.5, $\vec{P}(\vec{r})$ can be written as

$$\vec{P}(\vec{r}) = \sum_{jmn} \vec{P}_n(\vec{r}_\parallel - \vec{r}_j - \vec{r}_n - \vec{r}_m, z), \quad (2.16)$$

with $\vec{P}_n(\vec{r}_\parallel)$ representing the polarization current flowing within one of the M^2 pillars occupying the n -th pixel inside the j -th supercell.

As a consequence, $\vec{P}(\vec{q}, z)$ becomes a product of sums over exponential factors that can be traced back to the various levels of the metasurface structure

$$\begin{aligned} \vec{P}(\vec{q}, z) &= \frac{1}{4\pi^2} \iint_{-\infty}^{\infty} d\vec{r}_\parallel^2 e^{-i\vec{q}\cdot\vec{r}_\parallel} \sum_{jmn} \vec{P}_n(\vec{r}_\parallel - \vec{r}_j - \vec{r}_n - \vec{r}_m, z) = \\ &= \underbrace{\sum_j e^{-i\vec{q}\cdot\vec{r}_j}}_{\text{supercell}} \underbrace{\sum_n e^{-i\vec{q}\cdot\vec{r}_n}}_{\text{supercell}} \underbrace{\sum_m e^{-i\vec{q}\cdot\vec{r}_m}}_{\text{pixel}} \underbrace{\vec{P}_n(\vec{q}, z)}_{\text{pillar}}. \end{aligned} \quad (2.17)$$

2.2. TAILORING THE FAR-FIELD RESPONSE OF METASURFACES

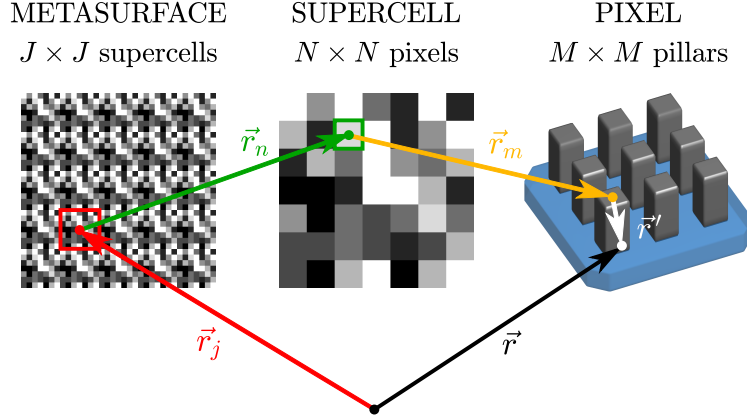


Figure 2.5: Definition of the cascade of position vectors used to specify the sites of the various entities within the structural hierarchy of our metasurface. The current distribution extracted from the FDTD simulations of individual building blocks is expressed relatively to their centers (\vec{r}'). In the global reference frame, this amounts to $\vec{r}' = \vec{r}_{\parallel} - \vec{r}_j - \vec{r}_n - \vec{r}_m$ and $z' = z$.

Its insertion into Equation (2.15) finally yields an expression for the electric field

$$\begin{aligned} \vec{E}^\dagger(\vec{q}, z) &= 4\pi^2 \int dz' \vec{G}(\vec{q}, z, z') \sum_j e^{-i\vec{q}\cdot\vec{r}_j} \sum_n e^{-i\vec{q}\cdot\vec{r}_n} \sum_m e^{-i\vec{q}\cdot\vec{r}_m} \vec{P}_n^\dagger(\vec{q}, z') = \\ &= \sum_j e^{-i\vec{q}\cdot\vec{r}_j} \sum_n e^{-i\vec{q}\cdot\vec{r}_n} \sum_m e^{-i\vec{q}\cdot\vec{r}_m} \vec{E}_n^\dagger(\vec{q}, z), \end{aligned} \quad (2.18)$$

that has the form of a discrete Fourier transform and is therefore suitable for the calculations aimed at finding the optimal supercell design.

Before we get to this point, we should first address the procedure for obtaining the electric field $\vec{E}_n^\dagger(s_x, s_y)$ generated by the individual building blocks, which were, in this particular application, titanium dioxide pillars on top of a SiO_2 substrate. Utilizing the advanced simulation setup accounting for the interaction of the pillars with their immediate neighbours (the finer points of this approach are outlined in [Introduction](#)), we calculated the current distribution induced within pillars with a square base (to ensure isotropic response), constant height of $H = 600$ nm, and width ranging from 100 to 300 nm with a step of 5 nm. The spacing between the pillars included in the FDTD simulations (we used 3×3 arrays) was set to $\Lambda = 400$ nm, i.e. the same value as in the future metasurface. The layout of the simulated structures is for convenience displayed in Figure 2.6(a).

There is one thing we have completely disregarded so far and that is the field $\vec{E}_0^\dagger(\vec{r})$ of the original wave illuminating the metasurface and propagating further along the optical axis. For our calculations to be correct, we have to incorporate it into the above analysis. As it turns out, the remedy is rather simple and straightforward, since our approach based on the current distribution instead of fields allows us to easily decouple the scattered field from the driving field. Let us, for a moment, imagine the upper surface of the substrate supporting the metasurface as a regular array of square apertures (each with area Λ^2) smoothly sewn together. If we decide to focus on only one of these apertures (essentially a single unit cell of the metasurface) and blind the rest, the driving electric field within the $z = 0$ plane reads

$$\vec{E}_0^\dagger(x, y, 0) = \vec{E}_0^\dagger \text{rect}\left(\frac{x}{\Lambda}\right) \text{rect}\left(\frac{y}{\Lambda}\right), \quad (2.19)$$

with the rectangular function $\text{rect}(x)$ defined by Equation (I.5). Note that we implicitly assume the driving field to be roughly constant within one unit cell of the metasurface. As long as the beam

2.2. TAILORING THE FAR-FIELD RESPONSE OF METASURFACES

width is much larger than Λ , this simplification is perfectly justifiable. Also, by adding together the contributions—properly weighted, of course—from all the illuminated unit cells, one should recover the original beam profile. Anyway, recalling that in the reciprocal space, the rectangular function translates into the sinc function

$$\begin{aligned}\vec{E}_0^\uparrow(\vec{q}, 0) &= \frac{\vec{E}_0^\uparrow}{4\pi^2} \int_{-\infty}^{\infty} dx \int_{-\infty}^{\infty} dy \operatorname{rect}\left(\frac{x}{\Lambda}\right) \operatorname{rect}\left(\frac{y}{\Lambda}\right) e^{-iq_x x} e^{-iq_y y} = \frac{\vec{E}_0^\uparrow}{4\pi^2} \int_{-\frac{\Lambda}{2}}^{\frac{\Lambda}{2}} dx \int_{-\frac{\Lambda}{2}}^{\frac{\Lambda}{2}} dy e^{-iq_x x} e^{-iq_y y} = \\ &= \vec{E}_0^\uparrow \frac{\Lambda^2}{4\pi^2} \operatorname{sinc}\left(\frac{q_x \Lambda}{2}\right) \operatorname{sinc}\left(\frac{q_y \Lambda}{2}\right),\end{aligned}\quad (2.20)$$

we obtain the following expression for the contribution of the driving wave to the far-field from a single unit cell of the metasurface

$$\vec{E}_0^\uparrow(s_x, s_y) = \vec{E}_0^\uparrow \frac{-i\Lambda^2}{2\pi} k s_z \frac{e^{ikr}}{r} \operatorname{sinc}\left(\frac{s_x k \Lambda}{2}\right) \operatorname{sinc}\left(\frac{s_y k \Lambda}{2}\right). \quad (2.21)$$

If we now add it to the field scattered by a single pillar with a current distribution $\vec{P}_n(\vec{r})$, the total field generated by one unit cell becomes

$$\vec{E}_n^\uparrow(s_x, s_y) = -2\pi i k s_z \frac{e^{ikr}}{r} \left[\vec{E}_0^\uparrow \frac{\Lambda^2}{4\pi^2} \operatorname{sinc}\left(\frac{s_x k \Lambda}{2}\right) \operatorname{sinc}\left(\frac{s_y k \Lambda}{2}\right) + 4\pi^2 \int_0^H dz' \vec{G}(k\vec{s}_\parallel, 0, z') \vec{P}_n(k\vec{s}_\parallel, z') \right]. \quad (2.22)$$

We should stress the importance of breaking down the driving field into separate contributions for each unit cell: it puts the scattered field into perspective and allows us to quantify the transmission efficiency of the individual pillars. In other words, we could have introduced the illuminating beam as a whole, but then we would have no direct way to tell, how much the metasurface building blocks affect the passing electromagnetic wave (although we could still compare them between themselves).

On that note, we plot in Figure 2.6(b) the relative field amplitudes generated in the $\vec{s}_\parallel = \vec{0}$ direction by the assortment of titanium dioxide pillars with widths ranging between 100 and 300 nm (from now on, we presume the driving field to be a part of the pillar field, even though we do not explicitly state it). The roughly circular distribution of the field amplitudes in the complex plane signifies that we should be able, at least in theory, to cover the full 0 to 2π range with a set of structures that are feasible to fabricate in reality. As for the transmission efficiency, the magnitude of the relative field amplitudes oscillating around 1 promises a potentially good overall efficiency of the whole metasurface. One could argue that transmission efficiency larger than 1 is a cause for alarm, yet it is not so—the pillars can effectively reduce the dielectric contrast between the SiO₂ substrate and the air and consequently suppress the reflections and power loss that the incident wave experiences at this interface.

Before we proceed with the description of our approach to finding the layout of a metasurface that would act as a fan-out element, it remains to clarify three things. Firstly, we evaluated the field amplitude only in the $\vec{s}_\parallel = \vec{0}$ direction because the angular separation between the diffracted beams is in practice usually very small (e.g. 0.1 degrees) and we can therefore adopt the paraxial approximation (assuming we use sufficiently large pixels to quench any parasitic side lobes that could appear at higher declination angles as a result of this simplification). Secondly, the requirement to suppress the zeroth order beam implies certain constraints to the inner structure of our metasurface. Inspection of Eq. (2.18) reveals that for the electric field in the $\vec{s}_\parallel = \vec{0}$ direction to be zero, the contributions from individual building blocks have to completely cancel each other out. An elegant solution to this problem is to have two supercells with an exactly opposite phase profile (but that are

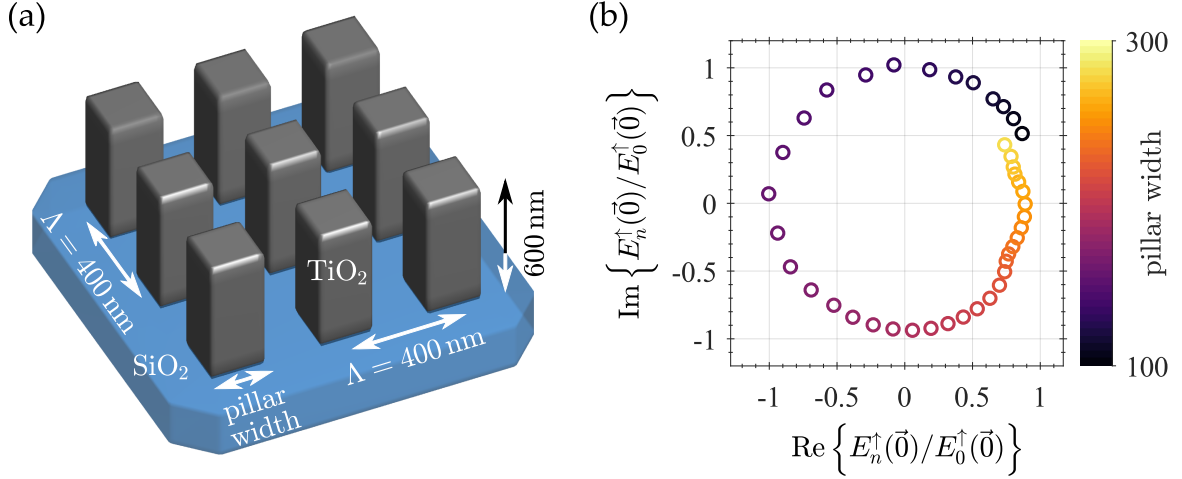


Figure 2.6: (a) Geometrical layout of titanium dioxide pillars in our FDTD simulations aimed at creating a database of building blocks for metasurfaces. By using a small 3×3 array in which only the central pillar is being illuminated by a plane wave source, one can account for the interaction of a pillar with its immediate neighbours. (b) Relative electric field amplitudes generated in the $\vec{s}_{\parallel} = \vec{0}$ direction by titanium dioxide pillars placed on top of a semi-infinite SiO_2 substrate. The width of the pillars was varied in the range between 100 and 300 nm, while their height was set identically to 600 nm. The visualization in the complex plane allows for a direct mutual comparison of the pillars both in terms of the strength (the radial distance from the origin) and the phase (the angular position) of the electromagnetic waves they emit. The chosen spectrum of pillars spans the whole 0 to 2π interval, granting the full phase modulation capacity to our metasurface designs.

otherwise identical) and tile with them the metasurface in a chessboard fashion. That way, the sum over the exponential factors associated with the supercell array will yield a Dirac comb profile with zero in its center. Finally, in order to keep the discussion clear and simple, we have withheld one important information regarding the far-field profile of a solitary supercell: the rectangular window does not have to be rectangular at all. Or more precisely, we need to adhere to the rectangular profile only in those scattering directions that will not become suppressed due to the periodical nature of our metasurface (see Figure 2.4 for better understanding of this point). Luckily for us, the discrete Fourier transform (DFT) inherently works under the assumption of periodical arrangement. Thus, as long as we set up correctly the grid of points (s_x, s_y) in which the DFT is evaluated so that it matches the angular distribution of our beam array, we do not need to be overly concerned about this fact.

The DFT and its numerical implementation in the form of the fast Fourier transform (FFT) lie at the core of many algorithms developed for finding the optimal distribution of phase within metasurfaces, e.g. the Gerchberg-Saxton algorithm and its numerous variants [45, 46]. In the end, we decided to employ a different method, namely the parallel recombination simulated annealing (PRSA) [44] which combines a genetic algorithm with a decision routine that is gradually adjusted throughout the evolution process and its formulation originates in the cooling process encountered in annealing of materials. As any other technique, PRSA has both its virtues and its faults. On one hand, it allows us to define a figure of merit (FOM) function that integrates all the various requirements such as the overall efficiency, uniformity, and suppression of the zeroth order. Furthermore, unlike some of the other algorithms, it is impervious to the inadvertent relaxation of the optimization process into a local minimum (we strive for the global one, naturally). On the other hand, as the genom of an object becomes larger—one supercell of our metasurface contains over 10^4 pixels corresponding to a genom of the same size—so does the number of iterations and the population size that are necessary for thorough exploration of the vast parameter space formed by all the possible genetical combinations. Having a database with 41 different pillars, this amounts to hardly imaginable 41^{10^4} unique pixel

2.2. TAILORING THE FAR-FIELD RESPONSE OF METASURFACES

configurations. Fortunately for us, the beam splitter possesses a 90 degree rotational symmetry that permits us to decompose its 2D phase profile into the superposition of two identical and mutually independent 1D phase profiles along the x and y axes. That reduces the previous enormous number to a more manageable level tallying “only” 41^{10^2} of possible genetical combinations.

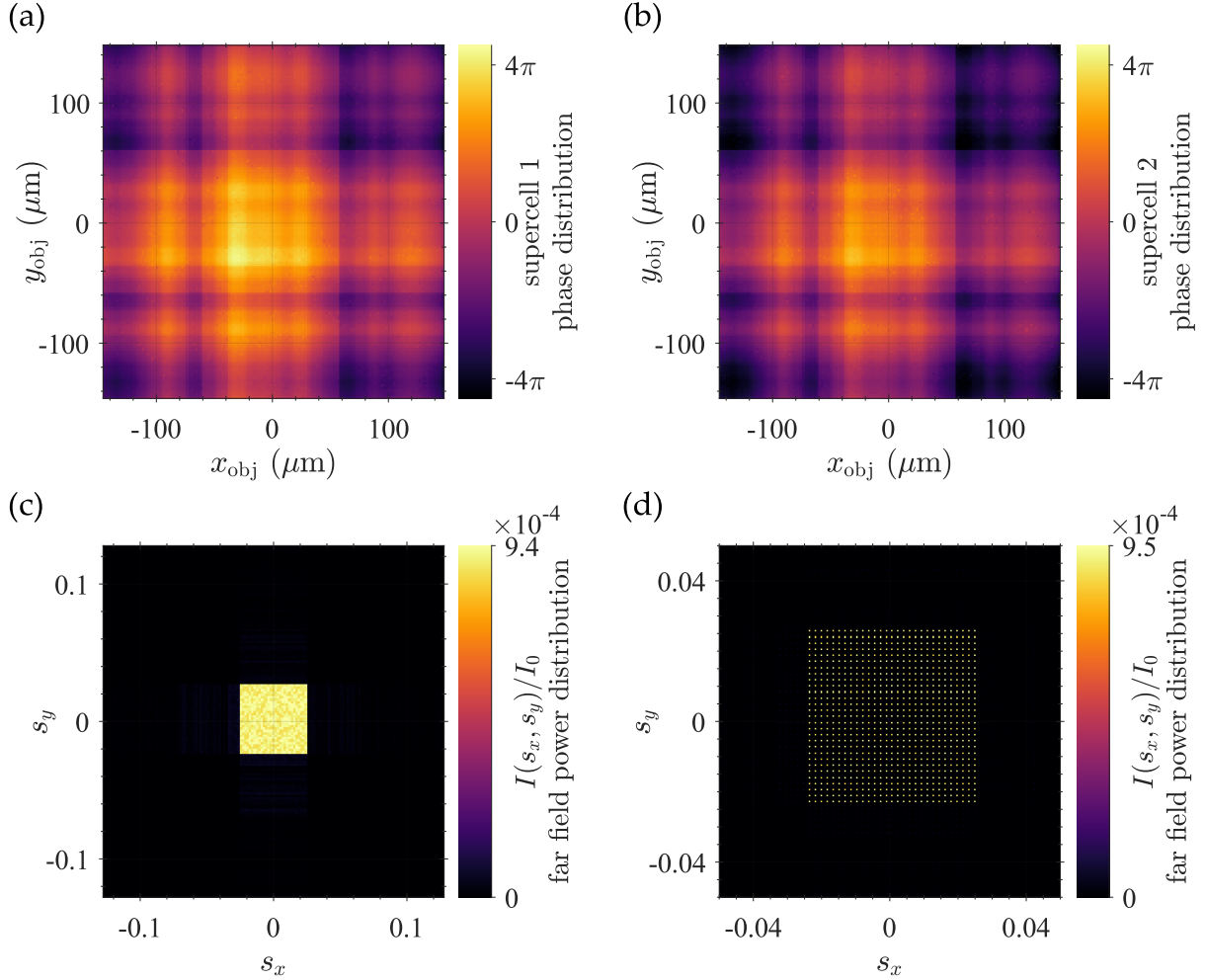


Figure 2.7: (a,b) Distribution of the phase within the two supercells constituting the metasurface for beam array generation. The phase was unwrapped to yield a continuous 2D profile, but upon reversing this step, one can map it directly onto the discrete phase distribution presented in Figure 2.6(b). The two phase maps clearly resemble each other, the only apparent difference between them being the overall π phase shift necessary for suppression of the zeroth diffraction order. (c) The far-field profile generated by either of these two supercells has the desired form of a rectangular window with only slight deviations from the ideal rectangular shape, visible at close inspection. (d) Their chessboard arrangement then yields the 28×28 beam array with a 0.1 degree angular separation and a 76% overall energy conversion efficiency.

Without delving into the finer details of our rendition of PRSA, we present in Figure 2.7 the optimized phase distribution within the two supercells constituting our metasurface. Note that due to the variations in the magnitudes of the electric field amplitudes generated by individual TiO_2 pillars and their nonlinear phase distribution within the 0 to 2π interval, the two supercells cannot be derived from each other simply by adding π to their phase distribution. Instead, a more sophisticated approach involving minor adjustments to the FOM function needs to be adopted. More specifically, the two

supercells are optimized separately and the π difference in their phase profiles is ensured by imposing a severe penalty on the FOM of supercell pairs that do not comply with this constraint.

At last, panels (c) and (d) in Figure 2.7 show the 2D far-field power distributions generated by a single supercell and the whole metasurface assembled from the two supercell types using the chessboard arrangement. Our optimization procedure yielded a 28×28 beam array with roughly 76% conversion efficiency, high degree of uniformity and less than 0.13% of the original power transmitted in the $\vec{s}_{\parallel} = \vec{0}$ direction. One can hardly expect from the fabricated metasurface to exceed these theoretical values. If acting as an optical element with a sole purpose of diffracting light into a beam array, our metasurface probably cannot outperform the already existing devices. As we have stated at the beginning, the situation might be different, if our intention was to replace several lossy elements at once and the metasurface could serve a multi-purpose role.

To conclude this section, we successfully utilized the technique combining the Green’s function formalism with FDTD simulations of individual building blocks for designing a metasurface that upon illumination produces a regular beam array with predefined properties. This type of an optical element is rather common and there are quite many publications dealing with its design, including those based on metasurfaces [47]. That perhaps questions the novelty of this work and the impact it carries. It should be, however, perceived in the larger context of our extensive efforts to acquire the know-how necessary for development and subsequent fabrication of advanced dielectric metasurfaces with novel functionality.

2.3. Multipole expansion in stratified media

The analysis of far-field radiation patterns generated by light-scattering objects is often discussed in terms of the multipole expansion [48, 49], i.e. decomposition of the field into contributions from individual multipole moments. It facilitates the classification of modes excited in particles and often provides a valuable insight into the mechanisms governing certain effects, e.g. the Kerker effect [50, 51], in which various multipole moments mutually interfere, causing an object to radiate preferentially into one direction.

In free space, there is a direct relationship between the multipoles induced within an object and the far-field patterns they generate. Namely, to each multipole moment, we can assign exactly one of the vector spherical harmonics $\vec{Y}_l^m(\varphi, \theta)$. This set of functions—see Appendix B for their detailed definition—forms a complete basis in the spherical coordinate system and represents a standard mathematical tool for the description of vector fields in physics. The introduction of a substrate spoils this straightforward relationship and one vector spherical harmonics can be assigned to numerous multipole moments. Employing the plane wave decomposition of vector spherical harmonics [52] in combination with the matrix formalism describing the wave propagation in stratified media (presented in Appendix A), we evaluate in the paragraphs below the reflections experienced by the individual multipoles due to the presence of a general multilayer substrate with parallel planar interfaces and demonstrate the capabilities of this whole apparatus on one particular example, the multipole expansion of the field scattered by a diabolo cross-dimer [53].

The individual multipole moments can be calculated directly from the current distribution using relatively simple formulas [54]. This approach has, however, one drawback: it cannot be applied to inverted structures, i.e. apertures in otherwise homogeneous films. This is due to the unbounded nature of the currents flowing within the films—they can extend over a very large area, especially in metallic layers supporting surface plasmon polaritons (SPPs). In the light of the fact that SPPs do not radiate into the far-field, one could, in principle, use some form of adiabatic truncation, artificially limiting the integration volume involved in the calculation of the multipole moments. Instead, we propose a “cleaner” method treating apertures as particles embedded inside dielectric (or possibly metallic) layers. Furthermore, the multipole moments should not be determined directly from the current distribution, but rather from the generated far-field pattern, or to be more precise, the far-

field pattern that would be produced by the investigated structure (i.e. the aperture including the film) if it was located in a free space. This approach elegantly dodges the issue of the unbounded currents by switching the roles of the aperture and the film, perceiving the former as the actual place, where the currents are flowing. At the same time, this concept is fully compatible with the aforementioned matrix formalism and can be utilized for the multipole analysis of complex structures (such as the diabolo cross-dimer, for example).

Let us start the derivation of the expressions quantifying the contributions of individual multipole moments to the far-field in the presence of a substrate by writing down their free space counterparts. Adopting the mathematical notation employed in [54], the angular distribution of the electric field $\vec{E}_{\text{FF}}(\varphi, \theta)$ generated by the first four multipoles at the distance r from the origin reads

$$\vec{E}_{\text{FF}}(\varphi, \theta) = \frac{k_0^2}{4\pi\epsilon_0} \frac{e^{ik_0r}}{r} \left[\vec{n} \times (\vec{p}^e \times \vec{n}) + \frac{1}{c} (\vec{p}^m \times \vec{n}) - \frac{ik_0}{6} \vec{n} \times (\vec{Q}^e \times \vec{n}) - \frac{ik_0}{6c} (\vec{Q}^m \times \vec{n}) \right], \quad (2.23)$$

where k_0 stands for the free space wavenumber and \vec{n} represents the unit vector pointing from the origin towards the position at which the field is being evaluated. As for the rest of the symbols appearing in the above equation, \vec{p} denotes the dipole moment and we use the two superscripts to indicate its electric (^e) or magnetic (^m) nature. Similarly, the auxiliary vectors \vec{Q}^e and \vec{Q}^m can be related to the electric and magnetic quadrupole moments. We refrained from including higher multipole moments, since their presence would needlessly clutter the discussion, without bringing any valuable insight to the matter. Anyway, the general formulation of our rendition of the multipole expansion permits their straightforward incorporation during the last stage of the derivation.

While the electric and magnetic dipole moments

$$\vec{p}^{e/m} = \begin{bmatrix} p_x^{e/m} \\ p_y^{e/m} \\ p_z^{e/m} \end{bmatrix} \quad (2.24)$$

appear in the above expression for the angular distribution of the electric field directly, the quadrupole moments

$$\vec{Q}^{e/m} = \begin{bmatrix} Q_{xx}^{e/m} & Q_{xy}^{e/m} & Q_{xz}^{e/m} \\ Q_{xy}^{e/m} & Q_{yy}^{e/m} & Q_{yz}^{e/m} \\ Q_{xz}^{e/m} & Q_{yz}^{e/m} & Q_{zz}^{e/m} \end{bmatrix} \quad (2.25)$$

enter it via the auxiliary vectors $\vec{Q}^{e/m}$, defined as

$$Q_\alpha^{e/m} = \sum_\beta Q_{\alpha\beta}^{e/m} n_\beta. \quad (2.26)$$

Note that in the above definition of the quadrupole moments, we have fully embraced their symmetric nature, in other words $Q_{yx}^{e/m} = Q_{xy}^{e/m}$, $Q_{zx}^{e/m} = Q_{xz}^{e/m}$, and $Q_{zy}^{e/m} = Q_{yz}^{e/m}$. Considering the fact that far away from the origin, the electric field is always orthogonal to the propagation direction, i.e. $\vec{E}_{\text{FF}} \perp \vec{n}$, it is more convenient to operate in the spherical coordinate system instead of the Cartesian one. The two are related via

$$\hat{r} = \begin{bmatrix} \cos \varphi \sin \theta \\ \sin \varphi \sin \theta \\ \cos \theta \end{bmatrix} \equiv \vec{n}, \quad (2.27)$$

$$\hat{\varphi} = \begin{bmatrix} -\sin \varphi \\ \cos \varphi \\ 0 \end{bmatrix}, \quad (2.28)$$

$$\hat{\theta} = \begin{bmatrix} \cos \varphi \cos \theta \\ \sin \varphi \cos \theta \\ -\sin \theta \end{bmatrix}. \quad (2.29)$$

Consequently, the electric field generated by the electric dipole moment can be rewritten in the following concise form

$$\begin{bmatrix} E_r \\ E_\varphi \\ E_\theta \end{bmatrix} \sim \vec{n} \times (\vec{p}^e \times \vec{n}) = \vec{n} \times \begin{bmatrix} 0 \\ -p_\theta^e \\ p_\varphi^e \end{bmatrix} = \begin{bmatrix} 0 \\ p_\varphi^e \\ p_\theta^e \end{bmatrix}, \quad (2.30)$$

where p_φ^e and p_θ^e correspond to the projections of \vec{p}^e onto the basis vectors of the spherical coordinate system

$$p_\varphi^e = \vec{p}^e \cdot \hat{\varphi} = -p_x^e \sin \varphi + p_y^e \cos \varphi, \quad (2.31)$$

$$p_\theta^e = \vec{p}^e \cdot \hat{\theta} = p_x^e \cos \varphi \cos \theta + p_y^e \sin \varphi \cos \theta - p_z^e \sin \theta \quad (2.32)$$

Similar treatment can be applied also to the rest of the terms occurring in the multipole expansion given by Eq. (2.23), namely

$$\vec{p}^m \times \vec{n} = \begin{bmatrix} 0 \\ -p_\theta^m \\ p_\varphi^m \end{bmatrix}, \quad (2.33)$$

$$\vec{n} \times (\vec{Q}^e \times \vec{n}) = \begin{bmatrix} 0 \\ Q_\varphi^e \\ Q_\theta^e \end{bmatrix}, \quad (2.34)$$

$$\vec{Q}^m \times \vec{n} = \begin{bmatrix} 0 \\ -Q_\theta^m \\ Q_\varphi^m \end{bmatrix}, \quad (2.35)$$

with

$$p_\varphi^m = -p_x^m \sin \varphi + p_y^m \cos \varphi, \quad (2.36)$$

$$p_\theta^m = p_x^m \cos \varphi \cos \theta + p_y^m \sin \varphi \cos \theta - p_z^m \sin \theta, \quad (2.37)$$

$$Q_\varphi^{e/m} = (Q_{yy}^{e/m} - Q_{xx}^{e/m}) \frac{1}{2} \sin 2\varphi \sin \theta + Q_{xy}^{e/m} \cos 2\varphi \sin \theta + Q_{yz}^{e/m} \cos \varphi \cos \theta - Q_{xz}^{e/m} \sin \varphi \cos \theta, \quad (2.38)$$

$$Q_\theta^{e/m} = (Q_{xx}^{e/m} \cos^2 \varphi + Q_{yy}^{e/m} \sin^2 \varphi + Q_{xy}^{e/m} \sin 2\varphi - Q_{zz}^{e/m}) \sin \theta \cos \theta + (Q_{xz}^{e/m} \cos \varphi + Q_{yz}^{e/m} \sin \varphi) \cos 2\theta. \quad (2.39)$$

As we have outlined at the beginning, it is our intention to determine the multipole moments induced within an object from the far-field pattern it would generate in free space. Let us assume that the investigated object—it can be a particle or an aperture in an otherwise homogeneous film—is fully contained within a region bounded by two parallel planes designated as z^\downarrow and z^\uparrow . Furthermore, let us express the far-field relatively to the z^\uparrow plane located right in the center of the region. The layout

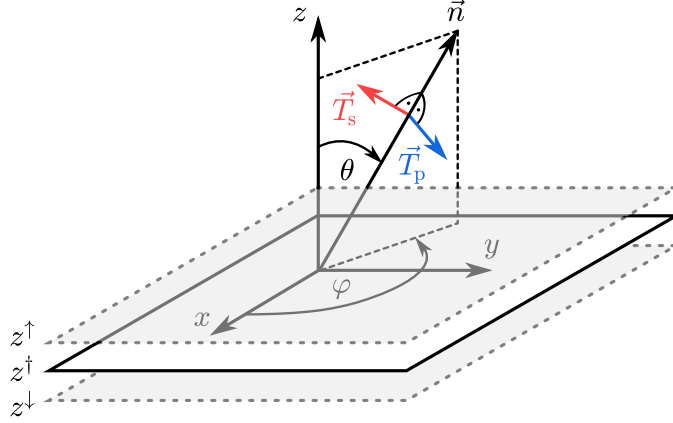


Figure 2.8: Layout of the coordinate system used for the calculation of the multipole moments. The object is fully contained within a source region bounded by two parallel planes z^\downarrow and z^\uparrow and the electric field $\vec{T}(\vec{q}, z)$ —we work with its projection onto the spherical basis vectors—is evaluated with respect to the z^\uparrow plane located in the center of the source region.

of the situation is schematically depicted in Figure 2.8. It should be stressed that for the moment, we ignore any other structures, a substrate or a superstrate surrounding the object of our interest. We tear it out, figuratively speaking, from the whole system, put it into free space and then study its far-field pattern. We shall eventually put it back into its original environment, but only after we calculate its multipole expansion.

Recalling Equation (I.1) linking the far-field to the angular spectrum representation of the near-field [2], the Fourier components of the electric field $\vec{T}^{\uparrow/\downarrow}(\vec{q}, z)$ in the upper (\uparrow) and the lower (\downarrow) halfspaces read

$$\vec{T}^{\uparrow/\downarrow}(\vec{q}, z) = \frac{r e^{-ik_0 r}}{-2\pi i k_{z0}} \vec{E}_{\text{FF}} \left(\frac{q_x}{k_0}, \frac{q_y}{k_0} \right) e^{ik_{z0}|z-z^\dagger|} = \frac{ik_0^2}{8\pi^2 \varepsilon_0 k_{z0}} e^{ik_{z0}|z-z^\dagger|} \left[\vec{n} \times (\vec{p}^e \times \vec{n}) + \dots \right], \quad (2.40)$$

where all the vectors in the square brackets should be expressed in terms of the lateral components of the propagation vector \vec{k} . For completeness, we provide below their definition with respect to the spherical coordinate system

$$q = k_0 \sin \theta, \quad (2.41)$$

$$q_x = k_0 \cos \varphi \sin \theta, \quad (2.42)$$

$$q_y = k_0 \sin \varphi \sin \theta, \quad (2.43)$$

$$k_{z0} = \pm k_0 \cos \theta. \quad (2.44)$$

Note that the plus sign in the vertical component of the propagation vector applies to the upper halfspace, while the minus sign to the lower one.

The electric field $\vec{T}^{\uparrow/\downarrow}(\vec{q}, z^{\uparrow/\downarrow})$ generated by the object at the borders of the region bounded by the $z^{\uparrow/\downarrow}$ planes can be calculated from the current distribution using the framework presented in Appendix A. Denoting by $E_{\text{src}}^{\pm s/p}$ the s- and p-polarized components of the upward (+) and downward (−) propagating waves emitted by the currents within the source region (\dagger), we find that

$$\vec{T}^\uparrow(\vec{q}, z^\uparrow) = \begin{bmatrix} T_s^\uparrow(\vec{q}, z^\uparrow) \\ T_p^\uparrow(\vec{q}, z^\uparrow) \end{bmatrix} = \begin{bmatrix} \dagger t_s^{\uparrow\uparrow}(\vec{q}) E_{\text{src}}^{+s}(\vec{q}) + \dagger t_s^{\uparrow\downarrow}(\vec{q}) E_{\text{src}}^{-s}(\vec{q}) \\ \dagger t_p^{\uparrow\uparrow}(\vec{q}) E_{\text{src}}^{+p}(\vec{q}) + \dagger t_p^{\uparrow\downarrow}(\vec{q}) E_{\text{src}}^{-p}(\vec{q}) \end{bmatrix}, \quad (2.45)$$

$$\vec{T}^\downarrow(\vec{q}, z^\downarrow) = \begin{bmatrix} T_s^\downarrow(\vec{q}, z^\downarrow) \\ T_p^\downarrow(\vec{q}, z^\downarrow) \end{bmatrix} = \begin{bmatrix} \dagger t_s^{\downarrow\uparrow}(\vec{q}) E_{\text{src}}^{+s}(\vec{q}) + \dagger t_s^{\downarrow\downarrow}(\vec{q}) E_{\text{src}}^{-s}(\vec{q}) \\ \dagger t_p^{\downarrow\uparrow}(\vec{q}) E_{\text{src}}^{+p}(\vec{q}) + \dagger t_p^{\downarrow\downarrow}(\vec{q}) E_{\text{src}}^{-p}(\vec{q}) \end{bmatrix}, \quad (2.46)$$

with the transmission coefficients $\dagger t_{s/p}^{\uparrow\uparrow}(\vec{q})$, $\dagger t_{s/p}^{\downarrow\uparrow}(\vec{q})$, $\dagger t_{s/p}^{\uparrow\downarrow}(\vec{q})$, and $\dagger t_{s/p}^{\downarrow\downarrow}(\vec{q})$ accounting for all the reflections experienced by the waves before they leave the source region and propagate freely. Without going into unnecessary details (for those we refer the reader to [Appendix A](#)), the most efficient and convenient way of determining these coefficients is to view the propagation of electromagnetic waves inside a stratified medium as a linear transformation between various states. In this particular case of a free standing source region, we have

$$\begin{bmatrix} E_\dagger^+ \\ E_\dagger^- \end{bmatrix} + \begin{bmatrix} E_{\text{src}}^+ \\ 0 \end{bmatrix} = \tilde{P}_\dagger^{-1} \tilde{M}_{\dagger 0} \begin{bmatrix} T^\uparrow \\ 0 \end{bmatrix} = \begin{bmatrix} u_{11} & u_{12} \\ u_{21} & u_{22} \end{bmatrix} \begin{bmatrix} T^\uparrow \\ 0 \end{bmatrix}, \quad (2.47)$$

$$\begin{bmatrix} E_\dagger^+ \\ E_\dagger^- \end{bmatrix} + \begin{bmatrix} 0 \\ E_{\text{src}}^- \end{bmatrix} = \tilde{M}_{\dagger 0} \begin{bmatrix} 0 \\ T^\downarrow \end{bmatrix} = \begin{bmatrix} v_{11} & v_{12} \\ v_{21} & v_{22} \end{bmatrix} \begin{bmatrix} 0 \\ T^\downarrow \end{bmatrix}, \quad (2.48)$$

where the transformation matrix $\tilde{M}_{\dagger 0}$ captures the reflection process at the upper and lower boundaries of the source region, \tilde{P}_\dagger describes the propagation inside it and the field amplitudes E_\dagger^+ and E_\dagger^- sew the two equations (and incidentally also the two halfspaces) together. Their mutual subtraction then yields the sought expressions for the transmission coefficients

$$\dagger t^{\uparrow\uparrow}(\vec{q}) = \frac{v_{22}(\vec{q})}{u_{11}(\vec{q}) v_{22}(\vec{q}) - u_{21}(\vec{q}) v_{12}(\vec{q})}, \quad (2.49)$$

$$\dagger t^{\uparrow\downarrow}(\vec{q}) = \frac{v_{12}(\vec{q})}{u_{11}(\vec{q}) v_{22}(\vec{q}) - u_{21}(\vec{q}) v_{12}(\vec{q})}, \quad (2.50)$$

$$\dagger t^{\downarrow\uparrow}(\vec{q}) = \frac{u_{11}(\vec{q})}{u_{11}(\vec{q}) v_{22}(\vec{q}) - u_{21}(\vec{q}) v_{12}(\vec{q})}, \quad (2.51)$$

$$\dagger t^{\downarrow\downarrow}(\vec{q}) = \frac{u_{21}(\vec{q})}{u_{11}(\vec{q}) v_{22}(\vec{q}) - u_{21}(\vec{q}) v_{12}(\vec{q})}. \quad (2.52)$$

The key step in the process of finding the multipole moments characterizing our object is to match the multipole expansion of the electric field given by Eq. (2.40) to the above pair of Equations (2.45) and (2.46) relying on the full current distribution. Instead of using the Cartesian-based representation of the multipole moments, we shall adopt an alternative notation, in which they are viewed as coefficients in the expansion of the electric field into vector spherical harmonics. Consequently, Eq. (2.40) can be recast as

$$\vec{T}^{\uparrow/\downarrow}(\vec{q}, z^{\uparrow/\downarrow}) = \sum_{l=1}^{\infty} \sum_{m=-l}^l Q_{1lm} \vec{T}_{1lm}^{\uparrow/\downarrow}(\vec{q}, z^{\uparrow/\downarrow}) + Q_{2lm} \vec{T}_{2lm}^{\uparrow/\downarrow}(\vec{q}, z^{\uparrow/\downarrow}), \quad (2.53)$$

where the functions $\vec{T}_{1lm}^{\uparrow/\downarrow}(\vec{q}, z^{\uparrow/\downarrow})$ and $\vec{T}_{2lm}^{\uparrow/\downarrow}(\vec{q}, z^{\uparrow/\downarrow})$ stand for the angular spectrum representation of the vector spherical harmonics $\vec{Y}_l^m(\varphi, \theta)$ and $\vec{n} \times \vec{Y}_l^m(\varphi, \theta)$ (see [52] for the detailed analysis of their plane wave decomposition)

$$\vec{T}_{1lm}^{\uparrow/\downarrow}(\vec{q}, z^{\uparrow/\downarrow}) = \frac{ik_0^2}{8\pi^2\varepsilon_0 k_{z0}} e^{\pm ik_{z0}(z^{\uparrow/\downarrow} - z_{\dagger})} \vec{Y}_l^{m\uparrow/\downarrow}(\vec{q}), \quad (2.54)$$

$$\vec{T}_{2lm}^{\uparrow/\downarrow}(\vec{q}, z^{\uparrow/\downarrow}) = \frac{ik_0^2}{8\pi^2\varepsilon_0 k_{z0}} e^{\pm ik_{z0}(z^{\uparrow/\downarrow} - z_{\dagger})} \vec{n} \times \vec{Y}_l^{m\uparrow/\downarrow}(\vec{q}). \quad (2.55)$$

The definition of the vector spherical harmonics, including the expressions linking the expansion coefficients Q_{1lm} and Q_{2lm} to the Cartesian-based multipole moments can be found in [Appendix B](#). Note that the functions $\vec{Y}_l^{m\uparrow/\downarrow}(\vec{q})$ and $\vec{Y}_l^m(\varphi, \theta)$ are identical in all respects except their arguments and special care is required while working in the reciprocal space due to the ambiguity in the sign of the vertical wavevector component k_{z0} . We emphasize this fact by placing arrows in the superscript of $\vec{Y}_l^{m\uparrow/\downarrow}(\vec{q})$. We have now all ingredients necessary for the calculation of the expansion coefficients Q_{1lm} and Q_{2lm} . Exploiting the mutual orthogonality of the vector spherical harmonics

$$\int_0^{2\pi} d\varphi \int_0^\pi d\theta \sin\theta \vec{Y}_l^m(\varphi, \theta) \cdot \vec{Y}_{l'}^{m'*}(\varphi, \theta) = l(l+1) \delta_{ll'} \delta_{mm'}, \quad (2.56)$$

$$\int_0^{2\pi} d\varphi \int_0^\pi d\theta \sin\theta \left[\vec{n} \times \vec{Y}_l^m(\varphi, \theta) \right] \cdot \left[\vec{n} \times \vec{Y}_{l'}^{m'*}(\varphi, \theta) \right] = l(l+1) \delta_{ll'} \delta_{mm'}, \quad (2.57)$$

$$\int_0^{2\pi} d\varphi \int_0^\pi d\theta \sin\theta \vec{Y}_l^m(\varphi, \theta) \cdot \left[\vec{n} \times \vec{Y}_{l'}^{m'*}(\varphi, \theta) \right] = 0, \quad (2.58)$$

we find, after switching back to the spherical coordinate system and expressing the electric field $\vec{T}^{\uparrow/\downarrow}(\vec{q}, z^{\uparrow/\downarrow})$ in terms of the azimuthal and declination angles, that

$$\begin{aligned} Q_{1lm} &= \frac{1}{l(l+1)} \frac{8\pi^2\varepsilon_0}{ik_0} \int_0^{2\pi} d\varphi \int_0^{\frac{\pi}{2}} d\theta \sin\theta \cos\theta e^{-ik_0 \cos\theta(z^{\uparrow} - z_{\dagger})} \vec{T}^{\uparrow}(\varphi, \theta, z^{\uparrow}) \cdot \vec{Y}_l^{m*}(\varphi, \theta) + \\ &+ \frac{1}{l(l+1)} \frac{8\pi^2\varepsilon_0}{ik_0} \int_0^{2\pi} d\varphi \int_{\frac{\pi}{2}}^\pi d\theta \sin\theta \cos\theta e^{-ik_0 \cos\theta(z^{\downarrow} - z_{\dagger})} \vec{T}^{\downarrow}(\varphi, \theta, z^{\downarrow}) \cdot \vec{Y}_l^{m*}(\varphi, \theta), \end{aligned} \quad (2.59)$$

$$\begin{aligned} Q_{2lm} &= \frac{1}{l(l+1)} \frac{8\pi^2\varepsilon_0}{ik_0} \int_0^{2\pi} d\varphi \int_0^{\frac{\pi}{2}} d\theta \sin\theta \cos\theta e^{-ik_0 \cos\theta(z^{\uparrow} - z_{\dagger})} \vec{T}^{\uparrow}(\varphi, \theta, z^{\uparrow}) \cdot \left[\vec{n} \times \vec{Y}_l^{m*}(\varphi, \theta) \right] + \\ &+ \frac{1}{l(l+1)} \frac{8\pi^2\varepsilon_0}{ik_0} \int_0^{2\pi} d\varphi \int_{\frac{\pi}{2}}^\pi d\theta \sin\theta \cos\theta e^{-ik_0 \cos\theta(z^{\downarrow} - z_{\dagger})} \vec{T}^{\downarrow}(\varphi, \theta, z^{\downarrow}) \cdot \left[\vec{n} \times \vec{Y}_l^{m*}(\varphi, \theta) \right]. \end{aligned} \quad (2.60)$$

The general formulation of the above overlap integrals allows us to expand an electric field into multipoles of any order, all one needs is an analytical expression for the respective vector spherical harmonics. The subsequent conversion of the expansion coefficients into the Cartesian-based multipole moments can be somewhat tricky but feasible. We should point out that even though the quadrupole moment tensor has nine components, only five of them are actually linearly independent. This stems

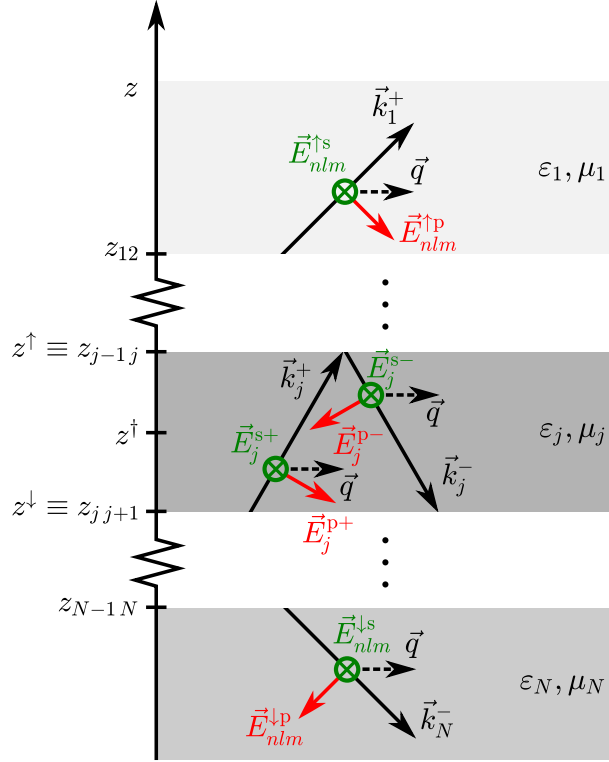


Figure 2.9: Layout of the coordinate system after the source region is reinstated back to its original position within the multilayer system as its j -th layer. The boundaries of the source region become interfaces separating it from the adjacent layers, each described by its own dielectric permittivity and magnetic permeability. The multipolar fields $\vec{E}_{nlm}^{\uparrow}(\vec{q}, z_{12})$ and $\vec{E}_{nlm}^{\downarrow}(\vec{q}, z_{N-1N})$ are obtained by propagating the waves emitted by the individual multipoles embedded within the j -th layer through the system, while accounting for all the possible reflections occurring inside it.

from the fact that for $l = 2$ (index l inherently defines the order of the multipole), there are only five possible values of the index m .

Let us recall that the investigated object is actually a part of a larger system that we have ignored for the purpose of calculating the multipole moments. For our analysis to be correct, it is now necessary to plug the object back into its original place and evaluate, how its surroundings affects the far-field patterns of the individual multipoles. Assuming the source region represents a j -th layer in the system consisting of N layers in total—the first and the last are in fact semi-infinite and correspond to the upper and lower halfspaces—each described by its own dielectric permittivity and magnetic permeability, the amplitudes of the electromagnetic waves emitted by the individual multipole moments and leaving the system have to account for all the possible reflections that could have occurred inside the multilayer system (see Figure 2.9 for its schematical representation and the definition of the coordinate system used in our analysis). Denoting z_{12} and z_{N-1N} the two interfaces separating all the various structures and substrate layers from the upper and lower halfspaces, the Fourier components of the multipolar electric field generated in these two halfspaces can be expressed as

$$\vec{E}_{nlm}^{\uparrow}(\vec{q}, z_{12}) = \begin{bmatrix} E_{nlm}^{\uparrow s}(\vec{q}, z_{12}) \\ E_{nlm}^{\uparrow p}(\vec{q}, z_{12}) \end{bmatrix} = \begin{bmatrix} t_s^{\uparrow\uparrow}(\vec{q}) T_{nlm}^{\uparrow s}(\vec{q}, z^{\uparrow}) + t_s^{\uparrow\downarrow}(\vec{q}) T_{nlm}^{\downarrow s}(\vec{q}, z^{\downarrow}) \\ t_p^{\uparrow\uparrow}(\vec{q}) T_{nlm}^{\uparrow p}(\vec{q}, z^{\uparrow}) + t_p^{\uparrow\downarrow}(\vec{q}) T_{nlm}^{\downarrow p}(\vec{q}, z^{\downarrow}) \end{bmatrix}, \quad (2.61)$$

$$\vec{E}_{nlm}^{\downarrow}(\vec{q}, z_{N-1N}) = \begin{bmatrix} E_{nlm}^{\downarrow s}(\vec{q}, z_{N-1N}) \\ E_{nlm}^{\downarrow p}(\vec{q}, z_{N-1N}) \end{bmatrix} = \begin{bmatrix} t_s^{\downarrow\uparrow}(\vec{q}) T_{nlm}^{\uparrow s}(\vec{q}, z^{\uparrow}) + t_s^{\downarrow\downarrow}(\vec{q}) T_{nlm}^{\downarrow s}(\vec{q}, z^{\downarrow}) \\ t_p^{\downarrow\uparrow}(\vec{q}) T_{nlm}^{\uparrow p}(\vec{q}, z^{\uparrow}) + t_p^{\downarrow\downarrow}(\vec{q}) T_{nlm}^{\downarrow p}(\vec{q}, z^{\downarrow}) \end{bmatrix}. \quad (2.62)$$

As before, the transmission coefficients $t_s^{\uparrow\uparrow}$, $t_s^{\downarrow\uparrow}$, $t_s^{\uparrow\downarrow}$, and $t_s^{\downarrow\downarrow}$, acting as proportionality factors between the electric fields inside the source region and the outer space, are determined from a coupled system of two equations treating the propagation inside stratified media as a linear transformation between states

$$\begin{bmatrix} E_j^+ \\ E_j^- \end{bmatrix} + \tilde{P}_j^{-1} \tilde{M}_{j0} \begin{bmatrix} T_{nlm}^{\uparrow} \\ 0 \end{bmatrix} = \tilde{P}_j^{-1} \tilde{M}_{j,j-1} \cdots \tilde{P}_2^{-1} \tilde{M}_{21} \begin{bmatrix} E_{nlm}^{\uparrow} \\ 0 \end{bmatrix} = \begin{bmatrix} q_{11} & q_{12} \\ q_{21} & q_{22} \end{bmatrix} \begin{bmatrix} E_{nlm}^{\uparrow} \\ 0 \end{bmatrix}, \quad (2.63)$$

$$\begin{bmatrix} E_j^+ \\ E_j^- \end{bmatrix} + \tilde{M}_{j0} \begin{bmatrix} 0 \\ T_{nlm}^{\downarrow} \end{bmatrix} = \tilde{M}_{j,j+1} \tilde{P}_{j+1} \cdots \tilde{M}_{N-1,N} \begin{bmatrix} 0 \\ E_{nlm}^{\downarrow} \end{bmatrix} = \begin{bmatrix} r_{11} & r_{12} \\ r_{21} & r_{22} \end{bmatrix} \begin{bmatrix} 0 \\ E_{nlm}^{\downarrow} \end{bmatrix}. \quad (2.64)$$

After several steps, we obtain the following relations

$$t^{\uparrow\uparrow}(\vec{q}) = \frac{r_{22}(\vec{q}) u_{11}(\vec{q}) - r_{12}(\vec{q}) u_{21}(\vec{q})}{q_{11}(\vec{q}) r_{22}(\vec{q}) - q_{21}(\vec{q}) r_{12}(\vec{q})}, \quad (2.65)$$

$$t^{\uparrow\downarrow}(\vec{q}) = \frac{r_{12}(\vec{q}) v_{22}(\vec{q}) - r_{22}(\vec{q}) v_{12}(\vec{q})}{q_{11}(\vec{q}) r_{22}(\vec{q}) - q_{21}(\vec{q}) r_{12}(\vec{q})}, \quad (2.66)$$

$$t^{\downarrow\uparrow}(\vec{q}) = \frac{q_{21}(\vec{q}) u_{11}(\vec{q}) - q_{11}(\vec{q}) u_{21}(\vec{q})}{q_{11}(\vec{q}) r_{22}(\vec{q}) - q_{21}(\vec{q}) r_{12}(\vec{q})}, \quad (2.67)$$

$$t^{\downarrow\downarrow}(\vec{q}) = \frac{q_{11}(\vec{q}) v_{22}(\vec{q}) - q_{21}(\vec{q}) v_{12}(\vec{q})}{q_{11}(\vec{q}) r_{22}(\vec{q}) - q_{21}(\vec{q}) r_{12}(\vec{q})}, \quad (2.68)$$

where $u_{ij}(\vec{q})$ and $v_{ij}(\vec{q})$ can be recognized as the coefficients from Eqs. (2.47) and (2.48) describing wave propagation in an isolated source region. Finally, summation over all the multipolar contributions yields the angular distribution of the total electric field in the far-field zone

$$\vec{E}_{\text{FF}}^{\uparrow}(\varphi, \theta) = -2\pi i k_1 \cos \theta \frac{e^{ik_1 r}}{r} e^{-ik_1 \cos \theta z_{12}} \sum_{nlm} Q_{nlm} \vec{E}_{nlm}^{\uparrow}(k_1 \cos \varphi \sin \theta, k_1 \sin \varphi \sin \theta, z_{12}), \quad (2.69)$$

$$\vec{E}_{\text{FF}}^{\downarrow}(\varphi, \theta) = 2\pi i k_N \cos \theta \frac{e^{ik_N r}}{r} e^{-ik_N \cos \theta z_{N-1N}} \sum_{nlm} Q_{nlm} \vec{E}_{nlm}^{\downarrow}(k_N \cos \varphi \sin \theta, k_N \sin \varphi \sin \theta, z_{N-1N}). \quad (2.70)$$

Note that once again, we invoke the link between the far-field and the Fourier representation of the near-field. We also diligently discriminate between the upper and lower halfspaces, keeping open the option of different optical properties in each. The last remark concerns the radial distance r , which is no longer measured with respect to the z^{\uparrow} plane inside the source region, but with respect to the absolute origin of the global coordinate system. This can lead to a phase shift in the fields that should be properly compensated. The exponential factors in the above equations take care of this problem in the vertical direction, but any misalignment in the lateral positions of the ‘‘source’’ and ‘‘global’’ origins would call for additional corrections.

The transition back to the Cartesian-based multipole moments can be carried out by retracing our steps and replacing the multipolar fields $T_{nlm}^{\uparrow P}(\vec{q}, z^\uparrow)$ and $T_{nlm}^{\downarrow P}(\vec{q}, z^\downarrow)$ in Eqs. (2.61) and (2.62) with their counterparts from Eq. (2.40). After embracing the spherical basis representation of the multipole moments introduced in Eqs. (2.30)–(2.39), the above two equations can be recast as

$$\vec{E}_{\text{FF}}^\uparrow(\varphi, \theta) = \begin{bmatrix} E_{\text{FF}}^{\uparrow s}(\varphi, \theta) \\ E_{\text{FF}}^{\uparrow p}(\varphi, \theta) \end{bmatrix} = \frac{k_0^2}{4\pi\epsilon_0} \frac{k_1 \cos \theta}{\sqrt{k_0^2 - k_1^2 \sin^2 \theta}} \frac{e^{ik_1 r}}{r} e^{-ik_1 \cos \theta z_{12}} e^{i\sqrt{k_0^2 - k_1^2 \sin^2 \theta}(z_{j-1j} - z_\uparrow)}$$

$$\begin{bmatrix} t_s^{\uparrow\uparrow} \left(\uparrow p_\varphi^e - \frac{1}{c} \uparrow p_\theta^m - \frac{ik_0}{6} \uparrow Q_\varphi^e + \frac{ik_0}{6c} \uparrow Q_\theta^m \right) + t_s^{\uparrow\downarrow} \left(\downarrow p_\varphi^e - \frac{1}{c} \downarrow p_\theta^m - \frac{ik_0}{6} \downarrow Q_\varphi^e + \frac{ik_0}{6c} \downarrow Q_\theta^m \right) \\ t_p^{\uparrow\uparrow} \left(\uparrow p_\theta^e + \frac{1}{c} \uparrow p_\varphi^m - \frac{ik_0}{6} \uparrow Q_\theta^e - \frac{ik_0}{6c} \uparrow Q_\varphi^m \right) + t_p^{\uparrow\downarrow} \left(\downarrow p_\theta^e + \frac{1}{c} \downarrow p_\varphi^m - \frac{ik_0}{6} \downarrow Q_\theta^e - \frac{ik_0}{6c} \downarrow Q_\varphi^m \right) \end{bmatrix}, \quad (2.71)$$

$$\vec{E}_{\text{FF}}^\downarrow(\varphi, \theta) = \begin{bmatrix} E_{\text{FF}}^{\downarrow s}(\varphi, \theta) \\ E_{\text{FF}}^{\downarrow p}(\varphi, \theta) \end{bmatrix} = -\frac{k_0^2}{4\pi\epsilon_0} \frac{k_N \cos \theta}{\sqrt{k_0^2 - k_N^2 \sin^2 \theta}} \frac{e^{ik_N r}}{r} e^{-ik_N \cos \theta z_{N-1N}} e^{-i\sqrt{k_0^2 - k_N^2 \sin^2 \theta}(z_{jj+1} - z_\downarrow)}$$

$$\begin{bmatrix} t_s^{\downarrow\uparrow} \left(\uparrow p_\varphi^e - \frac{1}{c} \uparrow p_\theta^m - \frac{ik_0}{6} \uparrow Q_\varphi^e + \frac{ik_0}{6c} \uparrow Q_\theta^m \right) + t_s^{\downarrow\downarrow} \left(\downarrow p_\varphi^e - \frac{1}{c} \downarrow p_\theta^m - \frac{ik_0}{6} \downarrow Q_\varphi^e + \frac{ik_0}{6c} \downarrow Q_\theta^m \right) \\ t_p^{\downarrow\uparrow} \left(\uparrow p_\theta^e + \frac{1}{c} \uparrow p_\varphi^m - \frac{ik_0}{6} \uparrow Q_\theta^e - \frac{ik_0}{6c} \uparrow Q_\varphi^m \right) + t_p^{\downarrow\downarrow} \left(\downarrow p_\theta^e + \frac{1}{c} \downarrow p_\varphi^m - \frac{ik_0}{6} \downarrow Q_\theta^e - \frac{ik_0}{6c} \downarrow Q_\varphi^m \right) \end{bmatrix}, \quad (2.72)$$

where we adopt the following new definitions of the multipole moments

$$\uparrow/\downarrow p_\varphi^{e/m} = -p_x^{e/m} \sin \varphi + p_y^{e/m} \cos \varphi, \quad (2.73)$$

$$\uparrow/\downarrow p_\theta^{e/m} = \pm p_x^{e/m} \cos \varphi \cos \theta \pm p_y^{e/m} \sin \varphi \cos \theta - p_z^{e/m} \sin \theta, \quad (2.74)$$

$$\uparrow/\downarrow Q_\varphi^{e/m} = \left[\left(Q_{yy}^{e/m} - Q_{xx}^{e/m} \right) \frac{1}{2} \sin 2\varphi + Q_{xy}^{e/m} \cos 2\varphi \right] \sin \theta \pm \left(Q_{yz}^{e/m} \cos \varphi - Q_{xz}^{e/m} \sin \varphi \right) \cos \theta, \quad (2.75)$$

$$\uparrow/\downarrow Q_\theta^{e/m} = \pm \left(Q_{xx}^{e/m} \cos^2 \varphi + Q_{yy}^{e/m} \sin^2 \varphi + Q_{xy}^{e/m} \sin 2\varphi - Q_{zz}^{e/m} \right) \sin \theta \cos \theta +$$

$$+ \left(Q_{xz}^{e/m} \cos \varphi + Q_{yz}^{e/m} \sin \varphi \right) \cos 2\theta. \quad (2.76)$$

As the arrows in the left superscript suggest, it takes into consideration a certain disparity between the upward and downward emitted waves, which get mixed up due to the reflections occurring inside the multilayer system. To be more specific, waves with a lateral wavevector $|\vec{q}| = k \sin \theta$ can propagate either upwards under the angle θ or downwards under the angle $\pi - \theta$ with respect to the vertical axis. Insertion of these two angles into the expressions for the vector spherical harmonics yields opposite signs in all the terms containing $\cos \theta$, while the rest of them are left unaffected. As a result, we must carefully keep the distinction between the upward (\uparrow) and downward (\downarrow) emitted waves and use the proper signs in the above expression for the multipole moments, namely the upper sign for \uparrow and the lower one for \downarrow .

Although it is not strictly necessary, we find it instructive to group together all the terms with the same dependence on the azimuthal angle—at the price of slightly more complex expressions, it allows us to readily identify any interference between various components of the multipole moments, which could be a valuable asset in the multipole analysis of light scattering objects. First, let us simplify the notation by factoring out the transmission coefficients so that we can return to the original representation of the Cartesian-based multipole moments

$$t_{s/p}^{\uparrow\uparrow} \uparrow p_{\varphi}^{e/m} + t_{s/p}^{\uparrow\downarrow} \downarrow p_{\varphi}^{e/m} = \left(t_{s/p}^{\uparrow\uparrow} + t_{s/p}^{\uparrow\downarrow} \right) \left(-p_x^{e/m} \sin \varphi + p_y^{e/m} \cos \varphi \right), \quad (2.77)$$

$$t_{s/p}^{\uparrow\uparrow} \uparrow p_{\varphi}^{e/m} + t_{s/p}^{\uparrow\downarrow} \downarrow p_{\varphi}^{e/m} = \left(t_{s/p}^{\uparrow\uparrow} - t_{s/p}^{\uparrow\downarrow} \right) \left(p_x^{e/m} \cos \varphi \cos \theta + p_y^{e/m} \sin \varphi \cos \theta \right) - \left(t_{s/p}^{\uparrow\uparrow} + t_{s/p}^{\uparrow\downarrow} \right) p_z^{e/m} \sin \theta, \quad (2.78)$$

$$t_{s/p}^{\uparrow\uparrow} \uparrow Q_{\varphi}^{e/m} + t_{s/p}^{\uparrow\downarrow} \downarrow Q_{\varphi}^{e/m} = \left(t_{s/p}^{\uparrow\uparrow} + t_{s/p}^{\uparrow\downarrow} \right) \left[\left(Q_{yy}^{e/m} - Q_{xx}^{e/m} \right) \frac{1}{2} \sin 2\varphi + Q_{xy}^{e/m} \cos 2\varphi \right] \sin \theta + \\ + \left(t_{s/p}^{\uparrow\uparrow} - t_{s/p}^{\uparrow\downarrow} \right) \left(Q_{yz}^{e/m} \cos \varphi - Q_{xz}^{e/m} \sin \varphi \right) \cos \theta, \quad (2.79)$$

$$t_{s/p}^{\uparrow\uparrow} \uparrow Q_{\varphi}^{e/m} + t_{s/p}^{\uparrow\downarrow} \downarrow Q_{\varphi}^{e/m} = \left(t_{s/p}^{\uparrow\uparrow} + t_{s/p}^{\uparrow\downarrow} \right) \left(Q_{xx}^{e/m} \cos^2 \varphi + Q_{yy}^{e/m} \sin^2 \varphi + Q_{xy}^{e/m} \sin 2\varphi - Q_{zz}^{e/m} \right) \sin \theta \cos \theta + \\ + \left(t_{s/p}^{\uparrow\uparrow} + t_{s/p}^{\uparrow\downarrow} \right) \left(Q_{xz}^{e/m} \cos \varphi + Q_{yz}^{e/m} \sin \varphi \right) \cos 2\theta. \quad (2.80)$$

If we now replace the transmission coefficients in the brackets with a new set of symbols, stating explicitly the link between the declination angle and the lateral wavevector, their natural argument,

$$\pm t_{s/p}^{\uparrow}(\theta) = t_{s/p}^{\uparrow\uparrow}(k_1 \sin \theta) \pm t_{s/p}^{\uparrow\downarrow}(k_1 \sin \theta), \quad (2.81)$$

$$\pm t_{s/p}^{\downarrow}(\theta) = \pm t_{s/p}^{\downarrow\uparrow}(k_N \sin \theta) + t_{s/p}^{\downarrow\downarrow}(k_N \sin \theta), \quad (2.82)$$

the individual components of the electric field generated in the far-field zone assume the following illuminating form

$$E_{\text{FF}}^{\uparrow/\downarrow s}(\varphi, \theta) = f^{\uparrow/\downarrow}(\theta) \left\{ \frac{1}{c} \left[p_z^m + t_s^{\uparrow/\downarrow}(\theta) \sin \theta + \frac{ik_0}{12} (Q_{xx}^m + Q_{yy}^m - 2Q_{zz}^m) - t_s^{\uparrow/\downarrow}(\theta) \sin \theta \cos \theta \right] + \right. \\ + \sin \varphi \left[-p_x^e + t_s^{\uparrow/\downarrow}(\theta) - \frac{1}{c} p_y^m - t_s^{\uparrow/\downarrow}(\theta) \cos \theta + \frac{ik_0}{6} Q_{xz}^e - t_s^{\uparrow/\downarrow}(\theta) \cos \theta + \frac{ik_0}{6c} Q_{yz}^m + t_s^{\uparrow/\downarrow}(\theta) \cos 2\theta \right] + \\ + \cos \varphi \left[p_y^e + t_s^{\uparrow/\downarrow}(\theta) - \frac{1}{c} p_x^m - t_s^{\uparrow/\downarrow}(\theta) \cos \theta - \frac{ik_0}{6} Q_{yz}^e - t_s^{\uparrow/\downarrow}(\theta) \cos \theta + \frac{ik_0}{6c} Q_{xz}^m + t_s^{\uparrow/\downarrow}(\theta) \cos 2\theta \right] + \\ + \frac{ik_0}{6} \sin 2\varphi \left[\frac{1}{2} (Q_{xx}^e - Q_{yy}^e) + t_s^{\uparrow/\downarrow}(\theta) \sin \theta + \frac{1}{c} Q_{xy}^m - t_s^{\uparrow/\downarrow}(\theta) \sin \theta \cos \theta \right] + \\ \left. + \frac{ik_0}{6} \cos 2\varphi \left[-Q_{xy}^e + t_s^{\uparrow/\downarrow}(\theta) \sin \theta + \frac{1}{2c} (Q_{xx}^m - Q_{yy}^m) - t_s^{\uparrow/\downarrow}(\theta) \sin \theta \cos \theta \right] \right\}, \quad (2.83)$$

$$E_{\text{FF}}^{\uparrow/\downarrow p}(\varphi, \theta) = f^{\uparrow/\downarrow}(\theta) \left\{ - \left[p_z^e + t_p^{\uparrow/\downarrow}(\theta) \sin \theta + \frac{ik_0}{12} (Q_{xx}^e + Q_{yy}^e - 2Q_{zz}^e) - t_p^{\uparrow/\downarrow}(\theta) \sin \theta \cos \theta \right] + \right. \\ + \sin \varphi \left[p_y^e - t_p^{\uparrow/\downarrow}(\theta) \cos \theta - \frac{1}{c} p_x^m + t_p^{\uparrow/\downarrow}(\theta) - \frac{ik_0}{6} Q_{yz}^e + t_p^{\uparrow/\downarrow}(\theta) \cos 2\theta + \frac{ik_0}{6c} Q_{xz}^m - t_p^{\uparrow/\downarrow}(\theta) \cos \theta \right] + \\ + \cos \varphi \left[p_x^e - t_p^{\uparrow/\downarrow}(\theta) \cos \theta + \frac{1}{c} p_y^m + t_p^{\uparrow/\downarrow}(\theta) - \frac{ik_0}{6} Q_{xz}^e + t_p^{\uparrow/\downarrow}(\theta) \cos 2\theta - \frac{ik_0}{6c} Q_{yz}^m - t_p^{\uparrow/\downarrow}(\theta) \cos \theta \right] + \\ + \frac{ik_0}{6} \sin 2\varphi \left[-Q_{xy}^e - t_p^{\uparrow/\downarrow}(\theta) \sin \theta \cos \theta + \frac{1}{2c} (Q_{xx}^m - Q_{yy}^m) + t_p^{\uparrow/\downarrow}(\theta) \sin \theta \right] - \\ \left. - \frac{ik_0}{6} \cos 2\varphi \left[\frac{1}{2} (Q_{xx}^e - Q_{yy}^e) - t_p^{\uparrow/\downarrow}(\theta) \sin \theta \cos \theta + \frac{1}{c} Q_{xy}^m + t_p^{\uparrow/\downarrow}(\theta) \sin \theta \right] \right\}, \quad (2.84)$$

with the functions $f^{\uparrow}(\theta)$ and $f^{\downarrow}(\theta)$ defined as

$$f^\uparrow(\theta) = \frac{k_0^2}{4\pi\epsilon_0} \frac{k_1 \cos \theta}{\sqrt{k_0^2 - k_1^2 \sin^2 \theta}} \frac{e^{ik_1 r}}{r} e^{-ik_1 \cos \theta z_{12}} e^{i\sqrt{k_0^2 - k_1^2 \sin^2 \theta} (z_{j-1j} - z_\dagger)}, \quad (2.85)$$

$$f^\downarrow(\theta) = -\frac{k_0^2}{4\pi\epsilon_0} \frac{k_N \cos \theta}{\sqrt{k_0^2 - k_N^2 \sin^2 \theta}} \frac{e^{ik_N r}}{r} e^{-ik_N \cos \theta z_{N-1N}} e^{-i\sqrt{k_0^2 - k_N^2 \sin^2 \theta} (z_{jj+1} - z_\dagger)}. \quad (2.86)$$

Since we do not usually directly map the electric field distribution during the measurements at our institute, but rather collect a signal integrated over a wide solid angle, it might be prudent to wield also expressions for the scattering cross-section. Recalling its definition in [Appendix A](#) and exploiting the mutual orthogonality of trigonometric functions, the integration of the Poynting vector over the azimuthal angle φ yields

$$\begin{aligned} C_{\text{sca}}^\uparrow &= \int_0^{\frac{\pi}{2}} d\theta \int_0^{2\pi} d\varphi r^2 \sin \theta \frac{|\vec{E}_{\text{FF}}^\uparrow(\varphi, \theta)|^2}{|\vec{E}_0|^2} = \frac{k_0^4}{16\pi\epsilon_0^2 |\vec{E}_0|^2} \int_0^{\frac{\pi}{2}} d\theta \sin \theta \frac{k_1^2 \cos^2 \theta}{k_0^2 - k_1^2 \sin^2 \theta} \\ &\left\{ \frac{2}{c^2} \left| p_z^{\text{m}} + t_s^\uparrow(\theta) \sin \theta + \frac{ik_0}{24} (Q_{xx}^{\text{m}} + Q_{yy}^{\text{m}} - 2Q_{zz}^{\text{m}}) - t_s^\uparrow(\theta) \sin 2\theta \right|^2 + \right. \\ &+ \left| -p_x^{\text{e}} + t_s^\uparrow(\theta) - \frac{1}{c} p_y^{\text{m}} - t_s^\uparrow(\theta) \cos \theta + \frac{ik_0}{6} Q_{xz}^{\text{e}} - t_s^\uparrow(\theta) \cos \theta + \frac{ik_0}{6c} Q_{yz}^{\text{m}} + t_s^\uparrow(\theta) \cos 2\theta \right|^2 + \\ &+ \left| p_y^{\text{e}} + t_s^\uparrow(\theta) - \frac{1}{c} p_x^{\text{m}} - t_s^\uparrow(\theta) \cos \theta - \frac{ik_0}{6} Q_{yz}^{\text{e}} - t_s^\uparrow(\theta) \cos \theta + \frac{ik_0}{6c} Q_{xz}^{\text{m}} + t_s^\uparrow(\theta) \cos 2\theta \right|^2 + \\ &+ \frac{k_0^2}{144} \left| (Q_{xx}^{\text{e}} - Q_{yy}^{\text{e}}) + t_s^\uparrow(\theta) \sin \theta + \frac{1}{c} Q_{xy}^{\text{m}} - t_s^\uparrow(\theta) \sin 2\theta \right|^2 + \\ &+ \frac{k_0^2}{36} \left| -Q_{xy}^{\text{e}} + t_s^\uparrow(\theta) \sin \theta + \frac{1}{4c} (Q_{xx}^{\text{m}} - Q_{yy}^{\text{m}}) - t_s^\uparrow(\theta) \sin 2\theta \right|^2 + \\ &+ 2 \left| p_z^{\text{e}} + t_p^\uparrow(\theta) \sin \theta + \frac{ik_0}{24} (Q_{xx}^{\text{e}} + Q_{yy}^{\text{e}} - 2Q_{zz}^{\text{e}}) - t_p^\uparrow(\theta) \sin 2\theta \right|^2 + \\ &+ \left| p_y^{\text{e}} - t_p^\uparrow(\theta) \cos \theta - \frac{1}{c} p_x^{\text{m}} + t_p^\uparrow(\theta) - \frac{ik_0}{6} Q_{yz}^{\text{e}} + t_p^\uparrow(\theta) \cos 2\theta + \frac{ik_0}{6c} Q_{xz}^{\text{m}} - t_p^\uparrow(\theta) \cos \theta \right|^2 + \\ &+ \left| p_x^{\text{e}} - t_p^\uparrow(\theta) \cos \theta + \frac{1}{c} p_y^{\text{m}} + t_p^\uparrow(\theta) - \frac{ik_0}{6} Q_{xz}^{\text{e}} + t_p^\uparrow(\theta) \cos 2\theta - \frac{ik_0}{6c} Q_{yz}^{\text{m}} - t_p^\uparrow(\theta) \cos \theta \right|^2 + \\ &+ \frac{k_0^2}{144} \left| -Q_{xy}^{\text{e}} - t_p^\uparrow(\theta) \sin 2\theta + \frac{1}{c} (Q_{xx}^{\text{m}} - Q_{yy}^{\text{m}}) + t_p^\uparrow(\theta) \sin \theta \right|^2 + \\ &+ \left. \frac{k_0^2}{36} \cos 2\varphi \left| \frac{1}{4} (Q_{xx}^{\text{e}} - Q_{yy}^{\text{e}}) - t_p^\uparrow(\theta) \sin 2\theta + \frac{1}{c} Q_{xy}^{\text{m}} + t_p^\uparrow(\theta) \sin \theta \right|^2 \right\}. \quad (2.87) \end{aligned}$$

A similar expression can be obtained also for the lower halfspace contribution to the scattering cross-section

$$C_{\text{sca}}^\downarrow = \frac{k_N}{k_1} \int_{\frac{\pi}{2}}^\pi d\theta \int_0^{2\pi} d\varphi r^2 \sin \theta \frac{|\vec{E}_{\text{FF}}^\downarrow(\varphi, \theta)|^2}{|\vec{E}_0|^2} = \frac{k_0^4}{16\pi\epsilon_0^2 |\vec{E}_0|^2} \frac{k_N}{k_1} \int_{\frac{\pi}{2}}^\pi d\theta \sin \theta \frac{k_N^2 \cos^2 \theta}{k_0^2 - k_N^2 \sin^2 \theta} \left\{ \dots \right\}, \quad (2.88)$$

where apart from changing the layer index and multiplying the expression by the factor k_N/k_1 , one needs only to replace the transmission coefficients ${}^\pm t_{s/p}^\uparrow$ with their ‘‘downward’’ counterparts ${}^\pm t_{s/p}^\downarrow$.

The above set of equations facilitates the multipole analysis of objects going well beyond the classical scenario of a free standing particle or even a particle on top of a substrate. To demonstrate the capabilities of the presented framework, we employ it for the decomposition of the fields generated by a diabolo cross-dimer, an object composed of two Babinet-complementary diabolo antennas placed on top themselves. Babinet's principle, a theoretical concept stating that there is a link between the fields generated by a particle and an aperture of the same shape, is one of the long-term topics pursued in our research group [53, 55, 56]. The diabolo cross-dimer then represents a theoretical design of a sandwich antenna that possesses overlapping electric and magnetic hotspots. The detailed description of this antenna and its properties, including the general role of the Babinet principle in plasmonics, can be found in the full article included in [Attachments](#). Here, we limit ourselves only to the multipole analysis of its far-field pattern and for that purpose, it suffices just to get a bit more familiar with its geometry, which is shown in the left panel of Figure 2.10: a diabolo with 110 nm long wings lies underneath an inverted diabolo (i.e. an aperture in the shape of a diabolo) with 200 nm wings in length, the two structures are mutually rotated by 90 degrees and separated by a 10 nm thick spacer layer with the refractive index equal to 1.5. Both the diabolo and its inverted counterpart are made of gold, their height is 30 nm and the whole sandwich structure is placed on top of a semi-infinite glass substrate. The dimensions of the diabolo cross-dimer were chosen so as to provide a maximum intensity of both the electric and the magnetic field at the telecommunication wavelength of 1550 nm.

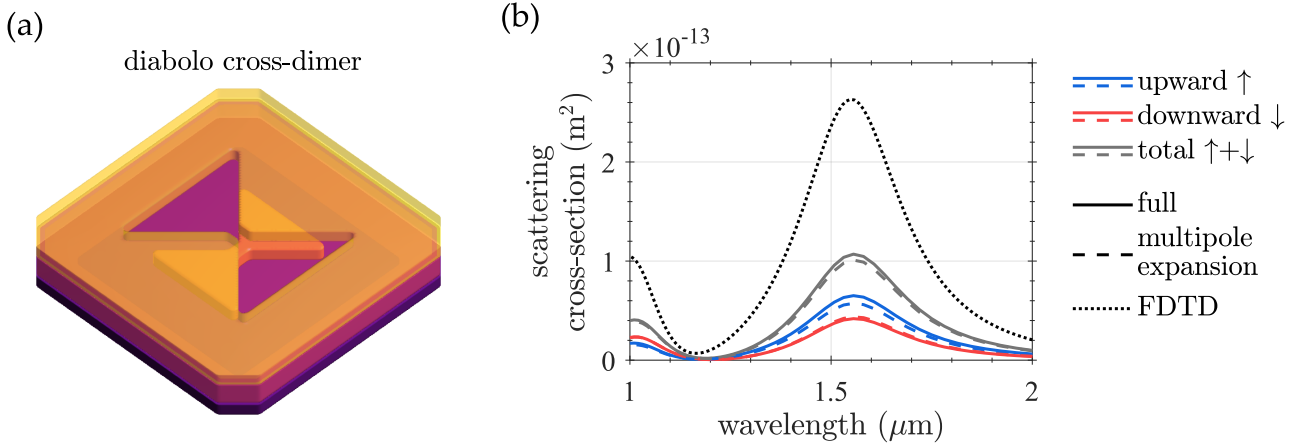


Figure 2.10: (a) Drawing of a diabolo cross-dimer, a sandwich antenna consisting of a gold diabolo underneath a larger inverted diabolo (an aperture in the shape of a diabolo milled into an otherwise homogeneous gold film). The two structures are separated by a thin dielectric spacer layer and mutually rotated by 90 degrees, hence the word “cross” in the name. By illuminating the antenna by an electromagnetic wave polarized along the long axis of the diabolo (and short axis of the inverted diabolo), the small region above the diabolo bridge becomes a hotspot with increased intensity of both the electric and the magnetic field. (b) Scattering cross-section of the diabolo cross-dimer calculated with three different procedures. The approach employing the full current distribution (solid line) corroborates the validity and the proper implementation of the presented scheme for the multipole expansion in stratified media (dashed line). The measurement of power flowing through a monitor box (dotted line), a standard procedure offered by the Lumerical FDTD Solutions software, also includes the power carried by evanescent waves and is, therefore, incompatible with the other two approaches.

In the right panel of Figure 2.10, we plot the scattering cross-section of our sandwich antenna calculated with three different procedures. While the multipole expansion and the approach based on the framework developed in [Appendix A](#) utilizing the full current distribution give very similar results, the spectral dependence obtained by measuring the power flowing through a monitor box surrounding the structure (FDTD) is completely off. This is due to the fact that the last approach

also incorporates the power carried by surface plasmon polaritons propagating along the gold film of the inverted diablo, whereas the other two take into account only the freely propagating waves. Nevertheless, the observed agreement between the results offered by the multipole expansion and the calculations based on the full current distribution validates the correct implementation of the apparatus presented above and we can proceed with the analysis of the individual multipole moments and their contributions to the total scattering cross-section.

The large number of different multipole moments (4 multipoles for each structures) and various cross-terms (28 in total) prevents us from plotting them all in a single figure without creating a complete chaos. Instead, we picked only those which contribute significantly to the total scattering cross-section, more than by 10% of its maximum value, to be precise. Keeping the distinction between the power scattered into the upper (\uparrow) and lower (\downarrow) halfspaces, we show in Figure 2.11 the scattering cross-section spectra of the most prominent contributors. We immediately see that the inverted diablo (particle 2), being larger, dominates the optical response of our sandwich structure. The diablo (particle 1) is strongly screened by the gold film extending above it, so there is only a slight direct contribution from its electric dipole moment to the power radiated into the lower halfspace. Its interaction with the electric dipole moment of the inverted diablo ($\vec{p}_1^e - \vec{p}_2^e$) is, on the other hand, much more significant. Note that as long as the total scattering cross-section remains positive, there is no need to be concerned about the negative sign of some of its parts.

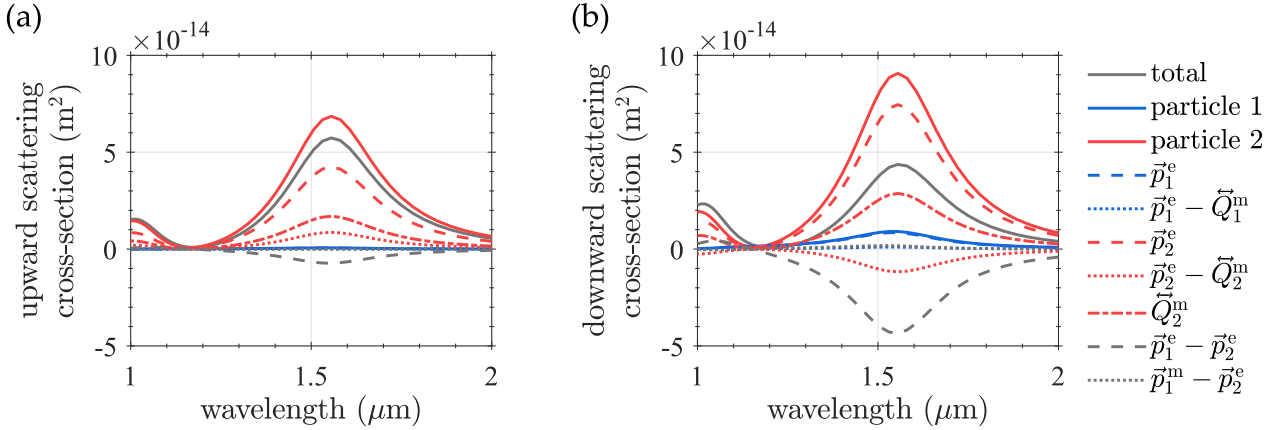


Figure 2.11: Decomposition of the scattering cross-section from Figure 2.10 into individual multipolar contributions. Being larger, the inverted diablo (particle 2) dominates the response of the compound structure. The less prominent diablo (particle 1) radiates preferentially into the lower halfspace (the right panel) due to the screening caused by the overarching gold film of its Babinet counterpart. Note that we plot only those multipoles that contribute significantly to the scattering cross-section, we discarded the rest to keep the figure intelligible.

Our original motivation for carrying out the multipolar analysis of the diablo cross-dimer was a question posed by one of the referees during the peer-review process we went through to publish our article on Babinet’s principle included in [Attachments](#). The question was, whether such a sandwich structure composed of a particle and an aperture—which is known to radiate partially as a magnetic dipole [57]—could exhibit the Kerker effect [50], i.e. preferential scattering of light into one direction. As it turns out, this particular geometrical configuration does not lead to this effect, the inverted diablo dominates the response and the power is radiated more or less isotropically (at least in the sense of the energy going upwards or downwards). Still, this question fueled our efforts to develop this valuable tool enabling calculation of the multipole expansion in objects embedded within stratified media.

Conclusions

This thesis represents a mixture of various simulation problems from nanophotonics and plasmonics that the author has come across during his involvement in research projects conducted at the Institute of Physical Engineering, Brno University of Technology. Their common denominator has been the necessity to venture beyond the standard analysis tools offered by commercial software and to develop procedures and semianalytical models that would more adequately reflect specific conditions encountered in our experiments. This has not only led to better agreement between measurements and theoretical predictions, but it has also improved our understanding of physical principles governing the processes that we have studied.

The most illustrative example of this is, perhaps, the plasmon enhanced electron paramagnetic resonance spectroscopy (plasmon enhanced EPR), a novel technique employing plasmonic antennas to locally enhance magnetic field and consequently boost absorption of radiation in materials exhibiting magnetic transitions between electronic states. Our theoretical calculations based on a simple oscillator model show that the magnetic transitions imprint themselves into the optical response of a plasmonic antenna by changing the oscillation amplitude of the electric dipole moment that is being induced within the antenna by incoming radiation. If we perceive the antenna as an open resonator, then its interaction with the magnetic material opens up an additional loss channel that reduces the quality of the resonator and leads to a slight drop in the power radiated by the antenna. We found that this drop in the radiated power—essentially the EPR signal that we aim to measure—is directly proportional to the average enhancement of the second power of the magnetic field within the volume V occupied by the studied magnetic material. This quantity, which we shall, for the sake of brevity, denote in the following as the average magnetic field enhancement, is the principal parameter that determines the ability of an antenna to enhance the EPR signal. As such, it should serve as the primary figure of merit during any search for antenna parameters that provide an optimized performance in EPR spectroscopic measurements.

As these measurements usually involve large area specimens, it seems only logical to upscale our system from a single antenna to a whole antenna array. This poses a computational challenge, since it introduces a new set of parameters (an array pitch) that substantially increase the time needed to find the optimal configuration. Another parameter that has to be taken into account is the substrate thickness: the optical wavelength in the 100 GHz–1 THz spectral range, where high-field EPR measurements take place, is comparable to typical dimensions of wafers used as substrates for EPR active materials. That leads inevitably to a build-up of Fabry-Perot oscillations inside the substrate that can significantly affect the antenna array optical response. Our calculations actually suggest that the Fabry-Perot oscillations forming between the antenna array and the backside of the substrate (possibly augmented with a mirror) play a major role in the enhancing effect of the antenna array system on the EPR signal.

To tackle the problem of finding the optimal configuration of an antenna array, and substrate parameters that would maximize the average magnetic field enhancement, we developed a semianalytical interaction model that combines numerical simulations with elements of waveguide theory and eigenmode expansion. Using the framework of overlap integrals as a tool to parametrize the interaction between antennas constituting our array and adopting several approximations regarding the optical response of plasmonic antennas within the THz spectral region, we were able to reduce the time consuming problem of simulating a large ensemble of mutually interacting antennas into a self-consistent system of linear equations, where each antenna is represented by a single parameter, namely its excitation amplitude. Apart from enabling rapid sweeps over the various antenna array parameters, our semianalytical interaction model also allowed us to formulate a more rigorous description of the plasmon enhanced EPR effect that classifies the interaction between the antenna and the magnetic material as a back-action of the polarization current flowing within the antenna on itself. This back-action is mediated by the magnetization current induced within the EPR active material.

A thorough analysis of both the electric and the magnetic dyadic Green’s functions revealed that it is, in fact, proportional to the second power of the magnetic field generated by the antenna (even though there are some correction terms arising from the presence of a substrate). We consider this result to be very important as it corroborates our earlier statements based on the grossly simplified oscillator model and places them on a more solid ground. Although originally developed for the purpose of parameter optimization in the plasmon enhanced EPR, our antenna interaction model is not limited to the THz spectral region—the validity of its underlying assumptions stretches as far as the near-infrared frequency range—and it could find its use in a number of applications, especially those involving arrays made of several types of antennas, such as spatially varying metasurfaces.

The entire framework of our antenna interaction model is built on numerical simulations and further processing of their results. A pivotal role in this post-processing is played by the polarization current that is induced within plasmonic antennas under an external illumination. Despite the need to handle large amount of data and develop procedures involving Green’s function formalism and wave propagation in stratified media, our preference of the polarization current over the electromagnetic field distribution (which is directly accessible in most simulation software) offers important advantages: firstly, it enables parametrization of the interaction between individual antennas, and secondly, far-field projections are not plagued by artifacts stemming from the finite size of a simulation region (in contrast to the electromagnetic field, there is no truncation at the simulation region boundary as the polarization current is fully confined to the interior of the antenna). The benefits of embracing the polarization current distribution as the primary quantity characterizing the optical response of simulated objects were highlighted the most in our study of plasmon enhanced EPR (Chapter 1), but the concept proved to be quite valuable also in other scenarios, such as the phase imaging of metasurfaces using coherence controlled holographic microscopy (Section 2.1), design of a metasurface-based optical element generating a regular beam array (Section 2.2), or multipole expansion of electromagnetic waves emitted by an object embedded within a stratified medium (Section 2.3).

Though not groundbreaking, the ideas and calculations presented in this thesis constitute a platform upon which the author intends to build more advanced models that would offer insight into the experiments conducted at our institute and also to address open issues in the exciting fields of optical metasurfaces and plasmon enhanced EPR spectroscopy. At the same time, this work will hopefully inspire others and help them, perhaps, with their own research, or just serve as a useful handbook of equations and formulas.

Appendix A

Far-field projections

The purpose of this appendix is to establish a link between the current distribution induced within some object and the radiation it generates in the far-field. Utilizing a matrix approach for the description of wave propagation inside stratified media [1], we gradually build a general framework that is applicable to a whole spectrum of situations, ranging from the calculation of the conventional scattering and extinction cross-sections to the evaluation of the Kerker effect in plasmonic dimers (Section 2.3), numerical simulations of experiments in the dark field configuration [58] or the design optimization of certain classes of metasurfaces (Section 2.2).

The cornerstone of the whole apparatus of far-field projections is the angular spectral representation of fields and the fact that a field distribution in a single plane $z = z_0$ incidentally determines the distribution in the rest of the space [2] (assuming this space is homogeneous)

$$\vec{E}(\vec{r}) = \iint_{-\infty}^{\infty} d\vec{q}^2 e^{i\vec{q}\cdot\vec{r}_{\parallel}} \vec{E}(\vec{q}, z_0) e^{ik_z(z-z_0)}, \quad (\text{A.1})$$

An intuitive interpretation of the above equation would be that any field distribution can be decomposed into a spectrum of electromagnetic waves with lateral momenta \vec{q} that can be individually propagated to the desired position \vec{r} and their superposition gives us the field $\vec{E}(\vec{r})$ at this new location. Note that the vertical wavevector component $k_z = \sqrt{k^2 - q^2}$ decides, whether the wave is propagating (the wavenumber k is larger than the magnitude of the lateral wavevector $q = |\vec{q}|$, i.e. $k \geq q$) or evanescent ($k < q$).

Our goal is the calculation of the far-field generated by an arbitrary current distribution that is spatially confined between two parallel planes positioned at z^{\uparrow} and z^{\downarrow} . The region between these two planes can be inhabited by various objects such as antennas or multilayered substrates, but outside of it, we require the space to be homogeneous so that the above wave projection concept can be employed. Assuming for the moment that the field distributions within those two planes are known (we shall return to this point later on), the electric field in the two halfspaces $z \geq z^{\uparrow}$ and $z \leq z^{\downarrow}$ reads

$$\vec{E}^{\uparrow}(\vec{r}) = \iint_{-\infty}^{\infty} d\vec{q}^2 e^{i\vec{q}\cdot\vec{r}_{\parallel}} \vec{E}(\vec{q}, z^{\uparrow}) e^{ik_{z1}(z-z^{\uparrow})}, \quad (\text{A.2})$$

$$\vec{E}^{\downarrow}(\vec{r}) = \iint_{-\infty}^{\infty} d\vec{q}^2 e^{i\vec{q}\cdot\vec{r}_{\parallel}} \vec{E}(\vec{q}, z^{\downarrow}) e^{-ik_{zn}(z-z^{\downarrow})} \quad (\text{A.3})$$

where the indices in the subscripts of the vertical wavevector components suggest that while the two halfspaces have to be homogeneous, each can have different optical properties.

Furthermore, the far-fields are not usually evaluated in the Cartesian coordinate system but it is more convenient to express them as a function of directional cosines x/r , y/r , and z/r (with r denoting the radial distance from the origin). Together, they form a unit vector \vec{s} that allows us to unambiguously distinguish between different emission directions. After switching to spherical coordinates, its components become

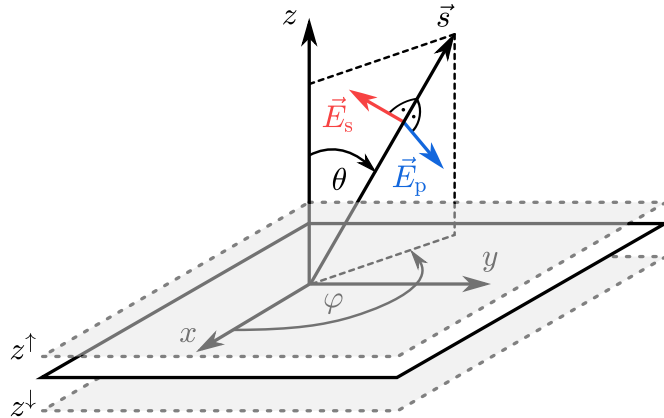


Figure A.1: The coordinate system used for the projection into the far-field. The sources are fully confined within the region $z^\downarrow \geq z \geq z^\uparrow$ and the radiation in the upper (lower) hemisphere is calculated from the field distribution in the $z = z^\uparrow$ ($z = z^\downarrow$) plane. The position on the hemispheres is usually expressed in terms of the directional cosines which together form the unit vector $\vec{s} = [x/r, y/r, z/r]$. Furthermore, far away from the sources where the radiative part of fields dominates, the electric field is mostly perpendicular to the propagation direction and it can be conveniently projected onto a two component basis corresponding to the s- and p-polarized waves, i.e. $\vec{E} = [E_\varphi, E_\theta] = [E_s, E_p]$.

$$s_x = \frac{x}{r} = \cos \varphi \sin \theta, \quad (\text{A.4})$$

$$s_y = \frac{y}{r} = \sin \varphi \sin \theta, \quad (\text{A.5})$$

$$s_{\parallel} = \sqrt{s_x^2 + s_y^2} = \sin \theta, \quad (\text{A.6})$$

$$s_z = \frac{z}{r} = \pm \sqrt{1 - s_{\parallel}^2} = \cos \theta, \quad (\text{A.7})$$

where the choice of the sign in the vertical component s_z is obviously related to the hemisphere in which the fields are calculated – the plus sign applies to the upper and the minus sign to the lower hemisphere. For clarity, the various coordinate systems are shown in Figure A.1, along with the region containing the sources of radiation.

The next step in the build-up of the apparatus facilitating projections into the far-field is perhaps the most crucial. Provided the radial distance from the origin is much greater than the optical wavelength ($r \gg \lambda$), the application of the stationary phase method [1] on the double integrals occurring in Eqs. (A.2) and (A.3) reveals that for any direction \vec{s} we choose, there is always only one plane wave from the whole angular spectrum that contributes to the far-field. The rest of them cancel each other out via interference. It is no surprise that the propagation direction of the one surviving plane wave coincides with the vector \vec{s} , the direction in which the far-field is being evaluated. Naturally, the suppression of all the other waves, both propagating and evanescent, substantially simplifies the calculation of the far-field, as it can be directly mapped onto the Fourier representation of the near-field, namely

$$\vec{E}_{\text{FF}}^\uparrow(s_x, s_y) = -2\pi i k_1 s_z \vec{E}^\uparrow(k_1 s_x, k_1 s_y, z^\uparrow) e^{-i s_z k_1 z^\uparrow} \frac{e^{i k_1 r}}{r}, \quad (\text{A.8})$$

$$\vec{E}_{\text{FF}}^\downarrow(s_x, s_y) = 2\pi i k_n s_z \vec{E}^\downarrow(k_n s_x, k_n s_y, z^\downarrow) e^{-i s_z k_n z^\downarrow} \frac{e^{i k_n r}}{r}. \quad (\text{A.9})$$

A distinctive property of plane waves is the perpendicularity of their propagation wavevector to the electric field (it is not necessarily true for anisotropic media, but we discarded those from our considerations earlier). It is, therefore, fitting to switch to spherical coordinate basis, in which the electric field has only two nonzero components E_φ and E_θ , alternatively labeled also as E_s and E_p (derived from the German words "senkrecht" and "parallel")

$$\vec{E}_{\text{FF}}^{\uparrow/\downarrow}(s_x, s_y) = \begin{bmatrix} E_s^{\uparrow/\downarrow}(s_x, s_y) \\ E_p^{\uparrow/\downarrow}(s_x, s_y) \end{bmatrix}, \quad (\text{A.10})$$

$$\vec{E}^{\uparrow/\downarrow}(q_x, q_y, z^{\uparrow/\downarrow}) = \begin{bmatrix} E_s^{\uparrow/\downarrow}(q_x, q_y, z^{\uparrow/\downarrow}) \\ E_p^{\uparrow/\downarrow}(q_x, q_y, z^{\uparrow/\downarrow}) \end{bmatrix}. \quad (\text{A.11})$$

The reason for changing the coordinate basis is not only to make the notation slightly more esthetic, but it brings also some practical benefits. Suppose that the sources are embedded within or placed on top of a substrate. Then the waves emitted by those sources will experience reflections at any interface they have to pass and it is well known that the reflection process depends on the polarization state of these waves – the reflection and transmission coefficients for s- and p-polarization can differ dramatically. By expressing the fields in the spherical coordinate basis, we can treat these two cases separately and avoid unnecessary chaos in the notation.

It now remains to concretize the link between the sources and the Fourier components of the electric field they generate in the two planes z^\downarrow and z^\uparrow enclosing the entire source region. Let us consider a general system consisting of $n - 2$ material layers indexed from 2 to $n - 1$, with the source currents fully confined within the j -th layer (for a sketch of this system see Figure A.2). Identifying z_{12} and z_{n-1n} , the topmost and the most bottom interfaces separating the multilayer from the upper and lower halfspaces, as the planes z^\uparrow and z^\downarrow , the electric field within these two planes can be written as

$$\vec{E}^\uparrow(\vec{q}, z^\uparrow) = \begin{bmatrix} E_s^\uparrow(\vec{q}, z_{12}) \\ E_p^\uparrow(\vec{q}, z_{12}) \end{bmatrix} = \begin{bmatrix} t_s^{\uparrow\uparrow}(\vec{q}) E_{\text{src}}^{+s}(\vec{q}) + t_s^{\uparrow\downarrow}(\vec{q}) E_{\text{src}}^{-s}(\vec{q}) \\ t_p^{\uparrow\uparrow}(\vec{q}) E_{\text{src}}^{+p}(\vec{q}) + t_p^{\uparrow\downarrow}(\vec{q}) E_{\text{src}}^{-p}(\vec{q}) \end{bmatrix}, \quad (\text{A.12})$$

$$\vec{E}^\downarrow(\vec{q}, z^\downarrow) = \begin{bmatrix} E_s^\downarrow(\vec{q}, z_{n-1n}) \\ E_p^\downarrow(\vec{q}, z_{n-1n}) \end{bmatrix} = \begin{bmatrix} t_s^{\downarrow\uparrow}(\vec{q}) E_{\text{src}}^{+s}(\vec{q}) + t_s^{\downarrow\downarrow}(\vec{q}) E_{\text{src}}^{-s}(\vec{q}) \\ t_p^{\downarrow\uparrow}(\vec{q}) E_{\text{src}}^{+p}(\vec{q}) + t_p^{\downarrow\downarrow}(\vec{q}) E_{\text{src}}^{-p}(\vec{q}) \end{bmatrix} \quad (\text{A.13})$$

where the transmission coefficients $t^{\uparrow\uparrow}(\vec{q})$, $t^{\uparrow\downarrow}(\vec{q})$, $t^{\downarrow\uparrow}(\vec{q})$, and $t^{\downarrow\downarrow}(\vec{q})$ account for all the possible reflections that the upward (E_{src}^{+s} , E_{src}^{+p}) and the downward (E_{src}^{-s} , E_{src}^{-p}) propagating waves generated by the source currents have to undergo before they leave the multilayer system.

The amplitudes of the source waves ($E_{\text{src}}^{\pm s}$, $E_{\text{src}}^{\pm p}$) can be calculated from the current distribution using the dyadic Green's function $\vec{G}(\vec{r}, \vec{r}')$ [2]

$$\vec{E}(\vec{r}) = \int_V d\vec{r}'^3 \vec{G}(\vec{r}, \vec{r}') \vec{P}(\vec{r}') = \int_V d\vec{r}'^3 \vec{G}(\vec{r}_\parallel - \vec{r}'_\parallel, z, z') \vec{P}(\vec{r}'_\parallel, z'), \quad (\text{A.14})$$

where we implicitly assume that the hosting environment possesses translational invariance along the lateral spatial coordinates \vec{r}_\parallel . Note that instead of the current distribution $\vec{j}(\vec{r})$, we prefer to work with the polarization vector $\vec{P}(\vec{r})$. Since those two are closely related to each other ($\vec{j} = -i\omega\vec{P}$ in the frequency domain), it does not make, from the conceptual viewpoint, much of a difference which one we choose to use. Anyway, in the reciprocal space, the convolution reduces to a straightforward multiplication of the Fourier components and only the integration over the vertical coordinate remains

$$\vec{E}(\vec{q}, z) = 4\pi^2 \int dz' \vec{G}(\vec{q}, z, z') \vec{P}(\vec{q}, z'). \quad (\text{A.15})$$

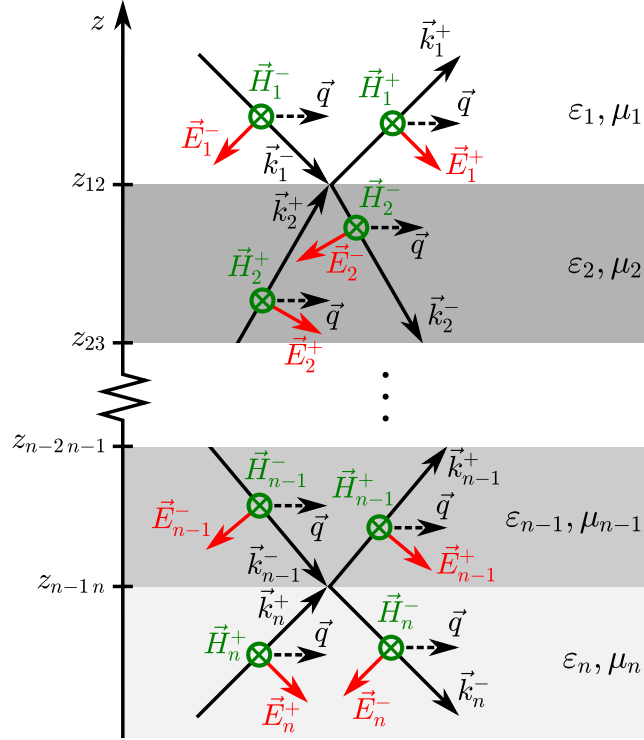


Figure A.2: Schematic depiction of a p-polarized plane wave with a lateral momentum \vec{q} propagating inside a stratified medium. Each layer is characterized by a relative permittivity ε_j and a relative permeability μ_j , and the position of the interface between two subsequent layers indexed j and $j+1$ is designated as z_{jj+1} . Finally, the sign in the superscript indicates whether the wave propagates in the positive (+) or the (-) negative direction of the z -axis. Note that the situation for an s-polarized is qualitatively similar, one has to only interchange the electric and magnetic field vectors.

Utilizing the above relation and recalling our decision to operate in the spherical coordinate basis, we finally obtain expressions for the amplitudes of the s- and p-polarized waves generated by the source currents

$$\begin{bmatrix} E_{\text{src}}^{\pm\text{s}}(\vec{q}) \\ E_{\text{src}}^{\pm\text{p}}(\vec{q}) \end{bmatrix} = \frac{i\omega^2 \mu_0 \mu_j}{2} \int_{z_{jj+1}}^{z_{j-1j}} dz' \vec{M}_{\text{sph}}^{\pm}(\vec{q}) \vec{P}(\vec{q}, z') e^{\pm i k_{zj}(z' - z_{jj+1})}, \quad (\text{A.16})$$

$$\vec{M}_{\text{sph}}^{\pm}(\vec{q}) = \begin{bmatrix} M_{\varphi x}^{\pm}(\vec{q}) & M_{\varphi y}^{\pm}(\vec{q}) & M_{\varphi z}^{\pm}(\vec{q}) \\ M_{\theta x}^{\pm}(\vec{q}) & M_{\theta y}^{\pm}(\vec{q}) & M_{\theta z}^{\pm}(\vec{q}) \end{bmatrix}, \quad (\text{A.17})$$

where the components of the tensor $\vec{M}_{\text{sph}}^{\pm}$ can be constructed, for example, from the Cartesian tensor $\vec{M}_{\text{cart}}^{\pm}$ using the following relations

$$M_{\varphi\beta}^{\pm} = -\sin \varphi M_{x\beta}^{\pm} + \cos \varphi M_{y\beta}^{\pm}, \quad (\text{A.18})$$

$$M_{\theta\beta}^{\pm} = \cos \varphi \cos \theta M_{x\beta}^{\pm} + \sin \varphi \cos \theta M_{y\beta}^{\pm} - \sin \theta M_{z\beta}^{\pm}. \quad (\text{A.19})$$

Since the detailed derivation of the whole apparatus of Green's functions can be easily found elsewhere (e.g. in [2]), we deem it sufficient to write down the expression for the Cartesian tensor $\vec{M}_{\text{cart}}^{\pm}$ without any further explanation

$$\vec{M}_{\text{cart}}^{\pm}(\vec{q}) = \begin{bmatrix} M_{xx}^{\pm}(\vec{q}) & M_{xy}^{\pm}(\vec{q}) & M_{xz}^{\pm}(\vec{q}) \\ M_{yx}^{\pm}(\vec{q}) & M_{yy}^{\pm}(\vec{q}) & M_{yz}^{\pm}(\vec{q}) \\ M_{zx}^{\pm}(\vec{q}) & M_{zy}^{\pm}(\vec{q}) & M_{zz}^{\pm}(\vec{q}) \end{bmatrix} = \frac{1}{k_j^2 k_{zj}} \begin{bmatrix} k_j^2 - q_x^2 & -q_x q_y & \mp q_x k_{zj} \\ -q_x q_y & k_j^2 - q_y^2 & \mp q_y k_{zj} \\ \mp q_x k_{zj} & \mp q_y k_{zj} & k_j^2 - k_{zj}^2 \end{bmatrix}. \quad (\text{A.20})$$

Employing Eqs. (A.18) and (A.19), the components of the tensor $\vec{M}_{\text{sph}}^{\pm}$ are found to be

$$\vec{M}_{\text{sph}}^{\pm}(\vec{q}) = \frac{1}{k_{zj}} \begin{bmatrix} -\frac{q_y}{q} & \frac{q_x}{q} & 0 \\ \pm \frac{q_x}{q} \frac{k_{zj}}{k_j} & \pm \frac{q_y}{q} \frac{k_{zj}}{k_j} & -\frac{q}{k_j} \end{bmatrix}. \quad (\text{A.21})$$

The last missing piece of the mosaic are the transmission coefficients $t^{\uparrow\uparrow}(\vec{q})$, $t^{\uparrow\downarrow}(\vec{q})$, $t^{\downarrow\uparrow}(\vec{q})$, and $t^{\downarrow\downarrow}(\vec{q})$ occurring in Eqs. (A.12) and (A.13). On that note, the transmission of plane waves through a stack of layers with varying optical properties (as well as the reflection from it) can be comprehensibly described in terms of Fresnel coefficients. First, let us consider a single planar interface between two isotropic materials, at which the electric and magnetic fields have to satisfy the customary boundary conditions [2]. Adopting the notation introduced in Figure A.2, these conditions yield the following relations for the amplitudes of the upward (+) and downward (-) propagating waves with a lateral momentum \vec{q}

$$E_1^+(\vec{q}) = t_{21}(\vec{q}) E_2^+(\vec{q}) + r_{12}(\vec{q}) E_1^-(\vec{q}), \quad (\text{A.22})$$

$$E_2^-(\vec{q}) = t_{12}(\vec{q}) E_1^-(\vec{q}) + r_{21}(\vec{q}) E_2^+(\vec{q}), \quad (\text{A.23})$$

where the order of indices in the subscript of Fresnel coefficients t_{12} , r_{12} , t_{21} , and r_{21} indicates the direction in which an electromagnetic wave passes through or is reflected from the interface. Note that these relations hold universally for both the p- and s-polarized electromagnetic waves. Equations (A.22) and (A.23) can be recast into a more compact matrix form

$$\begin{bmatrix} E_1^+ \\ E_1^- \end{bmatrix} = \frac{1}{t_{12}} \begin{bmatrix} t_{21}t_{12} - r_{21}r_{12} & r_{12} \\ -r_{21} & 1 \end{bmatrix} \begin{bmatrix} E_2^+ \\ E_2^- \end{bmatrix} = \vec{M}_{12} \begin{bmatrix} E_2^+ \\ E_2^- \end{bmatrix}, \quad (\text{A.24})$$

or alternatively

$$\begin{bmatrix} E_2^+ \\ E_2^- \end{bmatrix} = \vec{M}_{21} \begin{bmatrix} E_1^+ \\ E_1^- \end{bmatrix}, \quad (\text{A.25})$$

where the transformation matrices \vec{M}_{21} and \vec{M}_{12} are inversion of one another

$$\vec{M}_{21} = \vec{M}_{12}^{-1} = \frac{1}{t_{21}} \begin{bmatrix} 1 & r_{21} \\ -r_{12} & t_{21}t_{12} - r_{21}r_{12} \end{bmatrix}. \quad (\text{A.26})$$

For completeness, let us write down the expressions for the Fresnel coefficients $r_{12}^{s/p}(\vec{q})$ and $t_{12}^{s/p}(\vec{q})$ in the case of an ordinary material interface without any additional surface conductivity (arising, for example, from a 2D material such as graphene)

$$r_{12}^s(\vec{q}) = \frac{\mu_2 k_{z1} - \mu_1 k_{z2}}{\mu_2 k_{z1} + \mu_1 k_{z2}}, \quad (\text{A.27})$$

$$r_{12}^p(\vec{q}) = \frac{\varepsilon_2 k_{z1} - \varepsilon_1 k_{z2}}{\varepsilon_2 k_{z1} + \varepsilon_1 k_{z2}}, \quad (\text{A.28})$$

$$t_{12}^s(\vec{q}) = \frac{2\mu_2 k_{z1}}{\mu_2 k_{z1} + \mu_1 k_{z2}}, \quad (\text{A.29})$$

$$t_{12}^p(\vec{q}) = \frac{2\varepsilon_2 k_{z1}}{\varepsilon_2 k_{z1} + \varepsilon_1 k_{z2}} \sqrt{\frac{\mu_2 \varepsilon_1}{\mu_1 \varepsilon_2}}, \quad (\text{A.30})$$

with $k_{zj} = \sqrt{k_j^2 - q^2}$ denoting the vertical wavevector component. The Fresnel coefficients $r_{21}^{s/p}(\vec{q})$ and $t_{21}^{s/p}(\vec{q})$ corresponding to the reverse propagation across the interface are acquired simply by interchanging the indices in the above expressions.

The view of the reflection process as a linear transformation between two states has some far-reaching practical consequences: not only it gives us a direct relationship between the fields in the two media, but more importantly, it allows us to propagate plane waves even through more complex systems consisting of several layers using a mathematically clear and elegant procedure. As the amplitudes of the plane waves existing within such a system also have to obey the above relations, the overall response of the multilayer can be characterized by a single matrix \vec{M} created by stacking the transformation matrices associated with the various material interfaces present in the system. There is only one additional aspect of the process that needs to be taken into account – the phase accumulated by the plane waves during their propagation through the individual layers. Referring the reader to the schematic representation of a general stratified medium shown in Figure A.2, the complex amplitudes of the upward and downward propagating waves at the opposing interfaces demarcating the j -th layer are mutually related through

$$E_j^+(z_{j-1j}) = e^{+ik_{zj}d_j} E_j^+(z_{jj+1}), \quad (\text{A.31})$$

$$E_j^-(z_{j-1j}) = e^{-ik_{zj}d_j} E_j^-(z_{jj+1}), \quad (\text{A.32})$$

where the accumulated phases amount simply to the layer thickness $d_j = z_{j-1j} - z_{jj+1}$ times the vertical components $\pm k_{zj} = \pm \sqrt{k_j^2 - q^2}$ of the wavenumbers \vec{k}_j^\pm . In the matrix notation, these relations translate to

$$\begin{bmatrix} E_1^+(z_{j-1j}) \\ E_1^-(z_{j-1j}) \end{bmatrix} = \begin{bmatrix} e^{ik_{zj}d_j} & 0 \\ 0 & e^{-ik_{zj}d_j} \end{bmatrix} \begin{bmatrix} E_1^+(z_{jj+1}) \\ E_1^-(z_{jj+1}) \end{bmatrix} = \vec{P}_j \begin{bmatrix} E_1^+(z_{jj+1}) \\ E_1^-(z_{jj+1}) \end{bmatrix}. \quad (\text{A.33})$$

The usefulness of the above matrix formalism is best demonstrated on the basic problem of finding the amplitudes of waves reflected (r_{1n}) from and transmitted through (t_{1n}) a multilayer system comprised of $n - 2$ layers (indexed from 2 to $n - 1$). By stacking alternately the transformation matrices corresponding to interface crossings \vec{M} and propagation \vec{P} , a direct link between the waves in the 1-st and the n -th medium is established. Setting the amplitude of the incident wave to $E_1^- = 1$ and realizing that $E_n^+ = 0$, we obtain a linear system of two equations for the two unknown amplitudes r_{1n} and t_{1n}

$$\begin{aligned} \begin{bmatrix} r_{1n} \\ 1 \end{bmatrix} &= \vec{M}_{12} \vec{P}_2 \vec{M}_{23} \cdots \vec{M}_{n-2n-1} \vec{P}_{n-1} \vec{M}_{n-1n} \begin{bmatrix} 0 \\ t_{1n} \end{bmatrix} = \vec{M}_{1n} \begin{bmatrix} 0 \\ t_{1n} \end{bmatrix} = \\ &= \begin{bmatrix} m_{11} & m_{12} \\ m_{21} & m_{22} \end{bmatrix} \begin{bmatrix} 0 \\ t_{1n} \end{bmatrix} \end{aligned} \quad (\text{A.34})$$

with the following solution

$$r_{1n}(\vec{q}) = \frac{m_{12}(\vec{q})}{m_{22}(\vec{q})}, \quad (\text{A.35})$$

$$t_{1n}(\vec{q}) = \frac{1}{m_{22}(\vec{q})}. \quad (\text{A.36})$$

We should point out, that apart from the clarity it offers, the matrix approach is appealing also for its straightforward and easy implementation in computation algorithms.

In the context of this thesis and the issues it addresses, we are particularly interested in the scenario, where the source of the plane waves is not outside but embedded within the stratified medium (technically, this applies also to the case of plasmonic antennas placed on top of a substrate). Assuming the source is located inside the j -th layer, the fields in that layer and the upper halfspace are connected via a linear transformation

$$\begin{bmatrix} E_j^+ \\ E_j^- \end{bmatrix} + \begin{bmatrix} E_{\text{src}}^+ \\ 0 \end{bmatrix} = \tilde{P}_j^{-1} \tilde{M}_{j,j-1} \cdots \tilde{P}_2^{-1} \tilde{M}_{21} \begin{bmatrix} E^\uparrow \\ 0 \end{bmatrix} = \begin{bmatrix} m_{11} & m_{12} \\ m_{21} & m_{22} \end{bmatrix} \begin{bmatrix} E^\uparrow \\ 0 \end{bmatrix}, \quad (\text{A.37})$$

where $E_{\text{src}}^+(\vec{q})$ designates the amplitude of the wave emitted by the source in the positive direction of the z -axis and E^\uparrow stands for the amplitude of the wave leaving the multilayer upwards. Similar equation can be written also for the wave transmitted into the lower halfspace (E^\downarrow)

$$\begin{bmatrix} E_j^+ \\ E_j^- \end{bmatrix} + \begin{bmatrix} 0 \\ E_{\text{src}}^- \end{bmatrix} = \tilde{M}_{j,j+1} \tilde{P}_{j+1} \cdots \tilde{M}_{n-1,n} \begin{bmatrix} 0 \\ E^\downarrow \end{bmatrix} = \begin{bmatrix} n_{11} & n_{12} \\ n_{21} & n_{22} \end{bmatrix} \begin{bmatrix} 0 \\ E^\downarrow \end{bmatrix}, \quad (\text{A.38})$$

except $E_{\text{src}}^+(\vec{q})$ is now replaced by the amplitude $E_{\text{src}}^-(\vec{q})$ of the wave emitted by the source in the negative direction of the z -axis. A key role is played by the intermediary fields E_j^+ and E_j^- , as they sew together the halfspaces above and below the layer containing the source and ensure that the upward emitted wave can contribute to the amplitude of the wave transmitted into the lower halfspace and vice versa. Mathematically, this statement translates to

$$E^\uparrow(\vec{q}) = t^{\uparrow\uparrow}(\vec{q}) E_{\text{src}}^+(\vec{q}) + t^{\uparrow\downarrow}(\vec{q}) E_{\text{src}}^-(\vec{q}), \quad (\text{A.39})$$

$$E^\downarrow(\vec{q}) = t^{\downarrow\uparrow}(\vec{q}) E_{\text{src}}^+(\vec{q}) + t^{\downarrow\downarrow}(\vec{q}) E_{\text{src}}^-(\vec{q}), \quad (\text{A.40})$$

where the transmission coefficients $t^{\uparrow\uparrow}(\vec{q})$, $t^{\uparrow\downarrow}(\vec{q})$, $t^{\downarrow\uparrow}(\vec{q})$, and $t^{\downarrow\downarrow}(\vec{q})$ are easily obtained by subtracting Eqs. (A.37) and (A.38) from each other and matching the terms in front of the source amplitudes E_{src}^+ and E_{src}^- with their counterparts in Eqs. (A.39) and (A.40)

$$t^{\uparrow\uparrow}(\vec{q}) = \frac{n_{22}(\vec{q})}{m_{11}(\vec{q}) n_{22}(\vec{q}) - m_{21}(\vec{q}) n_{12}(\vec{q})}, \quad (\text{A.41})$$

$$t^{\uparrow\downarrow}(\vec{q}) = \frac{n_{12}(\vec{q})}{m_{11}(\vec{q}) n_{22}(\vec{q}) - m_{21}(\vec{q}) n_{12}(\vec{q})}, \quad (\text{A.42})$$

$$t^{\downarrow\uparrow}(\vec{q}) = \frac{m_{21}(\vec{q})}{m_{11}(\vec{q}) n_{22}(\vec{q}) - m_{21}(\vec{q}) n_{12}(\vec{q})}, \quad (\text{A.43})$$

$$t^{\downarrow\downarrow}(\vec{q}) = \frac{m_{11}(\vec{q})}{m_{11}(\vec{q}) n_{22}(\vec{q}) - m_{21}(\vec{q}) n_{12}(\vec{q})}. \quad (\text{A.44})$$

Far-field characterization of objects

The framework of far-field projections presented in this appendix serves as a platform for the calculation of various quantities characterizing the response of systems encountered in this thesis. The basic and most common is the scattering cross-section $C_{\text{sca}}(\omega)$ defined as the ratio of the power scattered by an object W_{sca} and the intensity I_0 of the plane wave illuminating it. Adhering to the notation used in the above paragraphs, the total power scattered by the object can be broken down into two distinct contributions $W_{\text{sca}}^{\uparrow}$ and $W_{\text{sca}}^{\downarrow}$, i.e. power emitted into the upper (\uparrow) and lower (\downarrow) halfspaces. Assuming the object is illuminated from above so that $I_0 = k_1 |\vec{E}_0|^2 / (2\mu_0\omega)$, the scattering cross-section is obtained by integrating the far-field Poynting vector over the azimuthal and declination angles φ and θ

$$C_{\text{sca}} = \frac{W_{\text{sca}}^{\uparrow} + W_{\text{sca}}^{\downarrow}}{I_0} = \int_0^{\frac{\pi}{2}} d\theta \int_0^{2\pi} d\varphi r^2 \sin\theta \frac{|\vec{E}_{\text{FF}}^{\uparrow}(\varphi, \theta)|^2}{|\vec{E}_0|^2} + \frac{k_n}{k_1} \int_{\frac{\pi}{2}}^{\pi} d\theta \int_0^{2\pi} d\varphi r^2 \sin\theta \frac{|\vec{E}_{\text{FF}}^{\downarrow}(\varphi, \theta)|^2}{|\vec{E}_0|^2}. \quad (\text{A.45})$$

If necessary, one can easily change the integration variables to the directional cosines s_x and s_y or the lateral wavevector components q_x and q_y by means of the substitutions prescribed by Eq. (A.4)–(A.7) and the interconnection between the far-field and the Fourier components of the near-field captured by Eqs. (A.8) and (A.9). Splitting the total scattering cross-section into two parts (one for each halfspace), we arrive at the following alternative integration schemes

$$\begin{aligned} C_{\text{sca}}^{\uparrow} &= r^2 \int_0^1 ds_{\parallel} \int_0^{2\pi} d\varphi \frac{s_{\parallel}}{\sqrt{1-s_{\parallel}^2}} \frac{|\vec{E}_{\text{FF}}^{\uparrow}(\varphi, s_{\parallel})|^2}{|\vec{E}_0|^2} = r^2 \iint_{s_{\parallel} \leq 1} ds_x ds_y \frac{1}{\sqrt{1-s_{\parallel}^2}} \frac{|\vec{E}_{\text{FF}}^{\uparrow}(s_x, s_y)|^2}{|\vec{E}_0|^2} = \\ &= 4\pi^2 \iint_{q \leq k_1} dq_x dq_y \frac{k_{z1}}{k_1} \frac{|\vec{E}^{\uparrow}(q_x, q_y, z^{\uparrow})|^2}{|\vec{E}_0|^2}, \end{aligned} \quad (\text{A.46})$$

$$\begin{aligned} C_{\text{sca}}^{\downarrow} &= \frac{k_n}{k_1} r^2 \int_0^1 ds_{\parallel} \int_0^{2\pi} d\varphi \frac{s_{\parallel}}{\sqrt{1-s_{\parallel}^2}} \frac{|\vec{E}_{\text{FF}}^{\downarrow}(\varphi, s_{\parallel})|^2}{|\vec{E}_0|^2} = \frac{k_n}{k_1} r^2 \iint_{s_{\parallel} \leq 1} ds_x ds_y \frac{1}{\sqrt{1-s_{\parallel}^2}} \frac{|\vec{E}_{\text{FF}}^{\downarrow}(s_x, s_y)|^2}{|\vec{E}_0|^2} = \\ &= 4\pi^2 \iint_{q \leq k_n} dq_x dq_y \frac{k_{zn}}{k_1} \frac{|\vec{E}^{\downarrow}(q_x, q_y, z^{\downarrow})|^2}{|\vec{E}_0|^2}. \end{aligned} \quad (\text{A.47})$$

Note that our definition of the scattering cross-section does not include the power scattered into guided waves such as surface plasmon polaritons occurring at metal-dielectric interfaces or waveguide modes supported by dielectric layers.

Another attribute frequently used for characterization of objects is the extinction cross-section C_{ext} . It essentially quantifies, how well an object dissipates the energy supplied by the source – in our case a plane wave propagating along a wavevector \vec{k}_0 . The losses suffered by the incident wave can be either due to scattering (into the far-field and guided modes) or absorption (within the substrate and the object itself). The expression for C_{ext} can be elegantly inferred from the balance between the power entering and leaving the region V enclosed by the planes z^{\uparrow} and z^{\downarrow} . Let us begin by specifying the spatial profile of the incident wave within the plane z^{\uparrow} . Embracing the spherical coordinate basis, its electric field components are

$$\vec{E}_0(\vec{r}_{\parallel}, z^{\uparrow}) = \vec{E}_0 e^{i\vec{k}_0 \cdot \vec{r}} = \begin{bmatrix} E_{s0} \\ E_{p0} \end{bmatrix} e^{i\vec{q}_0 \cdot \vec{r}_{\parallel}} e^{-ik_{z1}^{(0)} z^{\uparrow}}, \quad (\text{A.48})$$

where the minus sign in front of the vertical wavevector component $k_{z1}^{(0)} = \sqrt{k_1^2 - |\vec{q}_0|^2}$ indicates that the wave is propagating downwards.

Obviously, the power W_{in} entering the laterally unbound region V is in principle infinite, but since it does not appear in the final expression for the extinction cross-section, we have no reason to be concerned. As for the power leaving that region, it can be broken down into two parts: power emitted into the upper (W_{out}^\uparrow) and the lower ($W_{\text{out}}^\downarrow$) halfspace. Importantly, we have to take into account not only the scattered waves, but also the original wave that can be, in the presence of a substrate, partially reflected and contribute, therefore, to both the upward and the downward power flux. Employing one of the integration schemes shown in Eq. (A.46), the energy flowing into the upper halfspace amounts to

$$\begin{aligned} W_{\text{out}}^\uparrow &= \frac{4\pi^2}{2\mu_0\omega} \iint_{q \leq k_1} d\vec{q}^2 k_{z1} \left| \vec{E}_0^\uparrow(\vec{q}, z^\uparrow) + \vec{E}^\uparrow(\vec{q}, z^\uparrow) \right|^2 = \\ &= W_{\text{out}}^{\uparrow(0)} + W_{\text{sca}}^\uparrow + \frac{4\pi^2}{\mu_0\omega} \iint_{q \leq k_1} d\vec{q}^2 k_{z1} \text{Re} \left\{ \vec{E}_0^{\uparrow*}(\vec{q}, z^\uparrow) \cdot \vec{E}^\uparrow(\vec{q}, z^\uparrow) \right\}, \end{aligned} \quad (\text{A.49})$$

where the single non-zero Fourier component of the reflected electric field reads

$$\vec{E}_0^\uparrow(\vec{q}, z^\uparrow) = \frac{1}{4\pi^2} \iint_{-\infty}^{\infty} d\vec{r}_\parallel^2 e^{-i\vec{q}\cdot\vec{r}_\parallel} \vec{E}_0^\uparrow(\vec{q}_0) e^{i\vec{q}_0\cdot\vec{r}_\parallel} e^{-ik_{z1}^{(0)}z^\uparrow} = \begin{bmatrix} r_{1n}^s(\vec{q}_0) E_{s0} \\ r_{1n}^p(\vec{q}_0) E_{p0} \end{bmatrix} \delta(\vec{q} - \vec{q}_0) e^{-ik_{z1}^{(0)}z^\uparrow}. \quad (\text{A.50})$$

Similarly, the power flux through the z^\downarrow plane can be written as

$$\begin{aligned} W_{\text{out}}^\downarrow &= \frac{4\pi^2}{2\mu_0\omega} \iint_{q \leq k_n} d\vec{q}^2 k_{zn} \left| \vec{E}_0^\downarrow(\vec{q}, z^\downarrow) + \vec{E}^\downarrow(\vec{q}, z^\downarrow) \right|^2 = \\ &= W_{\text{out}}^{\downarrow(0)} + W_{\text{sca}}^\downarrow + \frac{4\pi^2}{\mu_0\omega} \iint_{q \leq k_n} d\vec{q}^2 k_{zn} \text{Re} \left\{ \vec{E}_0^{\downarrow*}(\vec{q}, z^\downarrow) \cdot \vec{E}^\downarrow(\vec{q}, z^\downarrow) \right\} \end{aligned} \quad (\text{A.51})$$

with the transmitted electric field given by

$$\vec{E}_0^\downarrow(\vec{q}, z^\downarrow) = \frac{1}{4\pi^2} \iint_{-\infty}^{\infty} d\vec{r}_\parallel^2 e^{-i\vec{q}\cdot\vec{r}_\parallel} \vec{E}_0^\downarrow(\vec{q}_0) e^{i\vec{q}_0\cdot\vec{r}_\parallel} e^{-ik_{z1}^{(0)}z^\downarrow} = \begin{bmatrix} t_{1n}^s(\vec{q}_0) E_{s0} \\ t_{1n}^p(\vec{q}_0) E_{p0} \end{bmatrix} \delta(\vec{q} - \vec{q}_0) e^{-ik_{z1}^{(0)}z^\downarrow}. \quad (\text{A.52})$$

The Fresnel reflection ($r_{1n}^{s/p}$) and transmission ($t_{1n}^{s/p}$) coefficients appearing in the above expressions and capturing the passage of the incident wave through the bare substrate can be calculated using Eqs. (A.35) and (A.36). Also note, that the square modulus in Eqs. (A.49) and (A.51) gives rise to three terms, two of which can be readily identified as the purely scattered power $W_{\text{sca}}^{\uparrow/\downarrow}$ and the power reflected from ($W_{\text{out}}^{\uparrow(0)}$) or transmitted through ($W_{\text{out}}^{\downarrow(0)}$) the substrate in the absence of the object. The affiliation of the remaining term can be established via the realization that the total power flux out of the region V must be equal to the incoming power minus the losses due to absorption. Splitting the absorption into two contributions, the power that would be lost within the bare substrate $W_{\text{abs}}^{(0)}$ and the correction brought about by the presence of the object W_{abs} , we obtain the following equality

$$W_{\text{out}} = W_{\text{out}}^\uparrow + W_{\text{out}}^\downarrow = W_{\text{in}} - W_{\text{abs}}^{(0)} - W_{\text{abs}}. \quad (\text{A.53})$$

Finally, recalling the definition of the extinction as the sum of the scattering and absorption $W_{\text{ext}} = W_{\text{sca}} + W_{\text{abs}}$ and recognizing that $W_{\text{out}}^{\uparrow(0)} + W_{\text{out}}^{\downarrow(0)} = W_{\text{in}} - W_{\text{abs}}^{(0)}$, we find the term corresponding to the interference between the incident and scattered waves to be directly linked to the sought extinction cross-section

$$C_{\text{ext}}^{\uparrow} = -4\pi^2 \iint_{q \leq k_1} d\vec{q}^2 \frac{k_{z1}}{k_1} \frac{2\text{Re} \left\{ \vec{E}_0^{\uparrow*}(\vec{q}, z^{\uparrow}) \cdot \vec{E}^{\uparrow}(\vec{q}, z^{\uparrow}) \right\}}{|\vec{E}_0|^2} = -\frac{8\pi^2}{|\vec{E}_0|^2} \frac{k_{z1}^{(0)}}{k_1} \text{Re} \left\{ \left[\begin{array}{cc} r_{1n}^{\text{s}*}(\vec{q}_0) E_{\text{s}0}^* & r_{1n}^{\text{p}*}(\vec{q}_0) E_{\text{p}0}^* \end{array} \right] \times \right. \\ \left. \times e^{ik_{z1}^{(0)} z^{\uparrow}} \left[\begin{array}{c} t_{\text{s}}^{\uparrow\uparrow}(\vec{q}_0) E_{\text{src}}^{+\text{s}}(\vec{q}_0) + t_{\text{s}}^{\uparrow\downarrow}(\vec{q}_0) E_{\text{src}}^{-\text{s}}(\vec{q}_0) \\ t_{\text{p}}^{\uparrow\uparrow}(\vec{q}_0) E_{\text{src}}^{+\text{p}}(\vec{q}_0) + t_{\text{p}}^{\uparrow\downarrow}(\vec{q}_0) E_{\text{src}}^{-\text{p}}(\vec{q}_0) \end{array} \right] \right\}, \quad (\text{A.54})$$

$$C_{\text{ext}}^{\downarrow} = -4\pi^2 \iint_{q \leq k_n} d\vec{q}^2 \frac{k_{zn}}{k_1} \frac{2\text{Re} \left\{ \vec{E}_0^{\uparrow*}(\vec{q}, z^{\downarrow}) \cdot \vec{E}^{\uparrow}(\vec{q}, z^{\downarrow}) \right\}}{|\vec{E}_0|^2} = -\frac{8\pi^2}{|\vec{E}_0|^2} \frac{k_{zn}^{(0)}}{k_1} \text{Re} \left\{ \left[\begin{array}{cc} t_{1n}^{\text{s}*}(\vec{q}_0) E_{\text{s}0}^* & t_{1n}^{\text{p}*}(\vec{q}_0) E_{\text{p}0}^* \end{array} \right] \times \right. \\ \left. \times e^{ik_{z1}^{(0)} z^{\uparrow}} \left[\begin{array}{c} t_{\text{s}}^{\downarrow\uparrow}(\vec{q}_0) E_{\text{src}}^{+\text{s}}(\vec{q}_0) + t_{\text{s}}^{\downarrow\downarrow}(\vec{q}_0) E_{\text{src}}^{-\text{s}}(\vec{q}_0) \\ t_{\text{p}}^{\downarrow\uparrow}(\vec{q}_0) E_{\text{src}}^{+\text{p}}(\vec{q}_0) + t_{\text{p}}^{\downarrow\downarrow}(\vec{q}_0) E_{\text{src}}^{-\text{p}}(\vec{q}_0) \end{array} \right] \right\}. \quad (\text{A.55})$$

We should point out that in certain circumstances, one or even both of the above expressions can be negative. This seemingly unreasonable and counterintuitive result is made possible by the generalization of the whole concept of extinction and scattering cross-sections to systems with a substrate. If an object is added to such a system, it can redistribute the flow of energy into the upper and lower halfspaces to such extent that in one of them, the new power flux exceeds the original value and we obtain a negative contribution to the extinction. Similarly, when a substrate is absorbing, the introduction of an object can alleviate these substrate losses, which leads to a negative correction to the overall absorption. Provided this reduction in absorption exceeds the energy dissipation due to scattering, the total extinction cross-section of the object will be negative.

Appendix B

Vector spherical harmonics

Vector spherical harmonics represent a complete set of orthogonal functions used for expressing vector fields in the spherical coordinate basis [22]. In electromagnetism, they constitute the bedrock on which the Mie theory, multipole expansion of fields and classical theory of light-matter interaction are built. Here, we recapitulate only their basic definition and properties necessary for understanding and implementation of the advanced procedure for calculating the multipole expansion in stratified media, developed in Section 2.3.

Designating r , φ , and θ as the variables forming the spherical coordinate system and \hat{r} , $\hat{\varphi}$, and $\hat{\theta}$ as the associated basis vectors, vector spherical harmonics $\vec{Y}_l^m(\varphi, \theta)$ are generated from scalar spherical harmonics $Y_l^m(\varphi, \theta)$ by means of the vector differential operator $\vec{\nabla}$

$$\vec{Y}_l^m(\varphi, \theta) = r \vec{\nabla} Y_l^m(\varphi, \theta), \quad (\text{B.1})$$

$$\hat{r} \times \vec{Y}_l^m(\varphi, \theta) = \vec{r} \times \vec{\nabla} Y_l^m(\varphi, \theta), \quad (\text{B.2})$$

where the index l can assume values from zero to infinity, while the index m is limited to integers running from $-l$ to l . Note that we omit here the ‘‘radial’’ vector spherical harmonics $\hat{r} Y_l^m(\varphi, \theta)$, since it does not appear in the multipole expansion of transverse electromagnetic waves. The scalar spherical harmonics themselves are built from associated Legendre polynomials $P_l^m(\cos \theta)$

$$Y_l^m(\varphi, \theta) = \sqrt{\frac{2l+1}{4\pi} \frac{(l-m)!}{(l+m)!}} P_l^m(\cos \theta) e^{im\varphi} \quad (\text{B.3})$$

which are, in turn, generated by Rodrigue’s formula

$$P_l^m(x) = \frac{(-1)^m}{2^l l!} (1-x^2)^{\frac{m}{2}} \frac{d^{l+m}}{dx^{l+m}} (x^2-1)^l, \quad (\text{B.4})$$

valid for $m \geq 0$. Finally, associated Legendre polynomials with a negative m are obtained via the relation

$$P_l^{-m}(x) = (-1)^m \frac{(l-m)!}{(l+m)!} P_l^m(x). \quad (\text{B.5})$$

To gain a clearer picture of what hides behind the rather abstract concept of vector spherical harmonics, we list below the first few of them:

$$\vec{Y}_0^0(\varphi, \theta) = \hat{r} \times \vec{Y}_0^0(\varphi, \theta) = \vec{0}, \quad (\text{B.6})$$

$$\vec{Y}_1^0(\varphi, \theta) = -\sqrt{\frac{3}{4\pi}} \sin \theta \hat{\theta}, \quad (\text{B.7})$$

$$\vec{Y}_1^{\pm 1}(\varphi, \theta) = -\sqrt{\frac{3}{8\pi}} e^{\pm i\varphi} (i \hat{\varphi} \pm \cos \theta \hat{\theta}), \quad (\text{B.8})$$

$$\hat{r} \times \vec{Y}_1^0(\varphi, \theta) = -\sqrt{\frac{3}{4\pi}} \sin \theta \hat{\varphi}, \quad (\text{B.9})$$

$$\hat{r} \times \vec{Y}_1^{\pm 1}(\varphi, \theta) = \sqrt{\frac{3}{8\pi}} e^{\pm i\varphi} (\mp \cos \theta \hat{\varphi} + i \hat{\theta}), \quad (\text{B.10})$$

$$\vec{Y}_2^0(\varphi, \theta) = -\frac{3}{2}\sqrt{\frac{5}{\pi}} \sin \theta \cos \theta \hat{\theta}, \quad (\text{B.11})$$

$$\vec{Y}_2^{\pm 1}(\varphi, \theta) = -\sqrt{\frac{15}{8\pi}} e^{\pm i\varphi} \left(i \cos \theta \hat{\varphi} \pm \cos 2\theta \hat{\theta} \right), \quad (\text{B.12})$$

$$\vec{Y}_2^{\pm 2}(\varphi, \theta) = \sqrt{\frac{15}{8\pi}} \sin \theta e^{\pm 2i\varphi} \left(\pm i \hat{\varphi} + \cos \theta \hat{\theta} \right), \quad (\text{B.13})$$

$$\hat{r} \times \vec{Y}_2^0(\varphi, \theta) = -\frac{3}{2}\sqrt{\frac{5}{\pi}} \sin \theta \cos \theta \hat{\varphi}, \quad (\text{B.14})$$

$$\hat{r} \times \vec{Y}_2^{\pm 1}(\varphi, \theta) = \sqrt{\frac{15}{8\pi}} e^{\pm i\varphi} \left(\mp \cos 2\theta \hat{\varphi} + i \cos \theta \hat{\theta} \right), \quad (\text{B.15})$$

$$\hat{r} \times \vec{Y}_2^{\pm 2}(\varphi, \theta) = \sqrt{\frac{15}{8\pi}} \sin \theta e^{\pm 2i\varphi} \left(\cos \theta \hat{\varphi} \mp i \hat{\theta} \right). \quad (\text{B.16})$$

The multipole expansion presented in Section 2.3 jumps forth and back between a Cartesian-based formulation of multipole moments and expansion coefficients Q_{1lm} and Q_{2lm} of individual vector spherical harmonics \vec{Y}_l^m and $\hat{r} \times \vec{Y}_l^m$. The following list specifies, how they are related to each other:

$$p_x^e = -\sqrt{\frac{3}{8\pi}} (Q_{111} - Q_{11-1}), \quad (\text{B.17})$$

$$p_y^e = -i\sqrt{\frac{3}{8\pi}} (Q_{111} + Q_{11-1}), \quad (\text{B.18})$$

$$p_z^e = \sqrt{\frac{3}{4\pi}} Q_{101}, \quad (\text{B.19})$$

$$p_x^m = c\sqrt{\frac{3}{8\pi}} (Q_{211} - Q_{21-1}), \quad (\text{B.20})$$

$$p_y^m = ic\sqrt{\frac{3}{8\pi}} (Q_{211} + Q_{21-1}), \quad (\text{B.21})$$

$$p_z^m = -c\sqrt{\frac{3}{4\pi}} Q_{201}, \quad (\text{B.22})$$

$$Q_{xx}^e = \frac{6i}{k_0} \sqrt{\frac{15}{2\pi}} \left(\frac{Q_{122} + Q_{12-2}}{2} - \frac{Q_{120}}{\sqrt{6}} \right), \quad (\text{B.23})$$

$$Q_{yy}^e = -\frac{6i}{k_0} \sqrt{\frac{15}{2\pi}} \left(\frac{Q_{122} + Q_{12-2}}{2} + \frac{Q_{120}}{\sqrt{6}} \right), \quad (\text{B.24})$$

$$Q_{zz}^e = \frac{12i}{k_0} \sqrt{\frac{15}{2\pi}} \frac{Q_{120}}{\sqrt{6}}, \quad (\text{B.25})$$

$$Q_{xy}^e = -\frac{6}{k_0} \sqrt{\frac{15}{2\pi}} \left(\frac{Q_{122} - Q_{12-2}}{2} \right), \quad (\text{B.26})$$

$$Q_{xz}^e = -\frac{6i}{k_0} \sqrt{\frac{15}{2\pi}} \left(\frac{Q_{121} - Q_{12-1}}{2} \right), \quad (\text{B.27})$$

$$Q_{yz}^e = \frac{6}{k_0} \sqrt{\frac{15}{2\pi}} \left(\frac{Q_{121} + Q_{12-1}}{2} \right), \quad (\text{B.28})$$

$$Q_{xx}^m = -\frac{6ic}{k_0} \sqrt{\frac{15}{2\pi}} \left(\frac{Q_{222} + Q_{22-2}}{2} - \frac{Q_{220}}{\sqrt{6}} \right), \quad (\text{B.29})$$

$$Q_{yy}^m = \frac{6ic}{k_0} \sqrt{\frac{15}{2\pi}} \left(\frac{Q_{222} + Q_{22-2}}{2} + \frac{Q_{220}}{\sqrt{6}} \right), \quad (\text{B.30})$$

$$Q_{zz}^m = -\frac{12ic}{k_0} \sqrt{\frac{15}{2\pi}} \frac{Q_{220}}{\sqrt{6}}, \quad (\text{B.31})$$

$$Q_{xy}^m = \frac{6c}{k_0} \sqrt{\frac{15}{2\pi}} \left(\frac{Q_{222} - Q_{22-2}}{2} \right), \quad (\text{B.32})$$

$$Q_{xz}^m = \frac{6ic}{k_0} \sqrt{\frac{15}{2\pi}} \left(\frac{Q_{221} - Q_{22-1}}{2} \right), \quad (\text{B.33})$$

$$Q_{yz}^m = -\frac{6c}{k_0} \sqrt{\frac{15}{2\pi}} \left(\frac{Q_{221} + Q_{22-1}}{2} \right). \quad (\text{B.34})$$

Bibliography

1. Born, M., *Principles of Optics* ISBN: 9781483103204 (Elsevier Science, City, 1980).
2. Novotny, L., and Hecht, B., *Principles of Nano-Optics* ISBN: 0521832241 (Cambridge University Press, 2006).
3. Weil, B., *Electron Paramagnetic Resonance 2e* 690 pp., ISBN: 047175496X (John Wiley and Sons, 2006).
4. Roessler, M. M., and Salvadori, E., Principles and applications of EPR spectroscopy in the chemical sciences, *Chem. Soc. Rev.* **47**, 2534–2553, doi:[10.1039/C6CS00565A](https://doi.org/10.1039/C6CS00565A) (2018).
5. Likhtenshtein, G. I., *Nitroxides : applications in chemistry, biomedicine, and materials science* ISBN: 978-3-527-31889-6 (Wiley-VCH, Weinheim, 2008).
6. Hinderbergerand, D., and Jeschke, G., in, 1529–1537 (2006), doi:[10.1007/1-4020-3910-7_170](https://doi.org/10.1007/1-4020-3910-7_170).
7. Borbat, P. P., Electron Spin Resonance in Studies of Membranes and Proteins, *Science* **291**, 266–269, doi:[10.1126/science.291.5502.266](https://doi.org/10.1126/science.291.5502.266) (2001).
8. Jeschke, G., and Polyhach, Y., Distance measurements on spin-labelled biomacromolecules by pulsed electron paramagnetic resonance, *Physical Chemistry Chemical Physics* **9**, 1895, doi:[10.1039/B614920K](https://doi.org/10.1039/B614920K) (2007).
9. Eaton, G. R., Weber, R. T., and Barr, D. P., *Quantitative EPR* ISBN: 978-3-211-92947-6 (Springer-Verlag KG, 2010).
10. Junk, M. J. N., *Assessing the Functional Structure of Molecular Transporters by EPR Spectroscopy* ISBN: 978-3-642-25135-1 (Springer-Verlag GmbH, 2012).
11. Gatteschi, D., Sessoli, R., and Villain, J., *Molecular Nanomagnets* doi:[10.1093/acprof:oso/9780198567530.001.0001](https://doi.org/10.1093/acprof:oso/9780198567530.001.0001) (Oxford University Press, 2006).
12. Reijerse, E. J., High-Frequency EPR Instrumentation, *Applied Magnetic Resonance* **37**, 795–818, doi:[10.1007/s00723-009-0070-y](https://doi.org/10.1007/s00723-009-0070-y) (2009).
13. Smith, G. M. *et al.*, Quasi-optical cw mm-wave electron spin resonance spectrometer, *Review of Scientific Instruments* **69**, 3924–3937, doi:[10.1063/1.1149200](https://doi.org/10.1063/1.1149200) (1998).
14. Burghaus, O. *et al.*, A novel high-field/high-frequency EPR and ENDOR spectrometer operating at 3 mm wavelength, *Measurement Science and Technology* **3**, 765–774, doi:[10.1088/0957-0233/3/8/013](https://doi.org/10.1088/0957-0233/3/8/013) (1992).
15. Gao, Z. *et al.*, Cross-Diablo Nanoantenna for Localizing and Enhancing Magnetic Field With Arbitrary Polarization, *Journal of Lightwave Technology* **30**, 829–833, doi:[10.1109/JLT.2011.2180511](https://doi.org/10.1109/JLT.2011.2180511) (2012).
16. Aydin, K. *et al.*, Investigation of magnetic resonances for different split-ring resonator parameters and designs, *New Journal of Physics* **7**, 168–168, doi:[10.1088/1367-2630/7/1/168](https://doi.org/10.1088/1367-2630/7/1/168) (2005).
17. Grosjean, T. *et al.*, Diabolo Nanoantenna for Enhancing and Confining the Magnetic Optical Field, *Nano Letters* **11**, 1009–1013, doi:[10.1021/nl103817f](https://doi.org/10.1021/nl103817f) (2011).
18. Etchegoin, P. G., Ru, E. C. L., and Meyer, M., An analytic model for the optical properties of gold, *The Journal of Chemical Physics* **125**, 164705, doi:[10.1063/1.2360270](https://doi.org/10.1063/1.2360270) (2006).
19. Bloch, F., Nuclear Induction, *Physical Review* **70**, 460–474, doi:[10.1103/PhysRev.70.460](https://doi.org/10.1103/PhysRev.70.460) (1946).
20. Kats, M. A. *et al.*, Effect of radiation damping on the spectral response of plasmonic components, *Optics Express* **19**, 21748, doi:[10.1364/OE.19.021748](https://doi.org/10.1364/OE.19.021748) (2011).

21. Neuman, T. *et al.*, Importance of Plasmonic Scattering for an Optimal Enhancement of Vibrational Absorption in SEIRA with Linear Metallic Antennas, *The Journal of Physical Chemistry C* **119**, 26652–26662, doi:[10.1021/acs.jpcc.5b08344](https://doi.org/10.1021/acs.jpcc.5b08344) (2015).
22. Bohren, C. F., and Huffman, D. R., *Absorption and Scattering of Light by Small Particles* doi:[10.1002/9783527618156](https://doi.org/10.1002/9783527618156) (Wiley, 1998).
23. Koppens, F. H. L., Chang, D. E., and de Abajo, F. J. G., Graphene Plasmonics: A Platform for Strong Light–Matter Interactions, *Nano Letters* **11**, 3370–3377, doi:[10.1021/nl201771h](https://doi.org/10.1021/nl201771h) (2011).
24. Kravets, V. G. *et al.*, Plasmonic Surface Lattice Resonances: A Review of Properties and Applications, *Chemical Reviews* **118**, 5912–5951, doi:[10.1021/acs.chemrev.8b00243](https://doi.org/10.1021/acs.chemrev.8b00243) (2018).
25. De Abajo, F. J. G., Colloquium: Light scattering by particle and hole arrays, *Reviews of Modern Physics* **79**, 1267–1290, doi:[10.1103/RevModPhys.79.1267](https://doi.org/10.1103/RevModPhys.79.1267) (2007).
26. Kravets, V. G. *et al.*, Singular phase nano-optics in plasmonic metamaterials for label-free single-molecule detection, *Nature Materials* **12**, 304–309, doi:[10.1038/nmat3537](https://doi.org/10.1038/nmat3537) (2013).
27. Vecchi, G., Giannini, V., and Rivas, J. G., Shaping the Fluorescent Emission by Lattice Resonances in Plasmonic Crystals of Nanoantennas, *Physical Review Letters* **102**, doi:[10.1103/PhysRevLett.102.146807](https://doi.org/10.1103/PhysRevLett.102.146807) (2009).
28. Henson, J. *et al.*, Plasmon-enhanced light emission based on lattice resonances of silver nanocylinder arrays, *Optics Letters* **37**, 79, doi:[10.1364/OL.37.000079](https://doi.org/10.1364/OL.37.000079) (2011).
29. Rodriguez, S. R. K. *et al.*, Quantum rod emission coupled to plasmonic lattice resonances: A collective directional source of polarized light, *Applied Physics Letters* **100**, 111103, doi:[10.1063/1.3693397](https://doi.org/10.1063/1.3693397) (2012).
30. Yu, R., Pruneri, V., and de Abajo, F. J. G., Resonant Visible Light Modulation with Graphene, *ACS Photonics* **2**, 550–558, doi:[10.1021/ph5004829](https://doi.org/10.1021/ph5004829) (2015).
31. Thackray, B. D. *et al.*, Super-Narrow, Extremely High Quality Collective Plasmon Resonances at Telecom Wavelengths and Their Application in a Hybrid Graphene-Plasmonic Modulator, *Nano Letters* **15**, 3519–3523, doi:[10.1021/acs.nanolett.5b00930](https://doi.org/10.1021/acs.nanolett.5b00930) (2015).
32. Ebbesen, T. W. *et al.*, Extraordinary optical transmission through sub-wavelength hole arrays, *Nature* **391**, 667–669, doi:[10.1038/35570](https://doi.org/10.1038/35570) (1998).
33. Markel, V., Coupled-dipole Approach to Scattering of Light from a One-dimensional Periodic Dipole Structure, *Journal of Modern Optics* **40**, 2281–2291, doi:[10.1080/09500349314552291](https://doi.org/10.1080/09500349314552291) (1993).
34. King, R., *Lateral Electromagnetic Waves : Theory and Applications to Communications, Geophysical Exploration, and Remote Sensing* ISBN: 978-1-4613-9174-6 (Springer New York, New York, NY, 1992).
35. Gradshteyn, I. S., and Ryzhik, I. M., *Table of Integrals, Series and Products* 2nd, ISBN: 0-12-373637-4 (Academic Press Inc., Oxford, 2007).
36. Khorasaninejad, M., and Capasso, F., Metalenses: Versatile multifunctional photonic components, *Science* **358**, eaam8100, doi:[http://dx.doi.org/10.1126/science.aam8100](https://doi.org/10.1126/science.aam8100) (2017).
37. Shi, Z. *et al.*, Single-Layer Metasurface with Controllable Multiwavelength Functions, *Nano Letters* **18**, 2420–2427, doi:<https://doi.org/10.1021/acs.nanolett.7b05458> (2018).
38. Huang, L. *et al.*, Volumetric Generation of Optical Vortices with Metasurfaces, *ACS Photonics* **4**, 338–346, doi:<https://doi.org/10.1021/acsp Photonics.6b00808> (2017).
39. Zhang, Y., Yang, X., and Gao, J., Orbital angular momentum transformation of optical vortex with aluminum metasurfaces, *Scientific Reports* **9**, doi:<https://doi.org/10.1038/s41598-019-45727-6> (2019).

40. Kolman, P., and Chmelík, R., Coherence-controlled holographic microscope, *Optics Express* **18**, 21990, doi:[doi:10.1364/OE.18.021990](https://doi.org/10.1364/OE.18.021990) (2010).
41. Lošt'ák, M. *et al.*, Coherence-controlled holographic microscopy in diffuse media, *Optics Express* **22**, 4180, doi:<https://doi.org/10.1364/OE.22.004180> (2014).
42. Kuang, Z. *et al.*, Ultrafast laser parallel microprocessing using high uniformity binary Dammann grating generated beam array, *Applied Surface Science* **273**, 101–106, doi:<http://dx.doi.org/10.1016/j.apsusc.2013.01.195> (2013).
43. Prongué, D. *et al.*, Optimized kinoform structures for highly efficient fan-out elements, *Applied Optics* **31**, 5706, doi:<https://doi.org/10.1364/AO.31.005706> (1992).
44. Wu, B., Kang, J., and Han, W., Design of Dammann grating based on the parallel recombination simulated annealing algorithm, *Optik - International Journal for Light and Electron Optics* **124**, 2928–2931, doi:<https://doi.org/10.1016/j.ijleo.2012.08.078> (2013).
45. Sinclair, G. *et al.*, Interactive application in holographic optical tweezers of a multi-plane Gerchberg-Saxton algorithm for three-dimensional light shaping, *Optics Express* **12**, 1665, doi:<https://doi.org/10.1364/OPEX.12.001665> (2004).
46. Latychevskaia, T., Iterative phase retrieval in coherent diffractive imaging: practical issues, *Applied Optics* **57**, 7187, doi:<https://doi.org/10.1364/AO.57.007187> (2018).
47. Lin, Z. *et al.*, High-efficiency Bessel beam array generation by Huygens metasurfaces, *Nanophotonics* **8**, 1079–1085, doi:<https://doi.org/10.1515/nanoph-2019-0085> (2019).
48. Radescu, E. E., and Vaman, G., Exact calculation of the angular momentum loss, recoil force, and radiation intensity for an arbitrary source in terms of electric, magnetic, and toroid multipoles, *Physical Review E* **65**, doi:<https://link.aps.org/doi/10.1103/PhysRevE.65.046609> (2002).
49. Alaei, R., Rockstuhl, C., and Fernandez-Corbaton, I., Exact Multipolar Decompositions with Applications in Nanophotonics, *Advanced Optical Materials* **7**, 1800783, doi:<https://doi.org/10.1002/adom.201800783> (2018).
50. Kerker, M., Wang, D.-S., and Giles, C. L., Electromagnetic scattering by magnetic spheres, *Journal of the Optical Society of America* **73**, 765, doi:<https://doi.org/10.1364/JOSA.73.000765> (1983).
51. Liu, W., and Kivshar, Y. S., Generalized Kerker effects in nanophotonics and meta-optics [Invited], *Optics Express* **26**, 13085, doi:<https://doi.org/10.1364/OE.26.013085> (2018).
52. Cappellin, C., Breinbjerg, O., and Frandsen, A., Properties of the transformation from the spherical wave expansion to the plane wave expansion, *Radio Science* **43**, n/a–n/a, doi:[doi:10.1029/2007RS003696](https://doi.org/10.1029/2007RS003696) (2008).
53. Hrtoň, M. *et al.*, Plasmonic Antennas with Electric, Magnetic, and Electromagnetic Hot Spots Based on Babinet's Principle, *Physical Review Applied* **13**, doi:[10.1103/PhysRevApplied.13.054045](https://doi.org/10.1103/PhysRevApplied.13.054045) (2020).
54. Alaei, R., Rockstuhl, C., and Fernandez-Corbaton, I., An electromagnetic multipole expansion beyond the long-wavelength approximation, *Optics Communications* **407**, 17–21, doi:<https://doi.org/10.1016/j.optcom.2017.08.064> (2018).
55. Křápek, V. *et al.*, Independent engineering of individual plasmon modes in plasmonic dimers with conductive and capacitive coupling, *Nanophotonics* **9**, 623–632, doi:<https://doi.org/10.1515/nanoph-2019-0326> (2019).
56. Horák, M. *et al.*, Limits of Babinet's principle for solid and hollow plasmonic antennas, *Scientific Reports* **9**, doi:<https://doi.org/10.1038/s41598-019-40500-1> (2019).

57. Bethe, H. A., Theory of Diffraction by Small Holes, *Physical Review* **66**, 163–182, doi:<https://doi.org/10.1103/PhysRev.66.163> (1944).
58. Jiang, L. *et al.*, Accurate Modeling of Dark-Field Scattering Spectra of Plasmonic Nanostructures, *ACS Nano* **9**, 10039–10046, doi:[10.1021/acsnano.5b03622](https://doi.org/10.1021/acsnano.5b03622) (2015).

List of Publications

1. Hrtoň, M. *et al.*, Optical excitation of acoustic surface plasmons in metallic nanoparticles, *Annalen der Physik* **524**, 751–756, doi:<https://doi.org/10.1002/andp.201200141> (2012).
2. Křápek, V. *et al.*, Spatially resolved electron energy loss spectroscopy of crescent-shaped plasmonic antennas, *Optics Express* **23**, 11855, doi:<https://doi.org/10.1364/OE.23.011855> (2015).
3. Babocký, J. *et al.*, Quantitative 3D Phase Imaging of Plasmonic Metasurfaces, *ACS Photonics* **4**, 1389–1397, doi:<https://doi.org/10.1021/acsp Photonics.7b00022> (2017).
4. Dvořák, P. *et al.*, Imaging of near-field interference patterns by aperture-type SNOM – influence of illumination wavelength and polarization state, *Optics Express* **25**, 16560, doi:<https://doi.org/10.1364/OE.25.016560> (2017).
5. Hrtoň, M., Křápek, V., and Šikola, T., Boundary element method for 2D materials and thin films, *Optics Express* **25**, 23709, doi:<https://doi.org/10.1364/OE.25.023709> (2017).
6. Dvořák, P. *et al.*, Near-field digital holography: a tool for plasmon phase imaging, *Nanoscale* **10**, 21363–21368, doi:<https://doi.org/10.1039/C8NR07438K> (2018).
7. Poyli, M. A. *et al.*, Controlling surface charge and spin density oscillations by Dirac plasmon interaction in thin topological insulators, *Physical Review B* **97**, doi:<https://doi.org/10.1103/PhysRevB.97.115420> (2018).
8. Horák, M. *et al.*, Limits of Babinet’s principle for solid and hollow plasmonic antennas, *Scientific Reports* **9**, doi:<https://doi.org/10.1038/s41598-019-40500-1> (2019).
9. Bouchal, P. *et al.*, High-Resolution Quantitative Phase Imaging of Plasmonic Metasurfaces with Sensitivity down to a Single Nanoantenna, *Nano Letters* **19**, 1242–1250, doi:<https://doi.org/10.1021/acs.nanolett.8b04776> (2019).
10. Křápek, V. *et al.*, Independent engineering of individual plasmon modes in plasmonic dimers with conductive and capacitive coupling, *Nanophotonics* **9**, 623–632, doi:<https://doi.org/10.1515/nanoph-2019-0326> (2019).
11. Hrtoň, M. *et al.*, Plasmonic Antennas with Electric, Magnetic, and Electromagnetic Hot Spots Based on Babinet’s Principle, *Physical Review Applied* **13**, doi:[10.1103/PhysRevApplied.13.054045](https://doi.org/10.1103/PhysRevApplied.13.054045) (2020).
12. Kepič, P. *et al.*, Optically Tunable Mie Resonance VO₂ Nanoantennas for Metasurfaces in the Visible, *ACS Photonics* **8**, 1048–1057, doi:[10.1021/acsp Photonics.1c00222](https://doi.org/10.1021/acsp Photonics.1c00222) (2021).

Attachments

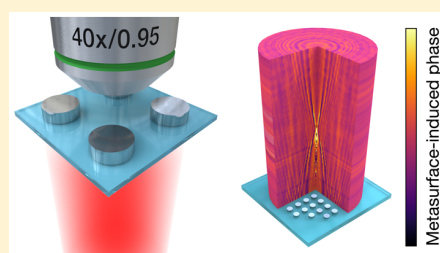
Quantitative 3D Phase Imaging of Plasmonic Metasurfaces

Jiří Babocký,^{†,‡} Aneta Křížová,^{†,‡} Lenka Štrbková,[†] Lukáš Kejík,[†] Filip Ligmajer,^{†,§} Martin Hrtoň,^{†,§} Petr Dvořák,^{†,§} Matěj Týč,[†] Jana Čolláková,^{†,§} Vlastimil Křápek,^{†,§} Radek Kalousek,^{†,§} Radim Chmelík,^{†,§} and Tomáš Šíkola^{*,†,§}[†]Central European Institute of Technology, Purkyňova 123, Brno, 612 00, Czech Republic[‡]TESCAN Brno, s.r.o., Libušina tř. 1, 623 00 Brno, Czech Republic[§]Institute of Physical Engineering, Brno University of Technology, Technická 2896/2, Brno, 616 69, Czech Republic

Supporting Information

ABSTRACT: Coherence-controlled holographic microscopy (CCHM) is a real-time, wide-field, and quantitative light-microscopy technique enabling 3D imaging of electromagnetic fields, providing complete information about both their intensity and phase. These attributes make CCHM a promising candidate for performance assessment of phase-altering metasurfaces, a new class of artificial materials that allow to manipulate the wavefront of passing light and thus provide unprecedented functionalities in optics and nanophotonics. In this paper, we report on our investigation of phase imaging of plasmonic metasurfaces using holographic microscopy. We demonstrate its ability to obtain phase information from the whole field of view in a single measurement on a prototypical sample consisting of silver nanodisc arrays. The experimental data were validated using FDTD simulations and a theoretical model that relates the obtained phase image to the optical response of metasurface building blocks. Finally, in order to reveal the full potential of CCHM, we employed it in the analysis of a simple metasurface represented by a plasmonic zone plate. By scanning the sample along the optical axis we were able to create a quantitative 3D phase map of fields transmitted through the zone plate. The presented results prove that CCHM is inherently suited to the task of metasurface characterization. Moreover, as the temporal resolution is limited only by the camera framerate, it can be even applied in analysis of actively tunable metasurfaces.

KEYWORDS: metasurface, plasmonic, phase, nanoantenna, holographic microscopy, 3D imaging



One of the fastest-growing areas of research in photonics is the field of metasurfaces,^{1–3} where nanoantennas and their ability to control light–matter interaction are utilized in light focusing,^{4–12} polarizing,^{13–16} and holography.^{17–20} In many of these metasurfaces, tailoring the near-field phase response among the individual building blocks is used to modify (e.g., to focus or to bend) the wavefront of light beam and thus modulate its far-field projection. In order to assess the performance of metasurfaces and verify their characteristics predicted by numerical simulations, it is of great importance to be able to quantitatively assess the phase distribution of the electric field in the sample plane, a process which is usually referred to as quantitative phase imaging. However, there are only few methods adequate to this task: (1) Traditionally, ellipsometry has been a method of choice for characterizing optical properties of materials,²¹ giving access also to their phase-altering properties.²² Its use in analysis of metasurfaces is, however, restricted to the special cases where the working principle of respective metasurface is manipulation of phase difference between s- and p-polarized light. Moreover, it often involves an inverse analysis, which becomes troublesome when dealing with samples of unknown structure and composition. (2) Scattering-type scanning near-field optical microscopy (s-SNOM), on the other hand, provides remarkable subdiffraction

lateral resolution and allows investigation of complex near-field patterns generated by nanoantennas, including the phase response.²³ Yet as it is a scanning probe technique, it is inherently slow. Further, its spectral window is usually limited to the infrared region, as the possibility of its extension to the visible has been only rarely reported.^{24,25} (3) The most straightforward acquisition of metasurfaces' phase spectra has been achieved with methods based on interferometry. These involve spectroscopic interferometries either with broadband continuous light sources^{26–31} or ultrashort laser pulses,^{32–36} where the phase shift between the reference and sample beam is determined with the aid of Fourier transformations between relevant domains (temporal/spatial and their corresponding reciprocals). The drawbacks associated with these methods involve problematic dispersion compensation, necessity of introducing a precise delay, and necessity of spectrum sampling with high resolution. Moreover, all aforementioned interferometric approaches provide phase information only from a single spot of a sample (whether optically focused or not). This seriously limits their use for characterization of metamaterials,

Received: January 11, 2017

Published: May 9, 2017

as the measured phase is either an average from a large sample area or a single value from a diffraction-limited spot.

Here we present a powerful quantitative phase-imaging technique that keeps all the benefits of the aforementioned interferometric approaches, provides unambiguous phase information from the whole field of view and thus overcomes the necessity for lateral sample scanning. Our method, which is based on principles of holographic microscopy, is fast and real-time, limited only by the speed of a CCD detector, and allows wide-field analysis of phase properties in situ, even in the diffuse environment.³⁷ To validate our approach, we first applied it to well-known plasmonic disc-shaped nanoantennas, where the phase of transmitted light can be easily predicted and controlled. Then we present an analytical model that relates the obtained phase image to the resonant properties of nanoantennas and thus provides a general framework for the use of holographic microscopy in metamaterial phase analysis. Finally, we demonstrate the unique features and large potential of this method by performing a 3D phase mapping of wavefronts behind a plasmonic zone plate.

RESULTS AND DISCUSSION

The principal element of our work is the coherence-controlled holographic microscopy (CCHM) and its ability to image both the amplitude and the phase of optical fields. Until now, it has found its use exclusively in fast characterization of live biological samples, where the phase contrast arises from the optical path difference.³⁸ Here, we employ it for the first time for spectrally resolved imaging of plasmonic metasurfaces, where the phase change is governed by the scattering properties of individual plasmonic building blocks. This included an upgrade of the conventional CCHM optical setup with a tunable laser and generalization of its theoretical framework toward arbitrary-distributed scatterers (see [Methods](#) for detailed description of CCHM and our experimental setup). The imaging of plasmonic nanoantennas by digital holographic microscopy was previously reported by Suck et al.,³⁹ who demonstrated the use of digital heterodyne holography for imaging of far-field maps produced by plasmonic nanoantennas. In their work, however, they focused only on measuring the intensity of the scattered field using the Kretschmann configuration⁴⁰ and monochromatic illumination. We take full advantage of the ability of CCHM to reconstruct the optical fields including their phase, which gives us more complete information about the fundamental properties of plasmonic antennas and which could be extremely valuable for design and optical characterization of metasurfaces and metamaterials.

Benchmark Sample. To demonstrate the capabilities of our method, we evaluated the phase response of a benchmark sample consisting of multiple arrays of plasmonic nanostructures ([Figure 1](#)). In order to have a simple, polarization independent response, we used silver disc-shaped nanoantennas with diameters ranging from 50 to 200 nm. In each array ($10 \times 10 \mu\text{m}$), the pitch was set to double of the disc diameter, so that the nanoantennas covered the same percentage of the surface ($\approx 20\%$). SEM analysis (see [Supporting Information, Figures S1 and S2](#)) revealed that due to limited resolution of PMMA, the fabrication of the arrays with 50 and 60 nm nanodiscs was not successful, and we left them out from subsequent optical measurements.

First, we measured extinction spectra of the aforementioned nanodisc arrays using conventional confocal optical spectroscopy (spot size $2 \mu\text{m}$) to verify their quality and spectral

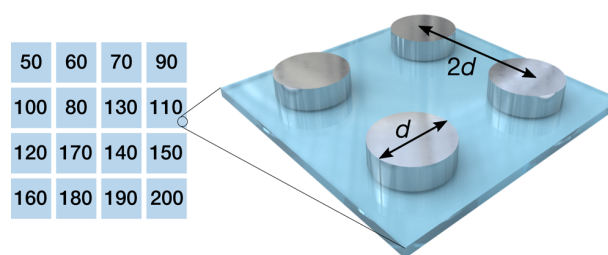


Figure 1. Benchmark sample consisted of silver nanodisc arrays (blue squares). Diameter d of nanodiscs (in nm) is denoted in each blue square; pitch of all arrays was fixed as $2d$.

position of their plasmonic resonances ([Figure 2a](#)). Strong dipolar plasmonic modes of the nanodiscs are apparent in the visible and near-infrared part of the spectrum, and in line with our expectations, they shift toward longer wavelengths with increasing nanodisc diameter.

The measurements were complemented by FDTD simulations of nanodisc arrays with geometrical parameters identical to those from the experiment. As simulations of the entire nanodisc arrays would require unreasonable computational power, we decided to simplify the task by employing periodic boundary conditions. In this way we were able to account for the mutual interaction while keeping the computational time short. The resulting extinction spectra are displayed in [Figure 2b](#), with the resonance peaks blue-shifted with respect to the experimental ones roughly by 20 nm for larger discs and by almost 90 nm for the smallest one. Additional simulations revealed that this spectral shift can be attributed to fabrication imperfections and a thin oxide layer that rapidly forms on the surface of silver nanodiscs (see [Figures S3 and S4 in Supporting Information](#)). Also note that the use of periodic boundary conditions leads to the appearance of a pronounced dip in the extinction spectrum, which moves toward longer wavelengths with increasing disc size and which is the result of a strong diffractive coupling between nanodiscs.^{41,42} However, in view of the fact that the calculated spectra adequately capture the resonant nature of the optical response of the fabricated nanodisc arrays and the absolute spectral position of the resonance is not central for our analysis of the image formation in CCHM (we are more interested in its relative position with respect to the phase profile obtained by CCHM), we consider the agreement between the simulations and the experiment to be sufficient for our purposes.

Next, we used our CCHM setup to obtain a series of images of the amplitude and phase distribution in the plane of nanodisc arrays (sample plane) while we swept the illumination wavelength in the 10 nm steps across the whole accessible spectral range of our microscope. In the subset of measured series of phase images, presented in [Figure 2c](#) (top), we can observe a rapid phase flip that moves toward arrays filled with larger discs (and with resonances at higher wavelengths) as the illumination wavelength is increased. The speckles observed in [Figure 2c](#) do not correspond to individual antennas as the size of these speckles (about $1.4 \mu\text{m}$) is pronouncedly larger than the antenna pitch (up to 400 nm for the largest antennas), as apparent from the zoom-in view (see [Supporting Information, Figure S5](#)). The random noise is caused by fabrication imperfections in terms of a variation of nanodisc dimensions (see further discussion in [Supporting Information](#)). To better visualize the information contained in the phase images, we

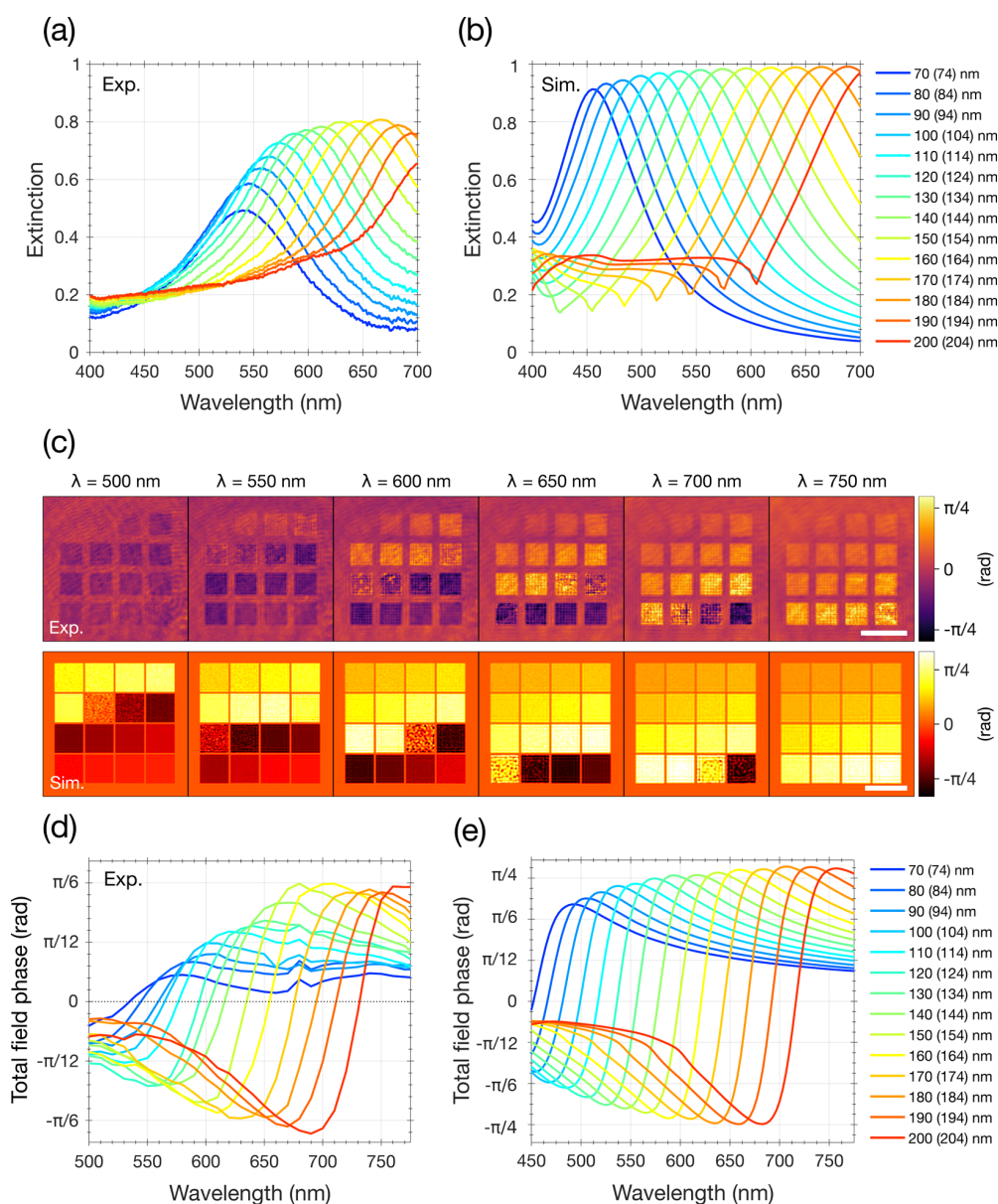


Figure 2. (a) Experimental and (b) FDTD-calculated extinction spectra of silver nanodisc arrays on glass. Both show characteristic plasmon resonances that red-shift with increasing disc diameter (indicated by line colors). The experimental extinction in (a) has been calculated by eq 1, T/T_{REF} , where T is the transmission through the nanodisc array and (T_{REF}) the transmission through the bare substrate. (c) Quantitative phase images of silver nanodisc arrays at a selected subset of illumination wavelengths, measured in CCHM (top) and theoretically calculated (bottom). Scale bars are $20 \mu\text{m}$. (d, e) Spectra of the total field phase at nanodisc arrays of various dimensions extracted from the full set of measured CCHM images (d) and from numerical simulations (e). The small mismatch between measured extinction maxima and zero-crossings in the measured phase spectra is caused by a slight oxidation of our silver nanodiscs during the time between the two measurements.

have extracted the average phase value for each array at all measured wavelengths and plotted the resulting spectra in Figure 2d (while compensating for a small background signal by subtracting the phase outside the arrays). Note that there is no need for phase unwrapping and corrections for 2π phase ambiguity when dealing with plasmonic metasurfaces since their phase shifts are typically smaller than 2π .

Apparently, the phase measured by CCHM exhibits an S-shaped flip from positive (above resonance) to negative values (below resonance) and goes to zero in both regions far from the resonance. That is in contrast with considerations based on a classical model of simple resonant systems, where the phase

changes monotonically from 0 to π (with $\pi/2$ at the resonance).⁴³ Although a single silver disc can be definitely considered such a simple resonant system, propagation of the scattered field through the microscope can lead to its significant phase shift. Furthermore, as the CCHM microscope detects the superposition of this scattered field with the original incident wave, the final phase image strongly depends on their relative amplitudes and phases. In the following, we will present a theoretical description of CCHM image formation that incorporates both of these aspects and is capable to fully reproduce the experimental data. With the optical response of individual building blocks as the only input of our model, we

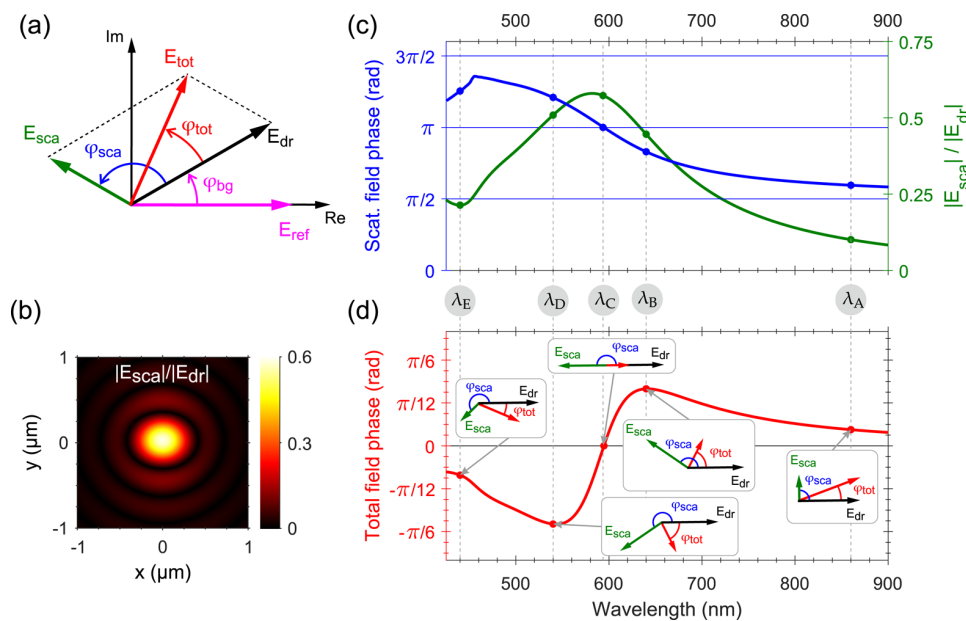


Figure 3. (a) Phasor diagram of the fields forming the signal measured in CCHM. Note that we follow a convention where a phase shift in the counterclockwise direction represents a phase delay. The field that drives the plasmonic structures is denoted as E_{dr} and it is phase-shifted with respect to the reference field E_{ref} by φ_{bg} due to an inevitable path difference between sample and reference arms. The field scattered by nanodiscs (E_{sca}) lags behind the driving one by an angle φ_{sca} . The total measured field E_{tot} is a sum of E_{dr} and E_{sca} , and its phase shift φ_{tot} with respect to the driving field is the ultimate quantity measured in CCHM. (b) Calculated distribution of the electric field amplitude produced in the image plane of the microscope (NA = 0.95, $\lambda = 580$ nm) by a single silver nanodisc with diameter 154 nm. (c) Calculated scattered field phase (blue) and amplitude (green) spectra for the 154 nm nanodisc; the values at each wavelength are extracted from the central part of field distributions that were obtained the same way as in (b); the values of the amplitude and phase at selected wavelengths $\lambda_A - \lambda_E$ (labeled by dots) are used in (d) to elucidate the total field phase formation using phasor diagrams. (d) Calculated phase spectrum of the total field resulting from the superposition of scattered and driving fields (with the superposition of phasors sketched in the boxes).

can thus calculate the phase distribution produced by an arbitrary metasurface that is directly comparable with the experiment.

Theoretical Description. To describe how the fields in the object plane translate into the image plane and how the spatial filtering (diffraction) affects the detected phase distribution, we shall invoke the theory of CCHM imaging, which is fundamentally similar to the classical Abbe theory.^{44,45} Disregarding the geometrical effects like inversion and magnification, the image formed in the image plane corresponds to the convolution of the distribution of sources in the object plane with the amplitude point spread function (PSF) of the microscope. In the reciprocal space this amounts to multiplying the Fourier transform of the sources' distribution by the coherent transfer function (CTF) of the microscope (i.e., the Fourier transform of the PSF). The above can be mathematically put as

$$\begin{aligned} E_{sca}(x_{img}, y_{img}) &\sim \iint dx_{obj} dy_{obj} \text{PSF}(x_{img} - x_{obj}, y_{img} - y_{obj}) P(x_{obj}, y_{obj}) \\ &= \int \int_{-\infty}^{\infty} dk_x dk_y e^{ik_x x_{img}} e^{ik_y y_{img}} P(k_x, k_y) \text{CTF}(k_x, k_y) \end{aligned} \quad (1)$$

where x_{img}, y_{img} denote the spatial coordinates in the image plane, x_{obj}, y_{obj} are the spatial coordinates in the object plane, k_x, k_y stand for the coordinates in the reciprocal space, and $P(x_{obj}, y_{obj})$ defines the distribution of the sources within the object plane. Note that throughout this work we shall use PSF and CTF to describe the impulse response of our system to a radiating point dipole. In this way the sources $P(x_{obj}, y_{obj})$ can be readily identified as the polarization vector induced within

our plasmonic structures. Furthermore, instead of using the continuous polarization vector we shall work with its integral over the volume of the individual discs, thus approximating them with a set of discrete point dipoles $p(x_{obj}, y_{obj})$ of matching strength and orientation. Since the size of the discs is relatively small and we are interested only in the dipolar mode, such simplification should not significantly affect our results.

The electric field in the object plane produced by a single point dipole located at (x_{obj}, y_{obj}) can be written in a compact form using the formalism of the dyadic Green's functions

$$\begin{aligned} E_{sca}^{dip}(x, y) &= \omega^2 \mu_0 \hat{G}(x - x_{obj}, y - y_{obj}) p \\ &= \omega^2 \mu_0 \int \int_{-\infty}^{\infty} dk_x dk_y e^{ik_x x} e^{ik_y y} \hat{M}(k_x, k_y) p e^{-ik_x x_{obj}} e^{-ik_y y_{obj}} \end{aligned} \quad (2)$$

where ω is the angular frequency, μ_0 the free space permeability, and p denotes the complex amplitude of the dipole. Note that the dyadic Green's function \hat{G} and its Fourier transform \hat{M} generally depend on the surroundings of the dipole. In the context of our experiment, we consider the dipole to be situated right on top of a planar glass substrate with an index of refraction $n = 1.47$. The relevant expressions for \hat{G} and \hat{M} can be found in ref 46.

Due to a cutoff in the spatial frequencies that can be transferred by an optical microscope (a fact that also manifests as the inherent inability to resolve two objects less than roughly half a wavelength apart), we need to restrict the integration in eq 2 to a region $\sqrt{k_x^2 + k_y^2} \leq \text{NA} \frac{2\pi}{\lambda}$, where λ denotes the free

space wavelength and NA is the numerical aperture of the used microscope objective (NA = 0.95 in our experiment).⁴⁴ Although a more elaborate procedure incorporating parameters such as the numerical apertures of all microscope components or the type of illumination is available,⁴⁷ the simple cutoff is sufficient for our purposes since it adequately captures the major principle of image formation in CCHM. Finally, the expressions for CTF and PSF, which allow us to mathematically propagate the fields produced by an arbitrary planar distribution of dipoles, are obtained by comparing eq 2 to eq 1

$$\text{CTF}(k_x, k_y) = \omega^2 \mu_0 \hat{M}(k_x, k_y) \Theta \left(\text{NA} \frac{2\pi}{\lambda} - \sqrt{k_x^2 + k_y^2} \right) \quad (3)$$

$$\begin{aligned} \text{PSF}(x, y) &= \text{IFFT}\{\text{CTF}(k_x, k_y)\} \\ &= \omega^2 \mu_0 \iint_{\sqrt{k_x^2 + k_y^2} \leq \text{NA} 2\pi/\lambda} dk_x dk_y e^{ik_x x} e^{ik_y y} \hat{M}(k_x, k_y) \end{aligned} \quad (4)$$

where $\Theta(z)$ is the Heaviside step function and $\text{IFFT}\{\}$ stands for the inverse Fourier transform.

Relying on the assumption that our nanodiscs are small enough to be approximated by point dipoles of matching optical properties, we used eq 4 to calculate the field distribution (essentially the PSF) produced in the image plane of the microscope by a single $D = 150$ nm silver disc at $\lambda = 580$ nm (see Figure 3b). Note that although we consider here a solitary disc, its optical response already incorporates the interaction with neighboring nanodiscs since it was obtained from the FDTD simulations of infinite nanodisc arrays (that were presented in Figure 2b). As expected for a point-like source, the calculated field distribution is very similar to an Airy disc. We repeated the calculations for all other experimentally relevant wavelengths, extracted the amplitudes and also the values of phase at centers of the Airy discs, and plotted the resulting spectra in Figure 3c. The phase spectrum strongly resembles the aforementioned ideal resonant system with two exceptions: The minor ones are the sharp feature around 460 nm and the incomplete π -shift when crossing the resonance. The former is due to the diffractive coupling between nanodiscs, while the latter has its origin in the optical properties of silver, namely in the interband transitions that affect the real part of its dielectric function even far away from their spectral positions.⁴⁷ The third, more important difference, is that the scattered field gains an additional $\pi/2$ phase delay after it propagates through the microscope. This can be readily explained on mathematical grounds: The field of a point dipole at its origin can be broken down into two parts, a purely real diverging term that is in phase with the driving field and a purely imaginary term, which is finite but shifted in phase by $\pi/2$. Importantly, only the latter is transferred through the microscope and participates in the image formation.⁴⁶ Thus, in the end, the diffraction not only limits the spatial resolution we can achieve, but it can also distort the information about the phase distribution in the object plane. As we shall see below, the additional $\pi/2$ phase delay is the main reason why our experimental data assume both positive and negative values. Note that one encounters the same phase shift when looking at the field scattered by an infinite plane of dipoles.⁴⁸ In that case, however, the reason for the $\pi/2$ lag is not the integration limits (i.e., spatial-frequency cutoff) but the singularity in the integrand itself (i.e., the $P(k_x, k_y)$ being the Dirac function).

Diffraction effects obviously play a critical role in the quantitative phase imaging. However, there is one more aspect of CCHM that must be taken into account in order to explain the characteristic S-shape of the measured phase spectra: In holographic microscopy, the electromagnetic field in the object arm is generally a superposition of scattered (or otherwise perturbed) and incident waves. It is this “total field” that eventually interferes with the field transferred by the reference arm. We present a simple phasor representation of the aforementioned process in Figure 3a. The phasor of the reference field \mathbf{E}_{ref} (violet arrow) is fixed to the x -axis, the phasor of the driving field \mathbf{E}_{dr} (black arrow) is shifted with respect to the reference field by an angle φ_{bg} that corresponds to the path difference between the object and reference arms caused by instrument imperfections. This background signal is eventually compensated by simple subtraction from the resulting image. The phasor of the field scattered by the plasmonic structures \mathbf{E}_{sca} (green arrow) lags behind the driving field by an angle φ_{sca} , as discussed above (see Figure 3c). The quantity we ultimately measure with CCHM is the phase delay φ_{tot} of the total field $\mathbf{E}_{\text{tot}} = \mathbf{E}_{\text{dr}} + \mathbf{E}_{\text{sca}}$ (red arrow) with respect to the driving field.³⁸ The presented phasor representation helps us to recognize the fact that the driving field is superposed to the scattered field and significantly alters the wavefront unless we filter it out, for example, via polarization resolved measurements. Therefore, a valid comparison between experiment and theory requires not only consideration of the field scattered by individual nanodiscs as in Figure 3c, but rather the full analysis of the total field \mathbf{E}_{tot} , as we will demonstrate now using the schematics in Figure 3d: For wavelengths well above the resonance (λ_A), the phasor of the scattered field is almost perpendicular to the driving field ($\approx \pi/2$ delay), which is a crucial prerequisite for a high phase contrast. However, the amplitude of the scattered field is rather small and the total phase delay is therefore only minute. As we move closer toward the resonance (λ_B), the orientation of the scattered field becomes largely antiparallel to the driving field ($\approx 4\pi/5$ delay). This is, however, redeemed by a substantial increase in its amplitude, resulting in a high total phase contrast. Once the scattered and driving fields become purely antiparallel (λ_C), the total phase rapidly falls to zero and turns increasingly negative as the phase delay of the scattered field exceeds π (λ_D). Eventually, by moving away from the resonance (λ_E) the amplitude of the scattered field starts to drop again and the phase contrast vanishes.

In order to theoretically validate the measured CCHM images that are shown in Figure 2d, we employed the same procedure as in the calculation of the field intensity and total phase maps of a single disc: First of all, we approximate each disc by a point dipole positioned at its center. The strength and the phase of the dipole was estimated from FDTD simulations, which were performed separately for each disc size. The resulting scattered field in the image plane is obtained, after transition from the continuous (eq 1) to the discrete representation, either by taking the convolution of PSF (defined in eq 4) with the discrete distribution of dipoles or alternatively by multiplying its Fourier transform by CTF (defined in eq 3) and taking the inverse Fourier transform

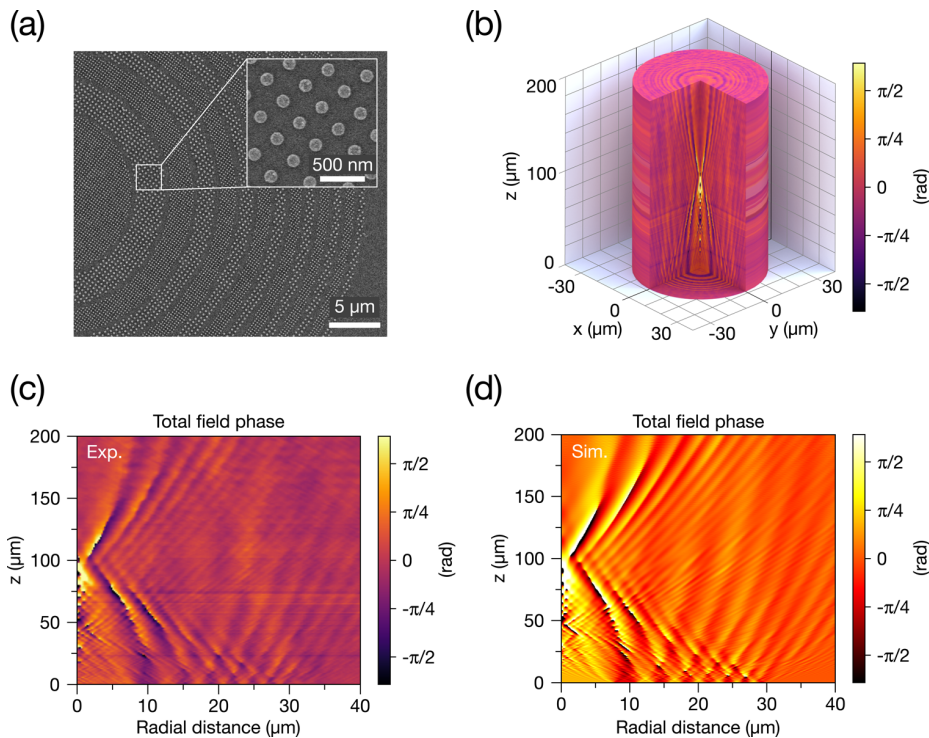


Figure 4. (a) SEM micrograph of the fabricated zone plate where individual zones are formed by silver nanodiscs (130 and 190 nm). (b) 3D visualization of the measured total phase distribution in the half-space above the plasmonic zone-plate. Measured (c) and simulated (d) phase map in the xz -plane above the zone plate where the main ($z \approx 100 \mu\text{m}$) and subsidiary ($z \approx 50 \mu\text{m}$, $z \approx 25 \mu\text{m}$) focal points are clearly distinguishable close to the zero radial distance.

$$\begin{aligned}
 E_{\text{sca}}^{\text{array}}(x_{\text{img}}, y_{\text{img}}) &= \sum_{j=1}^N \text{PSF}(x_{\text{img}} - x_j, y_{\text{img}} - y_j) p_j \\
 &= \iint_{\sqrt{k_x^2 + k_y^2} \leq \text{NA}2\pi/\lambda} dk_x dk_y e^{ik_x x_{\text{img}}} e^{ik_y y_{\text{img}}} \text{CTF}(k_x, k_y) p(k_x, k_y)
 \end{aligned}
 \quad (5)$$

where p_j are the complex amplitudes of the individual dipoles and $p(k_x, k_y) = \sum_{j=1}^N p_j e^{-ik_x x_j} e^{-ik_y y_j}$ is the Fourier transform of their distribution. Even though CTF offers a closed form expression and the equidistant distribution of dipoles in arrays of a particular size makes the calculation of its Fourier transform rather straightforward, the calculations in the reciprocal space are prone to numerical errors. For that reason, we decided to follow the PSF convolution approach and utilize the whole framework established so far to calculate a series of total phase images. We present the results directly below the corresponding experimentally obtained images in Figure 2c. From their comparison, it is clear that our model reproduces well all the important features observed in the measured CCHM images. In order to make a quantitative comparison, we have extracted the average phase from each array in our calculated images and plotted the resulting spectra in Figure 2e. While there are slight differences in the phase flip amplitudes and spectral positions, our model reproduces nicely the experimental data shown in Figure 2d, with their characteristic S-shaped phase flips situated close to the disc resonances. The ability of our theoretical model to reliably predict and interpret the outcomes of measurements facilitates the use of CCHM for design of plasmonic devices with complex functionality, namely for direct

inspection and verification of inner workings of metasurfaces based on new and unexplored concepts.

3D Phase Imaging. So far we have used CCHM only for evaluation of phase distribution in a single plane. Its major benefit, however, is the ability to produce 3D phase maps by z -stacking images taken at different defocus levels. To demonstrate the usefulness of this feature for characterization of plasmonic metamaterials, we have decided to perform a 3D phase imaging of the electric field produced behind a focusing plasmonic metasurface based on the principle of a zone plate (see Figure 4a). The zone plate was designed and fabricated according to a well-known analytical model which, for a desired focal length ($100 \mu\text{m}$), defines the overall geometry.⁴⁹ We have chosen the operational wavelength in the middle of our experimental range (630 nm) and filled the individual zones with previously studied nanodiscs (130 and 190 nm) that maximized the phase difference at this wavelength (approximately $\pi/5$, see Figure 2d). Although the analytical model prescribes a π -phase difference between the neighboring zones, even such a considerably smaller phase step is sufficient for acceptable focusing performance.

Using the precise sample positioning, we were then able to create a 3D experimental quantitative phase map of wavefronts propagating from the zone plate by z -stacking a series of CCHM phase images acquired above the sample plane in $1 \mu\text{m}$ steps (Figure 4b). The detail of the cross-section in the xz -plane, displayed in Figure 4c, clearly reveals stripes of constant phase originating at the sample surface and converging toward the main focal point at $z \approx 100 \mu\text{m}$, which is in good agreement with its planned position. We can also observe subsidiary focal points. Their positions, however, do not coincide with those of

an ideal zone plate (e.g., the secondary focal point should be situated at one-third and not at one-half of the zone plate focal length). We ascribe this discrepancy to the fact that the field distribution produced by our nanodiscs does not fully match the one from the design. More specifically, the transition between neighboring zones is not abrupt but gradual which makes them effectively narrower (see Figure S6 and related discussion in Supporting Information). Nevertheless, by feeding the real nanodisc distribution into the theoretical apparatus described above, we obtained a phase distribution (see Figure 4d) that perfectly matches experimental results, including the positions of the subsidiary focal points. The large phase values near the focal point nicely illustrate the fact that the total phase is a product of both phase and also amplitude of the scattered wave.

CONCLUSIONS

We have demonstrated the suitability of CCHM for optical characterization of plasmonic metasurfaces, especially those where the desired optical properties are achieved by an appropriate modulation of the phase of the passing electromagnetic wave. As a benchmark test we performed spectroscopic measurements of phase shifts produced by silver nanodisc arrays. The major advantage of CCHM over other phase-measuring techniques is its ability to provide spatially resolved phase information in the whole field of view in a single measurement at time scales limited only by the camera framerate. For a first time, we have utilized this unique property to create a 3D phase map of fields transmitted through a plasmonic zone plate. In addition, by recalling the basic principles governing the image formation in conventional microscopy, we have developed a model that enables theoretical prediction of the CCHM measurement results. This includes even measurements of phase changes caused by arbitrarily distributed scatterers, which constitutes a major and novel extension of the CCHM to the domain of nanophotonics. Although all our measurements are performed with plasmonic metasurfaces in the visible range, the whole concept can be extended not only to shorter or longer wavelengths (provided that the setup is composed of suitable optical elements and detector) but also to other types of metasurfaces (e.g., dielectric ones). We believe that the qualities described in this contribution justify our view of CCHM as a unique imaging technique with the potential to become a versatile tool in metamaterial and metasurface research.

METHODS

Coherence Controlled Holographic Microscopy. In our experiments, we used a coherence-controlled holographic microscope (CCHM) that was developed at our institute and is now commercially available (Tescan Q-Phase).⁵⁰ Although it is conventionally used for fast imaging of live biological samples using incoherent light sources,³⁸ we equipped it with a supercontinuum laser (Fianium SC480–10) with an acousto-optic tunable filter (AOTF) to perform spectrally resolved imaging of plasmonic nanostructures. The principle of CCHM is based on off-axis incoherent holography.^{38,47} Briefly, the light coming from a source is split into object and reference arms first (see Figure 5). The light in the object arm interacts with a studied sample, whereas the light in the identical reference arm passes only through a reference sample without nanoantennas. Both beams then interfere in a CCD detector plane, forming a

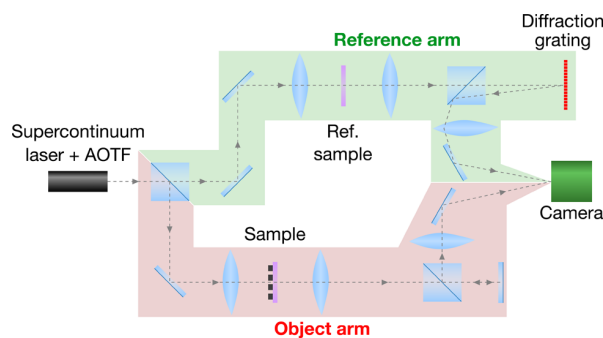


Figure 5. Optical setup of a coherence-controlled holographic microscope equipped with a supercontinuum laser and an acousto-optic tunable filter (AOTF). Detailed description can be found, for example, in ref 38.

pattern of interference fringes. As the beams interfere at an angle (off-axis setup), the phase-containing terms in the Fourier transform of the resulting interference pattern are (spatially) separated from amplitude-only ones. This allows us to independently extract these terms and then numerically reconstruct the complex amplitude of the wave at each point of the studied sample.⁵¹ Note that the lateral resolution of CCHM is comparable to conventional wide field optical microscopes, as discussed and demonstrated in ref 38. The temporal resolution depends on the camera sensitivity and light source intensity. Typical acquisition time for one phase image was approximately 300 ms with the current experimental setup. Covering the whole spectral region with 31 phase images usually took us several minutes, mainly due to lags caused by slow manual control of the laser wavelength.

Sample Fabrication. All nanostructures were fabricated by electron beam lithography (Tescan Mira 3 SEM with Raith Elphy EBL system) in 140 nm thick PMMA layer on a glass substrate. A thin layer of conductive polymer (Allresist Electra 92) was spin-coated on top of the resist to reduce charging effects during the exposure. Samples were developed in MIBK:IPA (1:3) solution (immersed for 60 s) and rinsed in IPA for 30 s. The development was followed by evaporation of 3 nm of Ti and 40 nm of Ag. The fabrication was finished by the lift-off process in acetone.

ASSOCIATED CONTENT

Supporting Information

The Supporting Information is available free of charge on the ACS Publications website at DOI: 10.1021/acsp Photonics.7b00022.

FDTD simulations of solitary nanodiscs and calculated field distributions behind ideal and realistic zone plates (PDF).

AUTHOR INFORMATION

Corresponding Author

*E-mail: sikola@fme.vutbr.cz.

ORCID

Filip Ligmajer: 0000-0003-0346-4110

Petr Dvořák: 0000-0003-3659-9249

Notes

The authors declare the following competing financial interest(s): J.B. and A.K. are employees of Tescan, a company

producing coherence-controlled holographic microscopes such as the one used in this study. All other authors declare no competing interests.

ACKNOWLEDGMENTS

This work was supported by the Grant Agency of the Czech Republic (Grant Nos. 15-21581S and 15-14612S), MEYS CR (Project No. LQ1601 – CEITEC 2020), Technology Agency of the Czech Republic (Grant No. TE01020233), and BUT (Project No. FSI/STI-J-15-2897). We acknowledge CEITEC Nano Research Infrastructure and Core Facility Experimental Biophotonics (both supported by MEYS CR within projects LM2015041 and LM2015062) for providing us with access to their facilities.

REFERENCES

- (1) Yu, N.; Capasso, F. Flat Optics with Designer Metasurfaces. *Nat. Mater.* **2014**, *13*, 139–150.
- (2) Kildishev, A. V.; Boltasseva, A.; Shalaev, V. M. Planar Photonics with Metasurfaces. *Science* **2013**, *339*, 1232009–1232009.
- (3) Zouhdi, S.; Sihvola, A.; Vinogradov, A. P. *Metamaterials and Plasmonics: Fundamentals, Modelling, Applications*; Springer Netherlands: Dordrecht, 2009.
- (4) Yu, N.; Genevet, P.; Kats, M. A.; Aieta, F.; Tetienne, J.-P.; Capasso, F.; Gaburro, Z. Light Propagation with Phase Discontinuities: Generalized Laws of Reflection and Refraction. *Science* **2011**, *334*, 333–337.
- (5) Li, Z.; Palacios, E.; Butun, S.; Aydin, K. Visible-Frequency Metasurfaces for Broadband Anomalous Reflection and High-Efficiency Spectrum Splitting. *Nano Lett.* **2015**, *15*, 1615–1621.
- (6) Khorasaninejad, M.; Chen, W. T.; Oh, J.; Capasso, F. Super-Dispersive Off-Axis Meta-Lenses for Compact High Resolution Spectroscopy. *Nano Lett.* **2016**, *16*, 3732–3737.
- (7) Khorasaninejad, M.; Zhu, A. Y.; Roques-Carmes, C.; Chen, W. T.; Oh, J.; Mishra, I.; Devlin, R. C.; Capasso, F. Polarization-Insensitive Metalenses at Visible Wavelengths. *Nano Lett.* **2016**, *16*, 7229–7234.
- (8) Garoli, D.; Zilio, P.; Gorodetski, Y.; Tantussi, F.; De Angelis, F. Beaming of Helical Light from Plasmonic Vortices via Adiabatically Tapered Nanotip. *Nano Lett.* **2016**, *16*, 6636–6643.
- (9) Ee, H.-S.; Agarwal, R. Tunable Metasurface and Flat Optical Zoom Lens on a Stretchable Substrate. *Nano Lett.* **2016**, *16*, 2818–2823.
- (10) Zhan, A.; Colburn, S.; Trivedi, R.; Fryett, T. K.; Dodson, C. M.; Majumdar, A. Low-Contrast Dielectric Metasurface Optics. *ACS Photonics* **2016**, *3*, 209–214.
- (11) Lin, D.; Holsteen, A. L.; Maguid, E.; Wetzstein, G.; Kik, P. G.; Hasman, E.; Brongersma, M. L. Photonic Multitasking Interleaved Si Nanoantenna Phased Array. *Nano Lett.* **2016**, *16*, 7671–7676.
- (12) Huntington, M. D.; Lauhon, L. J.; Odom, T. W. Subwavelength Lattice Optics by Evolutionary Design. *Nano Lett.* **2014**, *14*, 7195–7200.
- (13) Zhao, Y.; Alù, A. Tailoring the Dispersion of Plasmonic Nanorods To Realize Broadband Optical Meta-Waveplates. *Nano Lett.* **2013**, *13*, 1086–1091.
- (14) Abasahl, B.; Dutta-Gupta, S.; Santschi, C.; Martin, O. J. F. Coupling Strength Can Control the Polarization Twist of a Plasmonic Antenna. *Nano Lett.* **2013**, *13*, 4575–4579.
- (15) Duempelmann, L.; Luu-Dinh, A.; Gallinet, B.; Novotny, L. Four-Fold Color Filter Based on Plasmonic Phase Retarder. *ACS Photonics* **2016**, *3*, 190–196.
- (16) Zeng, J.; Gao, J.; Luk, T. S.; Litchinitser, N. M.; Yang, X. Structuring Light by Concentric-Ring Patterned Magnetic Metamaterial Cavities. *Nano Lett.* **2015**, *15*, 5363–5368.
- (17) Huang, L.; Chen, X.; Mühlenbernd, H.; Zhang, H.; Chen, S.; Bai, B.; Tan, Q.; Jin, G.; Cheah, K.-W.; Qiu, C.-W.; Li, J.; Zentgraf, T.; Zhang, S. Three-Dimensional Optical Holography Using a Plasmonic Metasurface. *Nat. Commun.* **2013**, *4*, n/a.
- (18) Chen, W. T.; Yang, K.-Y.; Wang, C.-M.; Huang, Y.-W.; Sun, G.; Chiang, I.-D.; Liao, C. Y.; Hsu, W.-L.; Lin, H. T.; Sun, S.; Zhou, L.; Liu, A. Q.; Tsai, D. P. High-Efficiency Broadband Meta-Hologram with Polarization-Controlled Dual Images. *Nano Lett.* **2014**, *14*, 225–230.
- (19) Zheng, G.; Mühlenbernd, H.; Kenney, M.; Li, G.; Zentgraf, T.; Zhang, S. Metasurface Holograms Reaching 80% Efficiency. *Nat. Nanotechnol.* **2015**, *10*, 308–312.
- (20) Huang, Y.-W.; Chen, W. T.; Tsai, W.-Y.; Wu, P. C.; Wang, C.-M.; Sun, G.; Tsai, D. P. Aluminum Plasmonic Multi-Color Meta-Hologram. *Nano Lett.* **2015**, *15*, 3122–3127.
- (21) Oates, T. W. H.; Wormeester, H.; Arwin, H. Characterization of Plasmonic Effects in Thin Films and Metamaterials Using Spectroscopic Ellipsometry. *Prog. Surf. Sci.* **2011**, *86*, 328–376.
- (22) Chen, W.-Y.; Lin, C.-H.; Chen, W.-T. Plasmonic Phase Transition and Phase Retardation: Essential Optical Characteristics of Localized Surface Plasmon Resonance. *Nanoscale* **2013**, *5*, 9950–9956.
- (23) Neuman, T.; Alonso-González, P.; Garcia-Etxarri, A.; Schnell, M.; Hillenbrand, R.; Aizpurua, J. Mapping the near Fields of Plasmonic Nanoantennas by Scattering-Type Scanning near-Field Optical Microscopy. *Laser Photon. Rev.* **2015**, *9*, 637–649.
- (24) Taubner, T.; Hillenbrand, R.; Keilmann, F. Performance of Visible and Mid-Infrared Scattering-Type near-Field Optical Microscopes. *J. Microsc.* **2003**, *210*, 311–314.
- (25) Li, Y.; Zhou, N.; Raman, A.; Xu, X. Three-Dimensional Mapping of Optical near Field with Scattering SNOM. *Opt. Express* **2015**, *23*, 18730–18735.
- (26) Drachev, V. P.; Cai, W.; Chettiar, U.; Yuan, H.-K.; Sarychev, A. K.; Kildishev, A. V.; Klimeck, G.; Shalaev, V. M. Experimental Verification of an Optical Negative-Index Material. *Laser Phys. Lett.* **2006**, *3*, 49–55.
- (27) Stoller, P.; Jacobsen, V.; Sandoghdar, V. Measurement of the Complex Dielectric Constant of a Single Gold Nanoparticle. *Opt. Lett.* **2006**, *31*, 2474–2476.
- (28) Börzsönyi, A.; Kovács, A. P.; Görbe, M.; Osvay, K. Advances and Limitations of Phase Dispersion Measurement by Spectrally and Spatially Resolved Interferometry. *Opt. Commun.* **2008**, *281*, 3051–3061.
- (29) O'Brien, K.; Lanzillotti-Kimura, N. D.; Suchowski, H.; Kante, B.; Park, Y.; Yin, X.; Zhang, X. Reflective Interferometry for Optical Metamaterial Phase Measurements. *Opt. Lett.* **2012**, *37*, 4089.
- (30) Gennaro, S. D.; Sonnefraud, Y.; Verellen, N.; Van Dorpe, P.; Moshchalkov, V. V.; Maier, S. a.; Oulton, R. F. Spectral Interferometric Microscopy Reveals Absorption by Individual Optical Nanoantennas from Extinction Phase. *Nat. Commun.* **2014**, *5*, 3748.
- (31) Pshenay-Severin, E.; Falkner, M.; Helgert, C.; Pertsch, T. Ultra Broadband Phase Measurements on Nanostructured Metasurfaces. *Appl. Phys. Lett.* **2014**, *104*, 221906.
- (32) Lepetit, L.; Chériaux, G.; Joffre, M. Linear Techniques of Phase Measurement by Femtosecond Spectral Interferometry for Applications in Spectroscopy. *J. Opt. Soc. Am. B* **1995**, *12*, 2467.
- (33) Meshulach, D.; Yelin, D.; Silberberg, Y. Real-Time Spatial-spectral Interference Measurements of Ultrashort Optical Pulses. *J. Opt. Soc. Am. B* **1997**, *14*, 2095.
- (34) Dorrer, C.; Belabas, N.; Likforman, J.-P.; Joffre, M. Spectral Resolution and Sampling Issues in Fourier-Transform Spectral Interferometry. *J. Opt. Soc. Am. B* **2000**, *17*, 1795.
- (35) Dolling, G. Simultaneous Negative Phase and Group Velocity of Light in a Metamaterial. *Science* **2006**, *312*, 892–894.
- (36) Onishi, S.; Matsuishi, K.; Oi, J.; Harada, T.; Kusaba, M.; Hirokawa, K.; Kannari, F. Spatiotemporal Control of Femtosecond Plasmon Using Plasmon Response Functions Measured by near-Field Scanning Optical Microscopy (NSOM). *Opt. Express* **2013**, *21*, 26631.
- (37) Lošťák, M.; Chmelík, R.; Slabá, M.; Slabý, T. Coherence-Controlled Holographic Microscopy in Diffuse Media. *Opt. Express* **2014**, *22*, 4180.

- (38) Slabý, T.; Kolman, P.; Dostál, Z.; Antoš, M.; Lošták, M.; Chmelík, R. Off-Axis Setup Taking Full Advantage of Incoherent Illumination in Coherence-Controlled Holographic Microscope. *Opt. Express* **2013**, *21*, 14747.
- (39) Suck, S. Y.; Bidault, S.; Bonod, N.; Collin, S.; Bardou, N.; De Wilde, Y.; Tessier, G. Digital Heterodyne Holography Reveals the Non-Quasi-Static Scattering Behaviour of Transversally Coupled Nanodisk Pairs. *Int. J. Opt.* **2012**, *2012*, 1–8.
- (40) Kretschmann, E.; Raether, H. Radiative Decay of Non-Radiative Surface Plasmons Excited by Light. *Z. Naturforsch., A: Phys. Sci.* **1968**, *23*, 2135–2136.
- (41) Auguie, B.; Barnes, W. L. Collective Resonances in Gold Nanoparticle Arrays. *Phys. Rev. Lett.* **2008**, *101*, 1–4.
- (42) Kravets, V. G.; Schedin, F.; Grigorenko, A. N. Extremely Narrow Plasmon Resonances Based on Diffraction Coupling of Localized Plasmons in Arrays of Metallic Nanoparticles. *Phys. Rev. Lett.* **2008**, *101*, 1–4.
- (43) Yu, N.; Capasso, F. Flat Optics: Controlling Wavefronts with Optical Antenna Metasurfaces. *IEEE Antennas Propag. Soc. AP-S Int. Symp.* **2013**, *19*, 2341–2342.
- (44) Born, M.; Wolf, E. *Principles of Optics*; Cambridge University Press, 1999.
- (45) Chmelík, R.; Slabá, M.; Kollárová, V.; Slabý, T.; Lošták, M.; Čolláková, J.; Dostál, Z. The Role of Coherence in Image Formation in Holographic Microscopy. *Prog. Opt.* **2014**, *59*, 267–336.
- (46) Novotny, L.; Hecht, B. *Principles of Nano-Optics*, 2nd ed.; Cambridge University Press, 2012.
- (47) Cai, W.; Shalaev, V. *Optical Metamaterials*; Springer: New York, NY, 2010.
- (48) Fujiwara, H. *Spectroscopic Ellipsometry*; Wiley Blackwell (John Wiley & Sons), 2007.
- (49) Attwood, D. *Soft X-Rays and Extreme Ultraviolet Radiation: Principles and Applications*; Cambridge University Press, 2007.
- (50) Kolman, P.; Chmelík, R. Coherence-Controlled Holographic Microscope. *Opt. Express* **2010**, *18*, 21990.
- (51) Kreis, T. Digital Holographic Interference-Phase Measurement Using the Fourier-Transform Method. *J. Opt. Soc. Am. A* **1986**, *3*, 847.

Plasmonic Antennas with Electric, Magnetic, and Electromagnetic Hot Spots Based on Babinet's Principle

Martin Hroň¹, Andrea Konečná², Michal Horák¹, Tomáš Šikola^{1,3} and Vlastimil Křápek^{1,3,*}

¹Central European Institute of Technology, Brno University of Technology, Purkyňova 123, Brno 612 00, Czech Republic

²Materials Physics Center CSIC-UPV/EHU, Paseo Manuel de Lardizabal 5, San Sebastián 20018, Spain

³Institute of Physical Engineering, Brno University of Technology, Technická 2, Brno 616 69, Czech Republic



(Received 11 October 2019; revised manuscript received 10 March 2020; accepted 28 April 2020; published 19 May 2020)

We theoretically study plasmonic antennas featuring areas of extremely concentrated electric or magnetic field, known as hot spots. We combine two types of electric-magnetic complementarity to increase the degree of freedom for the design of the antennas: bowtie and diabolito duality and Babinet's principle. We evaluate the figures of merit for different plasmon-enhanced optical spectroscopy methods and optical trapping: field enhancement, decay rate enhancement, quality factor of the plasmon resonances, and trapping potential depth. The role of Babinet's principle in interchanging electric and magnetic field hot spots and its consequences for practical antenna design are discussed. In particular, diabolito antennas exhibit slightly better performance than bowties in terms of larger field enhancement and larger Q factor. For specific resonance frequency, diabolito antennas are considerably smaller than bowties, which makes them favorable for the integration into more complex devices but also makes their fabrication more demanding in terms of spatial resolution. Finally, we propose a Babinet-type dimer antenna featuring electromagnetic hot spot with both the electric and magnetic field components treated on an equal footing.

DOI: [10.1103/PhysRevApplied.13.054045](https://doi.org/10.1103/PhysRevApplied.13.054045)

I. INTRODUCTION

Plasmonic antennas (PAs) are metallic particles widely studied for their ability to control, enhance, and concentrate electromagnetic field [1]. Strikingly, the field in the vicinity of plasmonic antennas, the so-called near field, can be focused into a deeply subwavelength region. At the same time, the field is strongly enhanced with respect to the driving field, which can be, e.g., a plane wave. Focusing of the field stems from the excitation of localized surface plasmons (LSP)—quantized oscillations of the free electron gas in the metal coupled to the evanescent electromagnetic wave propagating along the boundary of the metal.

In judiciously designed plasmonic antennas, local spots of particularly enhanced electric or magnetic field can be formed, referred to as hot spots. The hot spots typically arise from the interaction between adjacent parts of a plasmonic antenna separated by a small gap [2,3] but they can be also based on the lightning rod effect (a concentration of the field at sharp features of the antenna) [4–6] or combination of both. In various studies, electric hot spots have been reported over a broad spectral range from THz [5] (hot spot size $\lambda/60000$ predicted from electromagnetic simulations,

with λ denoting the wavelength of the incident wave) to visible [7] (hot spot size $\lambda/600$ and enhancement >500).

Depending on the enhanced field, hot spots can be classified as electric, magnetic, or electromagnetic. A variety of plasmonic antennas with specific shapes, sizes, and materials exists for both electric and magnetic hot spots. Electric hot spots have been observed in the nanorod dimer antennas, bowtie antennas [8], or chains of plasmonic nanoparticles [2,9]. Magnetic hot spots are formed in diabolito antennas [10], nanorings [11], or split-ring resonators [12]. Electromagnetic hot spots with simultaneous enhancement of both electric and magnetic field are unique for plasmonic antennas [13]. Their formation has been observed in dielectric resonators (silicon nanodimers) [14].

Hot spots can be involved in many applications including surface-enhanced Raman scattering [2,15,16], more efficient photocatalysis [17], or fluorescence of individual molecules [18]. Metallic resonators with enhanced magnetic field (magnetic hot spots) are used to increase the efficiency of magnetic spectroscopies such as electron paramagnetic resonance [19]. Electromagnetic hot spots can be useful for studies of materials with combined electric and magnetic transitions such as rare earth ions [20,21]. Combined enhancement of electric and magnetic field finds applications also in optical trapping [22], metamaterials [23], or nonlinear optics [24].

*vlastimil.krapek@ceitec.vutbr.cz

For experimental characterization of plasmonic hot spots, the available methods are, e.g., scanning near-field optical microscopy [14,25–27], photon-scanning tunneling microscopy [3], two-photon luminescence spectroscopy [28], or photothermal-induced resonance [29].

Bowtie geometry of plasmonic antennas features a particularly strong electric hot spot. Bowtie antennas are planar antennas consisting of two metallic triangular prisms (wings) whose adjacent apexes are separated by a sub-wavelength insulating gap. The hot spot arises from the interaction between the apexes combined with the lightning rod effect (the charge of LSP accumulates at the apexes). When the insulating gap is replaced with a conductive bridge, a *diabolo* plasmonic antenna is formed. Instead of charge accumulation, electric current is funneled through the bridge, resulting in a magnetic hot spot. Both the bowtie and diabolo antennas have been frequently studied [8,10,18,30–35].

Various optimization and modification approaches have been proposed with the aim to enhance the properties of the bowtie and diabolo antennas, including the gap optimization [30], fractal geometry [36], or Babinet’s principle. Babinet’s principle relates the optical response of a (direct) planar antenna and an inverted planar antenna with interchanged conductive and insulating parts. Both the direct and inverted antennas shall support LSP with identical energies, but with interchanged electric and magnetic near field [37,38]. Consequently, when the direct antenna features an electric hot spot, the inverted antenna features a magnetic hot spot and vice versa. The validity of Babinet’s principle for the plasmonic antennas has been experimentally verified [39,40], although some quantitative limitations have been found in particular in the visible spectral range [41,42].

A unique combination of Babinet’s complementarity and bowtie and diabolo duality extends a degree of freedom for the design of plasmonic antennas featuring hot spots. In our contribution we compare the two antennas featuring an electric hot spot (bowtie and inverted diabolo) and the other two featuring a magnetic hot spot (diabolo and inverted bowtie). By electromagnetic modeling we retrieve the characteristics of the hot spots and figures of merit of relevant plasmon-enhanced optical spectroscopy methods. Finally, we design Babinet dimer antennas featuring electromagnetic hot spots.

II. METHODS

In all simulations, the bowtie and diabolo antennas are represented by two gold triangles or triangular apertures (as shown in Fig. 1) of 30 nm height on a semi-infinite glass substrate. Babinet dimers are formed by two complementary PAs (direct and inverted, each of 30 nm height) vertically separated by a 10-nm-thick layer with the refractive index equal to 1.5 corresponding to

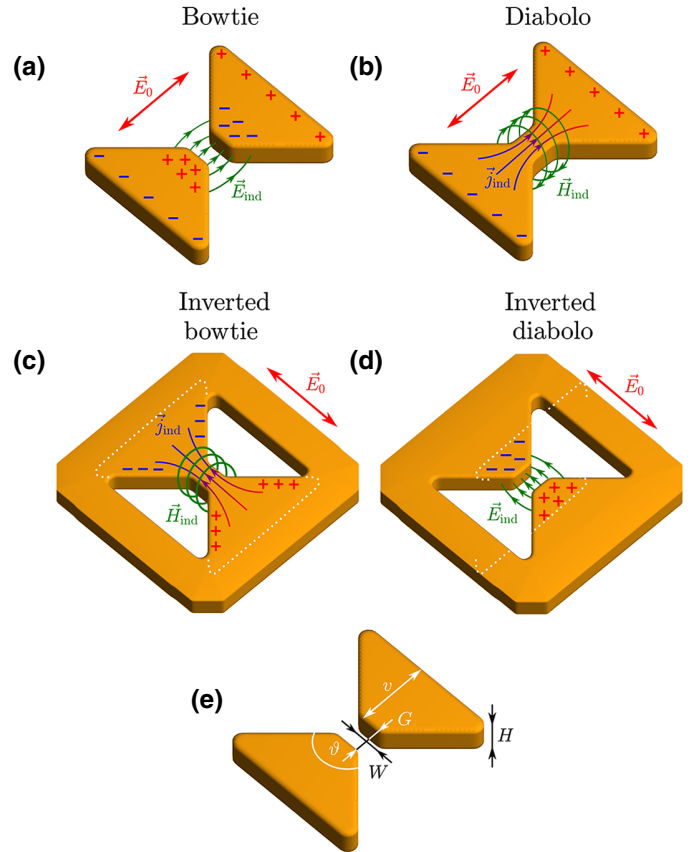


FIG. 1. Schemes of four plasmonic antennas featuring hot spots: (a) bowtie, (b) diabolo, (c) inverted bowtie, (d) inverted diabolo. Metallic and hollow parts are represented by golden and white color, respectively. Driving electric field is indicated by red arrows. Charge or current accumulation and formation of the electric or magnetic hot spot are shown as well. The dotted white line in (c) indicates the qualitative correspondence between the diabolo and inverted bowtie antennas, while the dotted white line in (d) indicates a similar correspondence between the bowtie and inverted diabolo antennas. Dimension parameters of the antennas are shown in (e).

poly(methyl methacrylate). The whole dimer lies on a semi-infinite glass substrate. The dielectric function of gold is taken from Ref. [43] and the refractive index of the glass is set equal to 1.47.

The electromagnetic field is calculated with the finite difference in time domain (FDTD) method using a commercial software Lumerical.

Scattering efficiencies and the near-field distribution are calculated using a plane wave as illumination. Transition decay rates are calculated as the decay rate of the power radiated by an oscillating electric or magnetic dipole into its surrounding (total decay rate) and into far field (radiative decay rate). The dipole is positioned at the vertical symmetry axis of the antenna. The decay rates are averaged over three orthogonal polarizations of the dipole.

III. RESULTS AND DISCUSSION

A. Plasmonic antennas, modes, and hot spots

Plasmonic antennas involved in the study and their operational principle are illustrated in Fig. 1. The *bowtie* antenna consists of two disjoint triangular gold prisms. An oscillating electric field applied along the long axis of the antenna drives the oscillations of charge that is funneled by the wings of the antenna and accumulated at the adjacent tips [Fig. 1(a)]. Combined effects of plasmonic field confinement, charge funneling, and charge concentration (lightning rod effect) give rise to an exceptionally high field in the area between the triangles, by orders of magnitude higher than the driving field. In the *diabolo* antenna, the triangles are connected with a conductive bridge, through which a concentrated current flows instead of charge accumulation [Fig. 1(b)]. A magnetic hot spot is formed around the bridge. The *inverted bowtie* antenna is formed by two disjoint triangular apertures in an otherwise continuous gold film. Babinet's principle predicts that for a complementary illumination (i.e., transverse oscillating electric field) a complementary magnetic hot spot is formed. This can be understood also intuitively as the antenna resembles a rotated diabolo antenna [see dotted line in Fig. 1(c)]. Finally, the *inverted diabolo* antenna, which on the other hand resembles the bowtie antenna, features an electric hot spot Fig. 1(d).

The dimension parameters of the antennas are schematically depicted in Fig. 1(d). The thickness of the gold film is set to $H = 30$ nm. The size of the right isosceles triangles (i.e., $\vartheta = 90^\circ$) is described by the wing length v . The opposite triangles share a common apex. The isolating gap

in bowtie antennas and the conductive bridge in diabolo antennas have the length G equal to the width W . These dimensions do not scale with the size of the antenna (the only scalable parameter is thus v) and are set to 30 nm to reflect a convenient resolution of fabrication methods such as electron-beam lithography and focused ion-beam lithography. In general, one could expect stronger hot spots for narrower gaps or bridges due to stronger charge or current concentration. All edges are rounded with a radius of 10 nm. The antennas are placed on a semi-infinite glass substrate (refractive index 1.47). The dielectric function of gold is taken from Johnson and Christy [43].

One of the quantities characterizing plasmonic response of antennas is their scattering efficiency Q_{scat} . It describes the power P_{scat} scattered by the antenna illuminated with a monochromatic plane wave with an intensity I_0 and is defined as $Q_{\text{scat}} = P_{\text{scat}}/(I_0 S)$, where S denotes the geometrical cross section of the antenna. Spectral dependencies of Q_{scat} for all four PA types are shown in Fig. 2 and the energies of the lowest scattering peak corresponding to a dipole plasmonic mode are shown in Fig. 3. We observe that Babinet's principle holds reasonably well. The peak energies of the scattering efficiency in the complementary PA (i.e., bowtie and inverted bowtie, diabolo and inverted diabolo) of the same size differ by less than 11%. The difference is less pronounced for large antennas, in line with the requirements of Babinet's principle: perfectly thin and opaque metal [42]. For the bowtie geometry, the scattering peaks of inverted PAs are less intense and red-shifted with respect to direct PAs (as is the case also for disc-shaped antennas [42]), while opposite is true for the diabolo geometry.

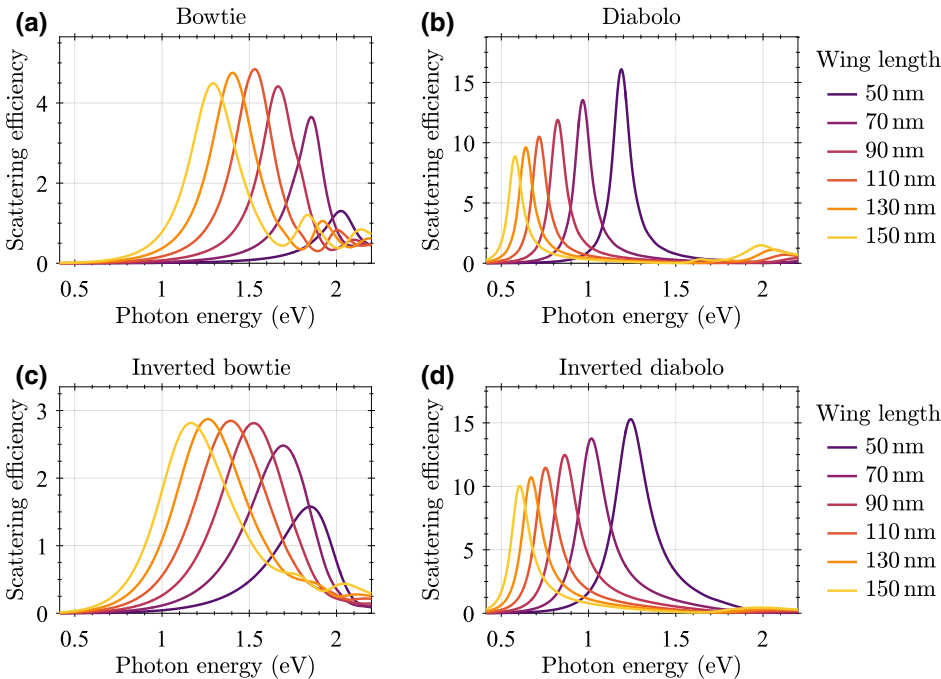


FIG. 2. Spectral dependence of the scattering efficiency Q_{scat} of (a) bowtie, (b) diabolo, (c) inverted bowtie, (d) inverted diabolo PAs for several values of the wing length v of the antennas.

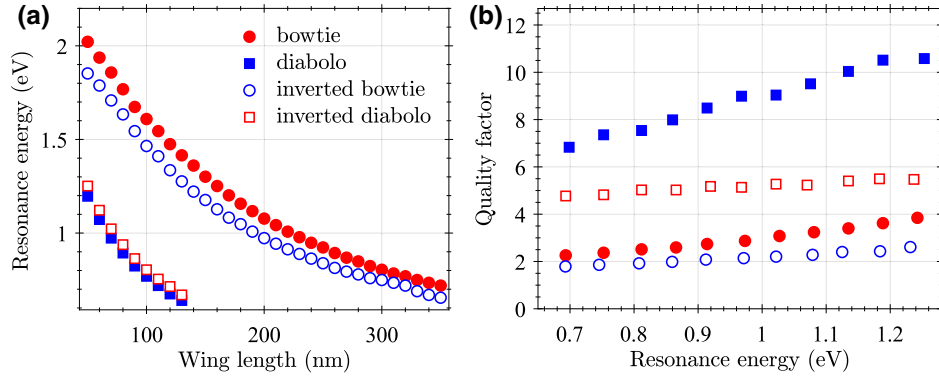


FIG. 3. (a) Peak energies of the scattering efficiency Q_{scat} of bowtie (red full circles), diabolo (blue full squares), inverted bowtie (blue empty circles), and inverted diabolo (red empty squares) PAs as functions of the PA dimension—length of the wing v . (b) Quality factors of LSP (represented by the peak energy of scattering cross sections divided by their full width at half maximum). Notice that circles and squares correspond to bowtie and diabolo PAs, full and empty symbols correspond to particles (direct PAs) and apertures (inverted PAs), and red and blue color corresponds to electric and magnetic hot spots, respectively.

Not surprisingly, the peak energies of the scattering cross section for the diabolo PAs are considerably smaller than that for the bowtie PAs of the same wing length v . In other words, for the same energy, the diabolo PAs are smaller by a factor of more than 2 than the bowtie PAs. This effect is explained by a larger effective size of connected (i.e., diabolo) antennas in comparison with disjoint ones (bowtie), which can be seen from Figs. 1(a) and 1(b), and has been observed previously [44]. There is an important practical consequence. The bowtie geometry allows achievement of the high resonance energies for which diabolo-type PAs can be too small for an involved fabrication technique. Considering the minimum wing length of 50 nm, diabolo antennas cover the LSP energy range up to 1.2 eV while bowtie antennas operate up to 2.0 eV. On the other hand, diabolo geometry allows for a more compact PA design and better integration to more complex devices, such as a scanning near-field probe with the electric hot spot [45]. Further, their lower footprint represents an advantage for the fabrication of PA arrays, where a higher planar density of hot spots is achieved.

Diabolo antennas, either direct or inverted, feature considerably more intense and narrower scattering peaks corresponding to larger quality factors than bowtie antennas (Fig. 3). This is probably related to lower radiative losses due to their smaller volume.

In the following, we compare the properties and performance of all four types of PAs. We adjust the dimensions of the compared PAs so that they all feature the LSP resonance (LSPR) at the same energy. Table I shows the dimensions of the antennas for two specific energies: 1.8 eV corresponding to the minimum absorption of gold (i.e., minimum of the imaginary part of dielectric function) and 0.8 eV corresponding to one of the optical communication wavelengths (1550 nm). We note that the former energy is accessible only with bowtie antennas. We therefore focus on the energy of 0.8 eV.

Figure 4 shows the formation of the hot spot. PAs featuring the lowest LSPR at the energy of 0.8 eV are illuminated by a plane wave with the same photon energy. Bowtie and inverted diabolo PAs feature the electric hot spot and delocalized magnetic field, while diabolo and inverted bowtie PAs feature the magnetic hot spot and delocalized electric field. Interestingly, the volume of all the hot spots is comparable despite pronounced differences in the dimensions of PAs. The fields exhibit clear Babinet's complementarity: their spatial distribution in direct and complementary antennas is qualitatively similar with interchanged electric and magnetic components. Nevertheless, the magnitudes of the complementary fields differ rather significantly. As an example, the electric field within the hot spot of the bowtie antenna has the relative magnitude around 25 while the magnetic field of the inverted bowtie has the maximal relative magnitude less than 10, i.e., almost three times weaker than expected. This observation is attributed to the finite thickness and conductivity of gold, which both limit the validity of Babinet's principle. As for the direct and inverted diabolo, the difference in the magnitudes of the electric and magnetic fields is less pronounced, but still quite significant. The bowtie and diabolo duality can be observed for the field forming the hot spot (e.g., electric for bowtie and magnetic for diabolo), which has a very similar spatial distribution in both cases. However, the distribution of the delocalized field (e.g., electric for bowtie and magnetic for diabolo) differs. In general, magnetic fields

TABLE I. Dimensions (wing length) of the antennas featuring the lowest LSPR at energies of 0.8 and 1.8 eV.

	Bowtie	Diabolo	Inverted bowtie	Inverted diabolo
0.8 eV	300 nm	95 nm	270 nm	100 nm
1.8 eV	75 nm	...	55 nm	...

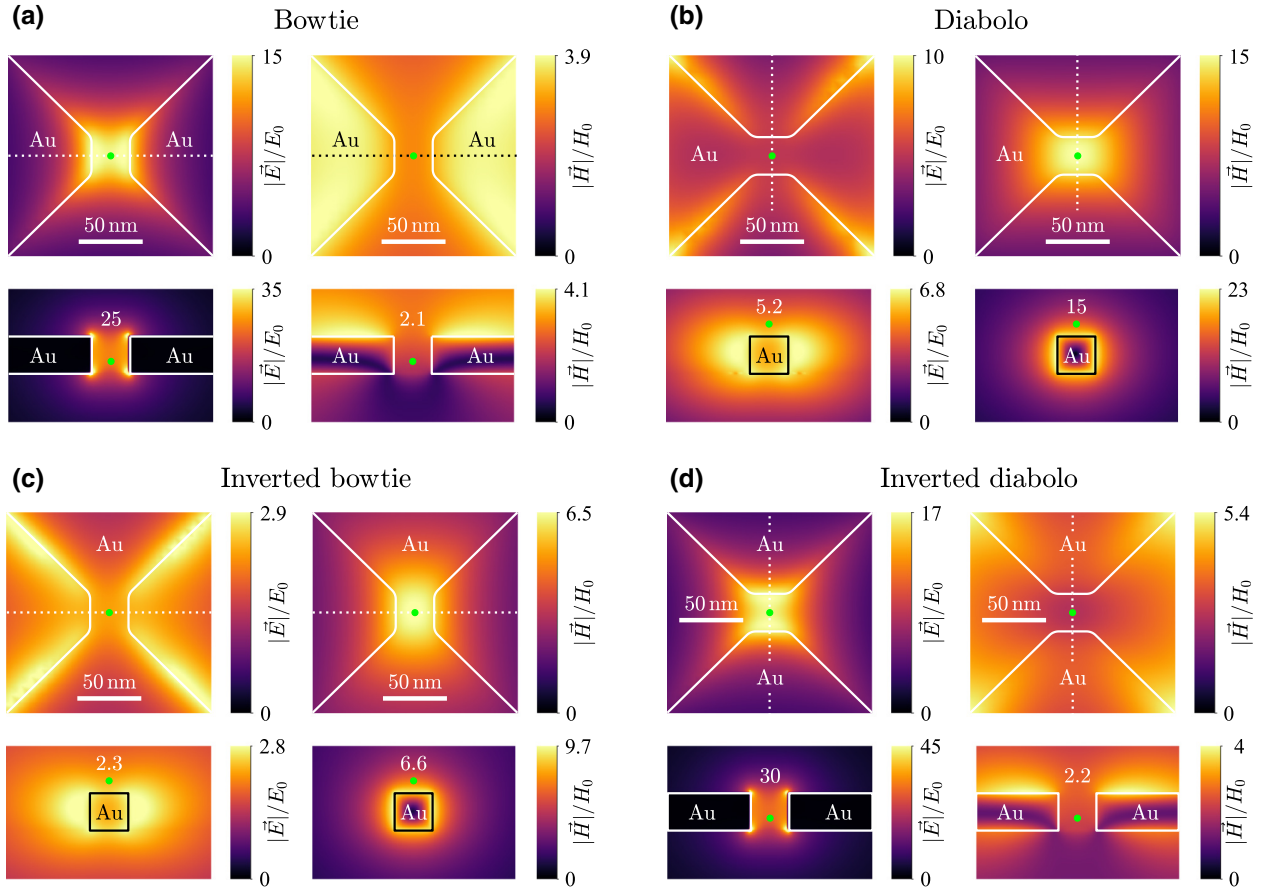


FIG. 4. Planar cross sections of the electric ($|\vec{E}|$) and magnetic ($|\vec{H}|$) field magnitudes divided by related magnitudes of the driving plane wave. The top two subplots in each panel show field distributions in the plane parallel to the PA plane, 10 nm above the upper PA boundary. The bottom two subplots then show field distributions in the vertical plane with the orientation indicated by white dotted lines in the in-plane field plots. The size of all PAs is set so that they feature the lowest LSPR at 0.8 eV, which is also the photon energy of the driving field. Solid white lines indicate antenna boundaries, while the hot spots are marked by the green point and the numbers correspond to the field enhancement in the hot spot. The figures show only the central part of the antennas with the metallic parts being denoted as Au for clarity.

are weaker than electric fields in agreement with previous findings [42,46].

B. Figures of merit for optical spectroscopy

Plasmonic antennas can be used to enhance absorption and emission of light. Consequently, they enhance the signal of interest in various optical spectroscopy techniques, including absorption spectroscopy, Raman spectroscopy, photoluminescence spectroscopy, and absorption spectroscopy of magnetic transitions. Here we define figures of merit (FOM) for plasmonic enhancement of different spectroscopy techniques and evaluate them for all four types of PAs. We consider a small volume of the analyzed material (e.g., molecule, quantum dot, nanostructured material, or just nanosized crystal) that fits into the size of the hot spot.

In the case of absorption spectroscopy, absorbed power (per unit volume) can be expressed using Fermi's golden rule as $P = 0.5\text{Re}[\sigma(\omega)]|E|^2$ where ω is the frequency of the probing radiation (in the following referred to as light), $\text{Re}[\sigma]$ is the real part of the complex conductivity of the analyte, and $|E|$ is the magnitude of the electric component of light. For simplicity we consider that the transition dipole moment of the analyte is parallel to the electric field in the hot spot, which is polarized along the axis of the PA. The presence of plasmonic antennas alters the magnitude of electric field exciting the analyte. For the driving field (a plane wave) with the electric field intensity E_0 , the electric intensity in the hot spot reads E_{HS} . We define the electric field enhancement $Z_E = |E_{\text{HS}}|/E_0$. Clearly, absorbed power is enhanced by the factor of Z_E^2 , which is thus suitable FOM for plasmon-enhanced absorption spectroscopy. Raman scattering is a two-photon process, where each of the subprocesses, i.e., absorption of the driving

photon and re-emission of the inelastically scattered photons, is enhanced by Z_E^2 (spectral dependence of Z_E can be neglected considering a low relative energy shift in the Raman scattering and large energy width of plasmon resonances). Therefore, FOM for the plasmon-enhanced Raman spectroscopy reads Z_E^4 .

Absorption spectroscopy of magnetic transitions is relevant for the study of rare-earth ions in the visible region [20,21]. Electron paramagnetic resonance is, in principle, also an absorption spectroscopy involving magnetic dipole transitions in the microwave spectral range. The absorbed power can be expressed as $P = 0.5\omega\text{Im}[\mu(\omega)]|H|^2$ where ω is the frequency of light, $\text{Im}[\mu]$ is the imaginary part of the complex permeability of the analyte, and $|H|$ is the magnitude of the magnetic component of light. For the magnetic field enhancement Z_H defined analogously to Z_E , the FOM for absorption spectroscopy of magnetic transition reads Z_H^2 .

We should note that the choice of the location in which we should evaluate the enhancement factors is somewhat arbitrary. In the case of the bowtie and inverted diablo, we decide to take the values from a spot positioned in the center of the gap, 10 nm above the substrate, while for the inverted bowtie and diablo, the spot is situated 10 nm above the center of the bridge. This choice gives us reasonable estimates that are close to the average values over the whole hot spots and it also ensures sufficient separation from the metal, which is relevant for dipolar emitters and their quenching. Ultimately, we can afford this slight inconsistency in the definition of the hot spot as we always compare a bowtie with an inverted diablo and an inverted bowtie with a diablo, i.e., PAs with the same definition of the hot spot. With this in mind, we can turn our attention back to the field enhancements Z_E and Z_H . The inspection of Fig. 5 shows that both Z_E and Z_H decrease with increasing energy as a consequence of decreased funneling effect (the size of the wings decreases while the size of the bridge or the gap is kept constant). The electric field enhancement Z_E ranges between 18 and 34 with the inverted diablo PA having slightly better performance than the bowtie. The magnetic field-enhancement ranges between 10 and 17 for the diablo PA but only between 4 and 8 for the inverted bowtie. Thus, the inverted diablo presents an excellent option for the electric field enhancement while the inverted bowtie does not perform particularly well for the magnetic field enhancement.

Luminescence spectroscopy is another important method that can benefit from plasmon enhancement. We consider a simple model based on the rate equation. A metastable excitonic state with the degeneracy g is populated through an external excitation with the rate γ_G . The generation is only efficient when the metastable state is unoccupied. For its population n , the total generation rate reads $(g - n)\gamma_G$. Excitons decay into the vacuum state via radiative and non-radiative recombination paths with the rates γ_{R0} and γ_{NR0} ,

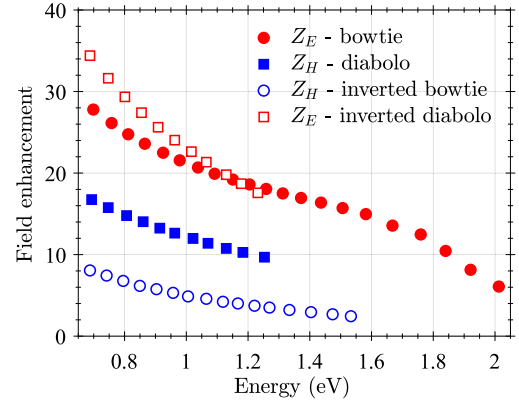


FIG. 5. Electric (red) and magnetic (blue) field enhancements for bowtie, diablo, and their Babinet complements in their respective hot spots. The electric field enhancement Z_E , defined as the ratio of magnitudes of the local electric field $|\vec{E}_{\text{HS}}|$ and the driving field E_0 , enters the figures of merit for plasmon-enhanced absorption spectroscopy (Z_E^2) and Raman scattering (Z_E^4). On the other hand, the magnetic field enhancement Z_H , defined as the ratio of the magnitudes of the local magnetic field intensity $|\vec{H}_{\text{HS}}|$ and the magnetic field intensity H_0 of the driving field, is important for plasmon-enhanced absorption spectroscopy of magnetic transitions (Z_H^2).

respectively. The rate equation reads

$$\frac{dn}{dt} = (g - n)\gamma_G - n\gamma_{R0} - n\gamma_{NR0}. \quad (1)$$

In the steady state, $dn/dt = 0$ and

$$n = g\gamma_G/(\gamma_G + \gamma_{R0} + \gamma_{NR0}). \quad (2)$$

Two regimes can be distinguished. In the linear (weak pumping) regime, $\gamma_G \ll \gamma_{R0} + \gamma_{NR0}$ and

$$n \approx g\gamma_G/(\gamma_{R0} + \gamma_{NR0}), \quad (3)$$

i.e., the population is proportional to pumping. In the saturation (strong pumping) regime, $\gamma_G \gg \gamma_{R0} + \gamma_{NR0}$ and $n \approx g$, i.e., the metastable state is fully occupied. The emitted power reads

$$P_{\text{PL}} = n\gamma_{R0}\hbar\omega, \quad (4)$$

where $\hbar\omega$ is the photon energy. In the linear regime, the emitted power can be expressed using the internal quantum efficiency $\eta_0 = \gamma_{R0}/(\gamma_{R0} + \gamma_{NR0})$ as

$$P_l = g\gamma_G\eta_0\hbar\omega \quad (5)$$

and in the saturation regime

$$P_s = g\gamma_{R0}\hbar\omega. \quad (6)$$

The presence of plasmonic antennas affects all three processes (generation, radiative decay, and nonradiative

decay). The effect on generation varies from very important in the case of photoluminescence [18] to negligible in the case of electroluminescence. In general, generation is a sequential inelastic process and cannot be described by a simple model. For that, we do not consider plasmon enhancement of generation in the following and focus on its influence on the radiative and nonradiative decay rates.

Spontaneous emission is affected via Purcell effect [47]. The emitter transfers its energy to PA where it is partially radiated into far field and partially dissipated. It is customary to express the rates of both processes in multiples of the spontaneous emission rate γ_{R0} : Z_R being the radiative enhancement and Z_{NR} the nonradiative enhancement [48,49]. The total radiative and nonradiative decay rates in the presence of plasmonic particles read $\gamma_R = Z_R\gamma_{R0}$ and $\gamma_{NR} = Z_{NR}\gamma_{R0} + \gamma_{NR0}$, respectively, and the internal quantum efficiency reads $\eta = \gamma_R/(\gamma_R + \gamma_{NR})$.

The figure of merit for plasmon-enhanced luminescence (only its emission part) is the rate of the powers emitted with and without the presence of the PA. For the linear regime, FOM is

$$F_l = \eta/\eta_0, \quad (7)$$

while for the saturation regime it reads simply

$$F_s = Z_R. \quad (8)$$

Consequently, only emitters with a poor internal quantum efficiency can benefit from plasmon enhancement in the linear regime while the emitters with a high internal quantum efficiency will suffer from the dissipation in metallic

PA. On the other hand, in the saturation regime plasmon enhancement is beneficial as long as $Z_R > 1$.

Figure 6 shows the spectral dependence of radiative and nonradiative enhancement factors (Z_R and Z_{NR} , respectively) for different types of PA with the maximum field enhancement at 0.8 eV. A pointlike isotropic emitter (i.e., all polarizations are involved with the same intensity) is positioned in the center of the PA 10 nm above the substrate (bowtie and inverted diablo) or 10 nm above the surface of gold (diablo and inverted bowtie). Such a separation shall suppress emission quenching due to nonradiative decay of the emitter. For the electric dipole transitions, a large radiative enhancement (several hundreds) is obtained for both the bowtie and inverted diablo. The inverted diablo offers approximately twice larger peak enhancement [Fig. 6(a)] than the bowtie PA. However, the bowtie benefits from a much lower nonradiative enhancement and is thus preferable for most emitters in the linear regime [Fig. 6(c)]. For magnetic dipole transitions, the diablo provides a considerably larger radiative enhancement than the inverted bowtie, but it also suffers from the considerably larger nonradiative enhancement [Fig. 6(b)]. In addition, the resonance of the inverted bowtie is considerably wider, which can prioritize this type of antenna for emitters with broad spectral bands. The preferred PA type therefore depends on specific application. We note that the peaks in the enhancement are spectrally shifted from the maximum field enhancement; the effect is particularly pronounced for the inverted bowtie.

At this point it is worthwhile to estimate the accuracy of the electromagnetic simulations and the relevance

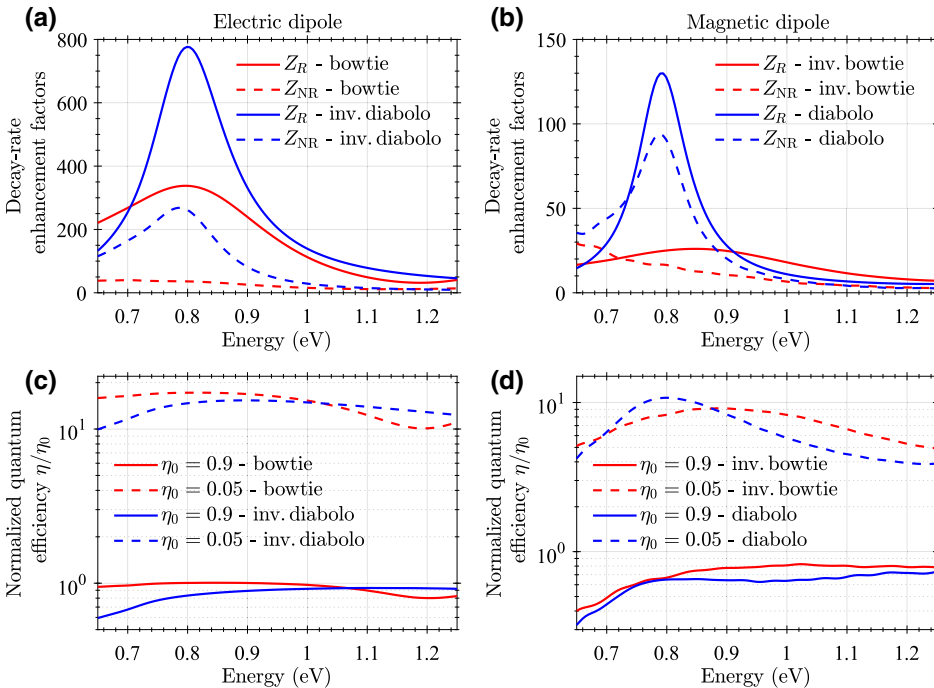


FIG. 6. Radiative and nonradiative enhancement factors Z_R and Z_{NR} , respectively, as functions of the photon energy for the (a) electric dipole transition and (b) magnetic dipole transition. The values are averaged over all possible polarizations of the transitions. Panels (c) and (d) then show enhancement of the overall quantum efficiency for two values of the internal quantum efficiency, namely $\eta_0 = 0.9$ (good emitter) and $\eta_0 = 0.05$ (poor emitter). Note that even though the radiative enhancement for direct and inverted diabolos is significantly higher than for their bowtie counterparts, their enhancement of quantum efficiency is due to their equally larger nonradiative enhancement more or less the same.

of their results for the experiment. Several authors compared experimental and calculated values of luminescence enhancement factors in various systems, including organic dyes coupled to bowtie antennas [18] (measured, up to 1340; calculated, 1690), MoS₂ coupled to bowtie antennas [50] (measured, 980; calculated, 982), and WSe₂ monolayer coupled to cavity-backed slot antennas [51] (measured: 340; calculated: 400). Apparently, there is a reasonable agreement between simulations and experiment with differences up to 20%. Further, the differences consist in a rather systematic overestimation of calculations due to model simplifications. Hence, the conclusions based on the simulations shall be robust and reproducible in the experiment.

C. Optical trapping

Apart from enhancing optical processes, electric hot spots can also serve as optical tweezers, i.e., they can be used to trap small objects. In the dipole limit, the optical force that facilitates this trapping is proportional to the gradient of the square of the electric field. Considering the evanescent nature of plasmonic near fields, electric hot spots in the vicinity of plasmonic structures can lead to very strong forces, stronger even than those encountered in tightly focused beams that are routinely used to manipulate both metallic and dielectric particles, living cells, DNA, or bacteria [52].

To estimate the strength of the trapping force provided by our structures, we calculated the energy required by a 20-nm polystyrene sphere to escape the potential well formed by the plasmonic hot spot. Considering the small size of the particle, we deem it sufficient to work within the dipole approximation, where the potential energy of the small sphere reads [53]

$$V = -\frac{\alpha}{2} |\vec{E}|^2, \quad (9)$$

where α is the polarizability of the polystyrene particle (permittivity 2.46). Note that we limit ourselves only to structures with electric hot spots as the magnetic dipole moment and consequently also the magnetic trapping potential for such a small polystyrene particle is negligible. Considering an illumination in the form of a 1-mW beam focused into a 2- μm spot (corresponding to the intensity of 318 kWm^{-2}) with the investigated structure in its centre, the magnitudes of the trapping potential (which we define as the potential difference between the hot spot and when we are away from it) are plotted in Fig. 7. As one might expect, the trapping potential mimics the field enhancement shown in Fig. 5, with larger values attained at lower resonance energies. Assuming that the system is at the room temperature ($T = 300$ K), the trapping energy at 0.8 eV becomes comparable to the thermal energy of the polystyrene particles, which indicates that these structures

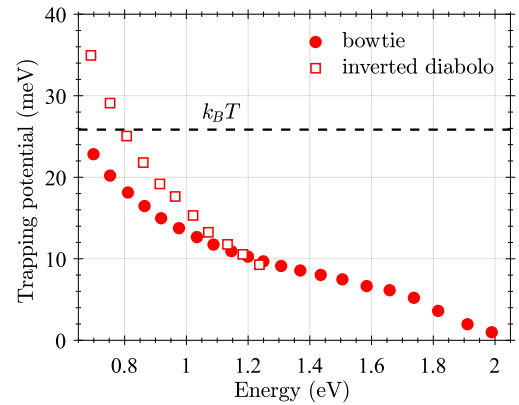


FIG. 7. Depth of the trapping potential for 20-nm polystyrene spheres induced by bowtie and inverted diabolo PAs illuminated by the light with the intensity of 318 kWm^{-2} . The potential is expressed at the energy of the lowest LSPR and displayed as a function of this energy. The dashed line indicates the thermal energy at room temperature ($k_B T = 26$ meV).

have a potential to serve as a dual purpose tool that is capable of capturing an object and enhance its optical response at nanoscale.

D. Materials beyond gold

To demonstrate the general validity of our results we now discuss two other plasmonic materials: silver and zirconium nitride (ZrN). Silver is a traditional plasmonic metal, which supports surface plasmon polaritons (SPP) in a broader spectral range than gold (up to the energy of 3 eV) and exhibits slightly lower electron scattering rate. On the other hand, silver PAs are not as stable as gold PAs and can degrade over time [54]. ZrN is a semiconductor from a class of transition-metal nitrides that supports SPP in the visible spectral range (up to 3 eV) under sufficiently large doping [55]. The electron scattering in ZrN is significantly larger than in gold. For our simulations, the dielectric function of silver has been taken from Johnson and Christy [43] and the dielectric function of the doped ZrN has been taken from Naik *et al.* [55]. The electron scattering time τ can be estimated from the dielectric function $\epsilon(\omega)$ as $\tau = -\text{Im}(\epsilon)/[\omega \text{Re}(\epsilon)]$, where Re and Im denote the real and imaginary part, and ω is the angular frequency. At the photon energy of 0.8 eV, τ reads 32 fs for silver, 8.2 fs for gold, and 0.8 fs for ZrN.

The energies of the lowest LSPR supported by silver and ZrN PAs are shown as Figs. S1(a) and S2(a) within the Supplemental Material [56]. The energy is only weakly dependent on the material of the PA, with a slight blueshift observed for the smallest silver PAs attributed to the large plasma frequency and the absence of interband transitions in silver in the respective energy range. The energies of LSPR in the Babinet-complementary PAs are nearly identical, with the differences up to 10% for gold and silver.

Notably, ZrN exhibits larger differences (up to 15%) at the energy of 2 eV (due to proximity of the plasma frequency and a related zero-cross-point of the real part of the dielectric function) but very low differences (below 5%) at energies below 1 eV where ZrN rapidly approaches the limit of perfect electric conductor.

The Q factors of the lowest LSPR supported by silver and ZrN PAs are shown as Figs. S1 and S2 within the Supplemental Material [56]. Typical values for silver PAs are by about 25% higher than for gold PAs, while the values for ZrN PAs are about four times lower. As expected, the Q factor decreases for decreasing electron scattering time. The relation is weaker than linear, since the total plasmon damping is in addition to the collision damping contributed also by the radiation damping and the Landau damping [57].

Figure 8 compares all three materials in terms of the figures of merit of optical spectroscopy and trapping. We show the results only for the better PA of the pair supporting a specific hot spot, which is the inverted diabolo PA for the electric hot spot and the diabolo PA for the

magnetic hot spot. Complete characterization including also the bowtie and inverted bowtie PAs is provided as Figs. S1 and S2 within the Supplemental Material [56]. The trends observed for gold PAs are qualitatively reproduced for silver and ZrN PAs. Low-scattering materials provide better FOM. The effect is most pronounced for the decay-rate enhancement factors, where the low scattering results in both high radiative decay-rate enhancement Z_R and low nonradiative decay-rate enhancement Z_{NR} .

Tables II and III summarize the FOM at the energy of 0.8 eV corresponding to the telecommunication wavelength of 1.55 μm . The dimensions of the antennas are adjusted to set the energy of the lowest LSPR to 0.8 eV (represented by the peak of the scattering cross section) so that we evaluate the resonant (maximum) values of the FOM. The antenna footprint F is defined as the area of smallest rectangle fully containing the antenna. Table II presents the FOM related to the electric hot spot: the Q factor defined as the peak energy divided by the FWHM of the scattering cross section, the electric field enhancement Z_E , the radiative (Z_R) and nonradiative (Z_{NR}) decay-rate

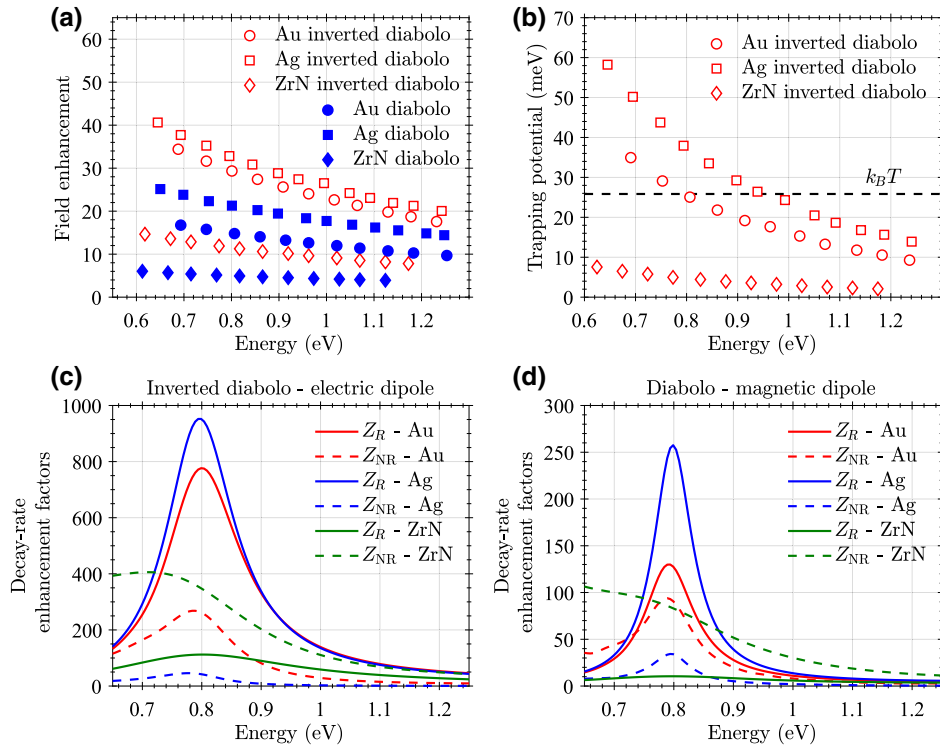


FIG. 8. Comparison of gold, silver, and ZrN PAs. (a) Field-enhancement factors for the electric field in inverted diabolo PAs (red) and the magnetic field in diabolo PAs (blue) expressed at the energy of the lowest LSPR as functions of this energy. (b) Depth of the trapping potential for 20-nm polystyrene spheres induced by inverted diabolo PAs illuminated by the light with the intensity of 318 kWm^{-2} . The potential is expressed at the energy of the lowest LSPR and displayed as a function of this energy. The dashed line indicates the thermal energy at room temperature ($k_B T = 26 \text{ meV}$). (c), (d) Radiative and nonradiative enhancement factors Z_R and Z_{NR} , respectively, as functions of the photon energy for (c) the inverted diabolo PA and the electric dipole transition and (d) the diabolo PA and the magnetic dipole transition. The values are averaged over all possible polarizations of the transitions. The energy of the lowest LSPR in the PAs is set to 0.8 eV.

TABLE II. Figures of merit related to the electric hot spot at the energy of 0.8 eV.

Material	Geometry	F [nm ²]	Q	Z_E	Z_R	Z_{NR}	V_{TB} [meV]
Silver	i. diabolo	5.8×10^4	5.6	33	952	48	37
	bowtie	41×10^4	2.4	24	304	1	16
Gold	i. diabolo	5.3×10^4	4.9	30	775	268	25.6
	bowtie	40×10^4	2.4	25	338	37	19.4
ZrN	i. diabolo	5.3×10^4	2.1	12	112	350	5.7
	bowtie	36×10^4	1.6	16	142	140	7.3

enhancements for an electric dipole transition, and the trapping barrier V_{TB} defined as the depth of the trapping potential for the illumination intensity of 318 kWm^{-2} . It includes only PAs with the electric hot spot, i.e., bowtie and inverted diabolo. Table III presents the FOM related to the magnetic hot spot: the Q factor, the magnetic field enhancement Z_H , and the radiative (Z_R) and nonradiative (Z_{NR}) decay-rate enhancements for a magnetic dipole transition. It includes PAs with the magnetic hot spot, i.e., inverted bowtie and diabolo.

There is a clear qualitative correlation between all FOM. Large values of Q factor correspond to a large field enhancement and large radiative decay enhancements, while nonradiative decay enhancements are small. Silver with the highest electron scattering time of all three materials involved in the study shows better performance compared to gold, which is superior to ZrN, the material with the lowest electron scattering time. The diabolo PAs offer better FOM (and lower footprint) than the bowtie PAs due to reduced radiation losses. This finding holds for both the bowtie and the inverted diabolo PAs supporting the electric hot spot and the inverted bowtie and the diabolo PAs supporting the magnetic hot spot.

E. Babinet dimer with electromagnetic hot spot

Bowtie and diabolo PAs enhance either an electric or a magnetic component of the field, while the other component is only weakly enhanced and spatially focused. In this section we propose a Babinet dimer antenna that forms an electromagnetic hot spot enhancing and focusing both components of the electromagnetic field equally. The Babinet dimer antenna is formed by a direct and an inverse PA, vertically stacked so closely that their individual electric

and magnetic hot spots overlap. We explore and compare two configurations, namely the Babinet bowtie dimer (BBD) [schematically depicted in Fig. 9(a)], consisting of a bowtie on top of an inverted bowtie PA, and the Babinet diabolo dimer (BDD) [sketched in Fig. 9(c)] made up by an inverted diabolo on top of a diabolo PA. In both configurations, the upper PA is rotated with respect to the bottom one by 90° so that both of them can be excited by the same source polarization (oriented along the long axis of the direct PA) and the upper and bottom PAs are separated by a 10-nm spacer layer with the refractive index equal to 1.5. As the individual modes in the closely spaced PAs exhibit strong interaction, the dimensions of the dimer constituents are adjusted so that the maximum field enhancement occurs at 0.8 eV for both the electric and magnetic component. For the BBD, the wing lengths of the top (\uparrow) and bottom (\downarrow) PAs are set to $v_\uparrow = 110 \text{ nm}$ and $v_\downarrow = 200 \text{ nm}$, while for the BDD, the optimal dimensions read $v_\uparrow = 200 \text{ nm}$ and $v_\downarrow = 110 \text{ nm}$. Note that the antenna providing the magnetic enhancement is in both cases situated underneath the one with the electric enhancement so that the electromagnetic hot spot is directly accessible from the top.

Figure 9(b) demonstrates the formation of the electromagnetic hot spot in the BBD. The dimer is illuminated by the field polarized along the long axis of the bowtie and perpendicular to the long axis of inverted bowtie, which results in formation of an electric hot spot (field enhancement 14) around the direct bowtie and a magnetic hot spot (field enhancement 13) around the inverted bowtie. The closely spaced hot spots overlap, yielding the maximum simultaneous enhancement of both fields close to 8.4 at the position indicated by the green point in Fig. 9. The inspection of Figs. 3 and 5 reveals that these values are similar

TABLE III. Figures of merit related to the magnetic hot spot at the energy of 0.8 eV.

Material	Geometry	F [nm ²]	Q	Z_H	Z_R	Z_{NR}
Silver	diabolo	4.8×10^4	9.7	21	257	34
	i. bowtie	34×10^4	1.9	7.5	40	5
Gold	diabolo	4.8×10^4	7.5	15	130	94
	i. bowtie	33×10^4	1.9	6.6	26	15
ZrN	diabolo	4.4×10^4	2.1	5.0	11	83
	i. bowtie	31×10^4	1.0	3.7	8	55

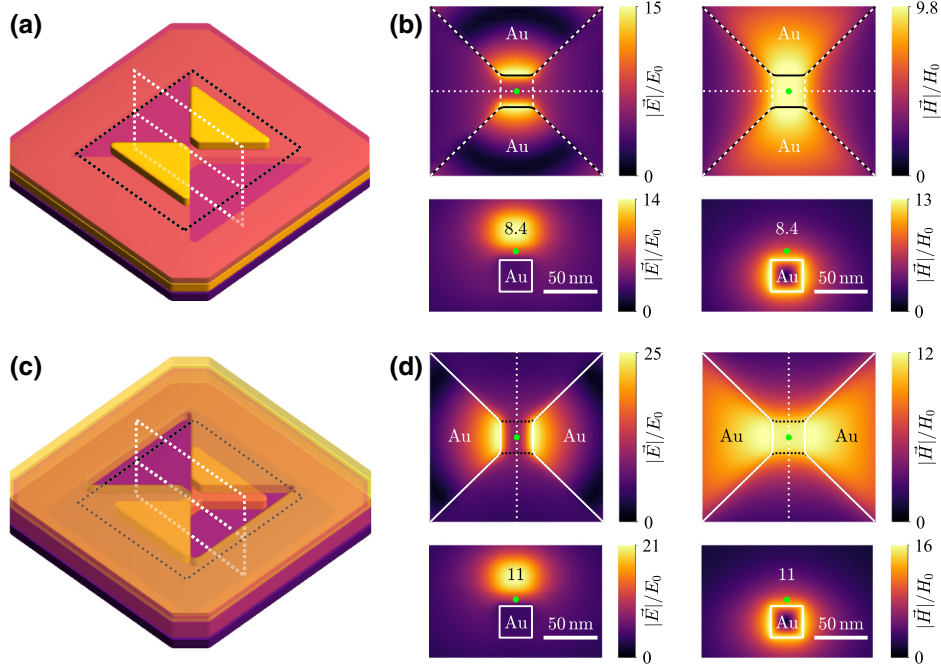


FIG. 9. (a) Schematic drawing of the BBD. A direct bowtie (wing length 110 nm) lies on top of an inverted bowtie (wing length 200 nm), they are mutually rotated by 90° and separated by a 10-nm spacer layer. (b) Distribution of the electric (left) and magnetic (right) fields in the vicinity of the BBD. The top two subplots show the fields in a plane parallel to the individual PAs, namely inside the spacer layer with 5-nm distance from both of them [indicated by a black dotted line in (a)]. The bottom two subplots then show the fields in a vertical plane perpendicular to the metal bridge of the inverted bowtie. The orientation of the plane is outlined by a white dotted line in the schematic drawing in (a) and also in the top two subplots showing the fields in the horizontal plane. (c) Schematic drawing of the BDD. A direct diablo (wing length 110 nm) lies underneath an inverted bowtie (wing length 200 nm), they are mutually rotated by 90° and separated by a 10-nm spacer layer. The distribution of the electric (left) and the magnetic (right) fields around the BDD is plotted in (d), with planar cross sections positioned and oriented in the same manner as in the case of BBD. Note that both BBD and BDD are illuminated with a plane wave polarized along the long axes of the direct PAs and the green point marks the position, in which the electric and magnetic field enhancements are equal in magnitude (with the value specified by the number).

to those obtained for single PAs of comparable size. This indicates that the enhancement mechanism based on the charge accumulation (or the current funneling) at the wing apices is rather robust and resistant to changes in surroundings of the PA. The other proposed design, BDD, possesses electromagnetic hot spot as well, with maximum simultaneous enhancement of 11, while the individual maxima read 21 (electric enhancement) and 16 (magnetic enhancement) [see Fig. 9(d)]. These values are again close to those encountered in single PAs, despite the partial screening of the bottom diablo by its upper counterpart. On the whole, the better performance of isolated diabolos (at least in terms of local field enhancement) imprints itself also into Babinet dimers.

So far we altogether disregard the vectorial nature of electromagnetic fields, which can be important in certain applications. In the designs proposed above, the electric and magnetic fields in the hot spot are perpendicular to each other, but one can achieve also other mutual orientations simply by rotating the vertically stacked antennas with respect to each other. Such control over the local

polarization state of the light is quite valuable, especially when we consider the aforementioned robustness with both the field amplitude and orientation tightly bound to the geometry of the PAs.

In comparison to previous proposals [58,59] and realizations [13] of plasmonic electromagnetic hot spots, our proposal brings two benefits. (i) It enhances both fields on equal basis, i.e., with the same amplitude, resonance frequency, and lateral spatial distribution. (ii) It involves two isolated antennas, which can be adjusted independently, allowing extended tunability of the hot spot.

Interestingly, BBD can be used as Huygens meta-atoms—building blocks of metasurfaces that simultaneously support electric and magnetic modes. Due to the so-called Kerker effect [60] the Huygens metasurfaces exhibit strongly directional scattering of light and allow achievement of metasurfaces with improved transmission efficiency [61]. The realization of Huygens meta-atom reported by Zhang *et al.* [61] is composed of a direct rodlike plasmonic antenna and an inverted rodlike plasmonic aperture positioned above each other, i.e., it can be

viewed as a BBD with bowties replaced with rods. Using bowtie antennas instead of rods shall preserve the directional scattering and enhance the light-matter coupling in the hot spot, paving the way towards multifunctional metasurfaces capable of simultaneous enhancement the light-matter interaction and light manipulation with high transmission efficiency. We note that the BBD discussed above is optimized for the field enhancement and exhibits rather low directionality of the scattering. Simultaneous optimization of both quantities is a subject for further investigation.

Ref. [61] also provides a possible fabrication protocol for the BBD. Alternatively, electron-beam lithography overlay process can be used [62,63].

IV. CONCLUSION

We perform a comprehensive study on the plasmonic antennas featuring electric, magnetic, and electromagnetic hot spots: bowtie and inverted diabolos, diabolos and inverted bowtie, and their dimers, respectively. We combine two types of electric-magnetic complementarity: bowtie and diabolos duality and Babinet's principle.

For a specific resonance frequency, diabolos antennas are significantly smaller than bowtie antennas, and thus harder to fabricate but easier to integrate. For the minimum wing length of 50 nm, bowties covered the energy range up to 2.0 eV while diabolos only up to 1.2 eV. Diabolos antennas also exhibit considerably narrower resonances related to a higher Q factor as a consequence of a lower scattering cross section.

We evaluate figures of merit for different methods of optical spectroscopy and for optical trapping. One of the most important figures of merit is the field enhancement in the hot spot, which is larger for the diabolos antennas than for the bowtie antennas (and also for the electric field than the magnetic field). For the luminescence, the key figure of merit is the radiative and nonradiative decay enhancement. Here, diabolos antennas exhibited a slightly stronger radiative decay enhancement than bowtie antennas but also pronouncedly stronger nonradiative enhancement, making the direct bowtie antenna a preferred option for the electric dipole transitions and the inverted bowties an equivalent alternative of the diabolos for the magnetic dipole transitions.

As for the material composition, we find better figures of merit for the plasmonic antennas made of materials with lower electron scattering rates. Silver is slightly better than gold, while zirconium nitride is considerably worse.

Finally, we propose Babinet dimer antennas enhancing both the electric and magnetic field on an equal basis and forming an electromagnetic hot spot, which finds applications in studies of rare earth ions, optical trapping, metamaterials, or nonlinear optics.

ACKNOWLEDGMENTS

We acknowledge the support by the Czech Science Foundation (Grant No. 17-25799S) and Ministry of Education, Youth and Sports of the Czech Republic (Project CEITEC 2020, No. LQ1601). Part of the work is supported by European Union's Horizon 2020 (Project PETER, No. 767227).

-
- [1] L. Novotny and N. van Hulst, Antennas for light, *Nat. Photonics* **5**, 83 (2011).
 - [2] S. Nie and S. R. Emory, Probing single molecules and single nanoparticles by surface-enhanced Raman scattering, *Science* **275**, 1102 (1997).
 - [3] J. R. Krenn, A. Dereux, J. C. Weeber, E. Bourillot, Y. Lacroute, J. P. Goudonnet, G. Schider, W. Gotschy, A. Leitner, F. R. Aussenegg, and C. Girard, Squeezing the Optical Near-Field Zone by Plasmon Coupling of Metallic Nanoparticles, *Phys. Rev. Lett.* **82**, 2590 (1999).
 - [4] J.-C. Weeber, J. R. Krenn, A. Dereux, B. Lamprecht, Y. Lacroute, and J. P. Goudonnet, Near-field observation of surface plasmon polariton propagation on thin metal stripes, *Phys. Rev. B* **64**, 045411 (2001).
 - [5] H. Gao, Q. Cao, M. Zhu, D. Teng, and S. Shen, Nanofocusing of terahertz wave in a tapered hyperbolic metal waveguide, *Opt. Express* **22**, 32071 (2014).
 - [6] M. Urbietta, M. Barbry, Y. Zhang, P. Koval, D. Sánchez-Portal, N. Zabala, and J. Aizpurua, Atomic-scale lightning rod effect in plasmonic picocavities: A classical view to a quantum effect, *ACS Nano* **12**, 585 (2018).
 - [7] F. Benz, M. K. Schmidt, A. Dreismann, R. Chikkaraddy, Y. Zhang, A. Demetriadou, C. Carnegie, H. Ohadi, B. de Nijs, R. Esteban, J. Aizpurua, and J. J. Baumberg, Single-molecule optomechanics in "picocavities", *Science* **354**, 726 (2016).
 - [8] L. Zhou, Q. Gan, F. J. Bartoli, and V. Dierolf, Direct near-field optical imaging of UV bowtie nanoantennas, *Opt. Express* **17**, 20301 (2009).
 - [9] A. Lee, G. F. S. Andrade, A. Ahmed, M. L. Souza, N. Coombs, E. Tumarkin, K. Liu, R. Gordon, A. G. Brolo, and E. Kumacheva, Probing dynamic generation of hot-spots in self-assembled chains of gold nanorods by surface-enhanced Raman scattering, *J. Am. Chem. Soc.* **133**, 7563 (2011).
 - [10] T. Grosjean, M. Mivelle, F. I. Baida, G. W. Burr, and U. C. Fischer, Diabolos nanoantenna for enhancing and confining the magnetic optical field, *Nano Lett.* **11**, 1009 (2011).
 - [11] M. Lorente-Crespo, L. Wang, R. Ortuno, C. García-Meca, Y. Ekinci, and A. Martínez, Magnetic hot spots in closely spaced thick gold nanorings, *Nano Lett.* **13**, 2654 (2013).
 - [12] I. C. Bicket, E. P. Bellido, S. Meuret, A. Polman, and G. A. Botton, Correlative electron energy loss spectroscopy and cathodoluminescence spectroscopy on three-dimensional plasmonic split ring resonators, *Microscopy* **67**, i40 (2018).
 - [13] Y. Chen, Y. Chen, J. Chu, and X. Xu, Bridged bowtie aperture antenna for producing an electromagnetic hot spot, *ACS Photonics* **4**, 567 (2017).
 - [14] R. M. Bakker, D. Permyakov, Y. F. Yu, D. Markovich, R. Paniagua-Domínguez, L. Gonzaga, A. Samusev,

- Y. Kivshar, B. Luk'yanchuk, and A. I. Kuznetsov, Magnetic and electric hotspots with silicon nanodimers, *Nano Lett.* **15**, 2137 (2015).
- [15] T. Itoh, Y. S. Yamamoto, Y. Kitahama, and J. Balachandran, One-dimensional plasmonic hotspots located between silver nanowire dimers evaluated by surface-enhanced resonance Raman scattering, *Phys. Rev. B* **95**, 115441 (2017).
- [16] Y. Tian, Z. Shuai, J. Shen, L. Zhang, S. Chen, C. Song, B. Zhao, Q. Fan, and L. Wang, Plasmonic heterodimers with binding site-dependent hot spot for surface-enhanced Raman scattering, *Small* **14**, 1800669 (2018).
- [17] T.-H. Yang, Y.-W. Harn, M.-Y. Pan, L.-D. Huang, M.-C. Chen, B.-Y. Li, P.-H. Liu, P.-Y. Chen, C.-C. Lin, P.-K. Wei, L.-J. Chen, and J.-M. Wu, Ultrahigh density plasmonic hot spots with ultrahigh electromagnetic field for improved photocatalytic activities, *Appl. Catal. B* **181**, 612 (2016).
- [18] A. Kinkhabwala, Z. Yu, S. Fan, Y. Avlasevich, K. Müllen, and W. E. Moerner, Large single-molecule fluorescence enhancements produced by a bowtie nanoantenna, *Nat. Photonics* **3**, 654 (2009).
- [19] A. Blank, E. Dikarov, R. Shklyar, and Y. Twig, Induction-detection electron spin resonance with sensitivity of 1000 spins: En route to scalable quantum computations, *Phys. Lett. A* **377**, 1937 (2013).
- [20] M. Kasperczyk, S. Person, D. Ananias, L. D. Carlos, and L. Novotny, Excitation of Magnetic Dipole Transitions at Optical Frequencies, *Phys. Rev. Lett.* **114**, 163903 (2015).
- [21] A. V. Malakhovskii, S. L. Gnatchenko, I. S. Kachur, V. G. Piryatinskaya, and I. A. Gudim, Transformation of the $\text{HoFe}_3(\text{BO}_3)_4$ absorption spectra at reorientation magnetic transitions and local properties in the excited 5F_5 states of the Ho^{3+} ion, *Phys. Rev. B* **96**, 224430 (2017).
- [22] M. L. Juan, M. Righini, and R. Quidant, Plasmon nanooptical tweezers, *Nat. Photonics* **5**, 349 (2011).
- [23] D. R. Smith, J. B. Pendry, and M. C. K. Wiltshire, Metamaterials and negative refractive index, *Science* **305**, 788 (2004).
- [24] M. W. Klein, C. Enkrich, M. Wegener, and S. Linden, Second-harmonic generation from magnetic metamaterials, *Science* **313**, 502 (2006).
- [25] K. Imura, H. Okamoto, M. K. Hossain, and M. Kitajima, Visualization of localized intense optical fields in single gold-nanoparticle assemblies and ultrasensitive Raman active sites, *Nano Lett.* **6**, 2173 (2006).
- [26] P. Kusch, S. Mastel, N. S. Mueller, N. Morquillas Azpiazu, S. Heeg, R. Gorbachev, F. Schedin, U. Hübner, J. I. Pascual, S. Reich, and R. Hillenbrand, Dual-scattering near-field microscope for correlative nanoimaging of SERS and electromagnetic hotspots, *Nano Lett.* **17**, 2667 (2017).
- [27] N. Caselli, F. La China, W. Bao, F. Riboli, A. Gerardino, L. Li, E. H. Linfield, F. Pagliano, A. Fiore, P. J. Schuck, S. Cabrini, A. Weber-Bargioni, M. Gurioli, and F. Intonti, Deep-subwavelength imaging of both electric and magnetic localized optical fields by plasmonic campanile nanoantenna, *Sci. Rep.* **5**, 9606 (2015).
- [28] P. Ghenuche, S. Cherukulappurath, T. H. Taminiau, N. F. van Hulst, and R. Quidant, Spectroscopic Mode Mapping of Resonant Plasmon Nanoantennas, *Phys. Rev. Lett.* **101**, 116805 (2008).
- [29] B. Lahiri, G. Holland, V. Aksyuk, and A. Centrone, Nanoscale imaging of plasmonic hot spots and dark modes with the photothermal-induced resonance technique, *Nano Lett.* **13**, 3218 (2013).
- [30] S. Dodson, M. Haggui, R. Bachelot, J. Plain, S. Li, and Q. Xiong, Optimizing electromagnetic hotspots in plasmonic bowtie nanoantennae, *J. Phys. Chem. Lett.* **4**, 496 (2013).
- [31] K. Schraml, M. Spiegl, M. Kammerlocher, G. Bracher, J. Bartl, T. Campbell, J. J. Finley, and M. Kaniber, Optical properties and interparticle coupling of plasmonic bowtie nanoantennas on a semiconducting substrate, *Phys. Rev. B* **90**, 035435 (2014).
- [32] S. Sederberg and A. Y. Elezzabi, Nanoscale plasmonic contour bowtie antenna operating in the mid-infrared, *Opt. Express* **19**, 15532 (2011).
- [33] B. J. Roxworthy, K. D. Ko, A. Kumar, K. H. Fung, E. K. C. Chow, G. L. Liu, N. X. Fang, and K. C. Toussaint, Application of plasmonic bowtie nanoantenna arrays for optical trapping, stacking, and sorting, *Nano Lett.* **12**, 796 (2012).
- [34] H. Guo, B. Simpkins, J. D. Caldwell, and J. Guo, Resonance spectra of diabolical optical antenna arrays, *AIP Adv.* **5**, 107149 (2015).
- [35] V. Krápek, A. Konečná, M. Horák, F. Ligmajer, M. Stöger-Pollach, M. Hrtoň, J. Babocký, and T. Šikola, Independent engineering of individual plasmon modes in plasmonic dimers with conductive and capacitive coupling, *Nanophotonics* **9**, 623 (2020).
- [36] S. Cakmakyapan, N. A. Cinel, A. O. Cakmak, and E. Ozbay, Validation of electromagnetic field enhancement in near-infrared through Sierpinski fractal nanoantennas, *Opt. Express* **22**, 19504 (2014).
- [37] F. Falcone, T. Lopetegi, M. A. G. Laso, J. D. Baena, J. Bonache, M. Beruete, R. Marqués, F. Martín, and M. Sorolla, Babinet Principle Applied to the Design of Metasurfaces and Metamaterials, *Phys. Rev. Lett.* **93**, 197401 (2004).
- [38] M. Hentschel, T. Weiss, S. Bagheri, and H. Giessen, Babinet to the half: Coupling of solid and inverse plasmonic structures, *Nano Lett.* **13**, 4428 (2013).
- [39] A. Bitzer, A. Ortner, H. Merbold, T. Feurer, and M. Walther, Terahertz near-field microscopy of complementary planar metamaterials: Babinet's principle, *Opt. Express* **19**, 2537 (2011).
- [40] T. Zentgraf, T. P. Meyrath, A. Seidel, S. Kaiser, H. Giessen, C. Rockstuhl, and F. Lederer, Babinet's principle for optical frequency metamaterials and nanoantennas, *Phys. Rev. B* **76**, 033407 (2007).
- [41] H. Mizobata, K. Ueno, H. Misawa, H. Okamoto, and K. Imura, Near-field spectroscopic properties of complementary gold nanostructures: Applicability of Babinet's principle in the optical region, *Opt. Express* **25**, 5279 (2017).
- [42] M. Horák, V. Krápek, M. Hrtoň, A. Konečná, F. Ligmajer, M. Stöger-Pollach, T. Šamořil, A. Paták, Z. Édes, O. Metelka, J. Babocký, and T. Šikola, Limits of Babinet's principle for solid and hollow plasmonic antennas, *Sci. Rep.* **9**, 4004 (2019).
- [43] P. B. Johnson and R. W. Christy, Optical constants of the noble metals, *Phys. Rev. B* **6**, 4370 (1972).
- [44] J. A. Scholl, A. García-Etxarri, A. L. Koh, and J. A. Dionne, Observation of quantum tunneling between two plasmonic nanoparticles, *Nano Lett.* **13**, 564 (2013).

- [45] M. Mivelle, I. Ibrahim, F. Baida, G. Burr, D. Nedeljkovic, D. Charraut, J.-Y. Rauch, R. Salut, and T. Grosjean, Bowtie nano-aperture as interface between near-fields and a single-mode fiber, *Opt. Express* **18**, 15964 (2010).
- [46] J. Zhou, T. Koschny, M. Kafesaki, E. N. Economou, J. B. Pendry, and C. M. Soukoulis, Saturation of the Magnetic Response of Split-Ring Resonators at Optical Frequencies, *Phys. Rev. Lett.* **95**, 223902 (2005).
- [47] E. M. Purcell, Spontaneous emission probabilities at radio frequencies, *Phys. Rev.* **69**, 681 (1946).
- [48] H. A. Atwater and A. Polman, Plasmonics for improved photovoltaic devices, *Nat. Mater.* **9**, 205 (2010).
- [49] Z. Édes, V. Křápek, and T. Šikola, Modeling of plasmon-enhanced photoluminescence of Si nanocrystals embedded in thin silicon-rich oxinitride layer, *Acta Phys. Pol. A* **129**, A70 (2016).
- [50] E. Palacios, S. Park, S. Butun, L. Lauhon, and K. Aydin, Enhanced radiative emission from monolayer MoS₂ films using a single plasmonic dimer nanoantenna, *Appl. Phys. Lett.* **111**, 031101 (2017).
- [51] M. Eggleston, S. Desai, K. Messer, S. Madhvapathy, J. Xiao, X. Zhang, E. Yablonovitch, A. Javey, and M. C. Wu, in *CLEO: 2015* (Optical Society of America, Washington, 2015), p. FTu1E.5.
- [52] D. Gao, W. Ding, M. Nieto-Vesperinas, X. Ding, M. Rahman, T. Zhang, C. Lim, and C.-W. Qiu, Optical manipulation from the microscale to the nanoscale: Fundamentals, advances and prospects, *Light: Sci. Appl.* **6**, e17039 (2017).
- [53] L. Novotny, R. X. Bian, and X. S. Xie, Theory of Nanometric Optical Tweezers, *Phys. Rev. Lett.* **79**, 645 (1997).
- [54] A. S. Baburin, A. M. Merzlikin, A. V. Baryshev, I. A. Ryzhikov, Y. V. Panfilov, and I. A. Rodionov, Silver-based plasmonics: Golden material platform and application challenges [invited], *Opt. Mater. Express* **9**, 611 (2019).
- [55] G. V. Naik, J. Kim, and A. Boltasseva, Oxides and nitrides as alternative plasmonic materials in the optical range [invited], *Opt. Mater. Express* **1**, 1090 (2011).
- [56] See Supplemental Material at <http://link.aps.org/supplemental/10.1103/PhysRevApplied.13.054045> for silver and ZrN plasmonic antennas.
- [57] S. V. Boriskina, T. A. Cooper, L. Zeng, G. Ni, J. K. Tong, Y. Tsurimaki, Y. Huang, L. Meroueh, G. Mahan, and G. Chen, Losses in plasmonics: From mitigating energy dissipation to embracing loss-enabled functionalities, *Adv. Opt. Photon.* **9**, 775 (2017).
- [58] P. Yu, S. Chen, J. Li, H. Cheng, Z. Li, and J. Tian, Co-enhancing and -confining the electric and magnetic fields of the broken-nanoring and the composite nanoring by azimuthally polarized excitation, *Opt. Express* **21**, 20611 (2013).
- [59] B. J. Roxworthy and K. C. Toussaint, Simultaneously tuning the electric and magnetic plasmonic response using capped bi-metallic nanoantennas, *Nanoscale* **6**, 2270 (2014).
- [60] M. Kerker, D.-S. Wang, and C. L. Giles, Electromagnetic scattering by magnetic spheres, *J. Opt. Soc. Am.* **73**, 765 (1983).
- [61] J. Zhang, M. ElKabbash, R. Wei, S. C. Singh, B. Lam, and C. Guo, Plasmonic metasurfaces with 42.3% transmission efficiency in the visible, *Light Sci. Appl.* **8**, 53 (2019).
- [62] G. Yoon, I. Kim, S. So, J. Mun, M. Kim, and J. Rho, Fabrication of three-dimensional suspended, interlayered and hierarchical nanostructures by accuracy-improved electron beam lithography overlay, *Sci. Rep.* **7**, 6668 (2017).
- [63] N. Liu, H. Guo, L. Fu, S. Kaiser, H. Schweizer, and H. Giessen, Three-dimensional photonic metamaterials at optical frequencies, *Nat. Mater.* **7**, 31 (2007).